Double-diffusive thermochemical convection in the liquid layers of planetary interiors : a first numerical exploration with a particle- in-cell method

Mathieu Bouffard

Numéro National de Thèse : 2017LYSEN063

THESE de DOCTORAT DE L'UNIVERSITE DE LYON

opérée par

l'Ecole Normale Supérieure de Lyon

Ecole Doctorale N° 52
Physique et Astrophysique de Lyon (PHAST)

Discipline : Sciences de la Terre et de l'Univers

Soutenue publiquement le 20/09/2017, par :

Mathieu BOUFFARD

Double-diffusive thermochemical convection in the liquid layers of planetary interiors: a first numerical exploration with a particle-in-cell method

Convection thermo-solutale double-diffusive dans les couches liquides internes des planètes: une première exploration numérique avec une méthode « particle-in-cell »

Devant le jury composé de :

Christensen, Ulrich R.	Professeur Max Planck Institute for Solar System Research, Göttingen	Rapporteur
Schaeffer, Nathanaël	Chargé de Recherche CNRS (CR1) ISTerre, Grenoble	Rapporteur
Guervilly, Céline	NERC Independent Research Fellow Newcastle University	Examinatrice
Chillà, Francesca	Professeur Laboratoire de Physique, ENS Lyon	Examinatrice
Labrosse, Stéphane	Professeur LGLTPE, ENS Lyon	Directeur de thèse
Choblet, Gaël	Chargé de Recherche CNRS (CR1) LPG, Nantes	Co-directeur de thèse

Ecole Normale Supérieure de Lyon

Abstract

Université Lyon 1
Laboratoire de Géologie de Lyon

Double-diffusive thermochemical convection in the liquid layers of planetary interiors: a first numerical exploration with a particle-in-cell method

by Mathieu BOUFFARD

Numerous planetary bodies contain internal liquid layers in which convective currents are generated by the combination of buoyancy sources of thermal and compositional origin. The strong difference between the thermal and chemical molecular diffusivities and the possibility of thermochemical coupling at melting or freezing boundaries create a convective regime that is much more complex than pure thermal convection, partly due to the potential occurrence of double-diffusive instabilities. Traditionally, numerical simulations have modeled the dynamics of the liquid part of planetary cores in a more simplistic way by neglecting the diffusivity difference and combining both fields into one single variable, an approximation that is convenient but maybe not relevant. However, distinguishing both fields and dealing with a large or infinite diffusivity ratio makes it compulsory to use numerical methods that minimize numerical diffusion as much as possible. In this thesis, I adapted a semi-Lagrangian particle-in-cell method into a pre-existing dynamo code to describe the weakly diffusive compositional field. I optimized the code for massively parallel computing and validated it on two different benchmarks. I compared the particle-in-cell method to Eulerian schemes and showed that its advantages extend beyond its lower numerical dissipation. Using this new tool, I performed first numerical simulations of rotating pure compositional and thermochemical convection in the limit of null chemical diffusivity. I explored the physics of pure compositional convection and addressed questions related to the existence and the dynamics of a stratified layer below the Earth's core mantle boundary. In particular, I showed that the stratification could potentially be of chemical origin and proposed some mechanisms to explain its formation. In the case of a thermally stratified layer, I performed a scaling analysis of fingering instabilities, wrote the first steps of a linear stability analysis and ran a few simulations of fingering instabilities in the rotating case. The potential effects of the magnetic field and the coupling of thermochemical boundary conditions in planetary cores are finally discussed in this thesis.

Résumé :

De nombreux corps du système solaire possèdent des enveloppes liquides internes, comme par exemple les noyaux métalliques des planètes telluriques et les océans profonds des satellites de glace de Jupiter et Saturne, dans lesquelles se produisent des courants de convection. La modélisation de la dynamique de ces enveloppes est cruciale pour comprendre la génération des champs magnétiques planétaires (pour les noyaux) et pour mieux déterminer l'habitabilité potentielle des satellites joviens. La convection dans ces enveloppes est généralement produite par la combinaison d'au moins deux sources de flottabilité : une source thermique et une source solutale. Une telle situation est plus complexe qu'un régime de convection purement thermique ou purement solutale, d'une part en raison de l'existence d'un couplage thermochimique lorsqu'un processus de fusion ou de cristallisation se produit à l'une des frontières de l'enveloppe, et d'autre part à cause de la forte différence de diffusivité moléculaire entre les champs thermique et compositionnel qui permet potentiellement le développement d'instabilité double-diffusives. Classiquement, ces complexités ont été ignorées dans les simulations numériques de la dynamo terrestre ; les champs thermique et compositionnel ayant été combinés en une seule variable nommée "codensité". Cette approche est sans doute simpliste mais permet d'esquiver une difficulté technique liée à la description du champ compositionnel dont la très faible diffusivité nécessite de recourir à des méthodes numériques adaptées. Cette thèse présente d'abord l'implémentation d'une méthode semi-Lagrangienne du type "particle-in-cell" dans un code de dynamo pré-existant, permettant ainsi de traiter de manière plus réaliste le champ de composition dans les enveloppes liquides internes des planètes. Les optimisations réalisées sont détaillées ainsi que les résultats de tests sur des cas de benchmarks qui valident cet outil. Une comparaison avec des méthodes Eulériennes est également présentée. Une première exploration de la physique de la convection compositionnelle et thermochimique en rotation dans la limite d'un nombre de Prandtl compositionnel infini est ensuite conduite dans le contexte du noyau liquide terrestre. Il est montré que la dynamique convective est très différente de celle de la convection thermique pure. Notamment, les matériaux légers injectés à la frontière graine/noyau liquide sont capables d'atteindre la frontière noyau/manteau et de s'y accumuler pour former une couche chimiquement stratifiée, dont l'existence a été évoquée théoriquement mais qui n'a jamais pu être produite dans de précédentes simulations. Enfin, la dynamique double-diffusive des couches stratifiées est également discutée et de premières simulations de "salt fingers" sont présentées dans le cas rotatif.

Remerciements

Cette thèse marque la fin de sept fantastiques années passées à l'ENS Lyon qui resteront définitivement gravées dans ma mémoire. Si chaque thèse a une histoire bien singulière, la mienne a sans doute été particulièrement mouvementée, dans tous les sens du terme. Ces trois années furent d'abord rythmées par de nombreux allers-retours entre Lyon et Nantes, deux villes très agréables à vivre. À raison d'environ 800 km par trajet et d'une moyenne de deux allers-retours par mois, j'ai sans doute parcouru en train près de 115 000 km pendant ma thèse, soit près de trois fois la circonférence terrestre. Mais ces années de travail furent aussi marquées par des événements familiaux tragiques qui ont profondément influencé leur déroulement. S'il m'a été malgré tout possible de rester jusqu'au bout investi dans cette thèse et de considérer qu'elle a représenté trois belles années, c'est en grande partie grâce à un certain nombre de personnes qu'il me tient à cœur de remercier ici.

Je crois d'abord avoir eu beaucoup de chance en travaillant avec mes deux directeurs, Stéphane Labrosse et Gaël Choblet. Pendant toute ma thèse, ils m'ont accordé une confiance et une liberté précieuses, tout en restant à la fois réactifs et disponibles. J'ai beaucoup apprécié leur lecture attentive de mes mails et documents divers (parfois sans doute un peu longs), leurs conseils judicieux et bien souvent complémentaires, mais aussi leur compréhension, leur soutien et leur bienveillance dans des moments parfois bien difficiles. Depuis le début de cette thèse et jusqu'à la dernière phase de sa rédaction, il a été pour moi extrêmement agréable de travailler avec eux, aussi bien scientifiquement qu'humainement ; aussi je veux pour tout cela leur adresser de sincères et chaleureux remerciements.

Ich bedanke mich bei Uli Christensen für seine Teilnahme an meiner Prüfungskommission und für seine ausschlaggebende Bemerkungen. Je remercie également Nathanaël Schaeffer pour ses conseils utiles lors de mon comité de suivi de thèse et pour avoir accepté de rapporter ce travail ainsi que Francesca Chillà et Céline Guervilly dont j'appécie beaucoup la participation à mon jury de thèse.

Tout au long de ces années, notre bureau des thésards et notre laboratoire lyonnais ont été bien animés grâce à de nombreux collègues et amis: Jean-Alexis, Théo, Hélène, Ulysse, Adrien, Nadège, Anaïs, Marie, Rémi, Yoann, Maëlis, Fanny, Ched, Ludo, Marine, Alexandra... Merci pour ces chouettes années passées avec vous ! Merci aussi à Pierre Thomas pour sa culture inépuisable, ainsi qu'à Fred Chambat, Patrick Thollot et bien d'autres grâce auxquels les discussions du midi ne manquaient ni d'intérêt ni d'humour.

J'ai également été très bien accueilli dans le labo nantais et, malgré ma présence intermittente, j'ai pu tisser des liens avec de nombreuses personnes. Merci à Ludivine, Marine, Laetitia, Ianis, Méric, Nadia, Diana, Joana, Alice, Marion, Felipe, Maïwenn, Katia et tous ceux que j'ai oubliés pour les moments très agréables et enrichissants passés avec vous ! Plus largement, je remercie toutes les personnes du LPG pour leur accueil et leur sympathie.

Au travers de divers congrès et workshops, j'ai aussi rencontré de nombreuses personnes auxquelles je dois beaucoup pour leurs conseils et leur sympathie qui m'ont permis d'apprécier tous les moments passés dans cette communauté scientifique.
- Un grand merci à Alex Fournier et Julien Aubert pour la considération, la sympathie et l'aide précieuse qu'ils m'ont témoignées tout au long de cette thèse.
- À Philippe Cardin, pour son optimisme enthousiasmant, nos *running sessions* et pour les discussions éclairantes que j'ai pu partager avec lui.

- À Hagay Amit, pour sa gentillesse et ses éclaircissements très utiles.
- À Renaud Deguen, Thierry Alboussière et Nicolas Coltice, pour leurs conseils et leur simplicité attachante.
- À Gabriel Tobie pour ses conseils et sa sympathie. C'est promis, j'appliquerai bientôt mon code aux satellites de glace.
- À Yanick Ricard pour ses cours inspirants qui ont confirmé mon goût pour la géophysique lorsque j'étais en master.
- À Henri Samuel pour m'avoir permis de sortir de quatre mois de blocage dans le développement de la méthode de traceurs.
- I thank Paul Tackley for his help on various topics during my PhD.
Plus largement, je remercie les autres thésards et chercheurs de la communauté géodynamo/Deep Earth que j'ai eu la chance de rencontrer et avec qui j'ai pu partager des moments aussi instructifs que conviviaux.

Cette thèse termine de longues études pendant lesquelles ma famille a toujours approuvé et soutenu mes choix, sans jamais chercher à les imposer. Parce qu'ils ont tant contribué à ce que je suis aujourd'hui, je veux remercier mes parents, pour leur amour et leur soutien depuis toujours, et ce malgré les épreuves traversées, ma grand-mère pour nos discussions enrichissantes et le vif intérêt qu'elle a porté à mes travaux scientifiques dès leur commencement, mon frère Nathan, pour son soutien franc et sincère, mon cousin Thomas pour nos débats philosophiques aussi passionnants que constructifs, ainsi que tout le reste de ma famille, pour tous les très bons moments passés ensemble.
Un grand merci également à Luc et Véro, Thérèse et Yves pour leur gentillesse et leur générosité, ainsi qu'à tous les autres membres de leur famille dont il me semble maintenant faire partie.

Bien des choses n'auraient pas été possibles sans les amis, leur soutien, les moments partagés autour de la danse, les câlins, fous rires, discussions et vacances passées ensemble... Du fond du cœur, merci à :
- Anne, pour ton amitié, ton écoute, pour ces heures passées en salle de danse à préparer compétitions et chorégraphies, et pour m'avoir montré ce qu'est le courage,
- Julien, pour ton amitié précieuse et ton affection, pour toutes nos discussions passionnées sur la danse et bien d'autres sujets, (et aussi pour ton obstination plus grande que la mienne qui m'a poussé à progresser encore plus en danse !),
- Valérie, pour être une amie si inspirante, avec qui chaque moment est à la fois profondément agréable et porteur,
- Robin, pour être un ami attentioné et plein d'humour,
- Delphine, pour ta spontanéité pétillante et ta bonne humeur,
- Marie L., pour ta gentillesse et ta douceur inégalables,
- Laure, en souvenir de notre amitié née autour de la danse et qui se prolonge désormais bien au-delà,
- Pol, pour le plaisir de te revoir à chacun de tes retours en France, nos diverses visites ensemble et nos nombreuses discussions,
- Marie M., pour être une amie géniale et avoir été coloc attentionnée. De la même manière que nous nous sommes retrouvés à Lyon trois ans après le lycée, j'espère que le hasard de la vie nous remettra aussi souvent que possible sur des chemins communs !
- Adrie, pour avoir fait naître chez moi une véritable passion qui illumine désormais presque chacune de mes journées.
Merci également à tous les autres amis de la danse, de l'ENS et d'ailleurs : Morgane, Léa, Quentin, Clara, Baptiste, Eva, Maxime, Thomas M., Thomas J., Erwan, Colin (pour avoir été mon premier stagiaire, puis un véritable ami), Sylvain, Dimitri, Marlène, Mathilde N., Alexis W., Adrien J. et Claire L., Martin et Sophie, Nicolas, Julia, Adrien et Isa, Audrey, Cathy et Julien...

Je ne peux hélas tous les citer ni les remercier très personnellement ici, mais chacun sait l'affection que je lui porte.

Quelques remerciements spéciaux:

- À Claire Chell, pour m'avoir aidé à retrouver ma voix lorsqu'elle était bien malmenée.
- Au réseau TGV de la SNCF sans lequel l'organisation de cette thèse aurait été bien différente. J'ai d'ailleurs pu constater, contre une croyance fort répandue, que la majorité des TGV sur cette ligne sont à l'heure.
- À Jaïna pour ses léchouilles réconfortantes.

Enfin, bien sûr, merci Benoît, pour ton amour et ton soutien sans faille qui m'ont porté plus haut pendant ces années.

Table des matières

1. Introduction **1**

2. Modélisation **13**
2.1 Principales approximations 14
2.1.1 Géométrie 14
2.1.2 Approximation de Boussinesq 14
2.1.3 Cadre de l'étude de la convection thermochimique 15
2.2 Principales équations 16
2.2.1 Conservation du moment 16
2.2.3 Conservation de l'énergie 17
L'hypothèse de codensité 18
L'approximation de nombre de Lewis infini 19
2.2.4 Equation d'induction 20
2.2.5 Equations complètes 21
2.3 Conditions aux limites 21
2.3.1 Conditions sur la vitesse 21
2.3.2 Conditions magnétiques 21
2.3.3 Conditions aux limites thermochimiques 21
Conditions indépendantes de type Neumann 23
Couplage thermochimique 26
2.4 Sur la nécessité d'utiliser une méthode numérique faiblement diffusive 29

3. Méthode numérique **31**
3.1 Distribution des traceurs dans la grille sphérique 33
3.1.1 Distribution initiale 33
3.1.2 Caractéristiques de la distribution 34
3.2 Schéma numérique 36
3.3 Interpolation des champs scalaires des traceurs vers la grille 37
3.3.1 Interpolation trilinéaire 37
3.3.2 Interpolation d'ordre plus élevé 38
3.3.3 Problème des cellules vides 39
3.4 Advection des traceurs 40
3.4.1 Accumulations et trous de traceurs 40
3.4.2 Interpolation de la grille vers les traceurs 41
a) Interpolation trilinéaire 41
b) Interpolations d'ordre plus élevé 42
Correction de la divergence 45
3.4.3 Interpolation aux pôles 45
3.4.4 Schéma temporel 45
3.4.5 Advection en coordonnées Cartésiennes 46
3.4.6 Comparaison des méthodes d'interpolation et des schémas temporels 46
Advection par un vortex de Taylor-Green 2D 47
Rotation d'un patch Gaussien 49
3.5 Diffusion 49
3.6 Implémentation des conditions aux limites 52
3.7 Conclusion et discussion 53

4. Optimisations pour calculateurs massivement parallèles **55**
4.1 Parallélisme 57

4.1.1 MPI 58
4.1.2 OpenMP 59
4.2 Optimisations des interpolations 60
4.2.1 Repérage des traceurs 60
4.2.2 Calcul des poids 61
Choix de la méthode 61
Stockage des poids 61
4.2.3 Tri des traceurs et optimisation du cache 61
Court rappel de l'architecture des systèmes de cache 62
Tri des traceurs 63
Méthode de "cell caching storage" 66
4.3 Optimisation du traitement des cellules vides pour les faibles rapports d'aspect 66
4.3.1 Méthode de régularisation de grille 67
Construction d'une grille auxiliaire 68
Interpolation des traceurs vers la grille auxiliaire 68
Complétion de la grille auxiliaire 70
Complétion de la grille sphérique initiale 71
Résultats et comparaison de l'efficacité pour différents rapports d'aspect 72
4.4 Solutions périodiques 73
4.5 Performances du code hybride 73
4.6 Conclusion et discussion 75

5. Validation et comparaison avec des méthodes Eulériennes 77
5.1 Benchmarking 78
5.1.1 En coquille sphérique 78
Résultats des benchmarks 78
Estimation du nombre optimal de traceurs 82
5.1.2 En sphère pleine 83
5.2 Comparaison avec des méthodes Eulériennes 83
5.2.1 Comparaison avec les schémas TVD et WENO sur des tests 1D et 2D 86
Advection d'un rectangle 1D 86
Tests de rotation 2D 87
5.2.2 Discussion 89
5.3 Autres avantages de la méthode de traceurs 91
5.3.1 Relaxation de la contrainte sur le nombre de Péclet 91
5.3.2 Suivi de la trajectoire des traceurs 91
Advection par un champ de vitesse synthétique 93
5.3.3 Visualisation 95
5.4 Conclusions 97

Convection chimique pure non-magnétique en rotation dans la limite de diffusivité nulle 99
6.1 Différences qualitatives avec la convection thermochimique à bas nombre de Lewis 101
6.2 Etude de la convection chimique pure 104
6.2.1 Démarrage de la convection 104
6.2.2 Instabilité des panaches 108
6.2.3 Evolution vers un état statistiquement stationnaire 108
Formation d'une couche chimiquement stratifiée sous la frontière supérieure 108
Forme du profil compositionnel 113
Variations latérales 115
6.3 Discussion et directions futures 118

7. Formation et dynamique d'une couche stratifiée sous la frontière noyau/manteau 121
7.1 Formation d'une couche chimiquement stratifiée sous la frontière noyau/manteau 123
7.1.1 Paramètres numériques 123
7.1.2 Mesure de l'épaisseur 123
7.1.3 Résultats préliminaires 125
Evolution temporelle 125
Propriétés de l'écoulement 126
7.2 Discussion: extrapolation au cas de la Terre 127
7.3 "Salt fingers" dans une couche thermiquement stratifiée 129
7.3.1 Analyse d'échelle 129
7.3.2 Analyse de stabilité linéaire 132
7.3.3 Simulations numériques 134
7.3.4 Discussion 137

8. Conclusion générale et perspectives 141
8.1 Résumé des principales contributions de cette thèse 141
8.2 Discussion sur le rôle du couplage thermochimique et du champ magnétique 142
8.3 Travail futur et perspectives 144
8.3.1 Améliorations numériques 144
8.3.2 Questions ouvertes sur la dynamique du noyau 144

A Construction d'une boucle convective axisymétrique 147

B Simulation préliminaire de l'océan de magma primitif de la Terre 151

C Vers des dynamos thermochimiques 153

D Article publié 157

Contents

Abstract iii

Remerciements v

Contents xi

1 Introduction 1

2 Modeling 13
2.1 General approximations . . . 14
2.1.1 Geometry . . . 14
2.1.2 The Boussinesq approximation . . . 14
2.1.3 Framework for the study of thermochemical convection . . . 15
2.2 General equations . . . 16
2.2.1 Momentum conservation . . . 16
2.2.2 Energy conservation . . . 17
2.2.3 Chemical transport equation . . . 18
The codensity hypothesis . . . 18
The infinite Lewis number approximation . . . 19
2.2.4 Induction equation . . . 20
2.2.5 Full set of equations . . . 21
2.3 Boundary conditions . . . 21
2.3.1 Kinematic conditions . . . 21
2.3.2 Magnetic conditions . . . 21
2.3.3 Thermochemical boundary conditions . . . 21
Independent thermal and compositional Neumann boundary conditions . 23
Thermochemical coupling . . . 26
2.4 On the necessity of a diffusion-free numerical method . . . 30

3 Numerical method 31
3.1 Particles distribution in a spherical grid . . . 33
3.1.1 Initial distribution . . . 33
3.1.2 Characteristics of the particles distribution . . . 34
3.2 General numerical scheme . . . 36
3.3 Interpolation of scalar fields from particles to grid nodes . . . 37
3.3.1 Trilinear interpolation . . . 37
3.3.2 Higher order interpolation schemes . . . 38
3.3.3 Problem of "empty cells" . . . 39
3.4 Advection of particles . . . 40
3.4.1 Tracers clustering and depletion . . . 40
3.4.2 Interpolation from grid to particles . . . 41
a) Trilinear interpolation . . . 41
b) Higher order interpolation schemes . . . 42

Correction for non-divergent flows . . . 45
3.4.3 Interpolation at poles . . . 45
3.4.4 Time scheme . . . 45
3.4.5 Advection in Cartesian coordinates . . . 46
3.4.6 Comparison of interpolation methods and advection schemes . . . 46
Advection by a 2D Taylor-Green vortex . . . 47
Rotation of a Gaussian patch . . . 49
3.5 Diffusion . . . 49
3.6 Numerical implementation of boundary conditions . . . 52
3.7 Conclusion and discussion . . . 53

4 Optimizations for High Performance Computing 55
4.1 Parallelism . . . 57
4.1.1 MPI . . . 58
4.1.2 OpenMP . . . 59
4.2 Optimization of interpolations . . . 60
4.2.1 Particles tracking . . . 60
4.2.2 Computation of the interpolation weights . . . 61
Choice of the weighting method . . . 61
Weights storage . . . 61
4.2.3 Particles sorting and optimization of cache use . . . 61
Brief reminder of cache systems architecture . . . 62
Particle sorting . . . 63
Cell caching storage . . . 66
4.3 Optimization of the treatment of empty cells for low aspect ratios . . . 66
4.3.1 Grid regularization method . . . 67
Construction of a coarser grid . . . 68
Interpolation from tracers to the coarse grid . . . 68
Completion of the coarse grid . . . 70
Completion of the fine grid from the coarse grid . . . 71
Results and comparison of efficiency for different aspect ratios . . . 72
4.4 Periodic solutions . . . 73
4.5 Scaling of the hybrid code . . . 73
4.6 Conclusion and discussion . . . 75

5 Validation and comparison with Eulerian methods 77
5.1 Benchmarking . . . 78
5.1.1 Spherical shell geometry . . . 78
Benchmarks results . . . 78
Estimation of the adequate number of tracers . . . 82
5.1.2 Full sphere geometry . . . 83
5.2 Comparison with Eulerian methods . . . 83
5.2.1 Comparison with TVD and WENO schemes on simple 1D and 2D advection tests . . . 86
Advection of a 1D rectangle . . . 86
2D rotating tests . . . 87
5.2.2 Discussion . . . 89
5.3 Other advantages of the PIC method . . . 91
5.3.1 Relaxation of the Peclet number constraint . . . 91
5.3.2 Monitoring of the trajectories of particles . . . 91
Advection by a synthetic convective-like velocity field . . . 93

5.3.3 Visualisation . . . 95
5.4 Conclusions . . . 97

6 Non-magnetic rotating compositional convection in the diffusivity-free limit 99
6.1 Qualitative differences with thermochemical convection at low Lewis number . . . 101
6.2 Study of pure compositional convection . . . 104
6.2.1 Convection onset . . . 104
6.2.2 Blob instability . . . 108
6.2.3 Evolution to a statistically steady-state . . . 108
Formation of a chemically stratified layer below the top boundary . . . 108
Shape of the stratified chemical profile . . . 113
Lateral variations . . . 115
6.3 Discussion and future directions . . . 118

7 Formation and dynamics of a stratified layer below the core mantle boundary 121
7.1 Formation of a chemically stratified layer below the Earth's core mantle boundary 123
7.1.1 Numerical setup . . . 123
7.1.2 Measure of the thickness . . . 123
7.1.3 Preliminary results . . . 125
Time evolution . . . 125
General characteristics of the flow . . . 126
7.2 Discussion: extrapolation to the Earth's case . . . 127
7.3 Salt fingers in a thermally stratified layer . . . 129
7.3.1 Scale analysis . . . 130
7.3.2 First steps of a linear stability analysis . . . 132
7.3.3 Numerical simulations . . . 134
7.3.4 Discussion . . . 137

8 General conclusion and perspectives 141
8.1 Summary of the main contributions of this thesis . . . 141
8.2 Discussion on the role of thermochemical coupling and magnetic field . . . 142
8.3 Future work and perspectives . . . 144
8.3.1 Numerical improvements . . . 144
8.3.2 Open questions in core dynamics . . . 144

A Construction of an axisymmetric convective loop 147

B Preliminary simulation of the primitive magma ocean of the Earth 151

C Towards thermochemically driven dynamos 153

D Published article 157

À mon grand-père, pour m'avoir transmis une passion pour les sciences, la musique et, sans doute, une certaine philosophie de la vie.

Chapter 1

Introduction

Far from being inert and motionless objects, most planetary bodies are animated by various movements. One may of course immediately think about the rotation of a planet around its star or that of a satellite around its planet, but large-scale motion can also occur within the planetary body itself. Some movements can consist solely in a deformation, like those triggered by tidal effects. On the contrary, other movements are associated to a real transport of matter across the entire body or within a smaller portion of the latter, a phenomenon called "convection". Evidence for the existence of convective currents in the most superficial layers of planets sometimes relies on simple direct observations of their surface: the effect of winds in the atmosphere of the Earth is felt by everyone and proving their existence on other planets such as Jupiter sometimes requires no more than a basic telescope. Convection in terrestrial seas and oceans is somewhat harder to evidence. If winds-driven surface movements leap to the eye, the deep ocean was assumed to be perfectly static by early oceanographers. The discovery of the global thermohaline circulation dates back 1908 (Sandström, 1908) and more quantitative measurements of oceanic currents since 2004 have improved our understanding of the internal motions of oceans (Baehr et al., 2004).

Acknowledging the existence of deeper movements below the surface of the Earth and other planets took even more time as definitive proofs could only be obtained by collecting indirect evidence of these movements based, for instance, on geological observations. A major example is plate tectonics, which has been directly related to solid-state convection in the Earth's mantle on geological time-scales by Pekeris (1935) then Holmes (1945), though the theory of mantle convection became generally accepted only in the 1960s. The later development of numerical simulations and imaging methods such as seismic tomography that permit a direct visualization of convective structures then confirmed the theory of a convecting mantle. On other telluric planets such as Mars and Venus, the presence of geological structures like volcanoes is sometimes interpreted as the consequence of a convective upwelling in the underneath mantle (Harder and Christensen, 1996; Nimmo and McKenzie, 1998). In icy satellites like Europa, several geological observations of the surface also suggest the present or past existence of some type of convection in the outer ice shell (Miyamoto et al., 2005). Among other observations, the discovery of a magnetic field at the planetary scale sets particularly interesting constraints on the internal dynamics of a planet. In our Solar system, space missions such as Mariner 10 and Galileo have confirmed the presence of magnetic fields around Ganymede (Kivelson et al., 1996), Mercury (Ness, 1979), Jupiter, Saturn, Uranus and Neptune. Magnetic fields probably also existed in the past around Mars and the Moon (Stevenson, 2003). Once attributed to a deeply buried giant magnet (Gilbert, 1958), it is nowadays consensual that the presence of a magnetic field around the Earth and other planetary bodies is most likely produced by dynamo action associated to convective motions in an electrically conducting fluid, *i.e.* the liquid portions of metallic cores for telluric planets and the layer of metallic H/He in giant planets (Braginsky and Roberts, 1995; Roberts and King, 2013; Stevenson, 2003). In addition, measures of magnetic induction by Galileo indicate the presence of liquid water oceans below the surface ice layer of Europa (Khurana et al., 1998; Kivelson et al., 2000) and Ganymede (Kivelson et al., 2002) that are probably convecting.

Initiating and sustaining convective currents requires a source of energy. Even though the mechanical forcing triggered by celestial movements (such as precession and nutation) can excite internal motions in some cases, convective movements within planets are usually caused by the presence of density inhomogeneities. In the self-gravitational field created by the planet, the latter induce an Archimedean buoyancy force able to initiate and maintain large-scale motions. In planetary interiors, density anomalies are most often the consequence of a combination of thermal and compositional effects.

Thermal fluctuations are almost always present in planets and can be due to energy received at the surface (for instance, the radiative heat emitted by the Sun that drives atmospheric and oceanic currents on Earth), or be a consequence of the release, over geological times, of the heat accumulated by the planet during its initial formation. For large enough planetary bodies, convection is usually a more efficient way to transport heat than thermal conduction through a motionless body. Secular cooling can also cause indirect thermal fluctuations within the planet, for instance via the release of latent heat if it triggers the gradual crystallization of some initially molten material. Other important sources of heat release include the decay of incorporated radioactive elements such as potassium, uranium and thorium. In planets, the dynamics of some layers is essentially driven by thermal convection. This is the case for the Earth's mantle in which the combination of secular cooling and radioactive heat production is sufficient to generate large-scale motion. Chemical effects are generally assumed to play a secondary role in mantle convection although they might be locally important, for example for the dynamics of plumes (Samuel and Farnetani, 2003) or that of possible thermochemical piles at the bottom of the mantle (Hernlund et al., 2015). It should also be noted that mantle convection may be indirectly influenced by the presence of chemicals such as water and CO_2 (Sandu et al., 2011), even if the role of the latter on buoyancy is neglected. Such chemicals indeed have a potentially strong effect on viscosity (Kohlstedt, 1992) and solidus temperature (Hirth and Kohlstedt, 1996; Eggler, 1976) and could favor some specific convective regimes (Mian and Tozer, 1990). The terrestrial dynamo may also have been driven exclusively by thermal convection in the metallic core of the Earth for the first billion years of its existence before the solid inner core nucleated, although recent re-estimations of the thermal conductivity (Pozzo et al., 2012; Gomi et al., 2013) and the possibility of crystallization of MgO or SiO_2 at the core mantle boundary have put this hypothesis into question (O'Rourke and Stevenson, 2016; Hirose et al., 2017).

Density anomalies can also be caused by local variations of the chemical composition. Planets are indeed not made of pure materials and incorporate numerous chemical elements in various concentrations and relative abundances (Allègre et al., 1995). During some thermodynamical reactions such as, for example, a crystallization or fusion, some elements partition preferentially in one phase for which they have more affinity, causing an enrichment near the fusion/crystallization front of either the solid or liquid phase in the corresponding element. An example of such a phenomenon that is of great importance for this thesis can be found in the metallic core of the Earth. Mainly formed of iron and nickel, the latter also incorporates a small amount (about 10 weight percents) of lighter elements whose precise nature is still debated (Poirier, 1994; Hirose et al., 2013). As the Earth's core cools down through geological times, its average temperature decreases. For reasons related to the thermodynamics of this system, it eventually started to crystallize at its center to form a solid inner core around 1 Ga ago, although the age of the inner core still varies among core evolution models (Labrosse, 2015). Some of the candidate light elements incorporated to the fluid core (especially oxygen) preferentially migrate into the liquid phase during the crystallization process, causing a local enrichment in light elements in the liquid outer core upon the inner core boundary (denoted ICB in the following). Immediately above the ICB, the liquid is lighter than the bulk outer core, resulting in a gravitational instability that can

drive convective currents. Crystallization and fusion may not be restricted to freezing/melting boundaries only and could also occur within a larger volume in a regime of iron snow, as proposed for Mercury (Vilim et al., 2010; Dumberry and Rivoldini, 2015) and Ganymede (Hauck et al., 2006; Zhan and Schubert, 2012; Christensen, 2015).

The case of convection driven both by thermal and compositional effects is referred to as *"thermochemical convection"* and is common among most liquid layers of planets on which we now concentrate, with various relative contributions of thermal and chemical effects. A first example is the thermohaline circulation in terrestrial oceans which is driven both by variations of temperature and salinity, the latter being usually the consequence of evaporation and melting (resp. freezing) of ice (resp. sea water). In the deep Earth, as mentioned above, the outer core of the Earth also falls in this category with compositional convection contributing to the dynamo power by up to 80% (Lister and Buffett, 1995a). Thermochemical convection is also likely present in the buried water oceans of many icy satellites such as Ganymede, Europa, Titan and Enceladus. These liquid layers have estimated thicknesses ranging from a a few tens of kilometers for Enceladus (Čadek et al., 2016; Beuthe et al., 2016) up to several hundreds for Ganymede (Vance et al., 2014) and would be in contact with an icy layer, at least at their top. In these layers, compositional effects originate from variations of salt concentration caused by melting or freezing of the ice layer(s) in contact with the liquid ocean (Zolotov and Shock, 2000). Another interesting example is the primitive magma ocean which is thought to have existed just after the initial formation of the Earth (Labrosse et al., 2007). The rapid cooling of this layer (due to the enormous radiative heat flow at its surface) caused the crystallization of its bottom with a subsequent local enrichment in heavy elements (Boukaré et al., 2015).

In these systems, a major difference between the temperature and compositional fields has to do with their molecular diffusion rates which can differ by several orders of magnitude. Their ratio is called the Lewis number:

$$Le = \frac{\kappa_T}{\kappa_C}, \tag{1.1}$$

where κ_T and κ_C are the thermal and chemical molecular diffusivities, respectively. In oceans and giant planets it is estimated to be close to 100 (Stern, 1960; Stevenson and Salpeter, 1977) and would reach 1000 in the case of planetary metallic cores (Braginsky and Roberts, 1995).

The situation of a convecting system driven by two buoyancy sources with different diffusivities is potentially much more complex than a system driven by pure thermal or pure chemical convection, for at least two reasons. First, when melting/freezing occurs, the thermal and chemical fields at the crystallizing/melting front are usually not independent; the amount of solute released being proportional to the melting/freezing rate and therefore to the local heat flux. This creates a potentially complex *thermochemical coupling*. Second, since both fields contribute to the overall density gradient, two main cases may be distinguished:

1. The global contribution of both fields is unstable to overturning convection. In astrophysics, this is usually more precisely defined using the Ledoux criterion (Ledoux, 1947) which states the following condition for instability:

$$\left(\frac{\partial \ln T}{\partial \ln p}\right) - \left(\frac{\partial \ln T}{\partial \ln p}\right)_{ad} > \left(\frac{\partial \ln \mu}{\partial \ln p}\right), \tag{1.2}$$

   where T is the temperature, μ the mean molecular weight, p is the pressure and the subscript "ad" denotes an adiabatic gradient. In this case the convective regime may consist of some kind of mix between pure thermal and pure chemical convection, which, due to

their different diffusivities, show very contrasting respective features (cf. the experiments by Cardin and Olson (1992)).

2. The global contribution of the two fields produces a stable density gradient *i.e.* the region is stable according to the Ledoux criterion. If both fields have a stabilizing effect, then no vertical movements are allowed (unless the above/underneath convection can penetrate the layer to some extent). However, the situation is much more complex if one of the fields has a destabilizing effect on the density gradient. In this case, even though the net contribution of both fields produces a stable density gradient, vertical movements can develop due to the difference of diffusivities and are qualified of *"double-diffusive convection"* (Turner, 1979).

FIGURE 1.1: Visualization of salt fingers in a laboratory experiment. A salty solution is poured at the top of a liquid with stable temperature gradient. The downward-moving fingers are made visible by adding fluorescein to the salt and lighting through a slit from below. Taken from Huppert and Turner (1981a).

The existence of double-diffusive instabilities may seem counter-intuitive at first, and this is the reason why many famous scientists such as Jevons and Rayleigh failed in discovering it, even when they observed it in experiments (Schmitt, 1995, 1996). Melvin Stern was the first to understand that the observed features were more than just an anecdotic property of thermal convection (Stern, 1960). Double-diffusive convection is known to exist in two different sub-types. If the slow diffuser is unstable, instabilities resembling elongated fingers can grow (see figure 1.1) and this case is therefore referred to as *fingering* convection. If the slow diffuser is stabilizing, vertical oscillations can be excited and typically evolve to a thermochemical layering as visible on figure 1.2. This second type of double-diffusive instability is called *diffusive* convection. The mechanisms by which each instability can grow are illustrated for a heat/salt system on figure 1.3. In the finger configuration, when a parcel of hot and salty fluid is displaced downward by random fluctuations, it is surrounded by colder and fresher water. Because thermal diffusion operates quickly, the parcel rapidly loses its heat and equilibrates thermally with its surrounding. However, during this process, it retains part of its salinity since salt is a slower diffusor than heat. Once it has equilibrated thermally, the portion of fluid is saltier thus denser than its surrounding and can therefore continue to sink. The reverse reasoning applies for the diffusive case. If a parcel of fluid is displaced downward, it rapidly adjusts its temperature and retains salinity. However,

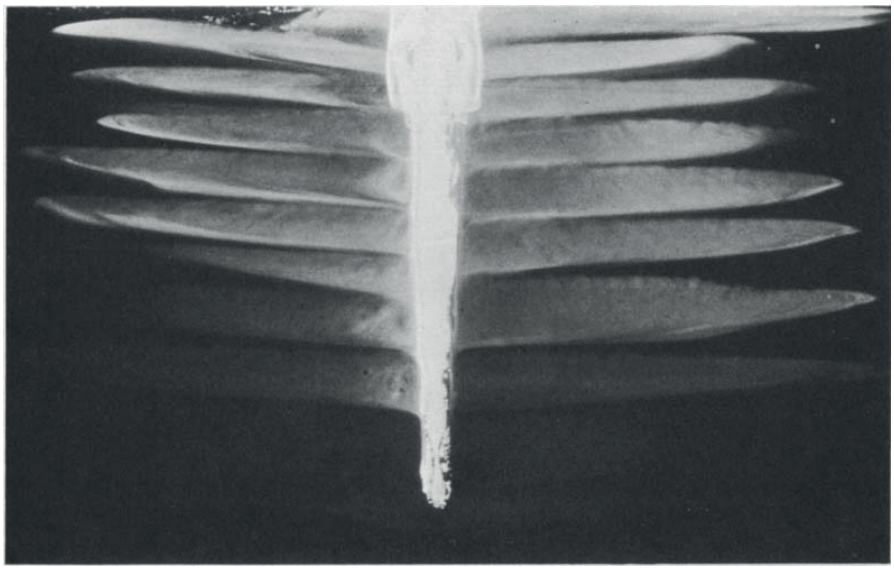

FIGURE 1.2: A series of layers formed by the melting of an ice block into a salinity gradient. Fluorescein dye, originally frozen into the ice, has been illuminated from the side to show the final distribution of the fresh water. Taken from Huppert and Turner (1980).

since the background salinity now increases with depth, the parcel becomes lighter than the ambient fluid at the same level and the buoyancy force drives it upward. But when back to its original position, the parcel is lighter than it was originally because of the heat gained. As a result, the parcel gains some energy and overshoots its original equilibrium position. This oscillatory process then repeats over and over. A summary of the various regimes of convective instability can be visualized on figure 1.4. It is interesting to understand that, contrary to the classic Rayleigh-Bénard convection in which it has a stabilizing effect, thermal diffusion *drives* double-diffusive convection by allowing the gravitational energy stored in the unstable component to be released, lowering the center of mass of the system.

The theory of double-diffusive convection has been essentially developed in the contexts of oceanography and astrophysics. Double-diffusive instabilities have been frequently observed in terrestrial oceans (Kunze, 2003), predicted in stars (Rosenblum et al., 2011), and extensively studied in non-rotating systems both theoretically (Huppert, 1976; Huppert and Turner, 1981b; Wood et al., 2013), experimentally (Turner, 1968; Huppert and Linden, 1979; Huppert and Turner, 1980; Beckermann and Viskanta, 1988) and numerically (Rosenblum et al., 2011; Traxler et al., 2011a,b), to give only a few references. Although several aspects still remain obscure, the physics of double-diffusive convection is relatively well understood. The linear stability analysis has been successful in accounting for the growth and size of instabilities, while weakly non-linear studies have permitted to discover various secondary instabilities explaining the planform selection of salt fingers, the saturation of fingering and diffusive instabilities as well as the transitions to thermochemical staircase regimes which are typical of double-diffusive convection (Radko, 2013).

The role played by double-diffusive instabilities is however not always consensual (see chapter 11 of the book by Radko (2013) for a review in different contexts). It is commonly admitted that double diffusive convection plays a role in various oceanic phenomena, though how exactly it does so still remains a controversial issue. Fingering convection is thought to be an important contributor to mixing processes in terrestrial oceans (Lee et al., 2014) and various examples corroborate this affirmation. For instance, measurements from the C-SALT program (Schmitt

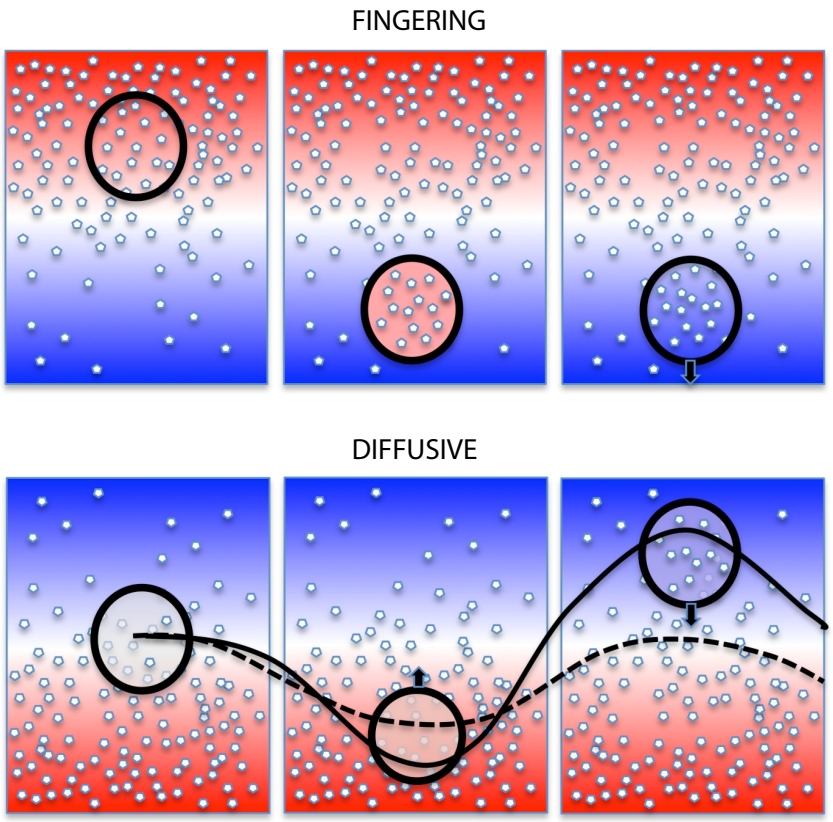

FIGURE 1.3: Schematic illustration of fingering (top) and diffusive (bottom) instabilities. The temperature field is represented with colors from red (hot) to blue (cold). The concentration in heavy salts is proportional to the density of white particles. Taken from Garaud (2013).

et al., 1987) showed that the transport of salt by the Caribbean staircase is more efficient than that of the North Atlantic turbulent subtropical gyre and acts to inject salt into the Antarctic Intermediate Water which affects thermohaline circulation. Similarly, Zodiatis and Gasparini (1996) showed that vertical transport of heat and salt by the Tyrrhenian thermohaline staircase could play a major role in controlling the Mediterranean climate. At a larger scale, fingering convection may also attenuate the oceanic signatures of climate changes (Johnson and Kearney, 2009) and would enhance the mixing and supply of nutrients in different regions, with biological implications (McGillicuddy et al., 1998). The role played by diffusive mixing is less clear but could be important at high latitudes (Radko, 2013).

In astrophysics, diffusive convection is referred to as "semi-convection" and is most commonly found outside the convective core of stars where it would play a role in mixing processes (Merryfield, 1995). Semi-convection could also have an important effect on the structure and evolution of giant gas planets (Gierasch and Conrath, 1987; Guillot et al., 2004) and could regulate both thermal and compositional mixing processes (Salpeter and Stevenson, 1976). More recently, Leconte and Chabrier (2012) showed that considering diffusive convection in gas giants changes a lot the vision brought by conventional models in terms of heat transfer, structure and composition, with potential impact on models of planetary formation.

In geophysical contexts other than oceanography, double-diffusive phenomena have been studied for almost 40 years essentially in magma chambers (Chen and Turner, 1980; Huppert and Sparks, 1984). They have also been evoked at the core mantle boundary (Kellogg, 1991; Hansen

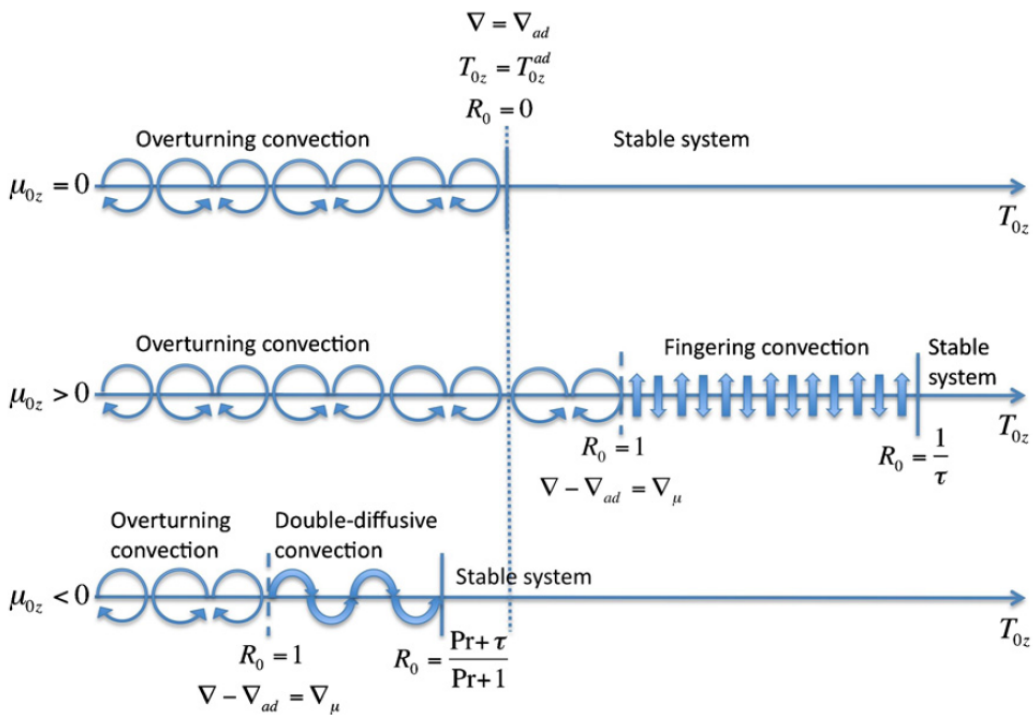

FIGURE 1.4: Summary of the various regimes of convective instability in the non-rotating case. T_{0_z} and μ_{0_z} denote the mean thermal and chemical background gradients. τ is the inverse of the Lewis number and Pr the thermal Prandtl number equal to ν/κ^T, where ν is the viscosity of the fluid. $R_0 = \beta\mu_{0_z}/\alpha T_{0_z}$ is the density ratio, with α and β the thermal and chemical expansivities, respectively. Taken from Rosenblum et al. (2011).

and Yuen, 1994) and, more recently, in the solid inner core (Deguen and Cardin, 2011). The existence and potential implications of double-diffusive convection have however received much less attention in the liquid layers of planetary interiors and are discussed below in this context.

As stated above, thermal and compositional effects are present in most of the internal liquid layers of planets, with different molecular diffusivities. In these layers, the presence of stratified regions has often been evoked which indicates that double-diffusive convection is theoretically possible. A graphic summary of the regions prone to double-diffusive instabilities and thermo-chemical convection in various planetary contexts can be visualized on figure 1.5. Examples of such regions include the liquid part of the metallic cores of many telluric planets (such as Mercury, the Earth and Ganymede) where the existence of stratified layers is very plausible. Stratification has been evoked for the Earth's core below the CMB (Gomi et al., 2013) and in a region above the ICB called the "F-layer" (Gubbins et al., 2008; Alboussière et al., 2010), but also for Ganymede (Christensen and Wicht, 2008) and Mercury (Christensen, 2006). As soon as either the thermal or compositional field has a destabilizing effect, these stratified layers become potential candidates for double-diffusive convection. The fingering case could be expected for a thermally stratified layer with a destabilizing effect of composition, whereas the reverse situation is prone to diffusive instabilities. The consequence of the presence of stratified layers in metallic cores may therefore not be limited to a pure filtering effect of the magnetic field, as is often assumed, since the vertical motions permitted by double-diffusive processes forbid to rule out that some dynamo action takes place in the stratified layer. Also, similarly to oceanic and astrophysical contexts, double-diffusive processes could play a role in the mixing and transport of chemicals across a stratified layer which may have some implications for dynamical and evolution models.

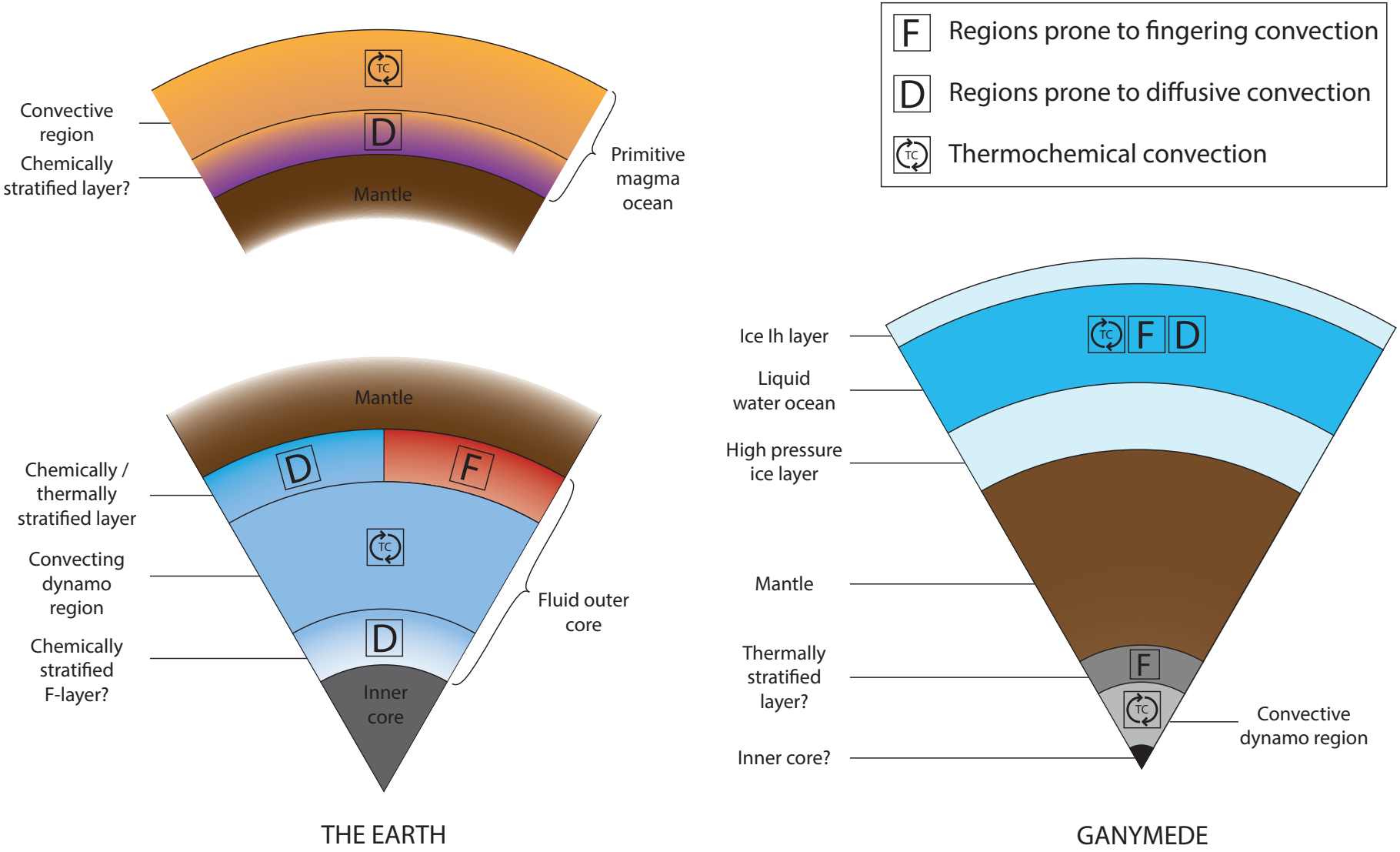

FIGURE 1.5: Illustration of the liquid regions potentially prone to thermochemical, fingering and diffusive convection in the Earth's core and primitive magma ocean, and in Ganymede. The scales are only approximately respected inside each figure, but not between the figures.

Like in terrestrial oceans and planetary cores, some regions of the internal water oceans of several icy satellites of the Solar system could also be stratified and prone to double-diffusive instabilities as was evoked for Europa (Thomson and Delaney, 2001; Vance and Brown, 2005) with several potential implications. Icy satellites receive a marked interest for being potential habitats for extraterrestrial life (Sotin and Tobie, 2004; Solomonidou et al., 2011). Habitability may depend on chemical exchanges between the surface and the underneath liquid ocean and on aqueous alteration of mantle rock with the ocean as observed on the Earth's seafloor, processes that are thought to be partly controlled by the dynamics of the liquid ocean. For example, the observation of nano-silica particles (Hsu et al., 2015) and the detection of molecular hydrogen (Waite et al., 2017) both probably emanating from the interior of Enceladus is considered to result from deep hydrothermal reactions. Some authors also explain the formation of "chaos terrains" at the surface of Europa by the presence of oceanic plumes produced by magmatic phenomena in the mantle or by a sufficiently turbulent convection (Thomson and Delaney, 2001; Soderlund et al., 2014). The same type of argument is invoked to explain part of the tectonic phenomena of the surface of Ganymede (Solomonidou et al., 2011). Taking into account the effects of both double-diffusive processes and thermochemical coupling at the ocean/ice boundary(ies) could complicate this picture. In addition, the role played by double-diffusive processes in terms of transport and mixing of chemicals could be important to better assess the dynamics and potential habitability of these oceans.

Double-diffusive thermochemical processes may also have occurred in the primitive magma ocean of the Earth. Since heavy elements are released by crystallization at the base of the ocean, a chemically stratified layer could form at the bottom. With a destabilizing effect of temperature throughout the magma ocean, the stratified layer could be prone to diffusive instabilities. The presence of a stratified layer with diffusive convection could have several implications on the dynamics and evolution of the primitive magma ocean.

Despite being potentially of great importance in cores and other internal liquid layers of planets, thermochemical convection and double-diffusive phenomena have surprisingly received relatively little attention so far in these contexts. Although thermochemical convection has been well studied theoretically, it seems that, contrary to the context of gas giants, none has so far really investigated in details the dynamics and potential implications of double-diffusive convection in planetary cores. Double-diffusive processes have been theoretically evoked at several occasions but usually in a relatively vague manner. Though some laboratory experiments of rotating thermochemical convection have been conducted (Cardin and Olson, 1992), no experiment has seemingly been designed specifically for the study of double-diffusive convection in the context of planetary cores. On the side of numerical modeling, almost all the simulations that have been conducted since the 1990s to explain the generation of planetary magnetic fields by dynamo action have considered exclusively thermal convection or rather, a combination of thermal and chemical effects into a single variable, neglecting the diffusivity difference. There may be several explanations to this fact. It should first be said that the modeling of the Earth's dynamo poses an immense challenge to numerical simulations as it operates in a regime that it presently completely out of reach in terms of computational demand. The present aim of numerical simulations is to derive scaling laws in a remote region of the parameter space, hoping extrapolation to the Earth's case is relevant. Even with thermal convection only, already 4 non-dimensional numbers control the convective regime. Accounting for compositional effects would add at least 2 non-dimensional numbers making the exploration of the parameter space even more fastidious. Furthermore, considering the compositional field in simulations also raises some technical difficulties (that will be clarified later) tied to its small diffusivity ($Le \sim 1000$). This is the reason why the few authors who have distinguished temperature and composition so far in planetary cores (Breuer et al., 2010; Manglik et al., 2010; Trümper et al., 2012; Takahashi, 2014) considered

very moderate values of the Lewis number ($Le \leq 10$).

It should however be emphasized that, despite neglecting compositional effects and running with control parameters that are very remote from realistic ones, dynamo simulations have been successful at reproducing many aspects of the Earth's magnetic field including its global morphology (Glatzmaier and Roberts, 1996; Kutzner and Christensen, 2002; Christensen et al., 2010), inversions (Glatzmaiers and Roberts, 1995) and even finer features such as a secular variation under the Atlantic ocean (Aubert et al., 2013). Furthermore, a recent study by Aubert et al. (2016) tends to validate the asymptotic relevance of classical numerical dynamo mechanisms. These successes are probably also part of the reasons why only recently have a few authors started to investigate the topic of thermochemical and double-diffusive convection in planetary cores. Considering the achievements of the present models, one may wonder whether making things more complex is really necessary. Several elements may yet justify the distinction of the thermal and compositional fields in numerical simulations and will be mentioned later in this thesis.

To summarize, it seems that the dynamics and the potential role played by thermochemical and double-diffusive convection in planetary cores remain largely to be investigated theoretically, experimentally and numerically. This assessment also applies to the oceans of icy satellites and to the primitive magma ocean of the Earth, which have been the objects of even fewer studies. Distinguishing both fields and dealing with a very weak chemical diffusivity however requires a dedicated numerical tool. One can wonder which numerical method is the most adapted to the description of thermochemical convection in the context of planetary dynamo simulations. In his book, Glatzmaier (2013) suggests that the modeling of chemical convection in the outer core can be performed via the use of Eulerian-Lagrangian approaches such as a *Particle-In-Cell* (PIC) method, an idea that Stéphane Labrosse also proposed and which largely guided my PhD. The initial goal of this work was first to implement a PIC method into a pre-existing dynamo code (PARODY, developed by E. Dormy and J. Aubert) to treat the weakly diffusive compositional field and, in a second phase, to perform first applications of this new tool to problems related to thermochemical convection, essentially in planetary cores.

This thesis is organized as follows. The physical and mathematical modeling of thermochemical convection are first presented in chapter 2 in the context of the Earth's outer core. The principles of the PIC method used to solve the chemical transport equation and the details of its implementation into PARODY are described in chapter 3. The necessity of improving the efficiency of this method is then pointed out in chapter 4 and followed by an enumeration of the principal optimizations brought to the code. Chapter 5 contains the results of two benchmark tests which validate the method plus a justification of the use of the PIC method based on comparison tests with state-of-the art Eulerian schemes developed for the hyperbolic equation. Other interesting applications of the PIC method are also underlined. In chapter 6, the results of a first series of simulations of pure compositional convection performed using this new tool are presented. Several aspects of the physics of rotating pure chemical convection are tackled, including the formation of a chemically stratified layer below the top boundary. Chapter 7 then focuses more specifically on problems related to stratification below the Earth's core mantle boundary. The formation of a chemically stratified layer is studied again with simulations of thermochemical convection in which the stirring effect of thermal convection is taken into account. The double-diffusive dynamics of a thermally stratified layer is then explored. A scale analysis is performed for the size of salt fingers in this context. The first steps of a linear stability analysis are then outlined and the results of first simulations of rotating fingering convection in a simple configuration are presented. A general conclusion finally summarizes the main contributions of this thesis and discusses briefly the effects of thermochemical coupling and magnetic field based on the preliminary results of two exploratory simulations (detailed in appendix) of the Earth's primitive magma ocean and

outer core. Future directions are then envisioned. The details of some calculations and a paper published during this PhD are also given in appendix.

Chapter 2

Modeling

In this chapter, the main equations governing the dynamics of double-diffusive thermochemical convection in a rotating spherical shell filled with an electrically conducting fluid are presented together with their non-dimensional equivalents. The full derivation of these equations is not recalled but the hypotheses they rely on are discussed, in particular the codensity and infinite Lewis number approximations. A mathematical formulation of the coupling of thermochemical boundary conditions is also proposed at the inner core boundary. Table 2.1 gathers the main variables, constants and dimensionless numbers that appear throughout this chapter and, when relevant, gives estimations of their realistic values in core conditions.

Although more focused on the Earth's outer core, the formalism developed through this chapter is relatively generic and can be applied with only minor modifications to different contexts, in particular that of other planetary cores. The modeling of water oceans in icy satellites or that of a primitive magma ocean can also be made in a very similar way by neglecting any magnetic effect and modifying accordingly the boundary conditions. If crystallization occurs at one boundary, a treatment similar to the Earth's inner core boundary (ICB) is needed.

2.1 General approximations

2.1.1 Geometry

A first approximation is made on the geometry of the system which is assumed to consist of a purely spherical shell comprised between inner and outer radii r_i and r_o, respectively, with aspect ratio $a = r_i/r_o$. Any topography and flattening at the boundaries is neglected. Spherical coordinates are used to locate any point of the spherical shell according to its radius r, colatitude θ and azimuth (longitude) ϕ as illustrated on figure 2.1, with corresponding unit vectors $(\vec{\mathbf{e}}_\mathbf{r}, \vec{\mathbf{e}}_\theta, \vec{\mathbf{e}}_\phi)$. Alternatively, Cartesian coordinates (x, y, z) with element vectors $(\vec{\mathbf{e}}_\mathbf{x}, \vec{\mathbf{e}}_\mathbf{y}, \vec{\mathbf{e}}_\mathbf{z})$ can also be used in some mathematical expressions.

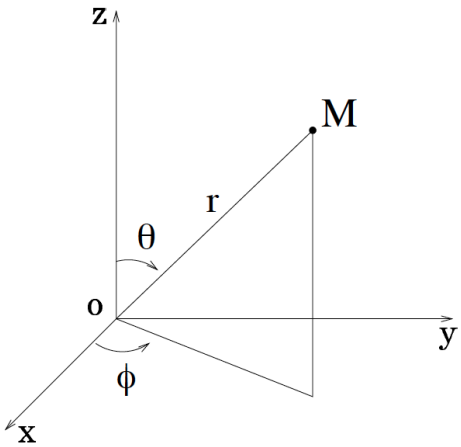

FIGURE 2.1: Illustration of a spherical system of representation. A point M can be located either by its Cartesian coordinates (x, y, z) or by its radius r, colatitude θ and azimuth ϕ.

2.1.2 The Boussinesq approximation

Although mechanical forcings such as precession and nutation cannot be excluded for driving dynamos (Tilgner, 2005; Cébron and Hollerbach, 2014; Le Bars, 2016), they are neglected in the frame of this work. The convective currents are assumed to originate from Archimedean forces due to thermal and compositional variations. Thermal effects may be a consequence of secular cooling, the heat extracted by the mantle at the top of the core and the release of latent heat caused by the inner core crystallization. The presence of radioactive elements cannot be excluded but is probably negligible (McDonough, 2003). Compositional effects may also have several origins. First, the inner core crystallization enriches the liquid locally in light elements at the bottom, potentially creating a gravitational instability. Also, the possibility of chemical exchange at the core mantle boundary (CMB) has been evoked. Release of light elements in the outer core would have resulted in a chemical stratification below the CMB (Buffett and Seagle, 2010) whereas magnesium exsolution or crystallization of SiO_2 could have been a possible mechanism to drive the geodynamo prior to the inner core crystallization (O'Rourke and Stevenson, 2016; Hirose et al., 2017).

Transport of heat and chemical elements can be performed by conduction and convection. Convection is studied within the Boussinesq approximation which consists in considering the fluid as incompressible except in the buoyancy terms. This hypothesis is questionable for the Earth's core across which the density varies by approximately 20% (Dziewonski and Anderson, 1981; Anufriev et al., 2005), but has worked relatively well for dynamo models so far.

2.1.3 Framework for the study of thermochemical convection

As stated in the introduction, 3 general cases may be encountered in convecting systems driven by two buoyancy sources with different diffusivities:

1. Both fields have a destabilizing effect according to the Ledoux criterion (1.2). This results in the creation of large-scale convective currents whose features are sensitive to the size of the domain and to the conditions imposed at its boundaries.

2. The global contribution of both fields to the density gradient is stable according to the Ledoux criterion, but one field has a destabilizing effect. Depending on whether this field is the fast or slow diffusor, this situation is prone to fingering or diffusive instabilities. The latter create their own spatial scale that is independent of the size of the global domain and is typically controlled by viscosity and by the diffusivity and background gradient of the fast diffusor (Radko, 2013). As will be shown in chapter 7, the expected size of salt fingers in core conditions is close to 20 cm which is orders of magnitude smaller than the thickness of the core or even that of a hypothetical stratified layer below the CMB.

3. Both fields have a stabilizing effect on the density gradient creating a strongly stable region.

In the Earth's core, these situations are not mutually exclusive: vigorous convection can well extend to the majority of the spherical shell with some regions or layers being stratified and prone to double-diffusive instabilities, the latter creating their own dynamics on a scale much smaller than the size of their host region. However, as will be later emphasized, numerical simulations currently operate in ranges of parameters which are very remote from the realistic values, owing to technical limitations. In particular, the viscosity of the fluid is several orders of magnitude too high. The expected length scale of double-diffusive instabilities in numerical simulations is consequently much larger than in core conditions and is comparable to the width of the layer in which these instabilities develop. The double-diffusive dynamics in these regions is therefore likely to be different from that in core conditions since the growing instabilities will quickly reach the boundaries of the layer before being affected by other secondary instabilities resulting for example in the formation of thermohaline staircases. Going in the direction of more realistic parameters will progressively decrease the spatial scale of the instabilities up to a point where their size will be small compared to that of their host region, allowing double-diffusive convection to develop its own internal dynamics far from the boundaries of the stratified layer. Unfortunately, as is shown in chapter 7, this point may not be presently attainable in direct numerical simulations.

Despite this limitation in full core modeling, it is still possible to study double-diffusive instabilities far from the boundaries of the stratified layer in numerically tractable simulations by "zooming" on a stratified environment to focus only on a few fingers/layers. In such a local study, equations are scaled differently using the typical size of the instabilities (rather than the size of the box) and tri-periodic boundary conditions are enforced allowing double-diffusive convection to fully develop, saturate under the effect of secondary instabilities and reach a statistically steady state the properties of which can be studied. It is in this framework that a large proportion of the numerical simulations of double-diffusive phenomena have been conducted (Radko, 2003; Prikasky, 2007; Traxler et al., 2011a,b; Rosenblum et al., 2011; Radko and Smith, 2012).

For the Earth's core, both approaches (global and local) are probably complementary. In this chapter, I concentrate on the modeling of thermochemical convection in the entire spherical shell the thickness of which is taken as the typical length scale. The second approach is tackled in chapter 7 in the context of salt fingers inside a thermally stratified layer.

2.2 General equations

2.2.1 Momentum conservation

The fluid considered is a mixture of a dominant component (iron in a metallic core) and a light constituent (or heavy one in the case of salt in water), whose compositional mass fraction is denoted by C and varies between $C = 0$ (pure iron) and $C = 1$ (pure light elements). In this context, the density can be modeled as a function of both temperature, T, and compositional mass fraction, C:

$$\rho = \rho_0 \left[1 - \alpha(T - T_0) - \beta(C - C_0)\right], \tag{2.1}$$

where T_0, C_0 and ρ_0 are the reference temperature, composition and density, respectively. α is the coefficient of thermal expansivity and β its analogous compositional coefficient. The momentum conservation is expressed in the form of the well-known Navier-Stokes equation, for an electrically conducting Newtonian rotating fluid in the Boussinesq approximation. The corresponding equation involves the Coriolis, Lorentz, pressure, inertia and viscous forces:

$$\begin{aligned} \frac{\partial \vec{\mathbf{u}}}{\partial t} + \vec{\mathbf{u}} \cdot \bar{\bar{\nabla}} \vec{\mathbf{u}} + 2\Omega(\vec{\mathbf{e}}_\mathbf{z} \times \vec{\mathbf{u}}) = -\frac{1}{\rho_0} \vec{\nabla} \Pi + \nu \vec{\nabla}^2 \vec{\mathbf{u}} \\ + (\alpha \Theta g_0 + \beta \xi g_0)\, \vec{\mathbf{e}}_\mathbf{r} + \frac{1}{\mu_0 \rho_0} \left(\vec{\nabla} \times \vec{\mathbf{B}}\right) \times \vec{\mathbf{B}}, \end{aligned} \tag{2.2}$$

where $\Theta = T - T_0$, $\xi = C - C_0$, $\vec{\mathbf{u}}$ is the fluid velocity, t the time, Ω the rotation rate of the planet around $\vec{\mathbf{e}}_\mathbf{z}$, Π the dynamical pressure, ν the kinematic viscosity and g_0 the gravitational acceleration. μ_0 denotes the magnetic permeability and $\vec{\mathbf{B}}$ the magnetic field.

The rotation period $1/\Omega$ is a possible choice of time scale and is often adopted to write the equations of geodynamo, as it is more relevant when deriving scaling laws in the diffusivity-free limit (Aubert et al., 2009). However, for historical reasons tied to the study of the onset of convection, most codes are formulated using the viscous time scale D^2/ν, with $D = r_o - r_i$ the thickness of the shell taken as the typical length scale and ν the kinematic viscosity. The Elsasser scale $(\rho_0 \mu \eta \Omega)^{1/2}$ is used for the magnetic induction $\vec{\mathbf{B}}$, where η is the magnetic diffusivity. Finally, using $(\rho_0 \nu \Omega)$ as a scaling for pressure, one can write the dimensionless momentum equation:

$$\begin{aligned} E\left(\frac{\partial \vec{\mathbf{u}}}{\partial t} + \vec{\mathbf{u}} \cdot \bar{\bar{\nabla}} \vec{\mathbf{u}} - \vec{\nabla}^2 \vec{\mathbf{u}}\right) + 2\vec{\mathbf{e}}_\mathbf{z} \times \vec{\mathbf{u}} + \vec{\nabla} \Pi = \\ (Ra_T \Theta + Ra_\xi \xi) \frac{1}{r_o} \vec{\mathbf{e}}_\mathbf{r} + \frac{1}{P_m} \left(\vec{\nabla} \times \vec{\mathbf{B}}\right) \times \vec{\mathbf{B}}, \end{aligned} \tag{2.3}$$

in which E is the Ekman number, defined by:

$$E = \frac{\nu}{\Omega D^2}, \tag{2.4}$$

with a typical value 10^{-15} in core conditions. P_m is the magnetic Prandtl number:

$$P_m = \frac{\nu}{\eta}, \tag{2.5}$$

which is close to 10^{-6} in the Earth's core. Ra_T and Ra_ξ are the thermal and compositional Rayleigh numbers, respectively:

$$Ra_T = \frac{g_0 \alpha T^* D}{\nu \Omega}, \quad Ra_\xi = \frac{g_0 \beta C^* D}{\nu \Omega}, \tag{2.6}$$

T^* and C^* being the scalings for temperature and composition. The latter depend on the prescribed boundary conditions which are discussed in the next section.

In the context of rotating planetary cores generating magnetic fields, a complex balance can be established involving the Coriolis, inertia, buoyancy, viscosity, pressure and Lorentz forces. The Coriolis force is usually assumed to be dominant in the Earth's core, at least at large scales. The Lorentz, buoyancy, pressure and inertia forces generally play a secondary role and their relative importances depend on the length scale and flow regime. The kinematic viscosity is very small ($\nu = 10^{-6}$ m^2 s^{-1}) which implies that the Reynolds number of the core is probably very large (Nataf and Schaeffer, 2015):

$$Re = \frac{UD}{\nu} \sim 10^8, \tag{2.7}$$

where $U \sim 10^{-4}$ m s^{-1} is the typical velocity in the core. Such a high value indicates that the core is probably in a turbulent state involving a wide range of length scales; the viscous force entering the force balance only at small scales. Close to the boundaries, the viscous force balances the Coriolis force within an Ekman boundary layer of thickness $DE^{1/2} \sim 1$ m in core conditions. Resolving all the relevant scales in the Earth's core in numerical simulations therefore constitutes a formidable challenge and is presently out of reach. So far, all numerical simulations and laboratory experiments performed on core convection have operated with dimensionless parameters which differ from the realistic conditions by several orders of magnitude with typical Ekman numbers in the range $10^{-3} - 10^{-8}$, Reynolds numbers $Re \lesssim 10^3$ and magnetic Prandtl close to unity.

2.2.2 Energy conservation

In an incompressible, homogeneous and isotropic fluid, the energy conservation can be expressed by the following transport equation:

$$\frac{\partial \Theta}{\partial t} = -\vec{\mathbf{u}} \cdot \vec{\nabla}\Theta + \kappa^T \nabla^2 \Theta + \sigma^T, \tag{2.8}$$

where κ^T is the thermal diffusivity and σ^T a possible source/sink term with diverse possible origins such as the heat produced by radioactive elements. Technically, this last term is usually not directly computed. In practice, the temperature is split into a variable part Θ_v and a stationary conductive reference profile Θ_s such that:

$$\frac{\partial \Theta_s}{\partial t} = 0 \quad ; \quad \kappa^T \nabla^2 \Theta_s = -\sigma^T, \tag{2.9}$$

where C_p is the heat capacity. Using this decomposition for the temperature, equation (2.8) becomes, for the variable part:

$$\frac{\partial \Theta_v}{\partial t} = -\vec{\mathbf{u}} \cdot \vec{\nabla}\Theta_v - \vec{\mathbf{u}} \cdot \vec{\nabla}\Theta_s + \kappa^T \nabla^2 \Theta_v. \tag{2.10}$$

In this equation, the sink term is compensated by the diffusive term of the conductive reference state.

Adopting the same scalings as for the momentum equation, one can write the dimensionless form of equation (2.8):

$$\frac{\partial \Theta}{\partial t} + \vec{\mathbf{u}} \cdot \vec{\nabla}\Theta = \frac{1}{P_T} \nabla^2 \Theta + \sigma^T, \tag{2.11}$$

where P_T is the thermal Prandtl number:

$$P_T = \frac{\nu}{\kappa^T}. \tag{2.12}$$

In core conditions, P_T is close to 0.1 but is often fixed to 1 in numerical simulations.

2.2.3 Chemical transport equation

In the Earth's fluid core, chemicals can be transported either by advection or diffusion. A transport equation similar to (2.8) can be written for the transport of light elements through the fluid shell:

$$\frac{\partial \xi}{\partial t} + \vec{\mathbf{u}} \cdot \vec{\nabla} \xi = \kappa^\xi \nabla^2 \xi + \sigma^\xi, \tag{2.13}$$

in which κ^ξ is the chemical diffusivity and σ^ξ a sink/source term analogous to σ^T. Its equivalent dimensionless expression reads:

$$\frac{\partial \xi}{\partial t} + \vec{\mathbf{u}} \cdot \vec{\nabla} \xi = \frac{1}{P_\xi} \nabla^2 \xi + \sigma^\xi, \tag{2.14}$$

where P_ξ is a chemical Prandtl number defined by:

$$P_\xi = \frac{\nu}{\kappa^\xi}. \tag{2.15}$$

Equation (2.14) is also equivalent to:

$$\frac{\partial \xi}{\partial t} + \vec{\mathbf{u}} \cdot \vec{\nabla} \xi = \frac{1}{Le P_T} \nabla^2 \xi + \sigma^\xi, \tag{2.16}$$

where Le is the Lewis number defined by the diffusivities ratio:

$$Le = \frac{\kappa^T}{\kappa^\xi} = \frac{P_\xi}{P_T}. \tag{2.17}$$

In planetary cores, the chemical diffusivity is much smaller than its thermal counterpart. Values of κ^T and κ^ξ vary across the literature (see table 2.1 for estimations of the diffusivities values) so that the Lewis number falls in the range $800 - 10^4$ and the chemical Prandtl number is comprised between 100 and 1000. Such high values are the source of several mathematical and numerical complications inherent to the weak chemical diffusivity. Equation (2.13) may be left unchanged or solved within two opposite approximations. The codensity approximation is equivalent to setting $Le = 1$ and combining equations (2.8) and (2.13) into one single equation. On the contrary, motivated by the strong difference in the diffusivities, one might choose to explore the infinite Lewis number limit. Both approximations are discussed below.

The codensity hypothesis

First proposed by Braginsky and Roberts (1995) and simultaneously by Lister and Buffett (1995b), this approach has been widely adopted since in almost all geodynamo simulations (see the works of Lister and Buffett (1995a); Kutzner and Christensen (2002); Christensen and Wicht (2008); Aubert et al. (2009); Sreenivasan and Jellinek (2012); Christensen (2015); Amit and Olson (2015); Monteux et al. (2015), to mention only a few authors) and relies on the assumption that the mixing action of the unresolved sub-grid-scale turbulence would lead to comparable effective

diffusivities for temperature and composition:

$$\kappa^T = \kappa^\xi = \kappa^{\text{turb}}, \tag{2.18}$$

where κ^{turb} is a homogeneous and isotropic *"turbulent"* or *"eddy"* diffusivity. Assuming the thermal and chemical boundary conditions are independent and of the same type (fixed value or fixed flux), this approximation allows to combine both sources of buoyancy into a single component named *codensity*, noted χ and defined by:

$$\chi = \alpha\Theta + \beta\xi, \tag{2.19}$$

and to solve only one transport equation for this new variable:

$$\frac{\partial \chi}{\partial t} = -\vec{\mathbf{u}} \cdot \vec{\nabla}\chi + \kappa^{\text{turb}}\nabla^2\chi + \sigma^\chi. \tag{2.20}$$

Like the hyperdiffusivity approach introduced in geodynamo simulations by Glatzmaiers and Roberts (1995), the codensity formulation can be viewed as an attempt to parametrize core turbulence, but it is essentially a convenient approach. Although it is easy to implement in codes of geodynamo and does not increase the computational demand, it remains very simplistic for a series of reasons. First, it seems important to state that the turbulent regime of the core is not known, though under the effect of rotation it is probably anisotropic (Braginsky and Roberts, 1995; Matsushima, 2004), as suggested by the low value of the Rossby number $Ro = ERe \sim 10^{-6}$. Rotating MHD turbulence is extremely complex and some of the results of the classic theory of turbulence (established for non-rotating and non-magnetic cases) may not apply in this context (Nataf and Gagniere, 2008; Nataf and Schaeffer, 2015). Turbulence may also be studied through different prisms: while some models favor a spectral description, other authors (Loper, 2007) consider buoyant plumes as the elementary structure at the origin of turbulent motions in the core. It seems therefore very unlikely that such a rough parametrization can account for all these complexities and be relevant at all, even though it could be appropriate in some specific turbulent regimes. The use of codensity may be even more problematic inside stratified layers, the existence of which has been evoked for some planetary cores (Manglik et al., 2010; Christensen, 2015) including that of the Earth (Gomi et al., 2013). In such a context, it is likely that turbulence will be much less efficient if not absent and that the mixing of properties will rather be performed by molecular diffusion (Braginsky and Roberts, 1995). To finish, the thermal and chemical boundary conditions usually differ in liquid cores and should be included as distinct conditions for the two fields. In addition, these are coupled through the melting/freezing process at the interface, a phenomenon that cannot be properly described by the codensity approach and requires the fields to be treated separately.

Consequently, rather than betting on uncertain parameterizations of turbulence, one can instead solve the laminar flow considering two distinct transport equations for temperature and composition and try to derive scaling laws, hoping the latter can be safely extrapolated to core conditions. When keeping distinct transport equations, one is faced with a choice: solving a very small (but finite) chemical diffusivity, or exploring the infinite Lewis number, an approximation discussed in the next paragraph.

The infinite Lewis number approximation

As previously stated, the chemical and thermal diffusivities differ by several orders of magnitude in planetary cores. The large estimation of the Lewis number can motivate the exploration of the limit $Le = +\infty$, which is equivalent to $\kappa^\xi = 0$ and thus $P_\xi = +\infty$. However, switching to

the limit has profound consequences. Mathematically speaking, the second-order equation (2.13) becomes hyperbolic:

$$\frac{\partial \xi}{\partial t} = -\vec{\mathbf{u}} \cdot \vec{\nabla}\xi + \sigma^{\xi}, \tag{2.21}$$

which has implications for the type of boundary conditions one is mathematically allowed to prescribe. In addition, with $\kappa^{\xi} = 0$, it is no longer possible to define a conductive reference state for the composition similarly to equation (2.9) which, as is shown in section 2.3, leads to several complications.

If one succeeds in getting around these mathematical difficulties, then a second point remains delicate. One may indeed wonder whether completely neglecting diffusive transport of chemicals would lead to miss part of the physics, particularly that of double-diffusive phenomena. Intrinsically, double-diffusive processes are essentially driven by the thermal diffusivity and damped by viscous forces and chemical diffusion. When $\kappa^{\xi} \ll \nu$ (which is true for the Earth's core), the chemical diffusivity is therefore expected to play a minor role. One can also argue that, for large Lewis numbers, the chemical diffusion is negligible on the time scale of a simulation and that studying this asymptotic limit is interesting on a theoretical point of view.

To finish, it would not be honest to omit to mention that the infinite Lewis number limit is also motivated by a choice of convenience. Indeed, solving a very small (but non-zero) chemical diffusivity requires to resolve the chemical diffusive scale which, for high Lewis numbers, can only be achieved at the price of unattainable resolutions. Mathematically, this is expressed by a criterion on the grid Peclet number which measures the ratio of advection and diffusion in the grid. This number should be less than a value close to unity to avoid spurious oscillations:

$$Pe = \frac{\max(U\Delta x)}{\kappa^{\xi}} < \sim 1, \tag{2.22}$$

where U is the fluid velocity at a given position in the grid and Δx the grid spacing at this position. This requirement disappears when the diffusivity is neglected, although a diffusion-free numerical method becomes necessary in this case. For these reasons, the infinite Lewis number approximation is adopted in the rest of this work, with a few exceptions.

2.2.4 Induction equation

For the simulation of non-magnetic convection (for example in the oceans of icy satellites), the previous equations are sufficient. In metallic cores however, electric currents can be generated. For a homogeneous and isotropic conducting fluid well above its Curie temperature, the following induction equation can be derived from Maxwell's equations:

$$\frac{\partial \vec{\mathbf{B}}}{\partial t} = \vec{\nabla} \times \left(\vec{\mathbf{u}} \times \vec{\mathbf{B}}\right) + \eta \vec{\nabla}^2 \vec{\mathbf{B}}, \tag{2.23}$$

to which we should add the condition:

$$\vec{\nabla} \cdot \vec{\mathbf{B}} = 0, \tag{2.24}$$

where $\vec{\mathbf{B}}$ is the magnetic field vector and η the magnetic diffusivity. The dimensionless induction equation then yields:

$$\frac{\partial \vec{\mathbf{B}}}{\partial t} = \vec{\nabla} \times \left(\vec{\mathbf{u}} \times \vec{\mathbf{B}}\right) + \frac{1}{P_m} \vec{\nabla}^2 \vec{\mathbf{B}}, \tag{2.25}$$

where P_m is the magnetic Prandtl number defined above.

2.2.5 Full set of equations

The complete problem is therefore governed by a total of 6 equations involving 6 independent dimensionless numbers ($E, Ra_T, Ra_\xi, P_m, P_T, Le$):

$$\begin{cases} E\left(\dfrac{\partial \vec{\mathbf{u}}}{\partial t} + \vec{\mathbf{u}} \cdot \bar{\bar{\nabla}}\vec{\mathbf{u}} - \vec{\nabla}^2\vec{\mathbf{u}}\right) + 2\vec{\mathbf{e}}_\mathbf{z} \times \vec{\mathbf{u}} + \vec{\nabla}\Pi = \\ \quad (Ra_T\Theta + Ra_\xi\xi)\dfrac{1}{r_o}\vec{\mathbf{e}}_\mathbf{r} + \dfrac{1}{P_m}\left(\vec{\nabla} \times \vec{\mathbf{B}}\right) \times \vec{\mathbf{B}}, \\ \dfrac{\partial \Theta}{\partial t} + \vec{\mathbf{u}} \cdot \vec{\nabla}\Theta = \dfrac{1}{P_T}\nabla^2\Theta + \sigma^T, \\ \dfrac{\partial \xi}{\partial t} + \vec{\mathbf{u}} \cdot \vec{\nabla}\xi = \dfrac{1}{LeP_T}\nabla^2\xi + \sigma^\xi, \\ \dfrac{\partial \vec{\mathbf{B}}}{\partial t} = \vec{\nabla} \times \left(\vec{\mathbf{u}} \times \vec{\mathbf{B}}\right) + \dfrac{1}{P_m}\vec{\nabla}^2\vec{\mathbf{B}}, \\ \vec{\nabla} \cdot \vec{\mathbf{u}} = 0, \\ \vec{\nabla} \cdot \vec{\mathbf{B}} = 0. \end{cases} \tag{2.26}$$

Mathematically, prescribing boundary conditions is necessary to solve this system and this is the goal of the next section.

2.3 Boundary conditions

2.3.1 Kinematic conditions

The natural conditions for the velocity are non-penetration and no-slip at the boundaries:

$$\begin{cases} \vec{\mathbf{u}}(r_i, \theta, \phi) = \vec{\mathbf{0}}, & \forall(\theta, \phi), \\ \vec{\mathbf{u}}(r_o, \theta, \phi) = \vec{\mathbf{0}}, & \forall(\theta, \phi). \end{cases} \tag{2.27}$$

Free-slip conditions have also been adopted by some authors such as Kuang and Bloxham (1997) and result in the suppression of the Ekman boundary layers. For this reason, they are sometimes considered less physical so that no-slip conditions are usually preferred in most numerical simulations.

2.3.2 Magnetic conditions

It is classically assumed that the whole metallic core is electrically conducting while the mantle is a perfect insulator. This implies that the magnetic field outside the core derives from a scalar potential:

$$\begin{cases} \vec{\mathbf{B}} = -\vec{\nabla}\Phi, \\ \nabla^2\Phi = 0. \end{cases} \tag{2.28}$$

2.3.3 Thermochemical boundary conditions

Several authors (Kutzner and Christensen, 2002; Hori et al., 2012; Aubert et al., 2008a) have emphasized the role played by the distribution of buoyancy sources in the shell and at the boundaries on the morphology of the flow as well as on the characteristics of the magnetic fields such

Dimensionless numbers			
Symbol	Name of number	Definition	Core
Ra_T	Thermal Rayleigh	$g_0 \alpha T^* D/\nu\Omega$	–
Ra_ξ	Chemical Rayleigh	$g_0 \beta C^* D/\nu\Omega$	–
Ra	Total Rayleigh	$Ra_T + Ra_\xi$	–
E	Ekman	$\nu/2\Omega D$	10^{-15}
P_m	Magnetic Prandtl	ν/η	1.7×10^{-6}
P_T	Thermal Prandtl	ν/κ^T	0.1
P_ξ	Chemical Prandtl	ν/κ^ξ	$100 - 1000$
Le	Lewis	κ^T/κ^ξ	$800 - 10^4$
$\mathcal{R}$	Buoyancy ratio	f^T/f^ξ	0.3
$\mathcal{S}$	Coupling number	$C_0 \beta C_p/\alpha\mathcal{L}\zeta$	10
Dimensional variables			
Symbol	Name	Scaled by	Unit
Π	dynamics pressure	$\rho_0 \nu\Omega$	Pa
Θ	Temperature	$2\overline{f}_i^T/4\pi D\alpha\rho_0 g\nu$	K
ξ	Mass fraction of light elements	$\overline{f}_i^\xi/4\pi D\beta\rho_0 g\nu$	–
$\vec{\mathbf{u}}$	Fluid velocity	ν/D	m s^{-1}
$\vec{\mathbf{B}}$	Magnetic field	$(\rho_0\mu\eta\Omega)^{1/2}$	T
Dimensional constants			
Symbol	Name	Value	Unit
r_i	Present inner core radius	1221	km
r_o	Total core radius	3480	km
a	Aspect ratio ($= r_i/r_o$)	0.35	–
D	Depth of fluid core ($r_o - r_i$)	2259	km
g_0	Gravitational acceleration at the CMB	10.68	m s^{-2}
ρ_0	Reference density density	1.1×10^4	kg m^{-3}
Ω	Angular velocity of Earth	7.29×10^{-5}	s^{-1}
ν	Kinematic viscosity	5×10^{-7}	m^2 s^{-1}
κ^T	Thermal diffusivity	$5 \times 10^{-6} - 10^{-5}$	m^2 s^{-1}
κ^ξ	Chemical diffusivity	$10^{-9} - 6 \times 10^{-9}$	m^2 s^{-1}
η	Magnetic diffusivity	0.7	m^2 s^{-1}
μ_0	Magnetic permeability	$4\pi \times 10^{-7}$	H m^{-1}
C_p	Heat capacity	750	J kg^{-1} K^{-1}
α	Coefficient of thermal expansion	10^{-5}	K^{-1}
β	Coefficient of chemical expansion	0.83	–
$\mathcal{K}$	Partition coefficient (of O/Si/S)	0 / 1 / ~ 1	–
$\mathcal{L}$	Latent heat of crystallization	5×10^6	J kg^{-1}
T_0	Reference temperature	–	K
C_0	Reference mass fraction of light elements	0.1	–
Q_i	Total heat flux at the ICB	?	TW
Q_o	Total heat flux at the CMB	~ 13	TW
I_i	Total light elements mass flux at the ICB	10^5	kg s^{-1}
I_o	Total light elements mass flux at the CMB	?	kg s^{-1}
$f^T_{i/o}$	Inner/outer thermal buoyancy flux	$\alpha g Q_{i/o}/C_p$	kg m s^{-3}
$f^\xi_{i/o}$	Inner/outer chemical buoyancy flux	$\beta g I_{i/o}$	kg m s^{-3}

TABLE 2.1: Summary of the main variables, constants and dimensionless numbers with a few suggested values for the Earth's outer core taken from (Poirier, 1988; de Wijs et al., 1998; Roberts and King, 2013; Labrosse, 2015).

as its dipolarity and the presence of inversions, hence the necessity to choose carefully the thermochemical boundary conditions. In most dynamo simulations, temperature and composition are combined via the codensity approach and uniform boundary conditions of the Dirichlet or Neumann type are imposed for the codensity. $T^* = \Delta T$ is a natural choice when a fixed temperature (codensity) condition is involved, ΔT being the codensity drop between both boundaries. Neumann conditions would typically involve fixed and homogeneous heat (codensity) flow at each boundary which can be used to construct the temperature scale:

$$T^* = \frac{Q}{4\pi\rho C_p \nu D}, \tag{2.29}$$

where Q is the integrated homogeneous heat flow imposed at both boundaries.

Such boundary conditions are convenient to implement and are able to produce dynamo action in spherical shells with Earth-like features of the magnetic fields in the sense of Christensen et al. (2010). Although they can bring an interesting insight into the general mechanisms of magnetic field generation, such conditions are however not very realistic and may not capture finer details of the dynamics of the core for at least two reasons. First because the heat and solute flows are usually laterally variable on the boundaries. Some structures like a hemispherical differential growth rate of the inner core are very difficult to retrieve with homogeneous conditions but emerge more naturally when adding a laterally variable codensity flow perturbation at the CMB (Aubert et al., 2008a). Another example is the hemispheric magnetic dichotomy of the Martian surface which can be obtained in numerical simulations by imposing an impact-induced codensity flux perturbation at the CMB (Monteux et al., 2015), though other mechanisms have been proposed (Stanley et al., 2008). Second, the situation is further complicated by the fact that the thermochemical boundary conditions are not independent and should be distinguished as soon as crystallization or melting occurs at one boundary, which is the case at the ICB. Because some light elements partition into the remaining liquid during the crystallization process, the chemical flux is locally proportional to the growth rate of the inner core which itself depends on the local heat flow. This introduces a thermochemical coupling at the inner core boundary and therefore a potentially complex retroaction between both fields which is likely to affect the flow in the entire shell. However, the few authors who have distinguished thermal and chemical effects have so far prescribed independent and uniform thermochemical boundary conditions for simplicity (Manglik et al., 2010; Breuer et al., 2010; Trümper et al., 2012; Takahashi, 2014). The mathematical formulation of the thermochemical coupling, its implementation in numerical models and its effect on core flow and dynamo action therefore still remain to be investigated.

In this work, two types of boundary conditions are considered. Independent Neumann thermochemical conditions are used to study generic properties in rotating spherical shells whereas coupled conditions are preferred when focusing more on the terrestrial case. In the next two paragraphs, a mathematical formulation is presented for each approach. Extra difficulties associated with the implementation of boundary conditions in the infinite Lewis number limit are pointed out and a solution is proposed.

Independent thermal and compositional Neumann boundary conditions

For simplicity, let us first consider the following uncoupled Neumann thermochemical boundary conditions:

- The same total heat flow $Q_i = Q_o$ is imposed homogeneously at the bottom and top boundaries. In this case, $\sigma^T = 0$ since we are aiming at a steady-state situation.

- At the top boundary, the compositional flux equals zero. At the bottom boundary, a total flux of light elements I_i^ξ is homogeneously imposed and can be adjusted independently from the heat flow. A volumetric sink term σ^ξ must then be introduced in the entire shell to compensate for the injected bottom flux, so that a statistically stationary state can be reached.

The thermal and compositional buoyancy flows injected at the inner boundary write:

$$f_i^T = \frac{\alpha g}{C_p} Q_i \quad ; \quad f_i^\xi = \beta g I_i^\xi, \tag{2.30}$$

where C_p is the heat capacity, Q_i the total heat flow imposed at the inner core boundary and core mantle boundary, I_i^ξ the mass flux of light elements integrated on the inner core boundary. At the top boundary, the buoyancy flows are equal to:

$$f_o^T = f_i^T \quad ; \quad f_o^\xi = 0. \tag{2.31}$$

One can then derive corresponding scalings for the temperature and composition based on the total buoyancy flows injected in the shell:

$$T^* = \frac{2 f_i^T}{4\pi D \alpha \rho_0 g \nu} \quad ; \quad C^* = \frac{f_i^\xi}{4\pi D \beta \rho_0 g \nu}. \tag{2.32}$$

The expressions of the Rayleigh numbers become:

$$Ra_T = \frac{2 f_i^T}{4\pi \rho_0 \nu^2 \Omega} \quad ; \quad Ra_\xi = \frac{f_i^\xi}{4\pi \rho_0 \nu^2 \Omega}, \tag{2.33}$$

and their ratio is equal to the buoyancy ratio:

$$\mathcal{R} = Ra_T / Ra_\xi = 2 f_i^T / f_i^\xi. \tag{2.34}$$

The transport equation (2.11) for temperature is mathematically a second-order differential equation. Technically, this allows to enforce one condition at each boundary. As explained in section 2.2.2, the temperature Θ is classically split into a conductive reference state Θ_s and a variable part Θ_v to get rid of the source term in the transport equation. The thermal boundary condition is then enforced when solving for the temperature diffusion by accommodating the following condition on the variable part Θ_v:

$$\left. \frac{\partial \Theta_v}{\partial r} \right|_{r=r_{i/o}} = 0, \tag{2.35}$$

so that the heat flow is injected into the shell at the boundaries via the action of diffusion along the gradient of the static conductive reference temperature profile Θ_s:

$$Q_{i/o} = -\rho_0 C_p \kappa^T \left. \frac{\partial \Theta_s}{\partial r} \right|_{r=r_{i/o}}. \tag{2.36}$$

For finite Lewis numbers, a similar strategy can be used for the chemical transport equation by constructing an equivalent conducting reference profile. But doing so becomes problematic in the infinite Lewis number limit (and even for large but finite Lewis numbers) since when κ^ξ tends to 0, the conductive reference chemical profile must have an infinite gradient. Mathematically, the limit of infinite Lewis number is in fact more subtle because neglecting the chemical diffusivity causes equation (2.14) to become hyperbolic, thus first order. Since non-penetrative boundary

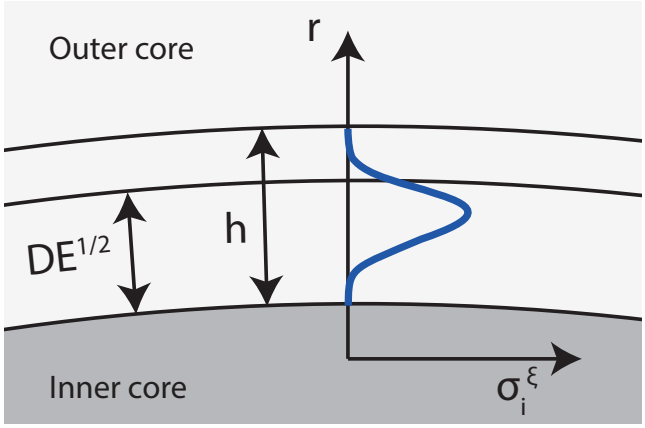

FIGURE 2.2: Illustration of the shape of the source term σ_i^ξ applied above the inner core boundary.

conditions are imposed for the flow, the radial velocity equals zero at each boundary. When solving the hyperbolic equation, this implies that no chemical "signal" imposed at a boundary can propagate inside the shell. The value of the composition at the boundary has therefore no effect on the solution and will in turn not be affected by the latter. Consequently, once the initial condition has been specified (for instance $C = 0$ everywhere), there is *mathematically* no need to impose any boundary condition. Despite that, in the terrestrial case, one may want to model the physical effect of the crystallization of the inner core by injecting light elements at the bottom of the outer core. A possible strategy is to inject light elements directly into the shell by introducing a source term σ_i^ξ within a thin layer of thickness h above the ICB, so that the integrated added mass fraction matches the ICB chemical flux:

$$4\pi \int_{r=r_i}^{r_i+h} r^2 \sigma_i^\xi(r) \mathrm{d}r = I_i^\xi. \tag{2.37}$$

The choice of an adequate function for $\sigma_i^\xi(r)$ requires some care. Indeed, since the velocity vanishes in the Ekman layer to accommodate the boundary conditions, any buoyant fluid injected at the bottom of this layer tends to remain "frozen" in the absence of chemical diffusion, hardly moves upward and does not participate in the convective dynamics. Adding the light elements slightly above in a region that roughly corresponds to the top part of the Ekman layer allows some destabilization and avoids accumulation of light elements in the layer over time. This can be performed smoothly using a Gaussian-like function:

$$\sigma_i^\xi(r) = \frac{\sigma_0}{r^2} \exp\left\{ -\left[r - \left(r_i + \frac{h}{2} \right) \right]^2 / \sigma^2 \right\}, \tag{2.38}$$

in which the constants are empirically set to $\sigma = h/5$ and $h = \frac{4}{3}E^{1/2}$, which is slightly larger than the thickness of the Ekman layer ($E^{1/2}$). The factor σ_0 must be computed using the value of the compositional flux. The shape of $\sigma_i^\xi(r)$ is schematically illustrated on figure 2.2.

Mathematically, this formulation is equivalent to solving the following transport equation:

$$\frac{\partial \xi}{\partial t} + \vec{\mathbf{u}} \cdot \vec{\nabla} \xi = \frac{1}{LePr_T} \nabla^2 \xi + \sigma^\xi + \sigma_i^\xi \mathcal{H}\left[(r_i + h) - r) \right], \tag{2.39}$$

and imposing no boundary conditions for the composition (at least, mathematically speaking).

The injection of light elements occurring in the ICB region is accounted for by the local source term $\sigma_i^\xi \mathcal{H}\left[(r_i + h) - r)\right]$, where $\mathcal{H}$ is a Heaviside function, and is balanced by a global sink term σ^ξ in the entire shell in order to allow the simulation to reach a statistically steady state. If a non-null compositional flux is imposed at the top boundary, a similar local source term can be applied by the same process. An alternative option would be to keep a diffusivity within a short distance from the boundary, but the connection with the non-diffusive portion of the shell is not evident. It should nevertheless be explored in the future.

In the next section, I show that the approach presented above, which is originally motivated by the infinite Lewis number limit and may look at first like a pure numerical "trick", can in fact be more physically justified by considering more closely the mechanisms of light elements release at the inner core boundary.

Thermochemical coupling

Although the uncoupled Neumann thermochemical conditions described in the last paragraph can be used to investigate generic questions in a rotating spherical shell, they are certainly not an adequate formulation of the realistic conditions at the Earth's inner core boundary (ICB). This region indeed bears several complexities, a quick overview of which is given below.

Because the Earth has been slowly cooling down since its initial formation, its liquid metallic core started to crystallize to form a solid inner core, probably around 1 Gy ago (Labrosse, 2015). For reasons tied to thermodynamics, the inner core started to crystallize at the center of the Earth and has been gradually growing since. In metallurgy, it is well known that an interface between liquid alloy metal and its corresponding solid is prone to morphological instabilities if the cooling rate exceeds a critical value creating a region formed of a mix between a liquid and a dendritic solid called a *"mushy zone"*. The conditions are likely to be satisfied at the ICB (Copley et al., 1970; Loper and Roberts, 1981; Loper, 1983; Chen and Chen, 1991; Deguen et al., 2007) so that the transition between the fluid outer core and the solid inner core may not be simply a sharp boundary. The existence of a mushy layer is compatible with seismic observations (Cao and Romanowicz, 2004) but its vertical extent is not well constrained. Deguen et al. (2007) advocate a thickness of order 1 km, but the mushy layer could be much thicker, even extending to the entire inner core (Fearn et al., 1981). The dynamics of a mushy zone is probably extremely complex. The general picture (illustrated on figure 2.3) is that of a liquid flow globally percolating downward with occasional chimneys producing strong upward chemical plumes (Loper, 1983; Bergman and Fearn, 1994). The dynamics of such a system may depend on the viscosity of the fluid and on the permeability and structure of the mush. The possibility of convection (Worster, 1997) and salt fingers (Fowler, 1985) within the mush has been evoked. To further complicate this picture, some authors have suggested the possibility that part of the crystallization occur above the ICB in a *slurry layer* (Loper and Roberts, 1981; Shimizu et al., 2005).

In numerical models, the details of this complexity are difficult to describe, first because the underlying physics is not fully understood and also because it would require an even finer resolution of the region above the boundary. In a first attempt to simplify the problem, one can however assume that the main effect of the mushy zone processes on the large-scale flow is to introduce a local proportionality between the injected heat and chemical flows. This allows to construct a simpler mathematical formulation that is detailed below. In this context, injecting light elements within a thin layer extending above the ICB as proposed in equation (2.37) appears less far-fetched since it can be viewed as a simplistic parametrization of the mushy zone processes.

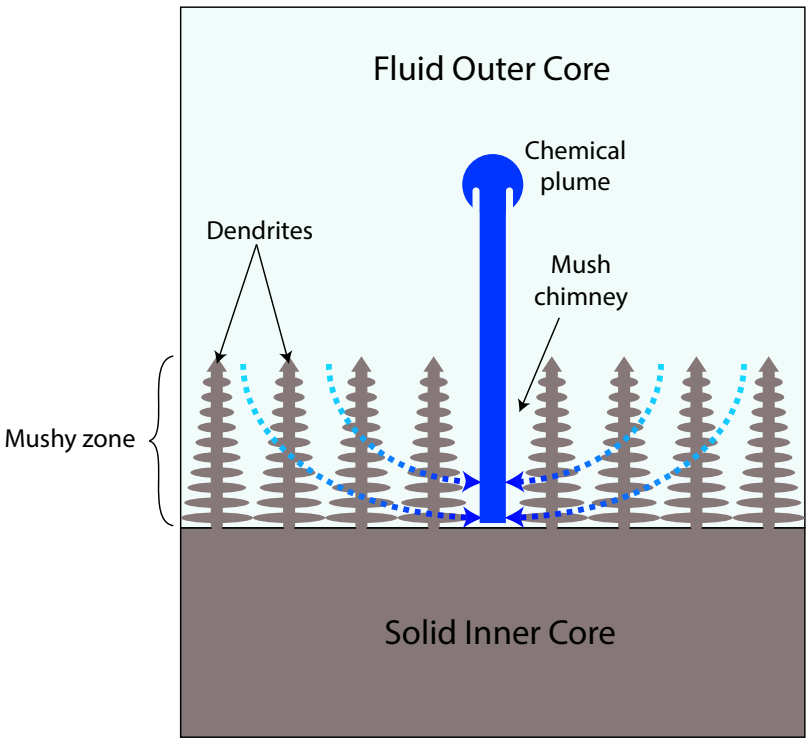

FIGURE 2.3: Simplified illustration of the possible structure of the ICB region. The inner core crystallizes in a "mushy layer" formed by a network of dendrites through which fluid from the outer core percolates downward, getting gradually richer in light elements. In some isolated locations in the mush, chimneys eject fluid enriched in light elements in the form of rising chemical plumes.

At the CMB, a relevant condition would be a heat flow per surface unit $\mathcal{Q}_o(\theta, \phi)$ imposed by mantle convection. For simplicity, one can enforce a homogeneous flux over the boundary, but a more realistic condition would be a laterally variable flow. In this case, the flow can be split into an average value and a perturbation:

$$\mathcal{Q}_o(\theta, \phi) = \overline{\mathcal{Q}}_o + q_o(\theta, \phi). \tag{2.40}$$

In this case, the corresponding mean buoyancy flux is:

$$\overline{f}_o^T = \frac{\alpha g}{C_p} \overline{Q}_o, \tag{2.41}$$

where $\overline{Q}_o = 4\pi r_o^2 \overline{\mathcal{Q}}_o$ is the mean heat flow integrated on the CMB surface. The flux $\mathcal{I}_o^\xi$ of light elements per surface unit at the top is set to zero if it is assumed that no chemical exchange occurs with the mantle. The corresponding chemical buoyancy flux integrated on the CMB also equals zero: $f_o^\xi = 0$.

At the ICB, the inner core crystallizes at the melting temperature T_m. Neglecting any topography of the ICB and compositional effects, T_m is assumed to be constant over the boundary. The local heat flux $\mathcal{Q}_i(\theta, \phi, t)$ into the outer core across a surface element dS is equal to the sum of the heat flux from the inner core $\mathcal{Q}_i^{\mathrm{IC}}$ assumed uniform, *i.e.* neglecting any possible IC dynamics, plus the latent heat $\mathcal{Q}_i^{\mathrm{L}}(\theta, \phi, t)$ released locally by the crystallisation:

$$\mathcal{Q}_i(\theta, \phi, t) = \mathcal{Q}_i^{\mathrm{IC}} + \mathcal{Q}_i^{\mathrm{L}}(\theta, \phi, t), \tag{2.42}$$

with:

$$\mathcal{Q}_i^{\mathrm{L}} = \rho \mathcal{L} \dot{r}_i, \tag{2.43}$$

where ρ is the local fluid density, $\mathcal{L}$ is the latent heat in the ICB conditions and $\dot{r}_i(\theta, \phi, t)$ the local growth rate of the inner core radius. The latter can be related to the rate of solid mass production:

$$\dot{m}_{icb}^s = \rho \dot{r}_i \mathrm{dS}. \tag{2.44}$$

The mass of light elements $\mathrm{d}m_{icb}^{\xi}$ released locally for a time increment dt is therefore:

$$\mathrm{d}m_{icb}^{\xi} = \rho(c_l - c_s)\dot{r}_i \mathrm{dSdt}, \tag{2.45}$$

where c_l and c_s are the local concentrations of light elements in the liquid and solid at the ICB, respectively. This corresponds to a dimensional mass flux per surface unit:

$$\mathcal{I}_i^{\xi} = \rho(c_l - c_s)\dot{r}_i \tag{2.46}$$

and substituting $c_s = \mathcal{K} c_l$, with $\mathcal{K}$ the partition coefficient, leads to the local equation:

$$\boxed{\mathcal{I}_i^{\xi}(\theta, \phi, t) = \frac{c_l(1-\mathcal{K})}{\mathcal{L}} \left(\mathcal{Q}_i(\theta, \phi, t) - \mathcal{Q}_i^{\mathrm{IC}}\right)} \tag{2.47}$$

in which the chemical and heat flows are locally linearly related. In the following equations, the partition coefficient is set to $\mathcal{K} = 0$ for simplicity, which would be correct if O is the dominant light element (Alfè et al., 2002). For Si, the value would be close to 1 (Alfè et al., 2002) in which case, no compositional buoyancy is produced by the growth of the inner core. The last equation becomes:

$$\mathcal{I}_i^{\xi} = \frac{c_l}{\mathcal{L}}(\mathcal{Q}_i - \mathcal{Q}_i^{\mathrm{IC}}). \tag{2.48}$$

To further simplify this expression, one can take the mean mass fraction of light elements C_0 in the outer core for c_l. In addition, $\mathcal{Q}_i^{\mathrm{IC}}$ is set to 0 (which corresponds to an insulating inner core) since it is a small contributor to the total ICB heat flux (Labrosse, 2015). The previous relation therefore reduces to:

$$\boxed{\mathcal{I}_i^{\xi}(\theta, \phi, t) = \frac{C_0}{\mathcal{L}} \mathcal{Q}_i(\theta, \phi, t).} \tag{2.49}$$

Another option would be to assume that the temperature in the inner core follows the same isentrope as the outer core which can be computed using evolution models.

In order to reach a statistically stationary state in the numerical simulations, the integrated mean ICB heat flow must be equal to the CMB heat flow:

$$\overline{I}_i^{\xi} = \frac{C_0}{\mathcal{L}} \overline{Q}_i = \frac{C_0}{\mathcal{L}} \overline{Q}_o. \tag{2.50}$$

The following mean thermal and compositional buoyancy fluxes are then used to define the dimensionless temperature and composition:

$$\overline{f}_i^T = \overline{f}_o^T = \frac{\alpha g}{C_p} \overline{Q}_o^s = \frac{\alpha g}{C_p} \overline{Q}_i^s \quad ; \quad \overline{f}_i^{\xi} = \beta g \overline{I}_i^{\xi}. \tag{2.51}$$

Note that only the super-adiabatic part $\overline{Q}_i^s$ of the mean heat flow is used to construct the thermal Rayleigh number. This flow represents a fraction ζ of the total ICB heat flow:

$$\overline{Q}_i^s = \zeta \overline{Q}_i. \tag{2.52}$$

In the coupled case, the buoyancy fluxes are thus related by:

$$\overline{f}_i^\xi = \mathcal{S} \overline{f}_i^T, \tag{2.53}$$

where $\mathcal{S}$ is a dimensionless coupling number analogous to a Stefan number and equal to:

$$\mathcal{S} = \frac{\beta C_p C_0}{\alpha \mathcal{L} \zeta}. \tag{2.54}$$

Using the parameters in table 2.1 for the Earth's outer core, it can be estimated that $\mathcal{S} \sim 10/\zeta$. This number can be simply related to the buoyancy ratio by:

$$\mathcal{R} = 2\overline{f}_i^T / \overline{f}_i^\xi = 2/\mathcal{S}. \tag{2.55}$$

Then, using again the mean integrated buoyancy flows, one can write the dimensionless temperature and composition:

$$T^* = \frac{2\overline{f}_i^T}{4\pi D \alpha \rho_0 g \nu} \quad ; \quad C^* = \frac{\overline{f}_i^\xi}{4\pi D \beta \rho_0 g \nu}, \tag{2.56}$$

which lead to the subsequent expressions for the Rayleigh numbers:

$$Ra_T = \frac{2\overline{f}_i^T}{4\pi \rho_0 \nu^2 \Omega} \quad ; \quad Ra_\xi = \frac{\overline{f}_i^\xi}{4\pi \rho_0 \nu^2 \Omega}. \tag{2.57}$$

The thermal and compositional Rayleigh numbers are not independent and, like the buoyancy flows, they are related by an expression involving the coupling number $\mathcal{S}$:

$$Ra_\xi = \frac{\mathcal{S}}{2} Ra_T. \tag{2.58}$$

Like in the uncoupled case, 6 independent dimensionless parameters govern the physical problem: $(E, Ra, P_m, P_T, Le, \mathcal{S})$ or, equivalently: $(E, Ra, P_m, P_T, Le, \mathcal{R})$.

Similarly to the uncoupled case, the light elements can be injected directly into the shell by introducing a local source term $\sigma_i^\xi(r, \theta, \phi, t)$ above the ICB such that:

$$\int_{r_i}^{r_i+h} r^2 \sigma_i^\xi(r, \theta, \phi, t) \mathrm{d}r = r_i^2 \mathcal{I}_i^\xi(\theta, \phi, t). \tag{2.59}$$

The source term $\sigma_i^\xi(\theta, \phi, t)$ has the same form as in the case of homogeneous conditions:

$$\sigma_i^\xi(r, \theta, \phi, t) = \frac{\sigma_0(\theta, \phi, t)}{r^2} \exp\left\{ -\left[r - \left(r_i + \frac{h}{2} \right) \right]^2 / \sigma^2 \right\}, \tag{2.60}$$

except that $\sigma_0(\theta, \phi, t)$ is now computed locally.

2.4 On the necessity of a diffusion-free numerical method

The formalism above was derived in the approximation of infinite Lewis number meaning that a hyperbolic equation is solved for the chemical transport equation in which the chemical diffusivity is totally neglected. As will be shown later in chapter 6, compositional structures become extremely thin in this case. A code designed to solve numerically the set of equations (2.26) with $Le = +\infty$ must therefore be able to account for the advection of small-scale chemical structures throughout a simulation without generating extra dissipation. With classic Eulerian (grid) descriptions, this is a difficult task to achieve as most methods produce a certain amount of numerical diffusion (see figure 2.4 for an illustration). A possible option is to resort to a Eulerian-Lagrangian description of the compositional field using a *Particle-In-Cell* method as advocated by G. Glatzmaier in his book (Glatzmaier, 2013). The next chapter presents the principles of this method and shows how it could be implemented in a pre-existing dynamo code. A justification of this method based on a comparison with some Eulerian schemes specifically designed to solve hyperbolic equations such as TVD and WENO is shown later in chapter 5.

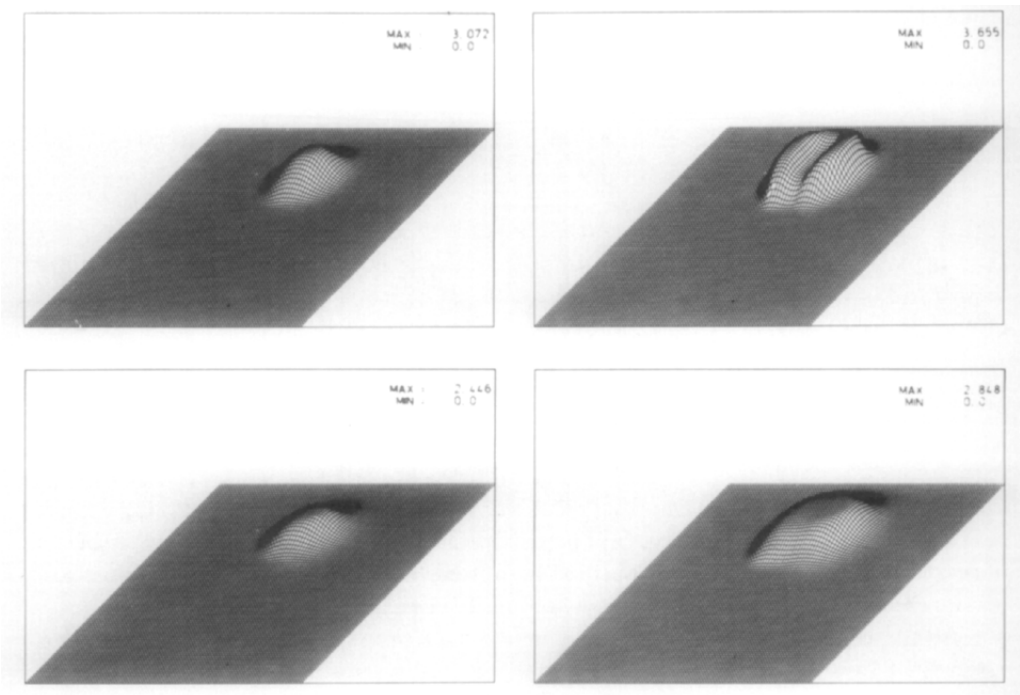

FIGURE 2.4: Illustration of the phenomenon of numerical diffusion when performing pure advection (solid-body rotation) of a cone and a cut-open cylinder when using a TVD scheme with a Van-Leer slope. Top row: shapes after one rotation. Bottom row: shapes after 6 rotations. Although no dissipation term is solved in the transport equation, the cone and cut-open cylinder are "smoothed" by an artificial diffusion of numerical origin. From Munz (1988).

Chapter 3

Numerical method

"Particle-In-Cell" (PIC) methods attempt to combine the best of both grid and particles approaches to solve transport equations in advection-dominated problems. Originally formalized in the late 1950s (Evans et al., 1957), they have since been developed into a series of variants ranging from mostly Eulerian to quasi fully Lagrangian methods. In one of the classic formulations of the PIC method, the main equations are solved on a numerical grid while some scalar fields are described by an ensemble of particles initially dispersed across the grid. Each particle is given some information, usually its coordinates and the local value of one or several scalar fields to describe, so that the particles distribution can be seen as a discrete sampling of the underlying continuous fields. Information can then be exchanged between particles and grid nodes by the means of linear or higher-order interpolations. In particular, the velocity known on the grid nodes can be interpolated at the position of particles to advect them (which is often called the *"push"* phase). Conversely, the scalar fields can be evaluated on the grid nodes from the particles distribution. In some contexts, PIC methods have also been referred to as *"marker-in-cell"* or *"tracers"* methods. For convenience, the terms "particles" and "tracers" will be used with equivalent meaning in the rest of this manuscript. The term "tracer" will however be preferred for its more passive connotation when the particles are simply advected without contributing to the buoyancy.

Among the features that are generally acknowledged for PIC methods are the lack of numerical dissipation (or at least, its strong reduction) and a certain robustness due to the absence of Courant type stability condition. Due to its partly Lagrangian characteristics, it can also provide a better insight into some of the properties of the flow since it allows to follow the trajectories of particles with time. A well recognized drawback is the potential accuracy deterioration resulting from high distortion in the flow. Various PIC methods have been designed to address numerous physical problems in hydrodynamics (Brackbill et al., 1988; Snider, 2001), plasma physics (Buneman, 1959; Birdsall, 1991; Honda et al., 2000; Fonseca et al., 2002; Tskhakaya et al., 2007), astrophysics (Sironi and Spitkovsky, 2009), meteorology (Lange, 1978), convection-dispersion problems in porous media (Huang et al., 1992) and solid mechanics (Bardenhagen and Kober, 2004), mostly in 2D and 3D Cartesian geometries and up to high-orders of accuracy (Edwards and Bridson, 2012). In some communities like plasmas physics, PIC methods became a corner stone of numerical simulations and gained so much popularity that they gave birth to dedicated websites, workshops and summer schools. In Earth and planetary sciences, PIC methods remained essentially limited to their successful application to transport in solid flows (Gerya and Yuen, 2003) including solid-state mantle convection (Tackley and King, 2003; Moresi et al., 2003) and have seemingly never been used for convection in planetary cores or internal liquid oceans so far.

Part of the work of this PhD was devoted to the adaptation of a PIC method to the study of thermochemical convection in the internal liquid layers of planets. For this purpose, it may seem easier to develop a new code from scratch that is well suited to the implementation of a PIC method, for example using a finite volumes method in a "Yin-Yang" configuration similarly to the mantle convection code StagYY (Tackley, 2008). However, for dynamo simulations, the use of

spectral methods allows a natural way of ensuring the continuity of the magnetic field with the exterior field, which is potential. Spectral methods are therefore most commonly used in the field of dynamo theory and simulations. Opting for a different approach may ease the implementation of the PIC part but would seriously complicate that of magnetic field boundary conditions (Matsui and Okuda, 2004). On the contrary, implementing a PIC method into a pre-existing dynamo code rewards us with a tool that is more versatile since it can be used for planetary dynamos as well as for convection only. I therefore implemented a PIC method in the pre-existing geodynamo code PARODY-JA developed by E. Dormy and J. Aubert (Dormy et al., 1998; Aubert et al., 2008b) to compute the advective part of the transport equation (2.14) for composition and, if desired, that of the identical equation (2.11) for temperature. In PARODY and other similar codes, the equations are discretized on N_r points in the radial direction using a classic finite difference scheme on a non-uniform grid refined near the boundary layers. On each concentric sphere, the physical quantities are decomposed on spherical harmonics up to degree ℓ_{max} and order m_{max}. The computation of non-linear terms cannot be directly performed in spectral space and should be first evaluated by finite differences on a spherical grid on Gauss collocation points involving N_θ points in latitude and N_ϕ in longitude before being transformed back to spectral space. The time-integration is performed using a semi-implicit scheme, Crank-Nicolson for diffusion and Adams-Bashforth for the other terms. This method is used to solve the set of equations (2.26). The advection of composition in equation (2.14) and, if desired, that of temperature in equation (2.11), is performed via a different numerical strategy relying on particles.

In this chapter, the principles of the PIC method implemented in PARODY are described. A word will first be said about the initial particles distribution. The general numerical scheme will then be presented as well as its different sub-steps: the interpolation of the compositional field from particles to grid nodes, the advection of the particles, the treatment of diffusion and eventually, that of boundary conditions. Although the adopted approaches are quite classic in the literature of PIC methods, their adaptation to the context of planetary dynamos raises a series of complex issues. A first difficulty comes from the implementation of a PIC method in full spherical geometry, especially due to the presence of points of singularity (poles and center) and to the irregularity of the grid. In addition, as will be shown in chapter 6, the method must be able to describe compositional structures that are extremely thin and often described by only a few grid points. Moreover, rotation usually plays an important role in these systems and can have a strong influence on the characteristics of the flow. The creation of shear and vorticity can be difficult to deal with for the PIC method which should be properly adapted. All along this chapter, these difficulties will be clearly identified and followed by a discussion of the proposed solutions.

3.1 Particles distribution in a spherical grid

3.1.1 Initial distribution

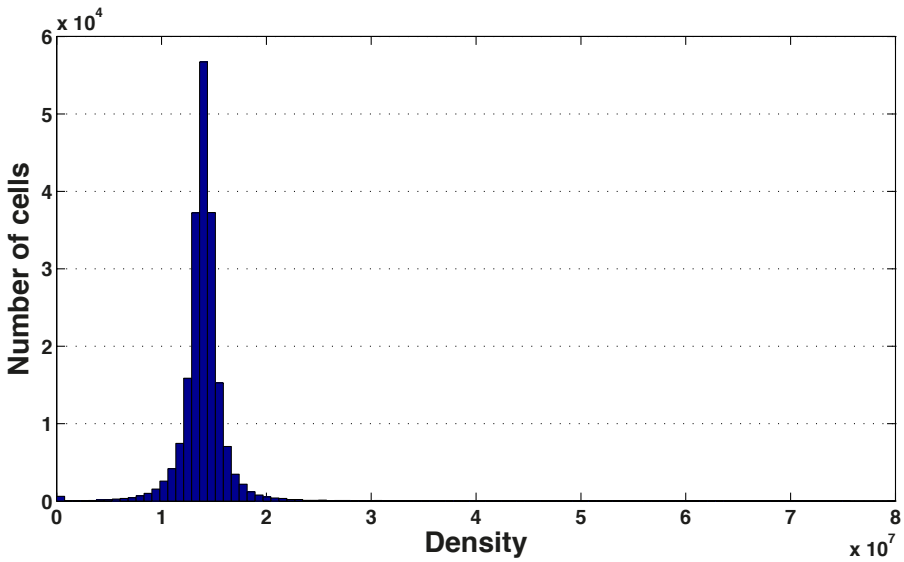

FIGURE 3.1: Histogram of the average density of particles (*i.e.* number of particles per volume unit) for $(N_r, N_\theta, N_\phi) = (40, 50, 100)$ with aspect ratio $r_i/r_o = 0.35$ and $N_{tra} = 5 \times 10^7$ randomly distributed particles. The mean value is 1.4×10^7, the standard deviation 2.26×10^6 and the maximal value 7.57×10^7. The volume of the sphere is 4.01 so that the expected mean density is 1.25×10^7. Values larger than 3×10^7 correspond to cells in the polar regions.

A large number N_{tra} of particles (typically a few 10^7 to several 10^9 tracers) are initially distributed across the whole computational domain. Each particle numbered p contains information regarding its coordinates r_p, θ_p, ϕ_p – giving its position in a spherical system of representation – and the local value of composition (and/or, if desired, temperature or any other scalar variable even if associated to different diffusivity) at the position of the particle. Numerically, this is materialized by an array with as many lines as particles and number of columns $3 + n_f$, where n_f is the number of scalar fields described by the particles; the first 3 columns containing the particles coordinates.

The choice of the initial distribution method may affect the solution in some cases and should ideally satisfy two criteria for the PIC method to work in an optimal way. It should first guarantee that the particles are globally homogeneously spread in order to avoid clustering effects, the latter being detrimental to the global accuracy of the method. Second, it should preferably be portable for different implementations so that for identical initial parameters, simulations start from the same particles distributions on two different computers. A random distribution is in that sense problematic since it produces clusters and also creates a portability issue unless the seed and random numbers generator scheme are explicitly set by the programmer. Contrary to the random distribution, a homogeneous distribution (obtained for instance by placing particles regularly on a 3D Cartesian grid) has the advantage of not showing any "pattern" or cluster inherent to random generation schemes and not posing any problem of porting and reproducibility. An interesting compromise consists in superimposing a random noise over a homogeneous distribution, but this has not yet been tested. The characteristics of a random distribution are shown

on figure 3.1. A homogeneous distribution produces similar features.

In practice, it seems that the initial distribution has only little impact on the final solution since the flow rapidly mixes the particles and creates a small amount of clustering anyway if the advection scheme is not accurate enough. An exception should be noted for the onset of convection in which an artificial periodicity (usually of degree 4) can appear if a homogeneous Cartesian distribution is adopted. If the convection onset is studied, it is preferable to use either a random initial distribution or to superimpose a random or controlled noise over a homogeneous Cartesian distribution.

3.1.2 Characteristics of the particles distribution

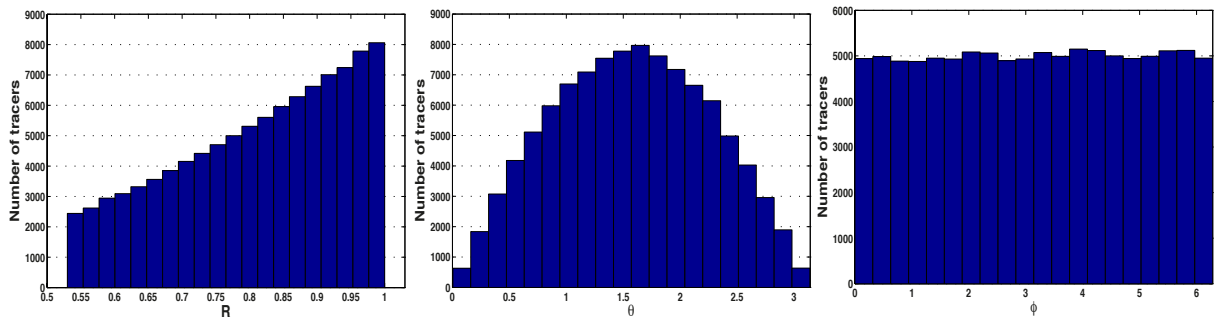

FIGURE 3.2: Histograms showing the average number of particles per grid cell along radius (left), latitude (middle) and longitude (right). The grid is $(N_r, N_\theta, N_\phi) = (20, 30, 60)$ with an aspect ratio $r_i/r_o = 0.35$ and $N_{tra} = 10^5$ particles randomly distributed.The grid spacing is regular in all three directions. The average number of particles per cell increases with the radius and decreases near the poles.

Although the previously proposed distribution methods ensure that the number of particles per unit of volume is constant on average in the domain (see figure 3.1), the number of particles per grid cell varies by several orders of magnitude due to the sphericity of the grid of PARODY. Indeed, the volume element is proportional to $r^2 \sin(\theta)$ in a spherical discretization along radius, latitude and longitude. In order to illustrate this particularity, the number of particles per cell is averaged along each direction and shown in the form of histograms on figure 3.2. For a different grid configuration with the same aspect ratio, two spherical maps corresponding to two different radii are also displayed on figure 3.3 to complete this view. At fixed radius, the number of tracers per grid cell varies by typically more than one order of magnitude. The same is true for the average number of particles per grid cell for radii taken near the bottom boundary and in the middle of the grid. These differences are exacerbated for grids with higher resolutions and dramatically worsen in full sphere or low aspect ratios for which the biggest cell of the grid is larger than the smallest by a factor exceeding 10^5. As will be emphasized in the next paragraphs, this particularity of the spherical grid is the source of many complications when implementing a PIC method in spherical geometry as it forces the programmer either to use an astronomically high number of particles or to deal with a large number of grid cells which do not contain particles.

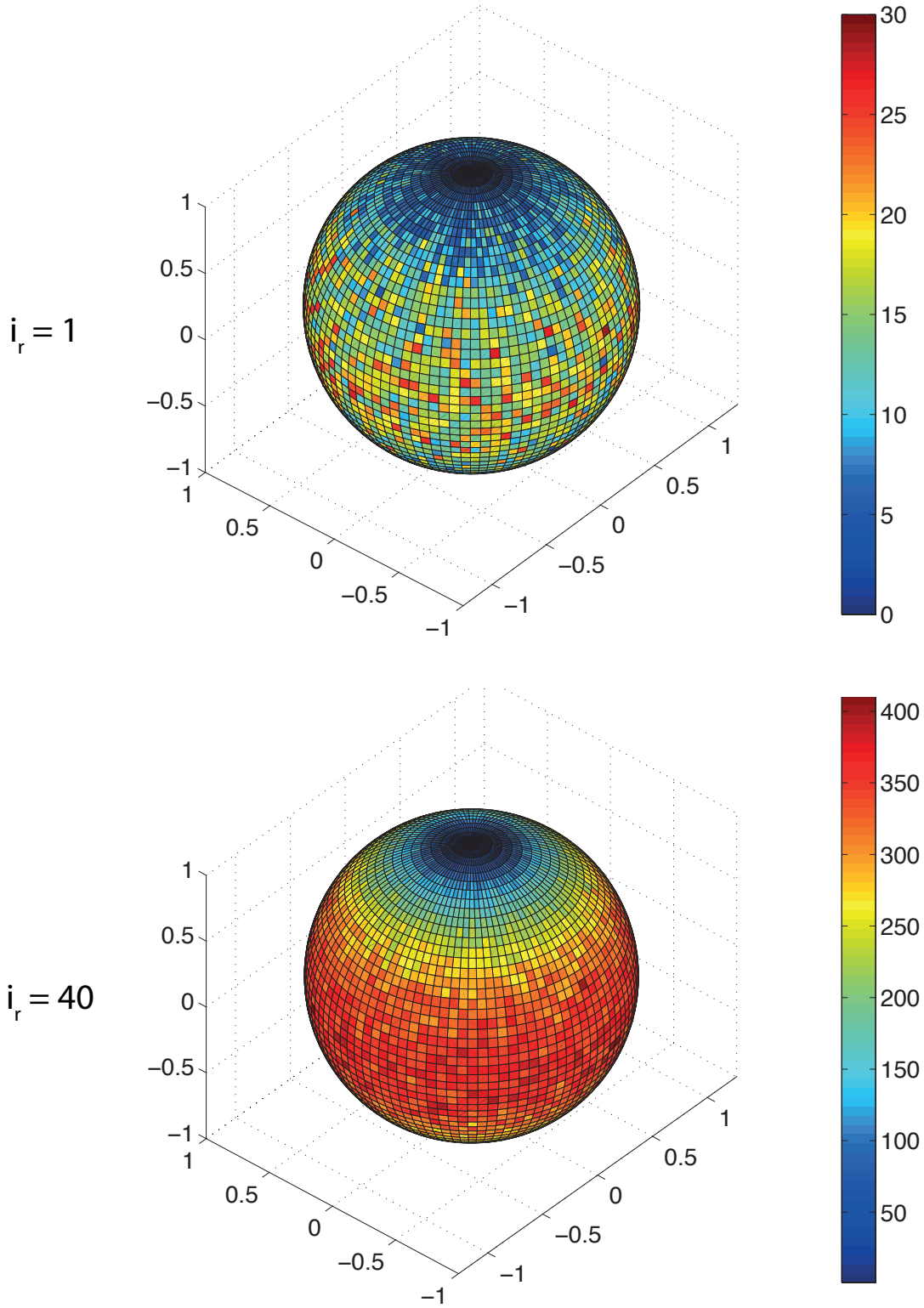

FIGURE 3.3: Number of tracers per grid cell on two spherical maps corresponding to different radii. The grid is $(N_r, N_\theta, N_\phi) = (80, 50, 100)$, with radial spacing decreasing geometrically near the boundaries. $N_{tra} = 5 \times 10^7$ particles were randomly distributed.

3.2 General numerical scheme

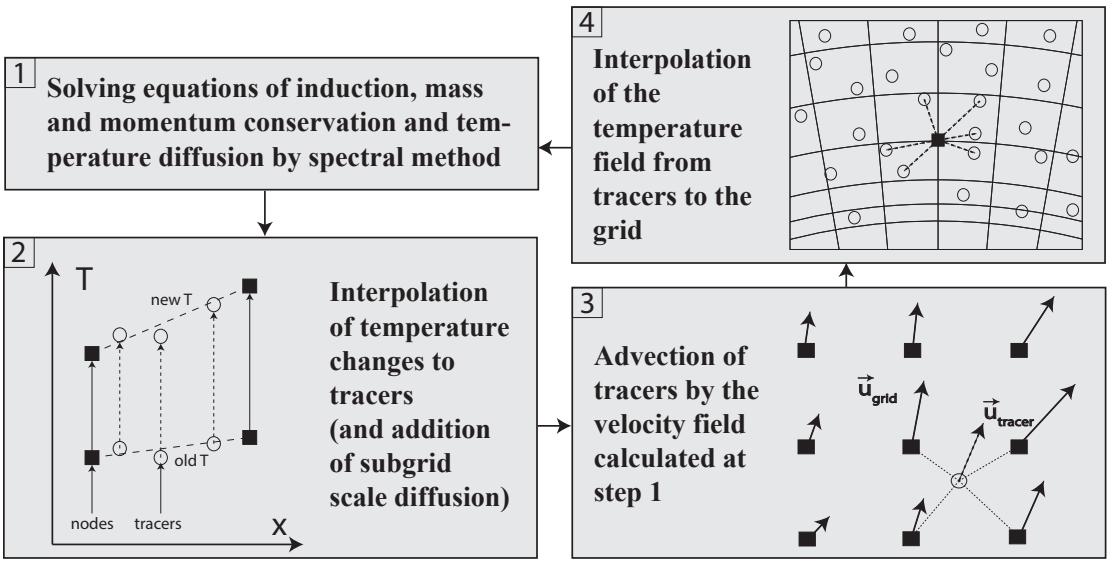

FIGURE 3.4: Schematic illustration of the main steps of the computational strategy for the treatment of temperature using a PIC method in the code PARODY. Steps 2, 3 and 4 are strictly identical for the compositional field.

The computational strategy to solve equations (2.11) and (2.14) by the PIC method is summarized in figure 3.4 and comprises the following steps:

1. The set of quations (2.26) is solved by the numerical scheme of PARODY described previously, except the advective part of equation (2.14) and, if desired, that of equation (2.11), which is solved with a different numerical strategy using tracers.

2. The composition (and/or temperature) diffusive changes are calculated from spectral space to the nodes of the Eulerian grid and communicated to the tracers by first-order (trilinear) interpolation. A process of subgrid-scale diffusion must also be introduced at this step to diffuse tracers-scale structures and is discussed in details in section 3.5. If diffusion is neglected, this step is skipped.

3. The tracers are advected by a 4th-order Runge-Kutta scheme in time using the velocity field which has been calculated on the Eulerian grid at step 1. The velocity of each tracer is evaluated by trilinear or semi-quadratic interpolation using the closest grid points (see step 3 in fig. 3.4).

4. The temperature and composition fields are evaluated linearly back from tracers to the Eulerian grid and finally re-integrated into spectral space.

The strategy would be identical for the treatment of any other scalar field obeying similar transport equation. All steps consist of interpolation between particles and grid nodes. The detailed principles of each step and their implementation in PARODY are described in sections 3.3 to 3.5. Furthermore, in the infinite Lewis number limit, enforcing compositional boundary conditions must be done through a specific treatment which is also explained in section 3.6.

3.3 Interpolation of scalar fields from particles to grid nodes

In the next paragraphs, the equations are written for temperature only, but one could write identical expressions for composition or any other scalar quantity. Notations similar to Gerya and Yuen (2003) are adopted to facilitate comparisons. The main difference with their work is that PARODY has a 3D spherical geometry and does not rely on a staggered grid.

3.3.1 Trilinear interpolation

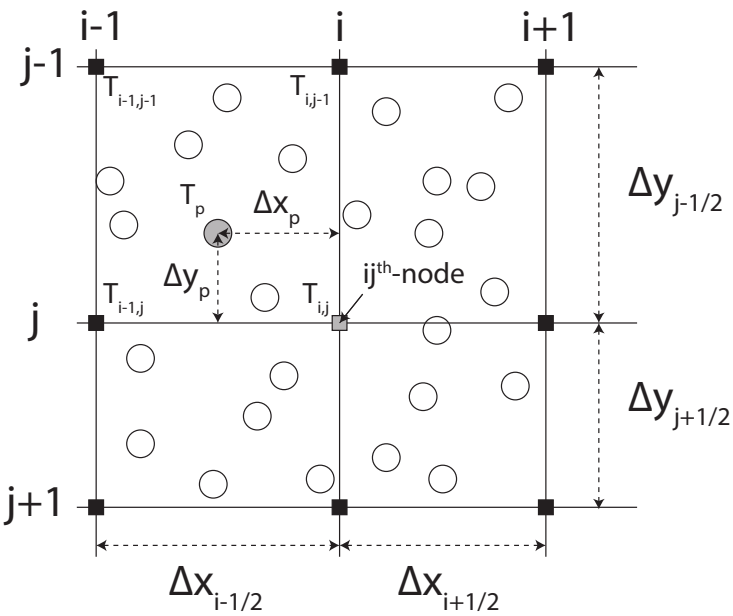

FIGURE 3.5: 2D Cartesian representation of the geometrical relations used for the first-order interpolation scheme of the temperature field. Grid nodes are drawn as solid squares, tracers as open circles. Adapted from Gerya and Yuen (2003).

To evaluate the temperature $T_{(i,j,k)}$ on the node (i, j, k) of the Eulerian grid, a weighted average is performed using all the tracers located in the surrounding grid cells (see step 4 on fig. 3.4 for an illustration):

$$T_{(i,j,k)} = \frac{\sum_p T_p \omega_{p(i,j,k)}}{\sum_p \omega_{p(i,j,k)}}, \tag{3.1}$$

where T_p is the temperature of the p-th tracer and ω_p the corresponding weight, based on a spherical approximation of the 3D equivalent of the 2D "area-weighting" method (Seldner and Westermann, 1988):

$$\omega_{p(i,j,k)} = \left(1 - \frac{\Delta r_p}{\Delta r}\right)\left(1 - \frac{\Delta \theta_p}{\Delta \theta}\right)\left(1 - \frac{\Delta \phi_p}{\Delta \phi}\right), \tag{3.2}$$

with: $\Delta r_p = |r_p - r_{(i,j,k)}|$, $\Delta \theta_p = |\theta_p - \theta_{(i,j,k)}|$, $\Delta \phi_p = |\phi_p - \phi_{(i,j,k)}|$,

$$\Delta r = \begin{cases} \Delta r_{i-1/2} = r_i - r_{i-1} & \text{if} \quad r_p \leq r_i \\ \Delta r_{i+1/2} = r_{i+1} - r_i & \text{if} \quad r_p \geq r_i \end{cases} \tag{3.3}$$

and similar expressions for $\Delta\theta$ and $\Delta\phi$. A 2D Cartesian illustration of the meaning of these quantities is given in figure 3.5. Note that if the grid spacing varies along a given direction (which

is the case for the radial direction in the boundary layers) this formulation introduces a bias, since two tracers at equal distance from r_i will not contribute with the same weights. However, this is less problematic for smooth variations of the grid spacing. In addition, this formulation only involves multiplications which makes it much cheaper than using weights proportional to the inverse of the distance between tracers and grid nodes as such an approach would involve one division and the evaluation of several intrinsic functions (sine, cosine, square root of) performed by rather costly internal algortihms. Also, this approximation of the "volume-weighted" method deteriorates when the curvature of the cell increases, which is the case close to the poles and to the sphere center. A way around this is to advect tracers in Cartesian geometry in these regions and this is described in more details in section 3.4.4.

3.3.2 Higher order interpolation schemes

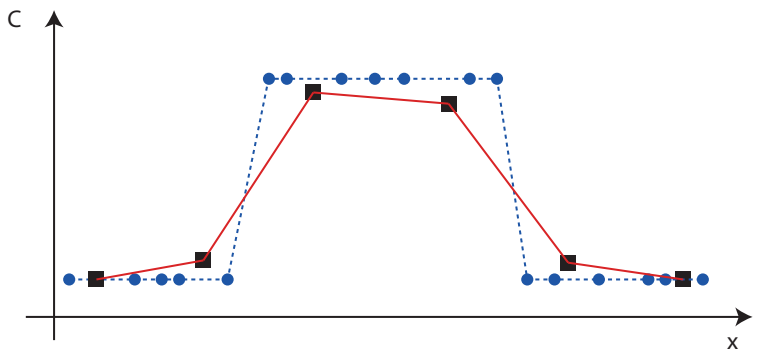

FIGURE 3.6: 1D schematic illustration of linear interpolation of a compositional rectangle from tracers (blue disks) to grid nodes (black squares). The field described by the tracers has a sharp transition (blue dashed line) whereas the field evaluated on the grid (red line) is smoother and spans over 4 grid points which is larger than the width of the rectangle. This is due to the fact that each grid point receives contributions from all the particles located within the closest neighbor nodes. Furthermore, since in this case the width of the rectangle is less than 3 grid points, the maximum value of the rectangle is also decreased.

Even though a trilinear interpolation method appears to be sufficient in practice in most cases, its limitations should be mentioned. As is shown in chapter 6, the compositional field typically consists of very thin "filamentary" plumes the width of which are often resolved by only a few grid points. The boundary of a plume may well fall between two grid nodes. Although the latter may be better described by the particles field, the interpolation from particles to the grid causes a contamination to a grid point that is outside the plume (see figure 3.6 for a simpler 1D illustration). A compositional plume therefore appears systematically larger by two grid points on the grid, a phenomenon which can be interpreted as numerical diffusion of the buoyancy source. At this point, it is however important to state that this error does not spread further (like it would by using finite differences) and remains constant over time. In addition, since the viscosity is non zero, the ascending velocity field created by the plumes is usually quite larger than the plume itself and is almost unaffected if the plume is only slightly diffused. The consequence on the global dynamics is therefore negligible.

It may however be worth considering the implementation of high-order interpolation schemes in the future. For instance, Edwards and Bridson (2012) use a fourth order accurate interpolation scheme based on approximation by cubic polynomials via a Moving Least Squares (MLS) method (Lancaster and Salkauskas, 1981). Since in the presence of shocks, kinks, or other sharp

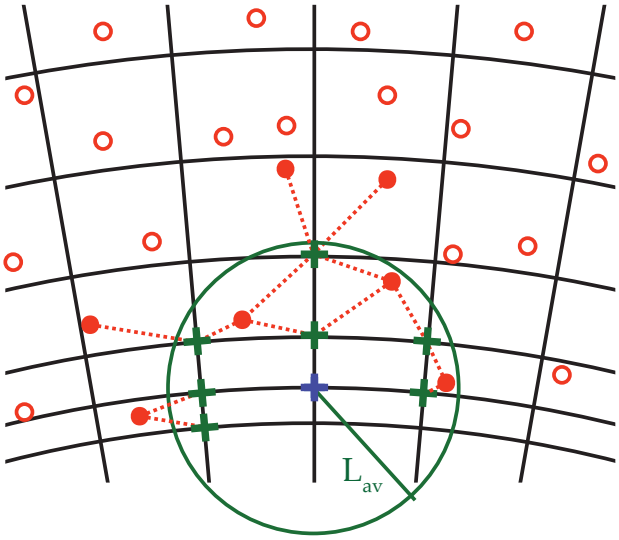

FIGURE 3.7: Illustration of the treatment of "empty cells". The blue cross (the center of the circle) has received no information during interpolation from tracers to grid because there were no neighboring tracers. A weighted average is performed using all the grid nodes located within a distance L_{av} which did receive some information from tracers (green crosses). The tracers represented as open circles did not contribute while those in plain circle did.

features, MLS can lead to severe overshoots and thence instability, Edwards and Bridson (2012) suggest Quasi-ENO MLS (Ollivier-Gooch, 1997) schemes should be used instead. In the future, it may be worth implementing and testing a similar scheme in PARODY. Not only can such an approach offer a better grid description of the compositional field, but it can help constructing a PIC method with global high-order accuracy, when also combined with a higher-order advection scheme (Edwards and Bridson, 2012). Note that computing directly the spectral decomposition of the scalar field from the information of millions of scattered particles is simply out of question in terms of computational cost.

3.3.3 Problem of "empty cells"

In section 3.1.2, I emphasized that the number of particles per grid cell varies by several orders of magnitude across the spherical grid of PARODY. For the interpolation scheme described in section 3.3.1 to be successful, each grid point should be surrounded by particles in the immediate neighboring cells. Consequently, one is forced to either introduce an intractably high number of tracers to ensure that each cell statistically contains at least one tracer, or to use a more reasonable number of tracers and deal with a minor fraction (yet possibly amounting to a significant number) of "empty" grid cells. Assuming an efficient treatment can be found for empty cells, the second option is obviously faster. Furthermore, since a small amount of clustering/depletion seems to be inevitable during a simulation, empty cells may exist anyway whatever the initial number of tracers, warranting the development of a specific treatment.

In a first naive attempt, I propose to give a value to each grid node around which no tracer was found by making a weighted average using all the surrounding grid nodes within a distance L_{av} from this node that did receive some information from tracers (see figure 3.7 for an illustration). The weight of each grid node used is equal to the inverse of its distance to the grid node considered. A first attempt is made by setting the distance L_{av} to the statistical mean distance

between neighboring tracers that we define by:

$$d_{tra} = \left[\frac{4\pi(r_o^3 - r_i^3)}{3N_{tra}}\right]^{1/3}, \tag{3.4}$$

where N_{tra} is the total number of inserted tracers. This should statistically estimate the minimum number of grid nodes to explore to make sure that at least one of them received some information from a tracer. Note that because the flow is non-divergent, the number of tracers per volume unit should theoretically remain constant through time across the grid and that this first try should therefore be sufficient for most grid nodes. However, small errors in tracers advection in regions of high shear and vorticity could locally create isolated tracer depletions. In case the first attempt failed with $L_{av} = d_{tra}$, a second is made by increasing the distance L_{av} to a length given as an input parameter. If still unsuccessful, an error message is returned meaning that too large a portion of the computational domain is now not covered by tracers.

Although this method allows to perform the interpolation from particles to grid in reasonable times, this problem of "empty cells" remains extremely complicated. In particular, for aspect ratios lower than 0.35, the number of empty cells skyrockets due to geometrical effects and the associated cost becomes prohibitive. Solving this issue then requires a more profound reflexion which is conducted in section 4.3 of the next chapter.

3.4 Advection of particles

Since the ensemble of particles can be seen as a discrete sampling of the underlying continuous field, advecting the particles with the flow is equivalent to advecting the scalar field. Moving a particle is performed by updating its coordinates in the particles array, leaving the columns containing the traced scalar fields untouched. The information related to the scalar fields therefore remains attached to a particle when the latter moves and does not spread to the surrounding particles or grid points. This is the reason why, by construction, the PIC method theoretically guarantees the absence of numerical diffusion. Sources of errors may however come from the way the velocity is interpolated at the particles positions and also from the degree of accuracy in the description of the trajectory of particles. Cumulated errors may result in small deformations of the advection pattern over time. In addition to causing detrimental clustering/depleting effects to the particles distribution, such phenomena may also introduce undesired numerical diffusion. In the next subsection, sources of errors in the advection process are first evoked in the context of planetary core flows. Different interpolation and advection schemes are then described and compared.

3.4.1 Tracers clustering and depletion

Planetary core flows are usually dominated by the strong influence of rotation via the Coriolis force and typically organize in the form of columnar vortices at low Ekman numbers (Roberts and King, 2013). As illustrated on figure 3.8, vorticity may result in particles depletion at the vortex center due to a centrifugal effect, if the advection scheme is not sufficiently accurate. Similarly, rapid variations of the velocity derivatives may lead to depletion or clustering effects. The accuracy of the advection schemes depends on:

1. the interpolation order for velocity (trilinear or quadratic),
2. the advection time scheme order.

Interpolation methods and time schemes should therefore be chosen keeping in mind these constraints imposed by the characteristics of planetary core flows.

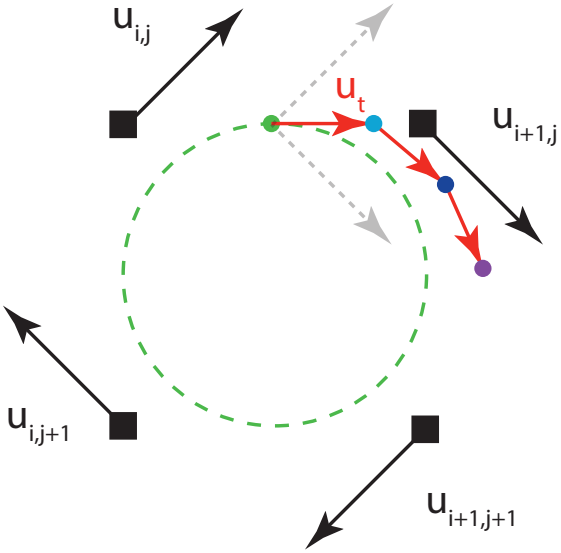

FIGURE 3.8: 2D schematic illustration of the centrifugation of a tracer in a vortex. Grid nodes are drawn by black filled squares. The velocity field $\mathbf{u}$ is represented by the black plain arrows. The initial position of the tracer is designated by the green filled circle and the large dashed green circle shows its theoretical trajectory corresponding to the velocity field. If a trilinear interpolation is used, then, at the initial position of the tracer, the interpolated velocity is colinear to the sum of the velocity vectors $\mathbf{u_{i,j}}$ and $\mathbf{u_{i+1,j}}$ and is represented by a red arrow originating from the green dashed circle. If a simple first-order advection scheme is used, the tracer moves directly to the location of the cyan plain circle, therefore deviating from the green plain circle. Because the cyan circle is very close to the grid node with velocity $\mathbf{u_{i+1,j}}$, the velocity interpolated at the cyan circle is almost colinear to $\mathbf{u_{i+1,j}}$ causing the tracer to move to the position of the dark blue circle, further away from its theoretical trajectory. At the dark blue circle, the velocity is still mainly influenced by $\mathbf{u_{i+1,j}}$, increasing the deviation from the green dashed circle. This situation can only be improved by using more corrective (higher-order) advection schemes.

3.4.2 Interpolation from grid to particles

a) Trilinear interpolation

Classic formulations of the PIC method involve linear interpolation from grid to particles. A field known on the grid can be interpolated linearly at the p-th tracer by using the points defining the corners of the grid cell in which the particle is located (see step 3 in fig. 3.4 for a 2D schematic illustration). In 3D geometry, this step requires 8 grid nodes. The corresponding expression is given for the temperature field but would be completely analogous for each of the velocity components:

$$
\begin{aligned}
T_p = & \\
& \left(1-\frac{\Delta r_p}{\Delta r_{i-1/2}}\right)\left(1-\frac{\Delta \theta_p}{\Delta \theta_{j-1/2}}\right)\left(1-\frac{\Delta \phi_p}{\Delta \phi_{k-1/2}}\right)\times T_{(i,j,k)} \\
+ & \left(\frac{\Delta r_p}{\Delta r_{i-1/2}}\right)\left(1-\frac{\Delta \theta_p}{\Delta \theta_{j-1/2}}\right)\left(1-\frac{\Delta \phi_p}{\Delta \phi_{k-1/2}}\right)\times T_{(i-1,j,k)} \\
+ & \left(1-\frac{\Delta r_p}{\Delta r_{i-1/2}}\right)\left(\frac{\Delta \theta_p}{\Delta \theta_{j-1/2}}\right)\left(1-\frac{\Delta \phi_p}{\Delta \phi_{k-1/2}}\right)\times T_{(i,j-1,k)} \\
+ & \left(\frac{\Delta r_p}{\Delta r_{i-1/2}}\right)\left(\frac{\Delta \theta_p}{\Delta \theta_{j-1/2}}\right)\left(1-\frac{\Delta \phi_p}{\Delta \phi_{k-1/2}}\right)\times T_{(i-1,j-1,k-1)} \\
+ & \left(1-\frac{\Delta r_p}{\Delta r_{i-1/2}}\right)\left(1-\frac{\Delta \theta_p}{\Delta \theta_{j-1/2}}\right)\left(\frac{\Delta \phi_p}{\Delta \phi_{k-1/2}}\right)\times T_{(i,j,k-1)} \\
+ & \left(\frac{\Delta r_p}{\Delta r_{i-1/2}}\right)\left(1-\frac{\Delta \theta_p}{\Delta \theta_{j-1/2}}\right)\left(\frac{\Delta \phi_p}{\Delta \phi_{k-1/2}}\right)\times T_{(i-1,j-1,k-1)} \\
+ & \left(1-\frac{\Delta r_p}{\Delta r_{i-1/2}}\right)\left(\frac{\Delta \theta_p}{\Delta \theta_{j-1/2}}\right)\left(\frac{\Delta \phi_p}{\Delta \phi_{k-1/2}}\right)\times T_{(i,j-1,k-1)} \\
+ & \left(\frac{\Delta r_p}{\Delta r_{i-1/2}}\right)\left(\frac{\Delta \theta_p}{\Delta \theta_{j-1/2}}\right)\left(\frac{\Delta \phi_p}{\Delta \phi_{k-1/2}}\right)\times T_{(i-1,j-1,k-1)}.
\end{aligned}
$$

The calculation of Δr_p, $\Delta \theta_p$ and $\Delta \phi_p$ requires the knowledge of the grid point closest to the tracer. Although trilinear interpolation has given good results for nearly all the simulations I have performed to date, it may be insufficient for more turbulent flows if the velocity has strong second and higher derivatives. In this case, it would be wise to resort to higher order interpolation methods. In addition to provide a better description of regions with strong vorticity, higher order interpolation methods are a necessary step towards the construction of higher order PIC methods.

b) Higher order interpolation schemes

Triquadratic interpolation

Quadratic interpolation has already been proposed in 2D, for instance by Brackbill et al. (1988). Fully quadratic interpolation in 3D can be done in the following way. For each grid node (i_0, j_0, k_0) corresponding to the position $(r_{i_0}, \theta_{j_0}, \phi_{k_0})$, one looks for coefficients $c^n_{\alpha\beta\gamma}$, (with $0 \leq \alpha \leq 2$, $0 \leq \beta \leq 2$ and $0 \leq \gamma \leq 2$), such that each component u^n $(1 \leq n \leq 3)$ of the local velocity around the grid node is best approximated by:

$$
u^n_{(i_0,j_0,k_0)}(r,\theta,\phi) = \sum_{0\leq(\alpha,\beta,\gamma)\leq 2} c^n_{\alpha\beta\gamma} r^\alpha \theta^\beta \phi^\gamma. \tag{3.5}
$$

The velocity is known at nodes $(i_0 \pm 1, j_0 \pm 1, k_0 \pm 1)$, which, for each component n, gives the following system:

$$
\forall (i,j,k) \in \{i_0 \pm 1\} \times \{j_0 \pm 1\} \times \{k_0 \pm 1\}, \quad u^n(r_i, \theta_j, \phi_k) = \sum_{0\leq(\alpha,\beta,\gamma)\leq 2} c^n_{\alpha\beta\gamma} r_i^\alpha \theta_j^\beta \phi_k^\gamma, \tag{3.6}
$$

which can then be expressed in terms of matrices:

$$\underbrace{\begin{pmatrix} r_{i_0-1}^{\alpha}\theta_{j_0-1}^{\beta}\phi_{k_0-1}^{\gamma}, & 0 \le (\alpha,\beta,\gamma) \le 2 \\ r_{i_0-1}^{\alpha}\theta_{j_0-1}^{\beta}\phi_{k_0}^{\gamma}, & 0 \le (\alpha,\beta,\gamma) \le 2 \\ r_{i_0-1}^{\alpha}\theta_{j_0-1}^{\beta}\phi_{k_0+1}^{\gamma}, & 0 \le (\alpha,\beta,\gamma) \le 2 \\ r_{i_0-1}^{\alpha}\theta_{j_0}^{\beta}\phi_{k_0-1}^{\gamma}, & 0 \le (\alpha,\beta,\gamma) \le 2 \\ r_{i_0-1}^{\alpha}\theta_{j_0}^{\beta}\phi_{k_0}^{\gamma}, & 0 \le (\alpha,\beta,\gamma) \le 2 \\ \vdots & \\ r_{i_0+1}^{\alpha}\theta_{j_0+1}^{\beta}\phi_{k_0+1}^{\gamma}, & 0 \le (\alpha,\beta,\gamma) \le 2 \end{pmatrix}}_{M_{(i_0,j_0,k_0)}} \underbrace{\begin{pmatrix} c_{000}^n \\ c_{001}^n \\ c_{002}^n \\ c_{010}^n \\ c_{011}^n \\ c_{012}^n \\ \vdots \\ c_{222}^n \end{pmatrix}}_{C_{(i_0,j_0,k_0)}^n} = \underbrace{\begin{pmatrix} u^n(r_{i_0-1},\theta_{j_0-1},\phi_{k_0-1}) \\ u^n(r_{i_0-1},\theta_{j_0-1},\phi_{k_0}) \\ u^n(r_{i_0-1},\theta_{j_0-1},\phi_{k_0+1}) \\ u^n(r_{i_0-1},\theta_{j_0},\phi_{k_0-1}) \\ u^n(r_{i_0-1},\theta_{j_0},\phi_{k_0}) \\ u^n(r_{i_0-1},\theta_{j_0},\phi_{k_0+1}) \\ \vdots \\ u^n(r_{i_0+1},\theta_{j_0+1},\phi_{k_0+1}) \end{pmatrix}}_{U_{(i_0,j_0,k_0)}^n}, \tag{3.7}$$

where $M_{(i_0,j_0,k_0)}$ is a 27×27 matrix, $C^n_{(i_0,j_0,k_0)}$ and $U^n_{(i_0,j_0,k_0)}$ vectors containing 27 components. The coefficients C^n can then be deduced by inverting the matrix M:

$$C^n = M^{-1}U^n. \tag{3.8}$$

There is one matrix $M_{(i_0,j_0,k_0)}$ for each grid node (i_0, j_0, k_0) and this matrix can be used for all the tracers whose closest grid point is (i_0, j_0, k_0). For a fixed grid, the matrices $M^{-1}_{(i,j,k)}$ can be computed at the beginning of the simulations and stored in memory. "Only" the multiplication is then needed. However, for a completely irregular grid, $N_r \times N_\theta \times N_\phi$ matrices should be computed. For a typical grid ($N_r = 100, N_\theta = 200, N_\phi = 400$), this represents about almost 6 billions reals which, in double precision, amounts nearly 50 Go. Fortunately, for regular grids, the matrices can be "collapsed". In PARODY this is the case along the longitude. In addition, the grid spacings in latitude are symmetric with respect to the equator. Similarly, the radial discretization is also symmetric with respect to the radius $(r_i + r_o)/2$. Consequently, only $N_r/2 \times N_\theta/2$ matrices need to be computed initially.

However, although the memory burden can be made acceptable, performing a triquadratic interpolation everywhere in the computational domain involves, for each tracer and each component of the velocity, a total of more than 800 multiplications (729 to compute C^n, then the evaluation of the velocity at the position of the tracer using equation (3.5)), which is clearly prohibitive when billions of tracers are used. However, the triquadratic approach can be either restricted to portions of the domain where it is really useful or when a very moderate number of particles are used. An alternative option is to use a compromise by performing the quadratic interpolation in only one direction for each velocity component. This is described in the next section.

Quadratic-bilinear

In this semi-quadratic method, quadratic interpolation is performed along one direction and the interpolation is linear in the other two directions. I implemented and tested two different versions of this method. In the first one, the quadratic interpolation is performed in the direction parallel to the velocity component. For example, for the radial component, this would read:

$$u_{r(p)} = \alpha r_p^2 + \beta r_p + \delta, \tag{3.9}$$

where the coefficients α, β and γ are determined so that the quadratic form fits the velocities $u^{lin}_{r(i-1)}$, $u^{lin}_{r(i)}$ and $u^{lin}_{r(i+1)}$ obtained by bilinear interpolation as represented on figure 3.9. This requires the inversion of a 3×3 matrix. For each grid node, the associated matrix can be computed during the initialization of the program and stored in memory to save computational cost. The

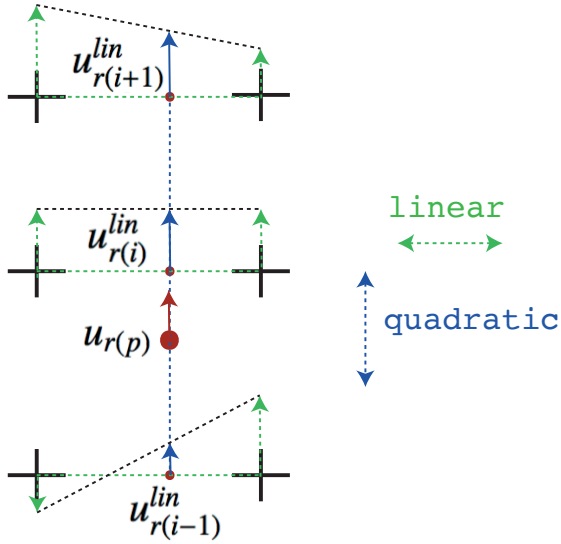

FIGURE 3.9: 2D illustration of the principle of the semi-quadratic interpolation for the radial component of the velocity. In this example, the quadratic interpolation is performed in the radial direction, parallel to the velocity component. Interpolation is bilinear in the perpendicular plane.

formalism is identical for the other velocity components.

In a second variant of this method, the quadratic interpolation is performed in the direction along which the velocity component has its highest second derivative. Both variants were compared for the benchmark tests and the results are in favor of the second (see section 5.1). Furthermore, although I find the trilinear interpolation to be sufficient most of the time, this semi-quadratic interpolation method produced significant improvement in some cases (see advection tests on figure 3.13 and the benchmarks results in tables 5.1 and 5.2 for a comparison with trilinear interpolation), while being only 30% more costly than the trilinear approach.

Other high-order schemes

Although the use of a classic second or higher order interpolation methods may help improving the global accuracy of the PIC method, such procedures may be problematic when fields with sharp transitions must be interpolated to the particles as they produce smoothing of the discontinuities. More sophisticated schemes would then be needed. For instance, Edwards and Bridson (2012) use a 4th order WENO scheme (Macdonald and Ruuth, 2008) offering the ability to interpolate sharp transitions to the particles while ensuring a high order PIC method everywhere. For the velocity field in the context of core dynamics, one may however wonder whether this would be necessary, since viscosity tends to smooth velocity gradients, not to mention that the implementation of a WENO scheme in spherical geometry may be arduous.

Direct evaluation using the spherical harmonics

One may also be tempted to compute the velocity of particles directly from an evaluation of spectral decomposition in spherical harmonics. Unfortunately, computing the Legendre polynomials is extremely expensive for high degrees ℓ and cannot be applied to millions of particles. Like the triquadratic interpolation scheme, the cost may however be acceptable if a small number

of tracers are passively advected with the flow. Combined with a second or higher-order interpolation scheme in radius, this would provide a convenient way to improve the accuracy of the interpolation. It should be tested and compared to other interpolation methods in the future.

Correction for non-divergent flows

In the previous formulations, velocity interpolation from grid points to particle locations is performed without considering the absence of divergence of the velocity field, which can lead to significant particle dispersion or clustering if those particles move through regions of strong velocity gradients. Rather than concentrating on higher order interpolation schemes, Meyer and Jenny (2004) (in 2D) then Wang et al. (2015) (in 3D) proposed to add a correction to the interpolated velocity of each particle meant to ensure the non-divergence of the flow and limit the clustering effect. However, their method is derived in Cartesian geometry and may not apply *as is* to a spherical grid. Indeed, it does not produce better results on benchmark tests when it is directly implemented in PARODY. Deriving equivalent formulation for a spherical grid could be extremely useful in the future as it is a cheaper way than higher-order interpolations to decrease particles clustering.

3.4.3 Interpolation at poles

The trilinear and higher-order schemes of velocity interpolation both become problematic near the poles, since the pole does not correspond to a node of the numerical grid. Adding one would not be very helpful since it is a point of singularity for the latitudinal and longitudinal components of the velocity. In both cases, when a tracer is located between a pole and the first increment of latitude, two points located opposite to the pole are used to perform a trilinear interpolation. In this case, the weights are modified and taken proportional to the inverse of the distance between the grid node and the tracer.

3.4.4 Time scheme

A key point for modeling rotation-influenced flows with high shear and vorticity is to use high-order time schemes for particles advection. Runge-Kutta (RK) schemes of 2nd and 4th order (RK2 and RK4) are frequently employed in PIC methods and were implemented in PARODY. Note that these are not truly Runge-Kutta methods since the velocities are all evaluated at present time t, not at intermediate times between t and $t + \Delta t$, Δt being the time step. For example, the modified Runge-Kutta 4th order method would read, for the radial component of particle p:

$$r_p^{n+1} = r_p^n + \frac{\Delta t}{6}(k_1 + 2k_2 + 2k_3 + k_4), \tag{3.10}$$

where n denotes the time step index, r_p^n and r_p^{n+1} are the radial positions of the tracer at time t_n and $t_{n+1} = t_n + \Delta t$, respectively. k_1, k_2, k_3 and k_4 are increments all computed at time t_n:

$$\begin{cases} k_1 = u_r(t_n, r_p^n) \\ k_2 = u_r\left(t_n, r_p^n + \dfrac{\Delta t}{2}k_1\right) \\ k_3 = u_r\left(t_n, r_p^n + \dfrac{\Delta t}{2}k_2\right) \\ k_4 = u_r(t_n, r_p^n + \Delta t k_3). \end{cases} \tag{3.11}$$

In the classic Runge-Kutta 4th order scheme, k_2 and k_3 are computed at times $t_n + \frac{\Delta t}{2}$ and k_4 at time $t_n + \Delta t$ which would be too expensive in our case. The "modified" scheme shown in

equation (3.11) is therefore not really 4th order in time and should rather be seen as a way to "correct" for the trajectory of the tracer. I also tested a Runge-Kutta-Fehlberg method of order 5 (Fehlberg, 1968) and obtained encouraging results for the description of eddies. A detailed comparison of these different tested time schemes together with different interpolation methods can be found in sections 3.4.6 and 5.1.

3.4.5 Advection in Cartesian coordinates

A major problem for the advection of tracers in spherical geometry is the presence of large gradients of u_ϕ in the vicinity of poles which dramatically distort the trajectories of the tracers. One way to circumvent this difficulty is to advect tracers in Cartesian coordinates within a cone surrounding the poles corresponding to $\theta \leq \theta_c$ and $\theta \geq (\pi - \theta_c)$. If a semi-quadratic interpolation is used, it is first performed along each spherical direction (r, θ, ϕ) before converting the velocity to Cartesian coordinates (x, y, z) to advect the tracer. Advection in full Cartesian coordinates is feasible but restricting it to a cone avoids costly spherical to Cartesian conversions. The optimal cone angle θ_c depends on resolution and time step but I estimated empirically that its value should be at least $\pi/5$. This method brought considerable improvement in the advection of tracers in the vicinity of poles, avoiding strong distortions of the trajectories. Figure 3.10 shows an example of distortion error when crossing a pole with two different values of θ_c.

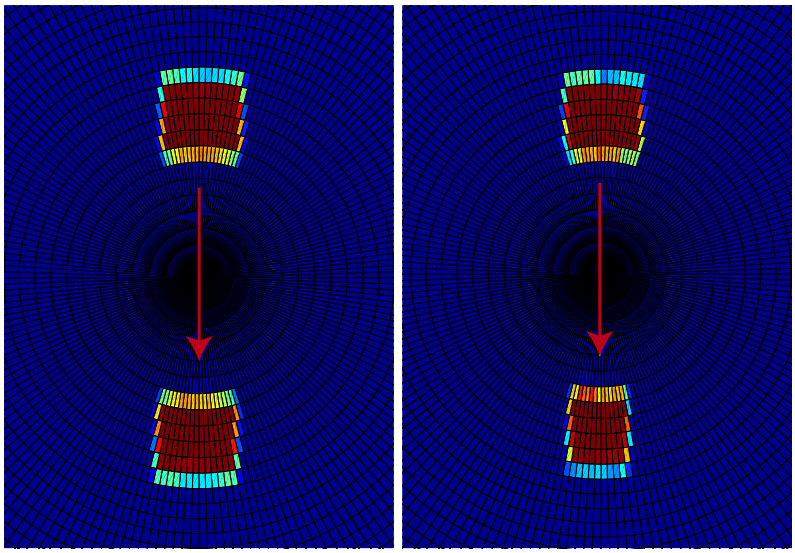

FIGURE 3.10: Advection of a patch by a solid-body rotation velocity field with a rotation axis contained in the equatorial plane. The shape of the patch can be compared before and after rotation, when the advection is performed in Cartesian coordinates when θ_c is set to a large enough value of $\pi/5$ (left) and with $\theta_c = \pi/50$ (right). When the cone is too narrow, the patch is seriously distorted.

3.4.6 Comparison of interpolation methods and advection schemes

In this section, simple tests are performed in an attempt to determine which combination of interpolation method and time scheme is preferable. Another comparison is performed with more physical flows in the benchmarking section of Chapter 5.

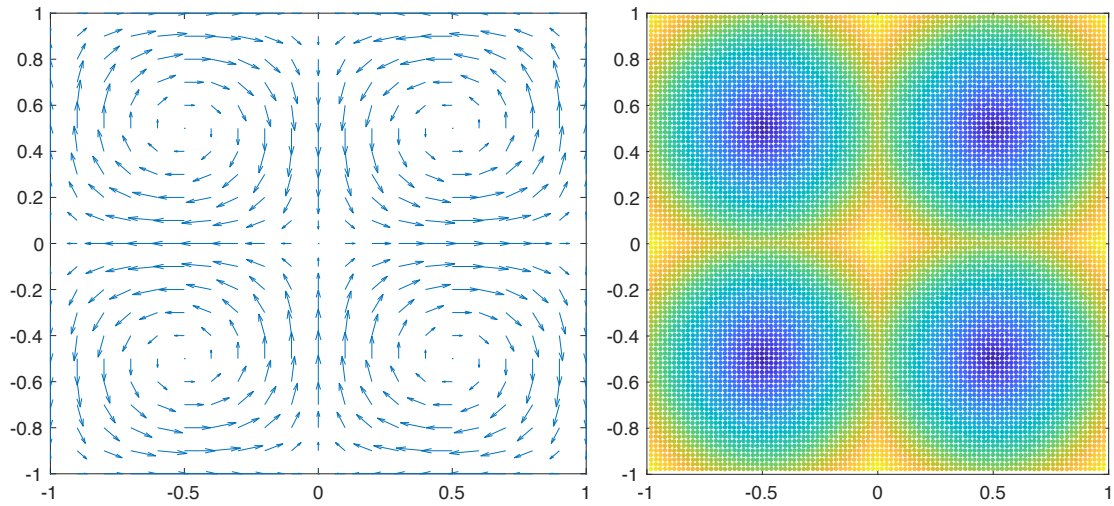

FIGURE 3.11: Left figure: velocity field corresponding to the modified Taylor-Green vortex. 9 points with $u_x = u_y = 0$ exist, one is the middle of the grid ($x = 0, y = 0$), 4 are located at the grid corners and 4 are located at coordinates ($x = -1, y = 0$), ($x = 1, y = 0$), ($x = 0, y = -1$) and ($x = 0, y = 1$). Right figure: initial tracers positions with regular Cartesian spacing with random perturbation. The color scale is proportional to the distance between the tracers and the center of their vortex. The total number of tracers is $N_{tra} = 9801$.

Advection by a 2D Taylor-Green vortex

As stated above in section 3.4.1, the influence of rotation in planetary cores enhances the formation of vortices which may produce particles centrifugation. Such an effect may occur when resorting to time schemes that do not correct sufficiently for the trajectory of the tracers and may also result from inaccurate interpolation of the velocity at the position of the tracer. In order to compare the efficacy of different combinations of interpolation methods and time schemes on the advection of tracers within vortices, I ran 6 simulation in 2D Cartesian geometry in which the tracers are advected by a constant velocity field $\mathbf{u}(x, y)$ corresponding to a 2D Taylor-Green vortex (Taylor and Green, 1937):

$$\begin{cases} u_x(x, y) = & u_0 \sin(\pi x) \cos(\pi y) \\ u_y(x, y) = & -u_0 \cos(\pi x) \sin(\pi y), \end{cases} \tag{3.12}$$

with $u_0 = 1$, $-1 \leq x \leq 1$ and $-1 \leq y \leq 1$; x and y being coordinates in the horizontal and vertical directions, respectively. The corresponding velocity field is non-divergent and can be visualized on the left panel of figure 3.11. This velocity field is non-divergent and consists of 4 vortices positioned in each quarter of the grid. In addition, neutral points exist at each corner of the vortices where the flow is convergent in one direction and divergent in the other. At these points, $u_x = u_y = 0$. The number of grid points is set to $N_x = N_y = 21$ in both directions and the total number of tracers is $N_{tra} = 9801$. Initially, tracers are regularly spaced and their positions are added a random perturbation of amplitude $0.1\Delta x$, where Δx is the grid spacing ($\Delta x = \Delta y$). The initial tracers distribution is displayed on the right panel of figure 3.11. The time step for advection is fixed to $\Delta t = 0.4\Delta x/u_0$. The tracers distribution across the grid domain after advection on 50000 time steps is shown on figure 3.12, for Runge-Kutta schemes of 1st, 2nd and 4th order (respectively denoted by RK1, RK2 and RK4) combined with either bilinear or biquadratic interpolation of the velocity.

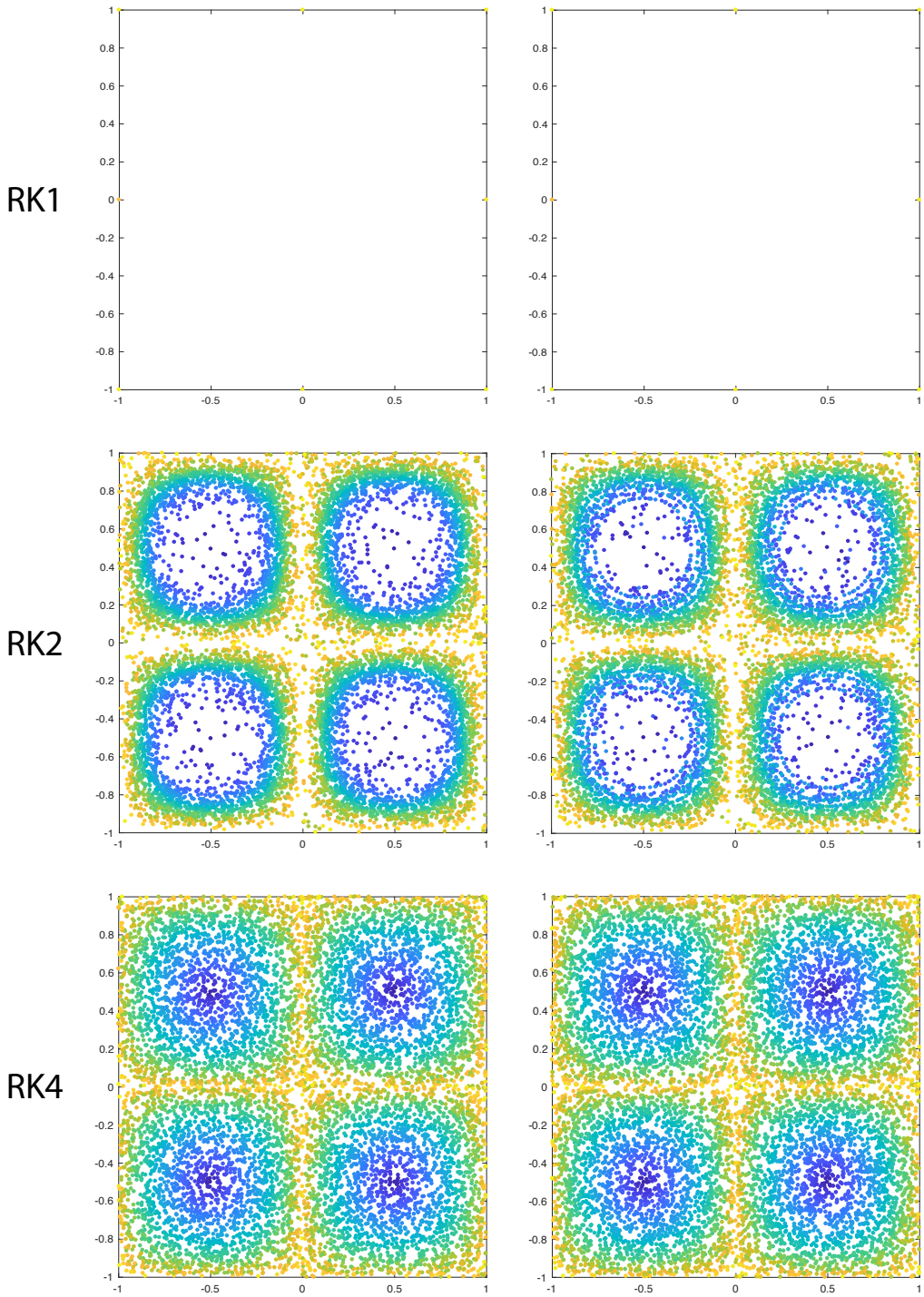

FIGURE 3.12: Advection of tracers by a modified vortex of Taylor-Green. Figures on the left and right columns are obtained using a bilinear and biquadratic interpolation, respectively. The rows display results produced by modified Runge-Kutta time schemes of 1st (Euler, RK1), 2nd (RK2) and 4th order (RK4), respectively (see section 3.4.4 for details). The total number of tracers is $N_{tra} = 9801$. The number of grid points is $N_x = N_y = 21$. In the images of the first row (RK1), the tracers have all migrated to one of the points with zero velocity are thus all superimposed. The colors refer to the initial distance of the tracers to the axis of their vortex. The tracers are not visible with the RK1 scheme since they all end-up superimposed on the neutral points.

When a RK1 scheme is used with either bilinear or biquadratic interpolation, tracers are dramatically centrifuged away from the vortices centers creating a large depletion around the vortex center and accumulation at neutral points (defined by $\mathbf{u} = \mathbf{0}$). Using higher order iadvection schemes significantly decreases the centrifugal effect, even with bilinear interpolation. The RK2 scheme still suffers from depletion in the vortices centers as well as near neutral points. The RK4 scheme gives excellent results everywhere in the grid even with bilinear interpolation, conserving a homogeneous distribution of tracers throughout the simulation, although there is still a small amount of clustering at a scale comparable to Δx. The benefit of using biquadratic interpolation is not obvious. Because it decreases the spatial error, the effect of the interpolation scheme might become clearer when varying the grid size in the presence of velocity fields with sharper variations. This simple test suggests that it is worth using higher-order advection schemes (RK4) for the description of vortices.

Rotation of a Gaussian patch

In this second test, I ran 3D simulations in spherical geometry to compare the efficacy of trilinear and quadratic-bilinear interpolation performed in the direction parallel to the velocity component. In this test, a Gaussian patch is initially placed on the equator ($\theta = \pi/2$, $\phi = 0$) and advected with a velocity field corresponding to solid-body rotation. Rotations are performed around two rotation axes: the polar axis ($\theta = 0$, the patch is advected along the equator), and an axis perpendicular to the polar axis ($\theta = \pi/2$, $\phi = \pi/2$) so that the patch passes alternately through each pole. After 20 turns, the profile of the Gaussian patch in the direction parallel to the velocity is compared with the initial profile (fig. 3.13a and 3.13b). When the patch is advected along the equator (fig. 3.13a) the profile is unchanged after 20 turns proving the absence of numerical diffusion, although a small delay can be observed with respect to the position of the initial profile. This delay is due to the fact that the velocity is proportional to $\sin\theta$, a concave function on $[0, \pi]$, which is slightly underestimated by a linear interpolation. However, this delay is small (corresponding to a velocity too low by only about 0.01% in this case) and is reduced when increasing the grid resolution. Note that a semi-quadratic interpolation in the direction parallel to the velocity will not be beneficial in this case. When the rotation axis is perpendicular to the polar axis, the Gaussian patch passes through a pole twice in one turn. The angular domain in which advection is performed in Cartesian coordinates is delimited by $\theta_c = \pi/4$. After 20 turns, the shape of the Gaussian is significantly altered due to residual spherical deformation when a trilinear interpolation is used (cf. fig 3.13c). This deformation can be reduced either by decreasing the time step or using a semi-quadratic interpolation. In this latter case, the Gaussian is only slightly stretched after 20 turns (see right panel on figure 3.13c). It should be emphasized that pole-crossing trajectories are usually not physically realistic in rotating convection, which makes the observed deformation less problematic.

3.5 Diffusion

When tracers are used for the description of temperature or composition in the finite Lewis number case, diffusion cannot be neglected and its treatment must be done with great care. The temperature (or composition) carried by the tracers must be modified so that the tracers take diffusion into account. First, the diffusive perturbation is interpolated from the grid and distributed among tracers:

$$\Delta T_{(i,j,k)} = {}^{1}T_{(i,j,k)} - T_{(i,j,k)}, \tag{3.13}$$

$${}^{t}T_p = T_p + \Delta T_p, \tag{3.14}$$

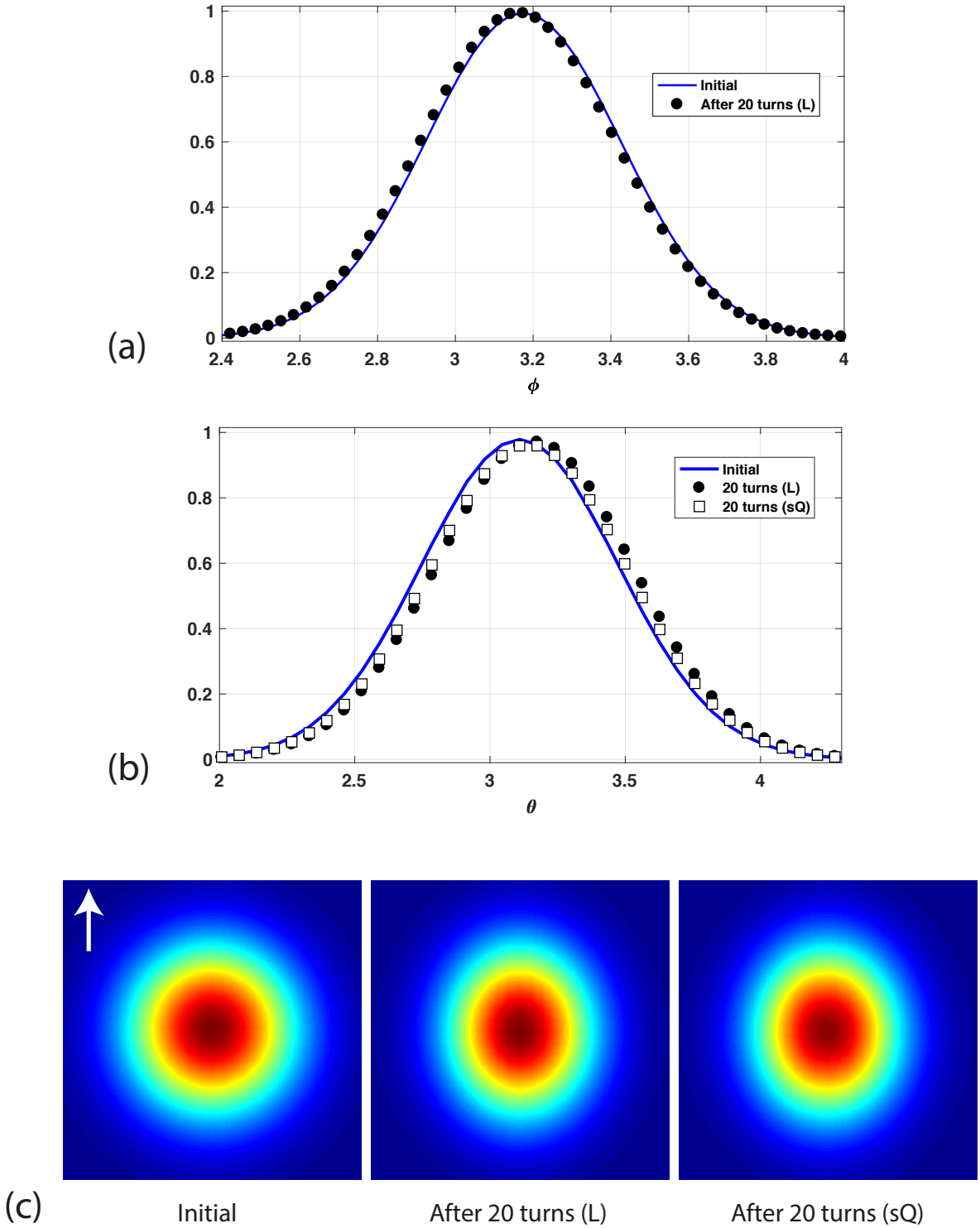

FIGURE 3.13: Results of the test of advection of a Gaussian patch by solid-body rotation around the polar axis (a) or an axis perpendicular to the polar axis (b). In (b) and (c) the patch crosses both poles during one rotation and the shape of the patch is compared before and after 20 rotations through the poles by either trilinear or semi-quadratic interpolation. The white arrow heads at the north pole and indicates the velocity direction. In all figures, (L) stands for trilinear interpolation and (sQ) for semi-quadratic performed in the direction parallel to the velocity components.

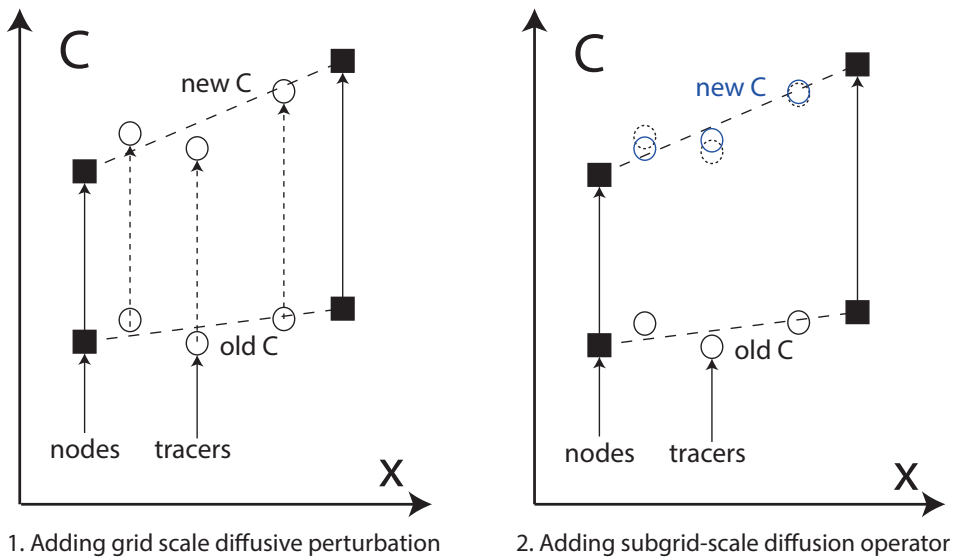

FIGURE 3.14: Schematic illustration of the treatment of diffusion. Grid nodes are represented by black filled squares while particles appear as open circles. Left: a diffusive perturbation is computed on the grid. The value of each grid node is updated to a new composition. The difference with the old value is interpolated to the particles and added to their information on composition. Right: in a second step, the "sub-grid" scale structures carried by the tracers are smoothed by partially realigning the particles with the linear profile of the grid-scale diffused field.

where ΔT is the temperature diffusive perturbation computed on the grid, ${}^1T$ is the diffused temperature field, T the field before diffusion, ${}^tT_p$ and T_p respectively the new and old temperatures of the p-th tracer and ΔT_p the temperature diffusive perturbation interpolated to the p-th tracer. It is important to notice that, because there usually are several tracers between two consecutive grid nodes, tracers may carry information that varies at a "tracers-scale" that is smaller than the grid scale. These "sub-grid" scale structures may be produced by grid-scale shear and entrainement and thus integrate some "memory" of the flow. At this step, it is therefore crucial *not* to replace T_p by ${}^1T_p$ (${}^1T_p$ being the interpolation of ${}^1T$ at the position of the p-th tracer), otherwise all the tracers subgrid scale structures would be completely removed. However, simply adding a diffusive perturbation computed at grid-scale is not sufficient and may lead to undesired numerical oscillations, because this process does not damp out subgrid (tracer) scale structures as diffusion should normally do. One solution (Gerya and Yuen, 2003) consists in correcting for the tracers temperature (or composition) by introducing a subgrid scale diffusion operation on a local time scale:

$$ {}^tT_{p(D)} = {}^1T_p - [{}^1T_p - {}^tT_p] \times \exp\left(\frac{-d\Delta t}{\Delta t_0}\right), \tag{3.15} $$

in which d is a numerical diffusion coefficient ($0 \leq d \leq 1$) and Δt_0 a characteristic timescale of the local diffusion defined for the corresponding cell of the grid:

$$ (\Delta t_0)_{(i,j,k)} = \left[\frac{\kappa_T}{3}\left(\frac{4}{\Delta r_i^2} + \frac{4}{r_i \Delta\theta_j^2} + \frac{4}{(r_i \sin(\theta_j)\Delta\phi_k)^2}\right)\right]^{-1}. $$

Finally, the field is updated on the grid. We proceed slightly differently from Gerya and Yuen (2003) for convenience. The temperature field is first updated on the grid using relation (3.1):

$$ T_{(i,j,k)(D)} = \frac{\sum_p {}^tT_{p(D)}\omega_{p(i,j,k)}}{\sum_p \omega_{p(i,j,k)}}. \tag{3.16} $$

Ultimately, to correct for the erroneous diffusion resulting from the interpolation to the grid that can alter the grid-scale solution, a final compensation is added to the tracers:

$$ {}^{t}T_{p(D-A)} = {}^{t}T_{p(D)} - (T_{(D)} - {}^{1}T)_p. \tag{3.17} $$

Although this subgrid-scale diffusion operator guarantees that all scales are diffused, it remains somehow artificial. In addition, it is controlled by a parameter d that should be tuned arbitrarily. In order to treat diffusion more correctly, I propose the following strategy:

1. Prior to diffusion, the field is evaluated on an auxiliary grid that is finer that the initial grid using for example polynomial interpolation within each cell of the coarser grid. The auxiliary grid must be fine enough to resolve the average particles-scale structures.

2. The diffusion is computed on the auxiliary grid so that all scales are correctly diffused on this grid.

3. The diffusive perturbation is communicated back from the auxiliary grid to the particles in a one step process.

Two interpolations would therefore be needed on a refined grid, instead of four on a coarser grid which may not be much more expensive. Moreover, it is certainly a more "physical" way to treat diffusion. I have not yet implemented this approach whose first step may carry special difficulties and should be thought carefully and I intend to test this in the future.

3.6 Numerical implementation of boundary conditions

Following equation (2.59), a volumetric source term is introduced in a thin spherical shell of thickness h above the bottom boundary. To do so, the tracers located within a distance h from the inner boundary are added a mass fraction $\delta C(r, \theta, \phi)$ so that:

$$ \rho \int_{\theta=0}^{\pi} \int_{\phi=0}^{2\pi} \int_{r=r_i}^{r_i+h} \delta C(r, \theta, \phi) \mathrm{d}V = F_i^{\xi} \Delta t, \tag{3.18} $$

where F_i^{ξ} is the total mass flux integrated over the inner boundary and Δt the time step. If the compositional flux does not vary over the inner boundary, this expression can be simplified:

$$ 4\pi\rho \int_{r_i}^{r_i+h} r^2 \delta C(r) \mathrm{d}r = F_i^{\xi} \Delta t. \tag{3.19} $$

As explained in section 2.3 a Gaussian-like function is used for δC:

$$ \delta C(r, \theta, \phi) = \frac{a(\theta, \phi)}{r^2} \exp\left\{ -\left[r - \left(r_i + \frac{h}{2} \right) \right]^2 / \sigma^2 \right\}, \tag{3.20} $$

in which $\sigma = h/5$ and $h = \frac{4}{3} E^{1/2}$, which is slightly larger than the thickness of the Ekman layer ($Ek^{1/2}$). The factor $a(\theta, \phi)$ is constant if the compositional flux is homogeneous and must be computed using its value. The formulation is strictly analogous when a compositional flux is imposed at the top boundary.

3.7 Conclusion and discussion

I succeeded in adapting a PIC method in the geodynamo code PARODY which required finding diverse strategies to solve problems inherent to the spherical geometry. First basic tests suggest that the use of RK2 or RK4 combined with triquadratic interpolation is preferable for adequate description of the flow in core conditions, yet not manageable in the entire computational domain. However, it may be feasible to perform adaptive advection method throughout the grid, which I intend to test in a near future. In portions where the velocity field has low vorticity and small second derivatives, a trilinear interpolation with a RK2 scheme may be sufficient while saving computation time. When the velocity components have a strong second derivative in only one direction, there could be a switch to quadratic-bilinear interpolation combined with a RK2 or RK4 scheme. In critical regions with strong vorticity and second derivatives, the combination of RK4 and triquadratic interpolation can be employed. The only inconvenient of such an adaptive scheme is that it requires a criterion, the definition of which is never straightforward. Another interesting direction is to add a correction to the particles velocity to better ensure the non-divergence of the velocity field. On the other hand, the diffusion process remains somehow artificial, particularly the subgrid-scale diffusion operator. A more physical way to treat the diffusion consisting in diffusing all scales in one single process should be tested. More generally, the diffusion problem addresses the question of the meaning of the "sub-grid" scale structures carried by the particles. A global limitation of the method is that the buoyancy is not computed at the particles positions. "Sub-grid" scales structures may therefore be entrained by a larger (grid) scale flow and their dynamics is probably not accurate, implying that they should not be trusted too much.

Once the method is implemented, another challenge is to make it computationally efficient so that it can be tested and used conveniently in the context of core dynamics. This is the goal of the next chapter.

Chapter 4

Optimizations for High Performance Computing

The success of nowadays numerical simulations in modeling increasingly complex physical phenomena can be attributed to a large extent to the rise of the computational power of modern processors (measured in *"floating point operations per second"* or FLOPS) and to the development of parallelism. Many codes now run on hundreds or even thousands of cores on massively parallel architectures that are available via super-computers at the regional or national scale. Due to the increasing pressure on these machines, users are often attributed a limited number of CPU hours per year for their research. The issue of performance then quickly comes into consideration: speeding-up a code by even a moderate factor 2 allows to run twice as many simulations for the same annual allocation. But efficiency is also a matter of "comfort" as it is not very convenient to manage simulations that take weeks to complete. Furthermore, performance is a notion frequently invoked to compare available codes. In this context, it is therefore crucial to sufficiently optimize a code so that it can become mainstream and convenient to use for the production of scientific data.

PIC methods are often reproached their high numerical cost. Not only do they significantly increase the memory consumption, but they also involve a large number of computations per time step. In order to develop a code that both runs in reasonable times and produces better results than other methods for equivalent numerical resources, it is essential to sufficiently optimize the PIC part of the code. Lots of efforts have already been made to increase the efficiency of PIC algorithms (Anderson and Shumaker (1995); Decyk et al. (1996); Elster (1994); Bowers (2001); Larsgård (2007), to name a few) and were used as sources of inspiration for improving the PIC method in PARODY. A prerequisite to any attempt of optimization is to focus first on identifying the most time consuming portions of the code. In the PIC method I implemented in PARODY, the most costly routines are, in decreasing order:

1. the interpolations from grid to particles. These include the advection step (which requires 4 interpolations from grid to particles with a RK4 scheme) and the diffusion process (2 interpolations), if the latter is not neglected.

2. the interpolation from particles to the grid (1 interpolation without diffusion, 3 if diffusion is considered). This step comprises the treatment of "empty cells" which can become extremely expensive for low aspect ratios r_i/r_o (see section 3.3.3).

3. the conversions between spherical and Cartesian coordinates.

4. to a lesser extent, the MPI communications.

Efforts should thus be mainly concentrated on the interpolations routines. Also, if the code is used in full sphere geometry or low aspect ratios (r_i/r_o close to 0), the number of nodes that did not receive information from the particles becomes enormous near the sphere center, making

their treatment by far the most time consuming portion of the code in this case.

Optimizing these aspects can be performed at different levels. Some optimizations operate at a very detailed level on isolated structures (for example loops). They address various aspects ranging from replacing expensive floating point operations by cheaper ones to enabling loops vectorization, to mention only a few. Although the most basic of these tricks can quickly become automatic for the average programmer, others are less straightforward and intuitive to implement. The latter require more advanced knowledge often coming under the competence of an engineer. In the extreme limit, extra improvements at this level can be achieved only by adapting the code specifically to take advantage of the architecture on which it runs. Although I have addressed these questions to a moderate extent for the Ada supercomputer of IDRIS (Orsay, France) on which I was attributed almost 700 000 hours during my PhD, the full details may rapidly become purely technical and non general, especially since they often address isolated issues and sometimes depend on the configuration of the machine. Despite being essential for the efficiency of the code, these low level refinements are not very generic and I judge them not worth mentioning here. On the contrary, other optimizations operate at a higher level and are more related to the algorithm of the global numerical strategy. These may be useful to others in different contexts which warrants, in my view, a whole chapter of this thesis. Though some of the strategies explained in the following have already been proposed in the scientific literature, I designed others to address problems that are more specific to PARODY. The latter are however not uninteresting as they may be inspiring for different situations in other codes.

In this chapter, I address more in-depth some questions related to the efficiency of the code that were already evoked in the previous chapter. I first detail the hybrid parallelism of the code. A series of optimizations of the interpolation routines are then presented and followed by the description of a more efficient treatment of "empty cells" for low aspect ratios based on an original approach. To finish, more general strategies such as computing a periodic solution by solving on a restricted domain are explained and the scaling of the full hybrid code is presented.

4.1 Parallelism

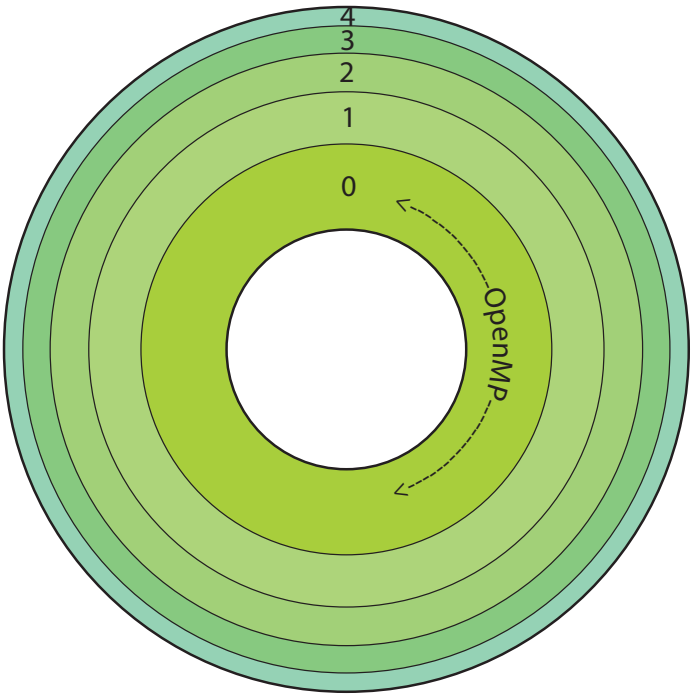

FIGURE 4.1: Schematic 2D illustration of the parallel decomposition in PARODY when favoring the PIC part. The domain is radially decomposed and each MPI process (from 0 to 4 here) is given a sub-shell of the whole spherical shell. The volumes of the sub-shells are (almost) identical. Within each MPI domain, the iterations of costly loops are shared between the cores of MPI process using OpenMP.

Nowadays, parallelism is a key element of High Performance Computing. It consists in distributing the calculations between the cores of a machine with suitable architecture. Classically, this can be done either via the paradigm of MPI (*Message Passing Interface*) or OpenMP, or via a combination of both called a "hybrid" parallelization. MPI is based on *distributed* memory. In a possible classical approach, each MPI process has its own version of the variables and arrays and performs operations on distinct subdomains. Communications between the MPI processes must be entirely implemented by the programmer with the help of pre-programmed functions available in the MPI library. On the other hand, OpenMP uses the concept of *shared* memory: all OpenMP threads share computations performed on arrays that are known by all threads. Communication and threads management can be either explicitly prescribed by the programmer (*coarse grain* approach) or be operated directly by OpenMP (*fine grain*). The goal of any parallel implementation is that a large number of cores can be used and that the computation time keep being inversely proportional to the number of cores for as long as possible. Depending on the algorithms, this can be more or less difficult to achieve. Globally, PIC methods can be easily implemented in parallel versions with a very high efficiency. Moreover, the parallelization issues of PIC methods are well documented (Liewer and Decyk, 1989; Elster, 1994; Larsgård, 2007). In the next sections, I describe how I implemented the PIC method in PARODY using MPI and OpenMP. Scaling tests of the full hybrid code are presented at the end of this chapter.

4.1.1 MPI

PIC methods can usually be easily and efficiently parallelized via an MPI domain decomposition (Liewer and Decyk, 1989). Each MPI process is assigned its own tracers, and the tracers that have moved from a domain to another need to be communicated. Communications are usually efficient because they only involve direct neighbors. Since all fields are expanded in spherical harmonics on each radial layer, many geodynamo codes including PARODY are already parallelized via an MPI domain decomposition in the radial direction. In PARODY, the radial discretization is regular in the middle of the grid and refined with a geometric progression close to the boundaries. The ratio of the regular/irregular portions and the stretching near the boundaries can be adjusted in the Par file. Since the amount of calculations is identical on each concentric sphere, an equal number of radial layers is attributed to each MPI domain. Because 2 buffer layers need to be exchanged with each direct neighbor, the number of layers per MPI domain must be at least 4. However, this decomposition is not well adapted to the PIC method because, due to the spherical geometry, the MPI domains have different volumes that are proportional to $r^3_{i_{rank}+n} - r^3_{i_{rank}}$, where n is the number of radial layers per MPI domain and $r_{i_{rank}}$ is the bottom radial layer of the MPI domain number i_{rank}. The MPI processes therefore have different numbers of tracers which creates a significant load imbalance. Since the cost of the PIC algorithm usually represents by far the most time consuming part of the code (unless fields are expanded up to high spherical harmonic degrees), I chose to rebalance the loads in favor of the PIC method by giving the MPI domains similar volumes (and therefore comparable numbers of tracers) rather than similar number of radial layers. This is done in the following way:

1. An equal number of radial layers is first attributed to each MPI domain. Each MPI domain has a rank i_{rank} and a number of radial layers $n_{\text{MPI}}(i_{rank})$.
2. The following procedure is applied:
   (a) The MPI processes number i^{max}_{rank} and i^{min}_{rank} with larger and smaller domain volumes, respectively, are looked for.
   (b) If $n_{\text{MPI}}(i^{max}_{rank}) > 4$, then the decomposition is modified by:
      - $n_{\text{MPI}}(i^{max}_{rank}) = n_{\text{MPI}}(i^{max}_{rank}) - 1$
      - $n_{\text{MPI}}(i^{min}_{rank}) = n_{\text{MPI}}(i^{min}_{rank}) + 1$
   (c) The new largest and smallest domains are then looked for again and the procedure continues until $n_{\text{MPI}}(i^{max}_{rank}) = 4$.

This rebalancing method decreased the CPU time consumption by at least a factor 2, but it requires the grid to have more numerous and more regularly spaced radial layers so as to give sufficient freedom for the rebalancing process. An illustration of the domain decomposition using this strategy is shown on figure 4.1. Note however that the number of computations for the Legendre transform in the spherical transform grows like $O(\ell^3_{max})$ whereas the number of tracers increases more slowly. As a result, when fields are decomposed up to high degrees of spherical harmonics (typically $\ell_{max} > 200$), the cost of the PIC method gradually becomes comparable to that of the spherical transforms, and even smaller. Furthermore, there are two competitive effects: the number of radial layers should be as low as possible in order to minimize the number of Legendre transforms, but high enough to give more freedom for the load balancing favorably to the PIC method. Consequently, it is necessary to reach a compromise for high spectral resolution. At $\ell_{max} = 300$ or higher, it is usually no longer worth rebalancing the domains in favor of the PIC part.

4.1.2 OpenMP

In the PIC algorithm, most of the time is spent in the loops performing the interpolations. I parallelized these loops using an OpenMP fine grain approach, sharing the iterations between the threads. However, performance issues can arise on machines where each processor has a local cache and each thread modifies adjacent variables located in the same cache line in the tracers array. Even though the threads modify different variables, OpenMP forces a memory update every time a thread modifies a variable in this cache line to ensure memory consistency, a phenomenon called "false sharing" and resulting in a dramatic loss of performance (see figure 4.2 for an illustration). To minimize this effect, I distributed the iterations by "packs" between the threads, and the size of the packs was optimized for the Ada supercomputer (GENCI/IDRIS, Orsay, France). Tests on this machine produced accelerations of 3.7, 6.8, 8 and 9.4 on 4, 8, 12 and 16 threads, respectively (see figure 4.13). The poor scalability beyond 8 cores comes mainly from the tracers to grid interpolation in which the threads write competitively into the same array, the spectral transform whose scaling degrades after 8 cores and also from the MPI communications. Note that the grid to tracers interpolations have a much better scalability however, particularly the advection process since the costs of threads management are small compared to the amount of computations per thread (a speed-up exceeding 12 was measured for this routine on 16 cores). The scaling is therefore improved in the infinite Lewis number case.

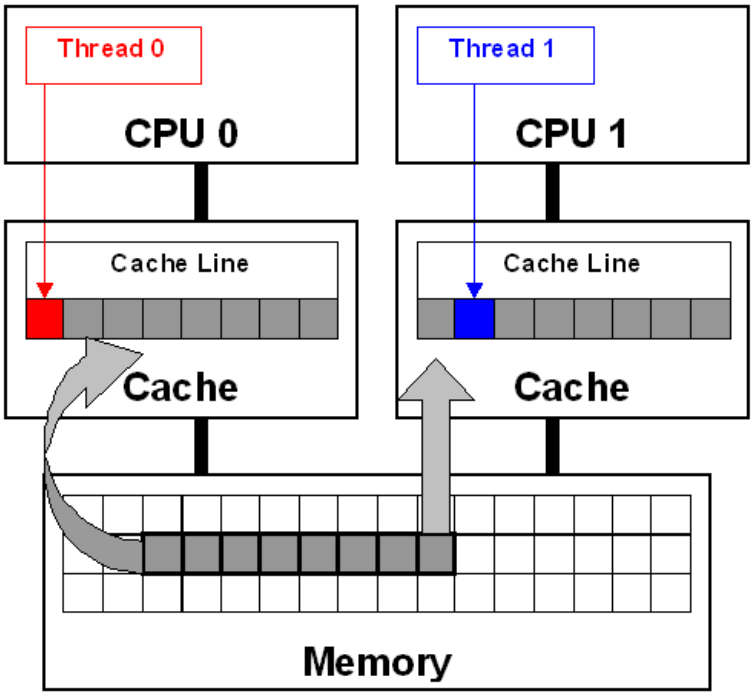

FIGURE 4.2: Illustration of the principle of false sharing. In this situation, two threads attempt to modify two consecutive data belonging to the same cache line. Credits: https://software.intel.com/en-us/articles/avoiding-and-identifying-false-sharing-among-threads.

It is also important to mention that the code highly benefits from the use of OpenMP. Not only does it provide a significant speed-up, but it also allows to use more memory per MPI process which is particularly appreciable considering the high memory burden represented by the PIC method. Without OpenMP, it would be very difficult to use high numbers of particles.

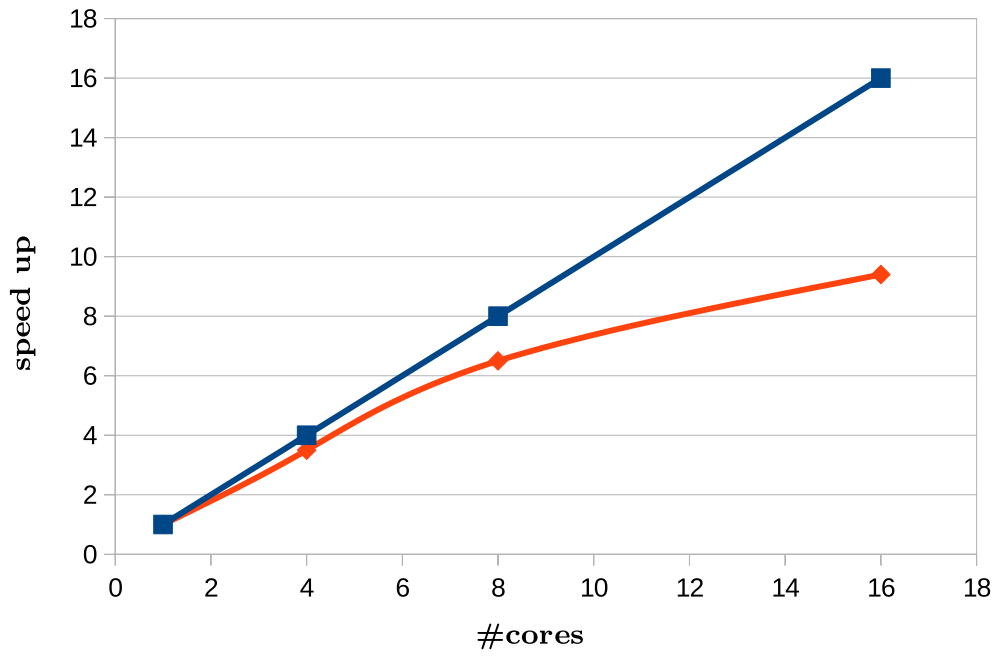

FIGURE 4.3: Speed-up using 8 MPI processes and varying number of OpenMP cores per MPI process (red curve). The ideal scaling is in blue. The grid configuration is: $N_r = 90$, $\ell_{max} = 44$. The number of tracers is $N_{tra} = 8 \times 10^7$. The diffusion is computed.

4.2 Optimization of interpolations

Most of the time consumed by the PIC portion of the code is spent in the interpolations between particles and grid. To reduce their numerical cost, one should concentrate on the following most expensive sub-steps:

1. The search for the grid cell each particle belongs to. If not done cautiously, this particles tracking phase can be very expensive.
2. The computation of the interpolation weights which depends on the chosen method.
3. The memory access of grid arrays which becomes almost random as tracers are gradually mixed by the flow.

Each of these points is addressed in the next subsections.

4.2.1 Particles tracking

Although it is almost immediate to localize a particle in a regular Cartesian grid, it can be more difficult to do so in a grid with irregular spacings without testing all grid nodes in each direction. In PARODY, the grid is regular along the longitude, but not in the other directions. It is however quasi-regular along the latitude, which can be exploited. Efficient particles tracking can be performed in the following way:

- Along the radius, the grid is not regular. However, since the MPI parallel decomposition is performed radially (see section 4.1.1 below), each MPI process is left with only a few radial layers. It is not very expensive to test all of them.
- Along the latitude, one can take advantage of the quasi-regularity of the grid. This allows to propose a first guess using the mean latitudinal increment and then explore only the 2 neighboring nodes as a verification.
- In longitude, the grid is regular. Locating a particle thus simply requires a modulo, minding the wrapping of the grid at $\phi = 2\pi$.

In addition, after the advection step, a significant proportion of tracers may still belong to their original grid cell which can be checked by a simple test. This observation can be used to make the tracking phase faster as most particles are thus already located. Also, between two advection steps, the positions of the tracers are unchanged and can thus be stored in memory to avoid any tracking phase in the other interpolations.

4.2.2 Computation of the interpolation weights

Choice of the weighting method

For each particle numbered p, a weighted contribution is given to/received from the 8 closest grid nodes. Eight weights $\omega_{p(i,j,k)}$ must therefore be computed. As discussed in section 3.3.1, using weights inversely proportional to the distance between particle and grid node may be slightly more accurate but is performed at the price of several costly floating point operations (trigonometric functions, square root of and a division). A way to decrease the computational cost is to opt for the "volume-weighting" method (Seldner and Westermann, 1988) explicated in section 3.3.1 as the latter only involves 3 multiplications.

Weights storage

The weights $\omega_{p(i,j,k)}$ need to be recomputed at each substep of the Runge-Kutta advection scheme because the velocity is successively evaluated at different locations. However, the tracers remain at a fixed position during the calculation of diffusion which involves a total of 5 successive interpolations (see section 3.5). After the advection process, the weights $\omega_{p(i,j,k)}$ can therefore be computed only once each time step and stored in memory to be directly reused every time an interpolation routine is called until the next advection step. Although it increases the memory requirements, storing both the positions of particles and the interpolation weights makes the treatment of the diffusion approximately 3 times faster.

4.2.3 Particles sorting and optimization of cache use

Another major source of inefficiency comes from the mixing action of the flow which gradually destroys the coherence of the initial distribution of particles. During the interpolations, this produces a strong performance drop since the grid arrays are accessed randomly which is highly non-optimal. An interesting approach consists in regularly sorting the particles to improve the efficiency of the memory access. To make the principles of this strategy more understandable, basic generalities concerning the memory hierarchy in most of today's computers are first recalled. The sorting method and its results in PARODY are then discussed.

Brief reminder of cache systems architecture

It is beyond the scope of this paragraph to discuss every details of the various existing and rapidly evolving computer architectures. I will however recall in a rather simplistic way some of the very general features that will help understand how particle sorting may increase the performance of the code.

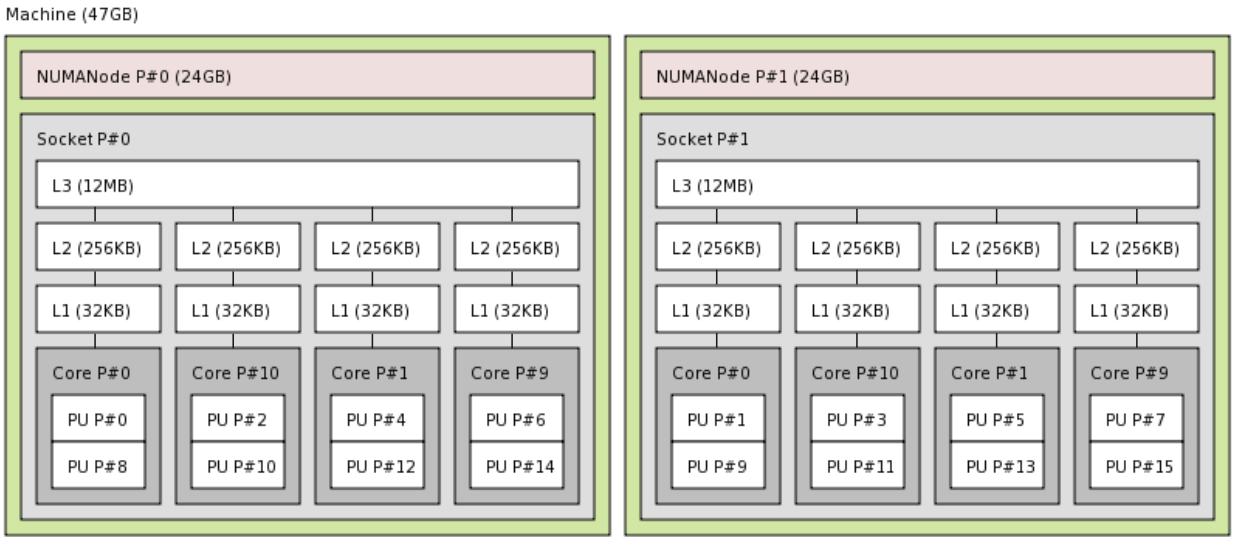

FIGURE 4.4: Architecture of a node containing 2 processors Intel X5672 Westmere tetra-cores 3,2 GHz (8 cores). The total node memory is 48 Go and for each processor, there exist 3 levels of cache memory. A first cache L3 of 12 MB is shared between the 4 cores of the processor. Then, each core has 2 private caches L2 and L1 with capacity 256 KB and 32 KB, respectively. Taken and adapted from: `http://www.ens-lyon.fr/PSMN`.

Before the mid 2000's, the development of more efficient computers mostly relied on increasing the *clock frequency* (expressed in Hertz), which is related to the number of operations a processor can perform each second. However, because thermal dissipation is proportional to the square of the frequency, the latter has today stabilized around 3 GHz after peaking at about 8.8 GHz. Increasing the frequency further raises enormous technical challenges. Nevertheless, the size of the transistors has continued to decrease so that more transistors can now be incorporated per surface unit on an electronic circuit although technological limits may soon be reached (Borkar and Chien, 2011; Bubnova, 2017). As the number of operations that can be performed per surface unit increases, it becomes crucial to transfer the data stored in memory fast enough to the CPU (*Central Processing Unit*), otherwise some computation time will be lost waiting for the data. The processor memory is therefore organized into (usually 3) subsequent memory levels called *caches*. Once some data is stored in the cache, the CPU can access it directly via the cache which decreases the mean access time. The closer a cache is to the CPU the faster data will transit to the latter, but the smaller the cache storage capacity. This architecture allows a more dynamic management of the memory; the goal of an effective memory system being that the effective access time that the processor sees is very close to the access time of the cache. An example of such an architecture is given in figure 4.4.

A consequence for the programmer is that a code should be written in such a way that data is loaded to the cache a minimal number of times and reused as much as possible once residing in the cache. This way, less time is lost waiting for transiting data. The strategies explained in the next two paragraphs are designed to optimize the cache use in that sense.

Particle sorting

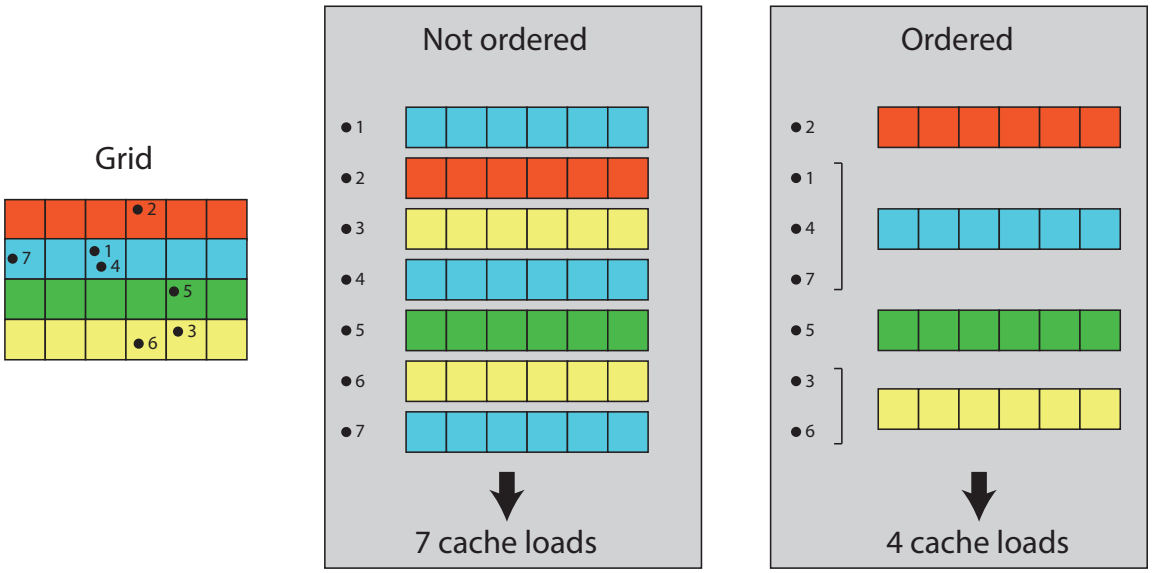

FIGURE 4.5: Simplified cartoon illustrating the cache use for sorted and unsorted tracers. The tracers are denoted by black points and are numbered following memory order. Each color represents a cache line for the scalar grid fields (for example, velocity). For unsorted tracers, a cache line must be loaded a large number of times (as many times as there are tracers in the worse case that is 7 times in this simplified cartoon). If tracers are sorted, each cache line is loaded only once and reused for all the tracers that reside in this cache line (only 4 cache loads in this illustration instead of 7).

One of the main sources of inefficiency in the PIC method is the mixing of the tracers with time, especially if the flow is strongly supercritical. A consequence of this phenomenon is that two tracers that are stored contiguously in memory might not be neighbors in space. Conversely, two tracers belonging to the same grid cell may be stored at very remote memory locations. When performing interpolations between tracers and grid, there thus is little chance that two successive tracers reside in the same grid cache line (see figure 4.5). In the worst case, a new cache line must be loaded for each tracer causing significant amount of time lost in memory transfer. In addition, if OpenMP is used to share the iterations of the interpolation loops between threads (see section 4.1.2), this causes potential conflict in memory access resulting in extra time spent in threads management and degraded scalability.

On the contrary, one might choose to keep the tracers "sorted" (or at least partially sorted) in grid cells order. In such a configuration, a grid cache line needs (ideally) to be loaded only once and can be reused for all the tracers that reside in this cache line as illustrated by a simplified cartoon on figure 4.5. Also, the competition in memory access for the OpenMP threads is reduced which improves the scalability. This idea of fully or partially sorting particles is not new and exists in many variants. For instance, Elster (1994) uses a domain decomposition with OpenMP and ensures that particles that are adjacent in memory belong to the same thread's subdomain. On the other hand, Bowers (2001) could obtain a gain of 40 to 70% by performing full particles sorting. Other authors Anderson and Shumaker (1995) reported similar performance improvements by using a different sorting method.

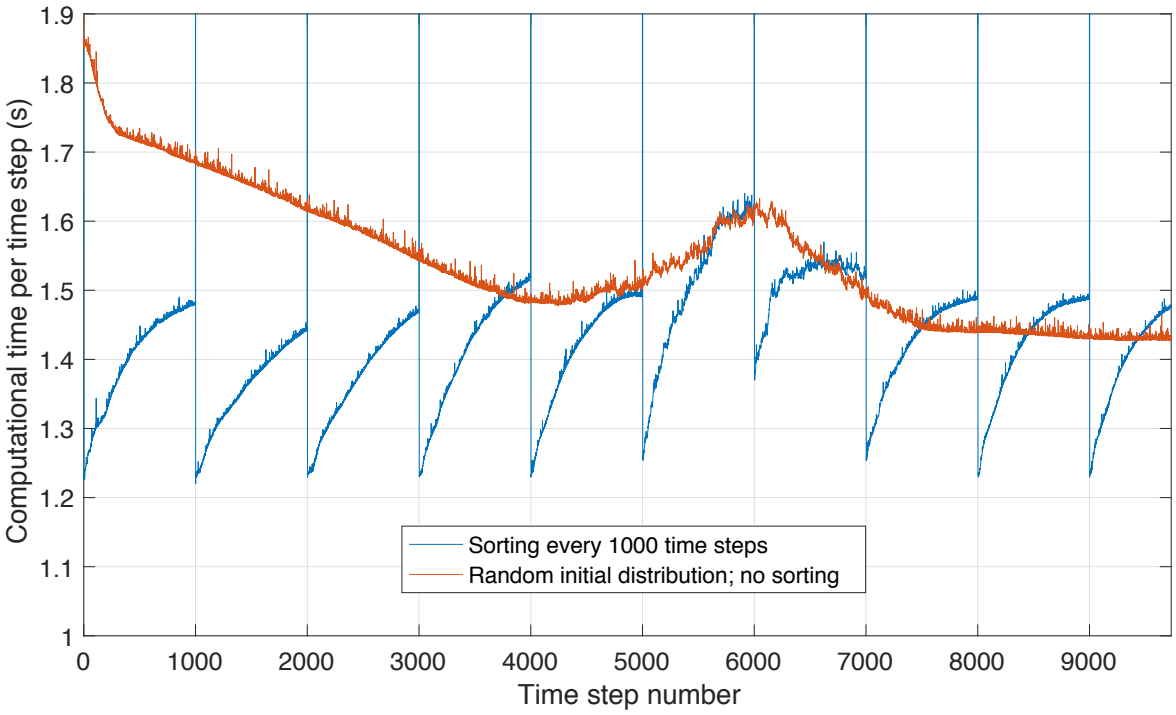

FIGURE 4.6: Blue curve: total time spent in the PIC portion of the code every time step. Tracers sorting is performed every 1000 time steps. Red curve: same simulation starting from randomly positioned tracers and performing no sorting. Both cases correspond to a simulation of the benchmark case 1 proposed by Christensen et al. (2001) with parameters: $N_r = 90$, $\ell_{max} = 120$, $N_{tra} = 150 \times 10^6$.

To sort the particles, two approaches can be envisioned:

1. Tracers are fully sorted only once every s steps. Between two sorting events, the tracers gradually get mixed and are therefore only partially sorted. However, since the mixing process usually takes a while, a gain in performance remains for several hundreds of time steps. In practice, I found it sufficient to perform sorting only once every 50, 100 or even 500 time steps, depending on the flow characteristics. To sort the particles, each grid cell is first attributed a cell number $n_c(i_\phi, i_\theta, i_r)$ so that:

$$n_c(i_\phi, i_\theta, i_r) = i_\phi + N_\phi(i_\theta - 1) + N_\phi N_\theta(i_r - 1) \tag{4.1}$$

   The particles are then sorted according to their cell number. Efficient sorting algorithms include the classic QuickSort and SortMerge methods. Both have been developed in OpenMP parallel versions (Umeda and Oya, 2015), the codes of which are available in many open source versions online. After comparing both algorithms for the PIC application, I opted for an OpenMP parallel version of the QuickSort algorithm.

2. Tracers are kept fully sorted at each time step. In this case, the QuickSort algorithm may not be the best option since its cost can degenerate in $\mathcal{O}(n^2)$ for already partially sorted arrays. One can however benefit from using the knowledge of the particles location to design a better algorithm similar to that proposed by Anderson and Shumaker (1995). In this method, the tracers that moved to another cell are copied to an auxiliary array while sequences of

tracers that remained in their cells are identified. Only the transiting particles (which represent a small subset of the particles array) are sorted and the full tracers array is finally rebuilt by copying alternately sorted transiting particles and retained portions. It may be worth using such a method when modeling turbulent flows which produce quick and efficient mixing of the tracers.

I implemented both approaches in PARODY. I tested the first version on the benchmark case 1 proposed by Christensen et al. (2001), which has a rather weak dynamics. As expected, the gain depends on the grid size. For a low resolution at $\ell_{max} = 44$, the computation time of the time step is reduced by only 10% whereas the gain reaches 20% of the total time step for $\ell_{max} = 96$. This is due to the fact that, at low resolution, a significant portion of the grid already fits into caches of low level whereas this is no longer true when the resolution is increased. Figure 4.6 displays the computation time spent in the PIC part per time step for $N_r = 90$, $\ell_{max} = 120$ and $N_{tra} = 150 \times 10^6$ particles on 128 cores (16 MPI $\times$ 8 OpenMP) for particles sorted every 1000 time steps and unsorted particles starting from random initial distribution. As can be measured at $t = 0$, the situation of fully sorted tracers is approximately 30% less costly than randomly distributed tracers. Surprisingly, the cost of initially randomly distributed particles decreases with time before stabilizing. This may be a consequence of MPI communications during which the particles that transit to a different MPI domain are copied into one block at the end of the particles array of the new MPI domain, causing partial restructuration of the particles array. However, a full sort of the particles is still more efficient, although the benefits are completely lost after about 500 time steps. Performing sorting every 50 or 100 time steps would therefore be a good compromise since at such frequencies, the sorting cost (about 1.3s) remains negligible.

The adjustment and the benefits of this method may therefore depend both on the numerical configuration (parallelization, resolution, number of tracers) as well as on the characteristics of the flow (large-scale or not). Table 4.1 gives details of the gain for a typical thermochemical convection run at $E = 10^{-3}$, $Ra = 5 \times 10^5$, $P_T = 1$, $Le = +\infty$, with $N_r = 150$, $\ell_{max} = 200$, $N_{tra} = 2 \times 10^8$ on 16 MPI process and 8 OpenMP cores per MPI process. The gain on the total time step is about 30% which is in line with other values proposed in the literature and shows that sorting particles can bring substantial benefits for the performance of the code.

There is however one limitation to this sorting method. Since the grid arrays are stored by radius, latitude and longitude, two consecutive radial layers can contain too many nodes to fit in a low-level cache for large arrays. Two cache loads or more would then be necessary for each tracer. A possible solution is to store the grid data in a cell caching system which is briefly described in the next subsection. Although I have not implemented such a method in PARODY because of its complexity, this should be kept in mind for future implementation in PARODY or other codes.

Routine	No sorting (s)	Sorting (s)	Gain
Advection	0.59	0.42	28.9%
Tracers to grid	0.88	0.49	44.32%

TABLE 4.1: Time spent in the advection and tracers to grid routines (in seconds), for the sorted and non-sorted cases.

Cell caching storage

Rather than storing the arrays in rows and columns, one can instead store the grid according to a *cell caching* system by defining successive subgrids that fit into the cache. For instance, the row storage of a 2D $m \times n$ array a would give:

$$a_{00}a_{01} \dots a_{0n}a_{10} \dots a_{mn}$$

whereas for a 4×4 cell caching storage this would become:

$$a_{00} \dots a_{03}a_{10} \dots a_{13}a_{20} \dots a_{33}a_{04} \dots a_{07}a_{14} \dots a_{17} \dots a_{mn}.$$

A more detailed description of the principles of "cell caching" storage of the grid data can be found in the thesis of Elster (1994). Such a method may not be convenient to use in PARODY since all arrays are more easily written along latitude and longitude when performing the spectral transforms. Moreover, a cell caching storage system complicates the computation of the other non-linear terms by finite differences. But naturally, this could be tested in the future. A very optimal method could be obtained by defining "blocks" of subgrids that fit into the cache and by sorting the tracers more coarsely by "blocks" number rather than by grid cells number, which would reduce the sorting cost. Each OpenMP thread would then be given a set of grid blocks. Such an implementation may however depend on the architecture of the machine and would be more technically challenging. It will require further investigation.

4.3 Optimization of the treatment of empty cells for low aspect ratios

This section addresses more specifically the problem of "empty cells" evoked in section 3.3.3 and posed by the irregularity of the spherical grid. A condition for the PIC method to produce optimal results is that there be a sufficient number of particles in all grid cells. For regular grids providing similar spatial resolution everywhere, this is easily ensured; the number of particles per cell remaining almost constant over the entire domain, at least for incompressible flows. Difficulties arise when the grid mesh becomes locally much finer than in the rest of the domain. Mesh refinement can either be purposely implemented by the programer to resolve local small-scale physical structures - a strategy frequently employed, for instance in plasmas physics simulations (Vay et al., 2004; Lapenta, 2007) and for the description of plumes in mantle convection problems (Heister et al., 2017) - or be a pure effect of the geometry of the grid. This is the case in spherical geometry since the infinitesimal volume element around a point of coordinates (r, θ, ϕ) is proportional to $r^2 \sin(\theta)$ which tends to 0 both at the sphere center and at the poles. When discretizing a sphere to define a numerical grid, this implies that, on a given concentric sphere, equatorial cells are bigger than polar ones. Similarly, for fixed latitude and longitude and for a regular radial spacing, cells located close to the sphere center are much smaller than those near the external boundary. The resolution (defined by the local grid spacing) can vary by a factor 100 throughout the grid but this variation is purely geometric: in polar regions and close the sphere center, the spatial resolution locally becomes much finer than what is required to resolve the relevant physical scales.

Whether mesh refinement is deliberately applied or is simply a consequence of the geometry of the problem, it raises a complicated issue for the particles distribution as one should try to have particles in each grid cell while minimizing the overall particles number. The solutions to this problem may however differ depending on whether a finer resolution is actually needed or not. If one wishes to describe locally smaller physical structures, then both the grid and the particles distribution should be refined so as to describe smaller scales. Various adaptive PIC methods

have been developed in this context. They rely on careful addition and removal of particles which poses tough numerical challenges and is often performed at the price of introducing unphysical numerical diffusion (Edwards and Bridson, 2012). Adding new particles can be achieved via particles splitting (Hong et al., 2008). Decreasing the number of particles can be performed either by directly removing or merging particles (Hong et al., 2008; Vranic et al., 2015). The latter option may better conserve the information carried by the particles while adding only moderate extra diffusion. In PARODY the situation is quite different as the grid refinement in the vicinity of poles and sphere center is purely artificial. Adapting the particles number in these regions is therefore still a possible valid option but is no longer compulsory since no particular smaller physical structure is to be resolved there. Considering the complexities associated with addition and removal of particles and the subsequent introduction of numerical diffusion, I chose not to implement this method in a first phase, although it could naturally be tested in the future.

Another option is to use a variant of the PIC method called "particles kernels" (Hong et al., 2008). In its principle, a kernel function is used around each particle to determine its contribution to a grid point. Each particle is given a radius that determines the volume of fluid it represents. Each grid point that is within a particle's radius is affected by that particle by an amount determined by distance and the kernel function shape. Despite having several advantages, this method may not be well adapted to PARODY since, in spherical geometry, it might be costly to determine all the points that fall within the kernel of a particle. In addition, a particle may contribute to a large number of points near the poles and sphere center.

Even though the two previous methods deserve to be tested, I propose an alternative approach that leaves the number of particles unchanged and does not require the use of kernels. Rather than adapting the particles, one can instead try to "loosen" the grid mesh to make the resolution as homogeneous and close to the "adequate" resolution as possible. This can be achieved by merging grid cells where the resolution is too fine to obtain a "coarser" and more regular grid. This "grid regularization" method is explained in details in the next paragraphs.

4.3.1 Grid regularization method

In geodynamo simulations, the radial resolution is usually set so as to correctly resolve the Ekman boundary layers and is therefore adequate throughout the domain. On the contrary, the "horizontal" resolution (given by the mid grid spacing in latitude and longitude) increases in polar regions and near the sphere center where it locally becomes uselessly high compared with the size of the physical structures to be resolved. The spectral resolution can therefore be relaxed when r decreases. In his code XSHELLS, Nathanaël Schaeffer solves equations up to a degree $\ell_{max}(r)$ that depends on the radius r:

$$\ell_{max}(r) = \begin{cases} \ell_{max}(r_o) & \text{if} \quad r \geq r_c \\ \ell_{max}(r_o)\sqrt{r/r_c} & \text{if} \quad r \leq r_c, \end{cases} \tag{4.2}$$

where $r_c = r_o/2$. This relation was empirically shown to provide sufficient resolution everywhere. Partial justification for its expression can be found in Marti and Jackson (2016). The corresponding sufficient spatial resolution s_h can be expressed as:

$$s_h(r) = \begin{cases} \dfrac{\pi r}{N_{lat}+1} & \text{if} \quad r \geq r_c \\ \dfrac{\pi r_c}{N_{lat}}\sqrt{r/r_c} & \text{if} \quad r \leq r_c, \end{cases} \tag{4.3}$$

where N_{lat} is the number of points in latitude.

The principle of the "grid regularization" method is the following. A "coarse" grid is initially constructed by merging adjacent cells on each concentric layer of the "fine" spherical grid. The coarse grid ensures sufficient resolution everywhere defined by equation (4.3) while minimizing the differences in cells volume. Then, at each time step, the following procedure is used for the interpolations from tracers to grid:

1. **Interpolation from tracers to the coarse grid**.
2. **Completion of the coarse grid**, if necessary, in case some nodes of the coarse grid did not receive information from the tracers. This step is analogous to the method described in the section 3.3.3 but involves a radically smaller number of grid nodes.
3. **Interpolation from the coarse grid to the fine grid**, which can be done linearly.

The construction of a coarse grid and each of the steps above are successively described in the next sections.

Construction of a coarser grid

A coarser and more regular grid can be obtained from the finer and less regular spherical grid by merging cells in latitude and/or longitude when the local resolution falls below the sufficient resolution defined in equation (4.3). To do so, I propose the following method:

1. The list of divisors $\{p_i\}$ of N_{lat} in growing order is established.
2. On each radial layer, cells are merged by packs of p_i such that merging cells by p_i satisfies the criterion defined in equation (4.3) but merging cells by p_{i+1} does not.
3. A node is also added at each pole on every radial layer.

An identical process is then performed along the longitude. Illustrations for the cells merging in latitude and longitude are displayed on figures 4.7 and 4.8, respectively. The obtained grid is "coarser" than the initial spherical grid. For a grid $(Nr, N_\theta, N_\phi) = (90, 150, 320)$ with regular spacing in radius and an aspect ratio $r_i/r_o = 0.01$, the volumes ratio between the largest and smallest cell of the grid is slightly more than 10^5 for the fine grid and less than 10^4 for the coarse grid. Note that when N_{lat} is even, this usually creates an asymmetry between the north and south poles: the last pack of cells near the south pole has one more cell than elsewhere on the radial layer (see figure 4.7). In the following, each grid will be referred to as "coarse" and "fine" grid, respectively.

Interpolation from tracers to the coarse grid

The information contained in the particles is first interpolated to the coarse grid's nodes by linear interpolation. Because the coarse grid's nodes may not be the corners of well defined cells, is it not possible to use the volume-weighting method described in section 3.3.1. Each tracer therefore gives a contribution with a weight equal to the inverse of the distance between tracer and grid node. Using equivalent notations as in section 3.3.1, this reads, for the temperature field:

$$T_{(i,j,k)} = \frac{\sum_p T_p \omega'_{p(i,j,k)}}{\sum_p \omega'_{p(i,j,k)}}, \tag{4.4}$$

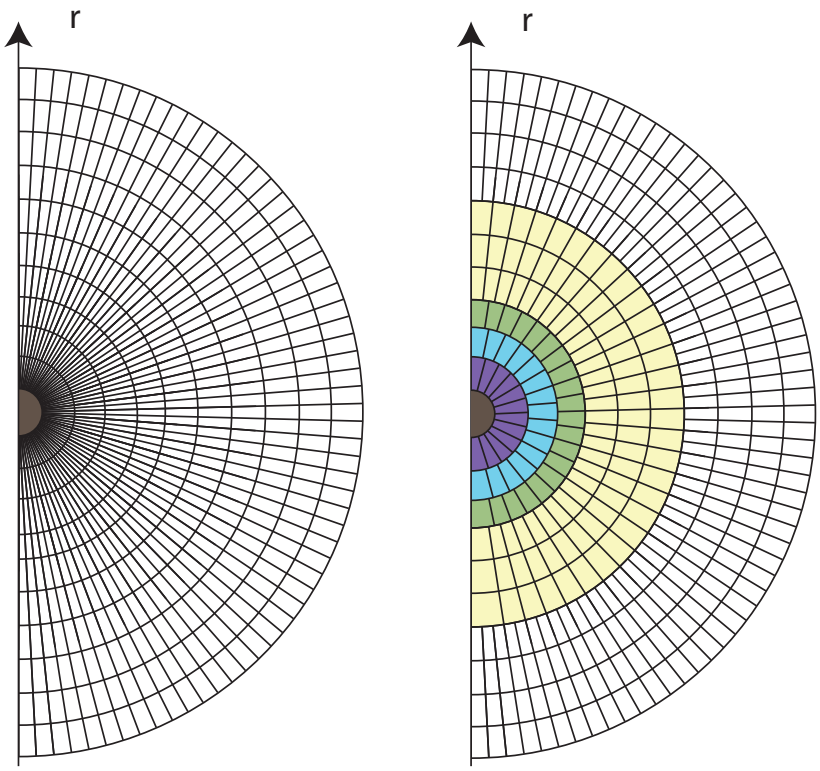

FIGURE 4.7: Longitudinal cut showing a fully spherical grid (left) and the same grid on which a certain number of cells have been merged along the latitude (right). In this case, $N_{lat} = 60$, whose first divisors are 2, 3, 4 and 5. In the blank region, no merging has been performed. In the colored regions, cells have been merged by packs of 2, 3, 4 or 5 cells. The size of the packs increases when progressing toward the sphere center. Note that the situation is not exactly symmetric at each pole. At the south pole, the packs have one more cell than everywhere else on the radial layer.

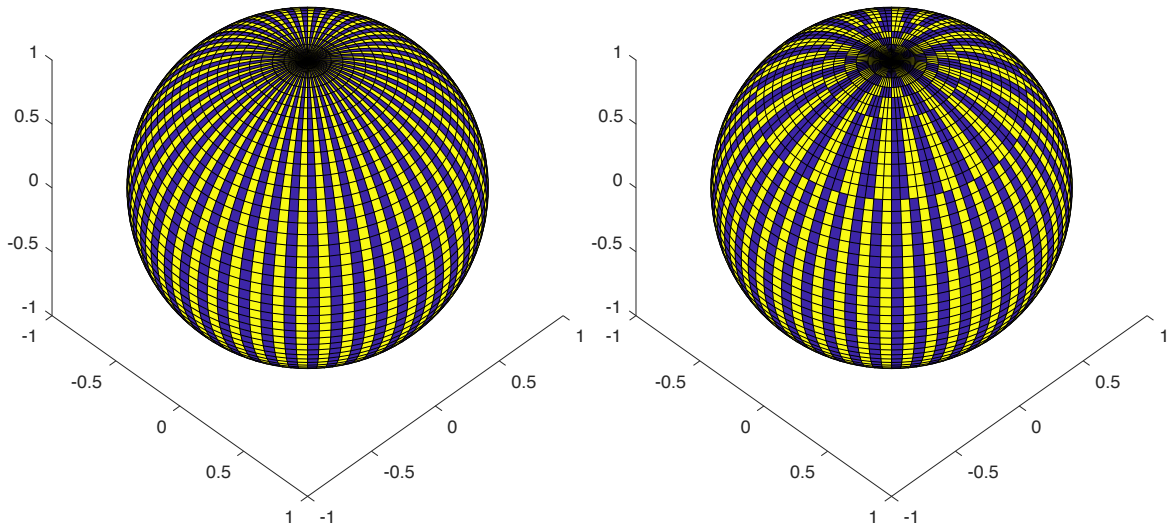

FIGURE 4.8: Spherical surface showing a fully spherical grid (left) and the same grid on which a certain number of cells have been merged along the longitude (right). $N_{lat} = 48$ and $N_{long} = 96$.

where the modified weights ω' are equal to:

$$\omega'_{p(i,j,k)} = d^{-1}_{p,(i,j,k)}, \tag{4.5}$$

with $d_{p,(i,j,k)}$ the distance between the particle p and the grid node (i, j, k). The computation of $\omega'_{p,(i,j,k)}$ involves many costly floating points operations (trigonometric functions, square root of and one division) which makes it more computationally demanding.

Completion of the coarse grid

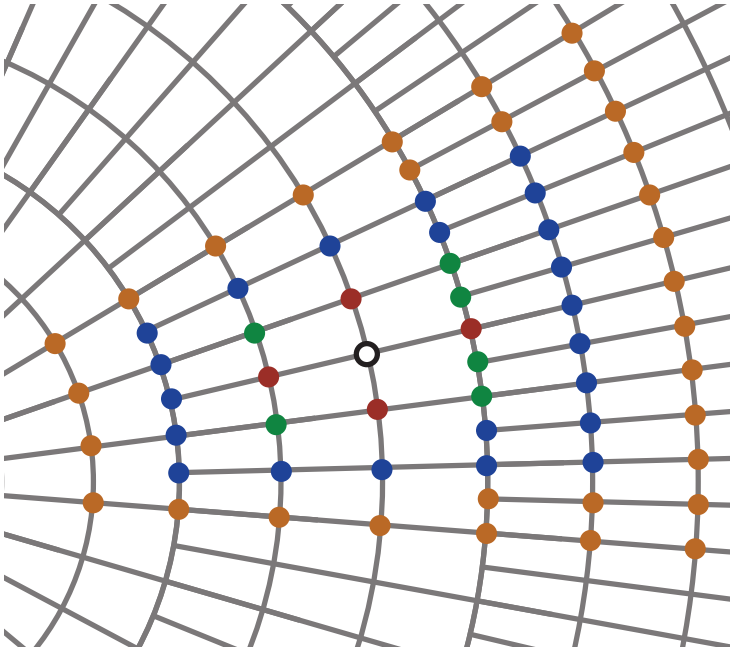

FIGURE 4.9: 2D Illustration of the coarse grid completion process. The white filled circle represents a node that has not received information from the particles during the tracers to coarse grid interpolation. To give this node a value, an average is computed using the 4 closest neighbors of the coarse grid (in red). In case none of these nodes has received information from the particles, the number of nodes of the coarse grid used for the average is progressively extended. The green nodes are first used and, if necessary, the blue then orange nodes until nodes of the coarse grid that received information from the tracers can be found.

The next step consists in filling the nodes of the coarse grid that received no information during the previous interpolation because there were no neighboring particles. The number of these nodes is by construction much lower in the coarse grid than in the fine grid for the same number of particles. The method to complete the coarse grid is the following:

1. The 6 closest neighbors (including, if relevant, an extra node placed at each pole) are tested and used to compute a weighted average (with weights inversely proportional to the distance between grid nodes). In practice, this is sufficient for the majority of nodes.

2. In case none of these neighbors has received information from the particles, the number of nodes of the coarse grid used for the average is gradually extended (see figure 4.9). One should however keep in mind the fact that the sampling might be biased because the number of merged cells in the coarse grid varies with latitude and radius. To compensate, the weights are divided by the number of merged cells in latitude and longitude.

Unless the number of tracers is very tiny, completing the coarse grid is extremely fast.

Completion of the fine grid from the coarse grid

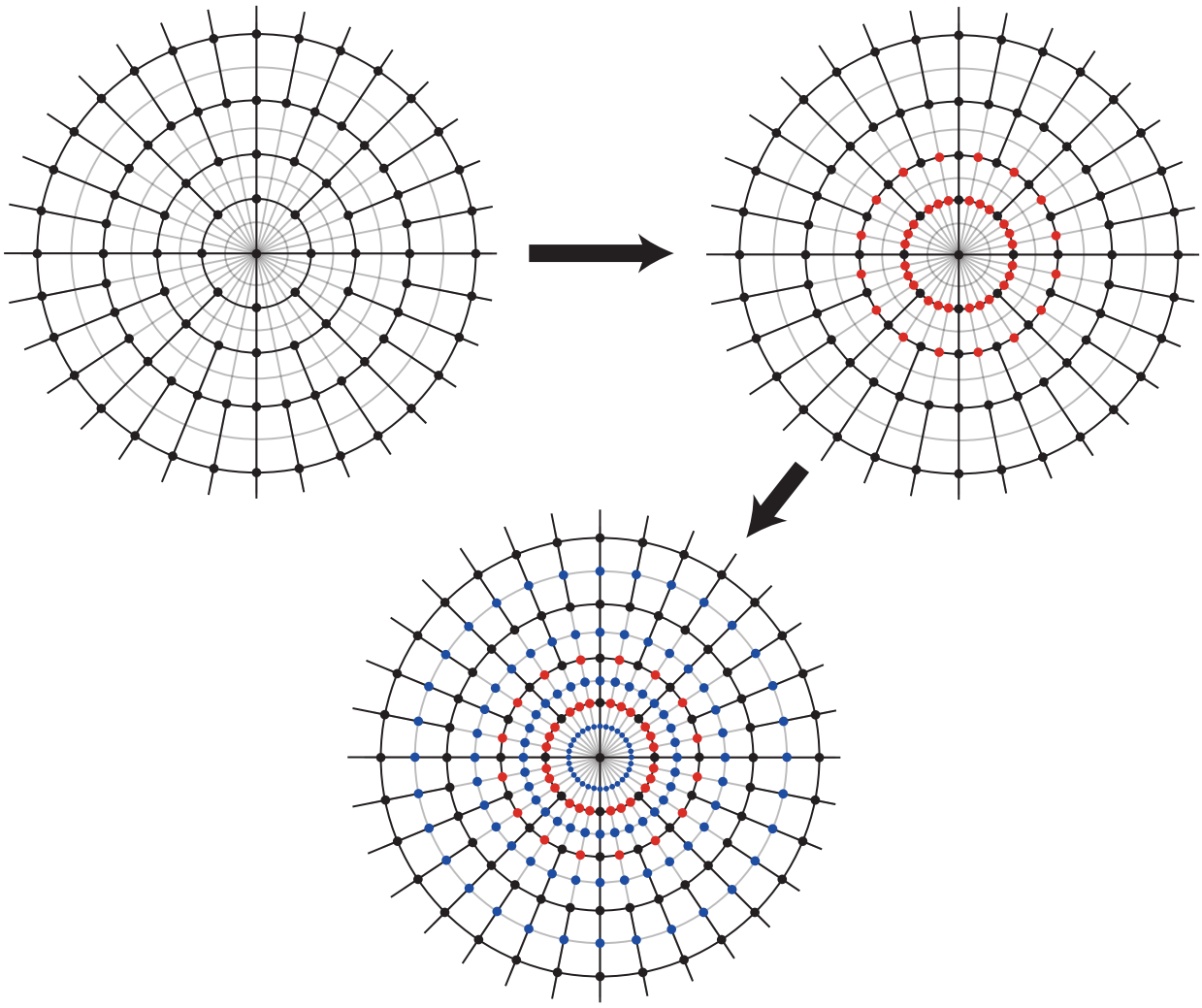

FIGURE 4.10: Polar view illustrating the process of completion of the fine grid with $N_{long} = 32$ points in longitude. The filled circles represent grid nodes. The node of the coarse grid are in black. In a first step, the missing longitudes on each latitude of the coarse grid (in red) are linearly completed (top right figure). Finally, the missing nodes (in blue) are linearly completed (bottom figure). An extra node placed at the pole is used for the closest nodes to the pole.

The fine grid finally needs to be completed from the coarse one. This can be done on each concentric sphere in a two-steps linear process that is illustrated and explained in figure 4.10. Other completion schemes could be thought about, but this one has the advantage of being simpler to implement. It is also computationally very cheap.

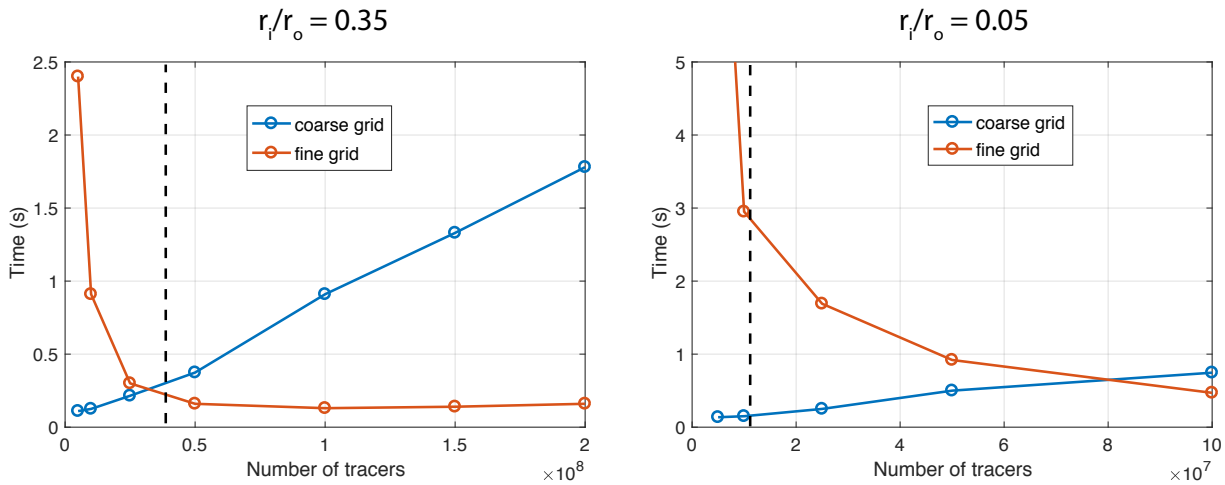

FIGURE 4.11: Time spent in the tracers to grid routine using trilinear interpolation in the spherical fine grid (red) and the method based on the construction of a coarse grid (blue) for two different aspect ratios r_i/r_o. Parameters used for the run are $\ell_{max} = 100$, $N_r = 150$, $N_\theta = 150$, $N_\phi = 320$. The vertical dashed lines indicate the number of particles corresponding to a "1/5" ratio criterion (see section 5.1.1) in chapter 5 for the definition of this criterion).

Results and comparison of efficiency for different aspect ratios

This subsection gives a comparison of the computation times using either the more naive treatment proposed in section 3.3.3 or the coarse grid method, for two aspect ratios (0.05 and 0.35), various numbers of particles (from 5×10^6 to 2×10^8) and grid parameters $(Nr, N_\theta, N_\phi) = (150, 150, 320)$. Computation times for the particles to grid routine are measured using 16 MPI process and 4 OpenMP threads per MPI process. The particles sorting strategy described in section 4.2.3 is applied in this test. The results are summarized in two plots gathered on figure 4.11. For both aspect ratios, the computation time increases almost linearly with the number of particles for the coarse grid method (blue curve on each plot). This is easily explained by the fact that the completion of the coarse and fine grids are very quick while the interpolation from particles to the coarse grid is expensive and has a cost proportional to the number of particles. For the fine grid method (red curve), decreasing the number of particles leads to a large number of "empty cells" with a high associated cost, whereas increasing particles gradually fills the "empty cells" while augmenting the number of trilinear interpolations. For aspect ratio 0.35, an optimal is reached at about 10^8 particles after which the time increases slowly again (see left plot on figure 4.11). On each plot, an estimation of the "adequate" number of particles for an Ekman number $E = 10^{-3}$ is indicated by a vertical dashed line. A detailed discussion about the basis for this estimation is detailed in the section 5.1.1 of the next chapter. For aspect ratio 0.35, the two curves intersect close to the dashed line which suggests that for aspect ratios larger than 0.35, the coarse grid method is more expensive for an adequate number of particles. On the contrary, the right plot corresponding to a lower aspect ratio of 0.05 shows that the coarse grid method is at least 10 times cheaper.

In conclusion, the method depicted in this chapter is successful in treating problems with low aspect ratios, at least from the point of view of numerical cost.

4.4 Periodic solutions

Even without the PIC method, simulations of planetary dynamos rapidly become very expensive when the control parameters are pushed in the direction of more realistic values. Progressing towards lower Ekman numbers automatically decreases the size of the structures and hence the grid resolution needs to be refined and the time step decreased to ensure the numerical stability of the solution. A classic strategy that is often adopted for the exploration of more extreme regimes consists in enforcing a periodicity in the solution. This way, the orders m of all fields can be partially degenerated which reduces the numerical cost associated with the Legendre transforms.

The same approach can be implemented with the PIC method. For instance, let us consider a simulation that requires N_{tra} particles in the full spherical shell on a (N_r, N_θ, N_ϕ) grid. If a 4-fold symmetry along the longitude is imposed in the solution, only $N_{tra}/4$ particles need to be initially spread in a reduced domain corresponding to a quarter of the spherical shell. The grid arrays are then defined only on $(N_r, N_\theta, N_\phi/4)$, plus 2 "buffer" points required in longitude on each boundary. As always, the situation is more delicate near the poles, since the velocity of a particle crossing a pole can be evaluated at positions in longitude that are outside the reduced domain. Around the poles, it is therefore mandatory to quadruplicate the velocity array in order to map the full spherical domain. At the end of the advection step, the coordinates of the particles are checked and periodic boundary conditions are enforced. Eventually, the interpolation from particles to grid can be performed on a quarter of the spherical shell. The total process is 4 times cheaper than computing the solution on the full spherical shell. Imposing a 4-fold or 8-fold symmetry in the solution allows to run simulations at $E = 10^{-3}$ very quickly (several time steps can be computed each second) and can be used to reach more extreme regimes (down to $E = 10^{-5}$).

4.5 Scaling of the hybrid code

FIGURE 4.12: The machine Ada. Credits: www.idris.fr.

I tested the performances of the hybrid code on the Ada supercomputer (GENCI/IDRIS, Orsay, France, see figure 4.12 for a photo of the machine). The parameters set for the run were: $\ell_{max} = 100$ and a radial discretization using $N_r = 400$. The aspect ratio is that of the Earth's core (0.35) and the number of tracers was set to 10^9. The code was run on numbers of cores ranging

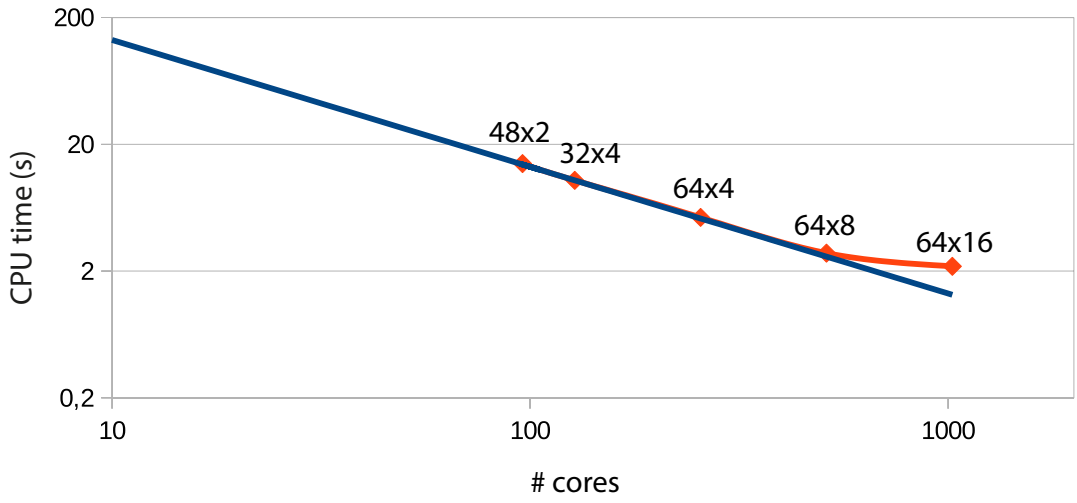

FIGURE 4.13: Mean computation time per time step for various parallel configurations $m \times n$, where m is the number of MPI processes and n that of OpenMP cores per MPI process. The grid resolution is $N_r = 360$, $\ell_{max} = 100$ with aspect ratio 0.35 and 10^9 tracers. The diffusion is computed and tracers are not sorted. Sorting tracers decreases the computation time by about 30% and neglecting diffusion by 20%. Sorting tracers and neglecting diffusion is about twice cheaper. The blue curve represents an ideal speed-up.

from 128 to 1024 (64 MPI $\times$ 16 OpenMP), without sorting tracers. The scaling is excellent up to 512 cores (64 MPI $\times$ 8 OpenMP), computing one time step in about 2 s in the finite Lewis number case. In the infinite Lewis number with sorted particles these times should be divided by almost 2. Comparing these computation times with non-PIC simulations is not obvious. Since in the limit of infinite Lewis number the compositional structures are very thin, they require a rather high spectral resolution to be adequately resolved (typically $\ell_{max} \sim 200$ or higher). At such resolutions, the cost of the Legendre transforms becomes comparable to the cost of the PIC method. Of course, with the codensity formulation, simulations are usually performed at much lower ranges of ℓ_{max} in which the cost of the PIC part is approximately 10 times that of the spectral transforms.

With only one dimension of MPI parallel decomposition, I estimate that, presently, 10^{10} constitutes an upper limit in the number of tracers that can be employed, restricting the reachable Ekman numbers to approximately $3 \times 10^{-4} - 10^{-5}$, depending on the adopted aspect ratio. Nevertheless, it should be emphasized that PIC methods can usually be parallelized in 2D or 3D with a high parallel efficiency. This method would therefore largely benefit from being implemented into a code that has more than one degree of MPI parallelization as it would make it theoretically suitable for simulations on tens of thousands of cores. Since part of the future of geodynamo simulations relies on exploring lower Ekman numbers and higher resolutions, 2D and 3D parallel codes will probably continue to be developed in the mid and long terms (Matsui et al., 2016). Furthermore, as we mentioned previously, the cost of the Legendre transforms grows faster than that of the PIC algorithm, which indicates that for geodynamo simulations involving very large spectral resolutions, the cost of the PIC method will be less of a concern, although it will substantially increase the memory requirements.

4.6 Conclusion and discussion

The various improvements of the PIC method enumerated in this chapter allowed to considerably reduce its computational cost. For low spectral resolutions, the PIC portion of the code is still about 10 times more expensive than the spectral transforms but the costs become comparable for spectral resolutions around $\ell_{max} = 200$ and for higher resolutions, the PIC method is no longer the limiting factor. In full spherical shell simulations, Ekman numbers down to $E = 3 \times 10^{-5}$ are presently attainable, and this limit can be pushed to $E = 10^{-5}$ if a periodic solution is enforced as the number of particles can be decreased (see the next chapter for an estimation of the adequate number of tracers). This leaves us with an explorable parameter space comprising 3 orders of magnitude for the Ekman number which is sufficient to establish scaling laws, provided a unique dynamical regime exists in that range. Even though further improvements can certainly still be brought to the present code, reaching lower Ekman numbers will probably be difficult without increasing the parallelism. In PARODY, the MPI decomposition is performed in one dimension (along the radius), due to the difficulties associated with the parallelization of spherical transforms. On the contrary, the PIC method can be easily parallelized in 3D with a high parallel efficiency. It would thus benefit from being implemented in other dynamo codes which are 2D-MPI such as CALYPSO, developed by H. Matsui. Another promising approach consists of using GPUs (*Graphics Processing Unit*) which, provided the PIC method is correctly adapted (Tang and Karniadakis, 2014; Snytnikov, 2015), may considerably cut the computation time. For example, Decyk and Singh (2014) report speeds-up of a factor 50 on GPUs compared to a single core of the Intel i7 processor. Even if an increasing number of super-computers now offer platforms supporting GPUs, time will tell whether this trend will continue to make GPUs a major element of future parallel computing.

Chapter 5

Validation and comparison with Eulerian methods

Chapters 3 and 4 provided a detailed description of the implementation and optimization of the PIC method in the code PARODY (called PARODY-PIC for simplicity in the following). Simple tests were conducted to compare different advection schemes and measure the efficiency of the code. Nevertheless, two points still need to be clarified before envisioning first applications.

On the one hand, even though the advection tests performed in chapter 3 produced encouraging results, the validity of the code for the modeling of complex flows in the context of planetary cores is still to be assessed. This can be classically done by comparing the results obtained with PARODY-PIC to that of other existing codes on benchmarks, which are simple and easily reproducible convection cases. In the context of convection in planetary cores, the pure thermal benchmark with dynamo action proposed by Christensen et al. (2001) and the double-diffusive benchmark designed by Breuer et al. (2010) are quite complementary choices to test our newly developed code in a spherical shell. For full sphere simulations, it is possible to use the benchmarks of Marti et al. (2014).

On the other hand, considering the multiple difficulties mentioned in the previous chapters, one may question the relevance of the choice of a PIC method to treat the compositional field, especially since numerous Eulerian schemes have been specifically designed for the hyperbolic equation. Because of the null chemical diffusivity, very thin compositional structures can be expected in numerical simulations, a prediction verified *a posteriori* in chapter 6. An appropriate numerical method should thus be capable of advecting chemical structures often described on a few grid points only without generating deformation and extra numerical dissipation. This ability can be evaluated qualitatively and quantitatively for different advection schemes on simple 1D and 2D Cartesian tests. Note that it is unfortunately not possible to perform a direct comparison with the Adams-Basforth method used to compute the advection terms in PARODY since this scheme is conditionally stable and diverges when solving for the hyperbolic equation.

In a first section, the results of the benchmark tests proposed by Christensen et al. (2001) and Breuer et al. (2010) are presented and used to estimate the adequate number of tracers for different Ekman numbers and aspect ratios. In a second part, advection tests in 1D and 2D Cartesian geometries are performed to compare the PIC method to some of the best Eulerian schemes specifically designed for their shock-capturing abilities. To finish, I show that the advantages of the PIC method in hydrodynamics contexts extend beyond its low dissipation.

5.1 Benchmarking

5.1.1 Spherical shell geometry

Benchmarks results

To validate the applicability of this PIC method to planetary studies in a spherical shell geometry, two benchmarks were tested. The first one is a case of pure thermal convection with magnetic field (case 1 proposed by Christensen et al. (2001)) in which the tracers are used for the description of temperature. The second benchmark is a non-magnetic double-diffusive convection case with a moderate Lewis number of 10 proposed by Breuer et al. (2010). In the latter, tracers are used only for composition, the temperature field being described on the Eulerian grid. Both benchmarks have a moderate Ekman number 10^{-3} and fixed temperature and composition at the boundaries. For each benchmark, various grid resolutions and numbers of tracers were explored. In all cases, the radial resolution was chosen so that at least 5 points are located within the Ekman boundary layers. Results are compared to reference states defined in each of the benchmarks corresponding papers (Christensen et al., 2001; Breuer et al., 2010). Since the definition of the standard solutions may be viewed as arbitrary, results of the PIC method are also compared to those obtained with PARODY using identical grid resolution and a full Eulerian description of all fields. The detailed results are given in tables 5.1 and 5.2.

Overall, results tend to converge to the solutions proposed as standards to an accuracy better than 3%. The differences drop to less than 1% when either the resolution, the precision of the interpolation or the order of the time stepping scheme are increased. In the thermal benchmark, case PT15 with the highest tested resolution differs by less than 0.5% from the standard. However, the convergence rate seems to be slightly slower than other codes. In order to determine whether differences in the initial particles distribution can influence the final solution, two simulations were run with identical resolution and number of particles but starting from homogeneously and randomly distributed particles, respectively (see PT5 and PT8 in table 5.1). The results differ by less than 0.1%, which suggests that the sensitivity of the final solution to the initial distribution is weak. The other simulations were therefore started with a homogeneous initial distribution to avoid problems of reproducibility inherent to the construction of a random initial state. Two empirical values (0.5 and 1) were also tested for the coefficient of numerical diffusion d introduced in equation (3.15). The results are in favor of a value of 0.5 (see PT5 and PT7) which was adopted in the rest of the simulations. Although setting $d = 0$ would destroy all the "memory" the tracers have incorporated (see section 3.5), this case should also be tested in the future.

In the thermal benchmark, the errors produced by the PIC method relative to the standard solution are mostly due to the four eddies that develop in the convection pattern in the middle of the grid. In these regions, inaccuracies of the advection scheme cause the tracers to be "centrifuged" from the eddies centers creating local "holes". The latter then vanish when the azimuthal drift establishes since the eddies are entrained before the tracers can be centrifuged, but the cumulated errors on the kinetic energy remain. Increasing the order of the advection time scheme appears to decrease the centrifugation of tracers, although the overall effect on the final solution is less clear (see PT5 and PT11, PT12 and PT13). Surprisingly, there is very little difference between the Runge-Kutta 2nd and 4th order at the tested resolution (PT12 and PT13), probably because this benchmark has a rather weak dynamics with a large-scale velocity field. For more strongly super-critical flows, I observed that it is safer to use the Runge-Kutta 4th order scheme. In addition, comparison between cases PT5, PT9, PT10, PT13 and PT14 suggests that adopting semi-quadratic interpolation rather than trilinear can provide some benefits, but only when the direction of the quadratic interpolation is determined using a criterion on the second derivative of the velocity. Another option to prevent the dispersion and clustering of particles is to ensure

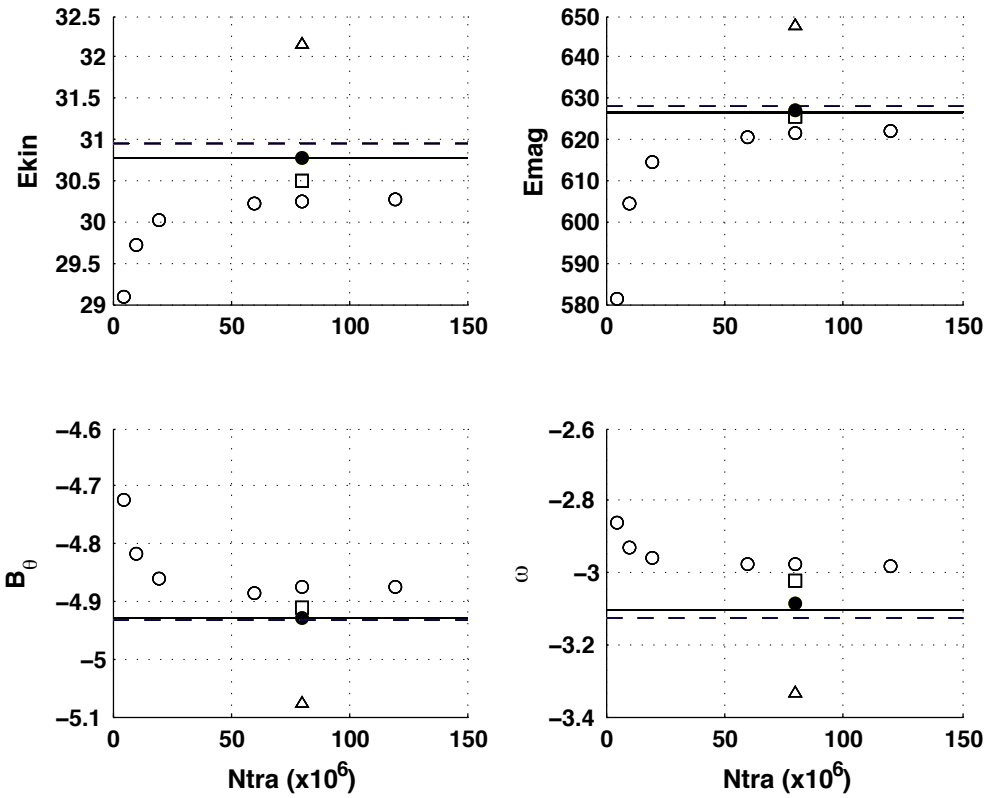

FIGURE 5.1: Comparison of part of the results of the benchmark proposed by Christensen et al. (2001). Cases PT0 to PT6: open circles - PT10: open square - PT11: open triangle - PT15: plain circle. The horizontal plain line corresponds to the value of the standard solution (case S). The horizontal dashed line shows the results obtained using PARODY without the PIC method (case P0). E_{kin} is the total kinetic energy, E_{mag} the total magnetic energy, B_θ is the magnetic field in the θ-direction taken at a fixed point and ω is the azimuthal drift. More precise definitions of these quantities can be found in the paper by Christensen et al. (2001).

a divergence-free velocity field by adding a correcting term in the interpolation of velocity from tracers to grid (Wang et al., 2015), a strategy I intend to test in the future. Note that this problem of centrifugation essentially occurs when eddies appear and remain at the same place for a long time, a situation that may be less of a concern in more time-dependent supercritical cases. Should areas of strong vorticity persist for a long time, more accurate time schemes and interpolations methods might be beneficial. Results obtained for this benchmark with $\ell_{max} = 44$ can be compared visually on figure 5.1.

For the double-diffusive benchmark of Breuer et al. (2010), it seems that, despite a very good overall agreement, the results obtained with the PIC method and the MagIC code do not converge exactly to the same values, particularly for the compositional Nusselt number (see table 5.2). It is however difficult to draw any definitive conclusion on this point since the results are sensitive to the adopted radial discretization, especially close to the boundaries, and also because MagIC uses a Chebychev decomposition in radius whereas Parody computes second-order finite differences. Furthermore, another variation between both codes appears in the stationary states. In this benchmark, the kinetic energy initially shows a series of periodic oscillations before bifurcating to a steady state. It is interesting to note that the number of these oscillations is lower with the PIC method and the switch to the steady state occurs much more rapidly, probably because the tracers provide some destabilizing effect.

	$(N_r, N_\theta, \ell_{max})$	$N_{tra}(10^6)$	d	T.s.	Int.	E_{kin}	E_{mag}	T	u_Φ	B_θ	ω
S						30.773	626.41	0.37338	-7.6250	-4.9289	-3.1017
P0	(90, 66, 44)					30.954	628.07	0.3728	-7.6523	-4.9332	-3.1256
PT0	(90, 66, 44)	1	0.5	RK4	L	-	-	-	-	-	-
PT1	(90, 66, 44)	5	0.5	RK4	L	29.099	581.09	0.3713	-7.6423	-4.7227	-2.8640
PT2	(90, 66, 44)	10	0.5	RK4	L	29.715	604.31	0.3715	-7.5857	-4.8161	-2.9296
PT3	(90, 66, 44)	20	0.5	RK4	L	30.025	614.50	0.3719	-7.5564	-4.8618	-2.9610
PT4	(90, 66, 44)	60	0.5	RK4	L	30.215	620.61	0.3721	-7.5444	-4.8855	-2.9776
PT5	(90, 66, 44)	80	0.5	RK4	L	30.237	621.33	0.3719	-7.5604	-4.8744	-2.9788
PT6	(90, 66, 44)	120	0.5	RK4	L	30.262	622.07	0.3719	-7.5602	-4.8766	-2.9810
PT7	(90, 66, 44)	80	1	RK4	L	29.940	616.41	0.3717	-7.5285	-4.8488	-2.9234
PT8	(90, 66, 44)	80-R	0.5	RK4	L	30.238	621.32	0.3721	-7.5430	-4.8858	-2.9790
PT9	(90, 66, 44)	80	0.5	RK4	sQ//	30.130	617.88	0.3720	-7.5836	-4.8536	-2.9690
PT10	(90, 66, 44)	80	0.5	RK4	sQ	30.503	625.79	0.3724	-7.5589	-4.9126	-3.0210
PT11	(90, 66, 44)	80	0.5	RKF5	L	32.168	647.82	0.3742	-7.6718	-5.0754	-3.3362
P1	(130, 96, 64)					30.865	627.30	0.3730	-7.3610	-4.9336	-3.1138
PT12	(130, 96, 64)	130	0.5	RK2	L	30.326	622.54	0.3728	-7.5683	-4.8887	-3.0072
PT13	(130, 96, 64)	130	0.5	RK4	L	30.326	622.55	0.3729	-7.5641	-4.8909	-3.0080
PT14	(130, 96, 64)	130	0.5	RK4	sQ//	30.250	620.35	0.3727	-7.5839	-4.8709	-3.0020
PT15	(150, 144, 96)	120	0.5	RK4	L	30.766	627.16	0.3733	-7.6152	-4.9291	-3.0871

TABLE 5.1: Benchmark case 1 results. S stands for the standard solution, as defined by Christensen et al. (2001). The cases denoted PTn and Pm are obtained with and without tracers, respectively. N_r and N_θ are the number of grid points in radius and in latitude. m_{max} is equal to ℓ_{max} in all simulations. N_{tra} is the number of tracers, d the numerical diffusion coefficient, introduced in equation (3.15). All simulations start from homogeneously distributed tracers except case PT8 which starts from randomly distributed tracers (R). Different time schemes (T.s.) were tested: Runge-Kutta 2nd and 4th orders and Runge-Kutta Fehlberg 5th order, denoted respectively by RK2, RK4 and RKF5. The interpolation scheme for the velocity (Int.) can be trilinear (L) or semi-quadratic either in the direction parallel to the velocity (sQ//) or in the direction of largest second order derivative (sQ); see section 3.4.2 for more details. E_{kin} is the total kinetic energy, E_{mag} the total magnetic energy, T, u_ϕ and B_θ are taken at a fixed point and stand respectively for the temperature, velocity in the ϕ-direction and magnetic field in the θ-direction. ω is the azimuthal drift. For a precise definition of these quantities and the standard solution, we refer the reader to the paper by Christensen et al. (2001).

Code	MagIC	Parody	Parody-PIC					
Res.	(61,288,96)	(90,192,64)	(90,192,64)				(120,320,96)	
Int.	-	-	L			sQ	L	sQ
T. s.	-	-	RK4			RK4	RK4	RK4
N_{tra}	-	-	70.10^6	110.10^6	160.10^6	110.10^6	110.10^6	110.10^6
Nu_T	1.0621	1.0622	1.0626	1.0626	1.0626	1.0625	1.0621	1.0621
$\pm$ SD	0.0000	0.0000	0.0000	0.0001	0.0001	0.0000	0.0000	0.0000
Nu_C	2.0544	2.056	2.0582	2.0570	2.0569	2.0607	2.0656	2.0668
$\pm$ SD	0.00006	0.0015	0.0009	0.0006	0.0006	0.0004	0.0013	0.0006
E_{kin}	106.72263	107.4256	107.7971	107.8250	107.8481	107.6679	107.0860	107.0831
$\pm$ SD	0.00201	0.0398	0.0078	0.0055	0.0035	0.0036	0.0061	0.0061
Eaz	9.44435	9.4233	9.4506	9.4545	9.4570	9.4386	9.4232	9.4268
$\pm$ SD	0.00028	0.0068	0.0004	0.0005	0.0003	0.0004	0.0007	0.0015

TABLE 5.2: Results of the benchmark of double-diffusive convection proposed by Breuer et al. (2010). MagIC is a pseudo-spectral code described in more detail in Christensen and Wicht (2007). Parody-PIC indicates results obtained with tracers. The resolution gives $(N_r, N_\phi, \ell_{max})$. In all simulations $m_{max} = \ell_{max}$. The interpolation scheme of velocity (Int.) can be trilinear (L) or semi-quadratic (sQ). In all simulations the time scheme for tracers advection is 4th order Runge-Kutta (RK4). The physical quantities measured are thermal and compositional Nusselt numbers at the bottom boundary as well as total kinetic energy and its azimuthal component. The standard deviations (SD) are also computed. We refer the reader to the paper by Breuer et al. (2010) for a more precise definition of these physical quantities. The numerical diffusion coefficient d is set to 0.5.

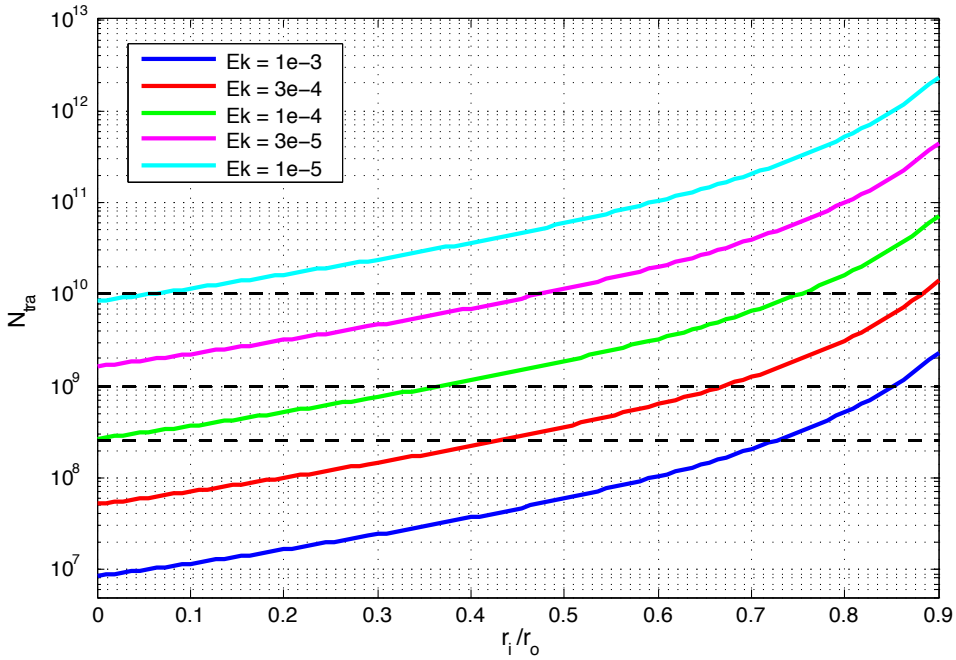

FIGURE 5.2: Estimation of the adequate number of tracers for different Ekman numbers and grid aspect ratios, based on a "1/4" criterion.

Estimation of the adequate number of tracers

Since most of the computation cost involved in the PIC method relates to interpolations between tracers and grid nodes, it is clear that the overall computational cost is roughly proportional to the number of tracers. Determining the minimum number of tracers that provides adequate resolution is therefore a crucial question. As mentioned earlier in section 3.3.3, the spherical geometry creates strong variability of the grid cell volumes throughout the grid, particularly if the aspect ratio (r_i/r_o) is low. However, the stretching of the grid in the vicinity of poles and at small radii is purely geometric and is not meant to describe any physical process. The number of tracers should therefore not be estimated based on the size of the smallest cells of the grid, but rather on the typical physical scales to be resolved. For convection in a rotating spherical shell, the main physical requirement is to resolve the Ekman boundary layers whose thickness scales as $E^{1/2}$.

For the benchmark case 1 (Christensen et al., 2001) with an Ekman number $E = 10^{-3}$, the effect of different numbers of tracers on the accuracy of the solution was studied for a fixed grid (PT0-6 in table 5.1; open circles on figure 5.1). When a very small number of tracers is used (PT0) the numerical solution does not converge to a stationary state and shows periodic oscillations of all the quantities measured in the benchmark, indicating that the number of tracers is probably too low to properly resolve all flow structures. Convergence to a (non-oscillatory) steady state is achieved for at least 5×10^6 tracers. Then, gradually increasing the number of tracers improves the accuracy of the solution up to about 6×10^7 tracers. However, Increasing the number of tracers further only slowly improves the convergence of the results which suggests that all flow structures are already well described by tracers. If we define the statistical mean distance between tracers by:

$$d_{tra} = \left[\frac{4\pi(r_o^3 - r_i^3)}{3N_{tra}}\right]^{1/3}, \tag{5.1}$$

then, in the configuration of the benchmark with aspect ratio 0.35 and Ekman number 10^{-3}, a

number of tracers $N_{tra} = 60 \times 10^6$ gives a distance d_{tra} which is roughly a fifth of the thickness of the Ekman boundary layer:

$$\frac{d_{tra}}{E^{1/2}} \simeq 0.196 \simeq 1/5. \tag{5.2}$$

In order to determine whether this "1/5" ratio can be applied as a criterion for different grid configurations and Ekman numbers, 3 simulations of non-magnetic double-diffusive convection were run with coupled boundary conditions, aspect ratio 0.35, Ekman number $E = 10^{-4}$ and numbers of tracers 250×10^6, 500×10^6 and 10^9 corresponding to ratios of roughly 1/4.1, 1/3.3 and 1/2.6, respectively. All 3 cases show similar qualitative and quantitative values for the time evolution of their kinetic energies and convective features which suggests that the "1/5" constraint can be relaxed to some extent. Note that, as is visible in the standard deviations on table 5.2, increasing the number of tracers reduces the numerical "noise" introduced by the particles which is theoretically proportional to $1/\sqrt{N_{tra}}$ (Keken et al., 1997). Figure 5.2 gives an estimation of the number of tracers based on a criterion of 1/4, for different aspect ratios and Ekman numbers. When the Ekman number drops under 10^{-4}, the number of tracers quickly jumps to several billions, particularly for high aspect ratios. For low Ekman numbers, a periodicity can be enforced in the solution (when it is not detrimental) to decrease the number of particles.

5.1.2 Full sphere geometry

In section 4.3, a strategy is described to extend the PIC method to full sphere simulations. This approach was shown to strongly reduce the computational time, but has not been validated yet on benchmarks. First tests on the benchmark case 1 proposed by Marti et al. (2014) gave encouraging results presaging a future applicability of the method, but a few pitfalls associated to the sphere center still require some extra care. Although the corresponding modifications are rather minor, they could not be implemented by the end of the redaction of this manuscript, for time reasons. However, testing the code in full sphere remains part of a near future work.

5.2 Comparison with Eulerian methods

In this section, I try to justify the choice of a PIC method rather than fully Eulerian approaches in the context of thermochemical convection at infinite Lewis number in planetary cores. At this point, it seems important to clarify what we mean by the "best" numerical method when it comes to solving a given physical problem. The answer may indeed not be unique and depends on various criteria such as the physical phenomena that need to be described, the available numerical resources, the history of the code in which the method is implemented and its perspectives of evolution. The "best" method may be defined as the one that gives a better approximation of the solution than other methods for comparable computation time, while being convenient to implement in existing codes and allowing easy evolution in the future. Certainly, the choice of a method is also a question of popularity: the widespread use of a numerical approach among a scientific community makes it an easier and more direct option, sometimes preventing the exploration of different strategies developed in other fields.

As stated in chapter 2, thermochemical convection in planetary cores can be modeled by solving the transport equation for composition. Assuming the diffusive term can be safely neglected, this equation becomes hyperbolic meaning that the compositional structures are purely advected by the flow without being diffused. *A posteriori* numerical simulations described in chapter 6 show that compositional convection develops through thin buoyant compositional plumes resembling ascending "filaments" which eventually break-up to form small chemical "blobs". The

thickness of these chemical plumes decreases with the Ekman number (see section 6.2.1) and typically represents only a few grid points (2 to 10). The advection method should therefore be able to capture strong discontinuities delimiting thin structures and successfully advect them across the grid without generating artificial diffusion. Numerous Eulerian schemes have been developed for this purpose in various contexts. An exhaustive and detailed description of all the existing schemes for solving the hyperbolic equation would be beyond the scope of this work and can be found in many classical books of numerical methods such as Hoffmann and Chiang (2000); LeVeque (2002). A review of the methods for advection-dominated problems is also given by Ewing and Wang (2001). I will however outline a brief and non-exhaustive summary of some of the most important steps in the development of efficient methods.

Classical finite-difference schemes for solving the hyperbolic equation include first (upwind, Lax method, Euler) and higher order schemes (such as the Lax-Wendroff, 2nd order up-wind, Beam-Warming, mid-point Leap-Frog, MacCormack and Runge-Kutta methods, to name a few). Although they usually increase the stability, implicit formulations appear to be less accurate than explicit formulations for solving the hyperbolic equation. First order methods are more associated with dissipative (diffusive) errors (see figure 5.3 for an illustration) whereas second order methods produce dispersion errors resulting in unphysical wiggles in the solution (cf. fig. 5.4). The addition of a second or fourth-order linear damping term can attenuate the oscillations and stabilize the solution but usually at the cost of extra non-physical dissipation, even when flux-corrector transport methods are applied via the introduction of an anti-diffusive term to remove part of the excessive damping.

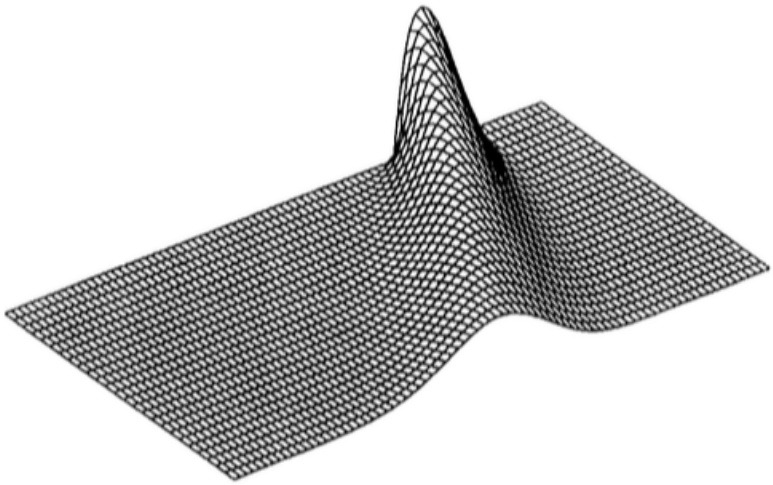

FIGURE 5.3: Illustration of a diffusive error when advecting a Gaussian by the implicit first-order upwind scheme with courant criterion $c = 1$. From Hoffmann and Chiang (2000).

"Modern" schemes have concentrated on stabilizing the solution (i.e. avoiding unphysical oscillations) while preserving the discontinuities as much as possible. A breakthrough was accomplished with the elaboration of the MUSCL scheme by Van Leer (1979) for solving compressible flows and then with the development of the concept of TVD (*Total Variation Diminishing*) schemes by Harten (1983). TVD schemes exist in a wide range of variants (Maciel, 2012). These can be first or second-order accurate in the smooth regions but necessarily degenerate to first-order accuracy in regions of high-gradients to prevent oscillations. Although being more expensive than schemes using simple linear damping terms, TVD schemes eliminate oscillations in the domain while better preserving discontinuities. A few years later, the *"(Weighted) Essentially Non-Oscillatory"*

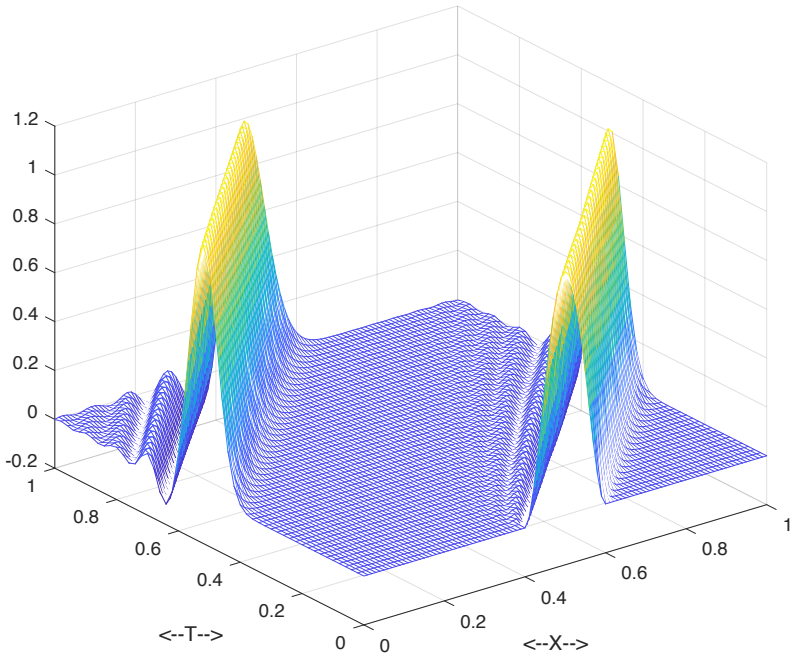

FIGURE 5.4: Illustration of a dispersion error when advecting a Gaussian with a Lax-Wendroff scheme.

ENO (Harten et al., 1987) and WENO (Liu et al., 1994) schemes were developed to guarantee a high-order accuracy everywhere (including near discontinuities) and can be constructed to arbitrary orders of accuracy; the most popular WENO schemes being 5th order accurate (Shu, 2009; Rathan and Raju, 2016; Zhu and Qiu, 2016). The MUSCL ad WENO schemes give excellent results for compressible and inviscid flows (Euler equation). To increase further the efficiency of the WENO scheme in 2D, Kubrak et al. (2013) used a dual meshing and computed the passive advection of a compositional field on a smaller grid (which, interestingly, bears some resemblance with a PIC method). This efficient strategy is however probably very costly in 3D. Other strategies include the refinement of the mesh near the discontinuities using the Finite Element Method (FEM) (Christensen and Yuen, 1984; Keken et al., 1997; Davies et al., 2007). A variant of this approach called "Marker chain" was compared to a tracers approach by Keken et al. (1997) who concluded that the Marker chain method is more accurate but not manageable for mixing of numerous and complex structures on long time scales as the length of the "chain" grows exponentially. They deduced that, provided the number of tracers is large enough to decrease the noise, the tracers approach is the most robust and convenient for the description of numerous plumes. More recently, Edwards and Bridson (2012) developed a 4th order accurate PIC method (named HOPIC) and compared it with high-order Eulerian schemes. HOPIC produced superior results on the same size grid, and for high accuracies, HOPIC also had lower compute time.

All methods have their pros and cons and may be more adapted to certain physical problems. In the following, I concentrate on 1D and 2D tests that can evaluate the capability of a scheme to advect tiny compositional structures across a grid with stationary incompressible flows. The PIC implemented in PARODY is adapted in Cartesian geometry and compared to TVD and WENO schemes which are well-known for their shock capturing abilities.

5.2.1 Comparison with TVD and WENO schemes on simple 1D and 2D advection tests

Advection of a 1D rectangle

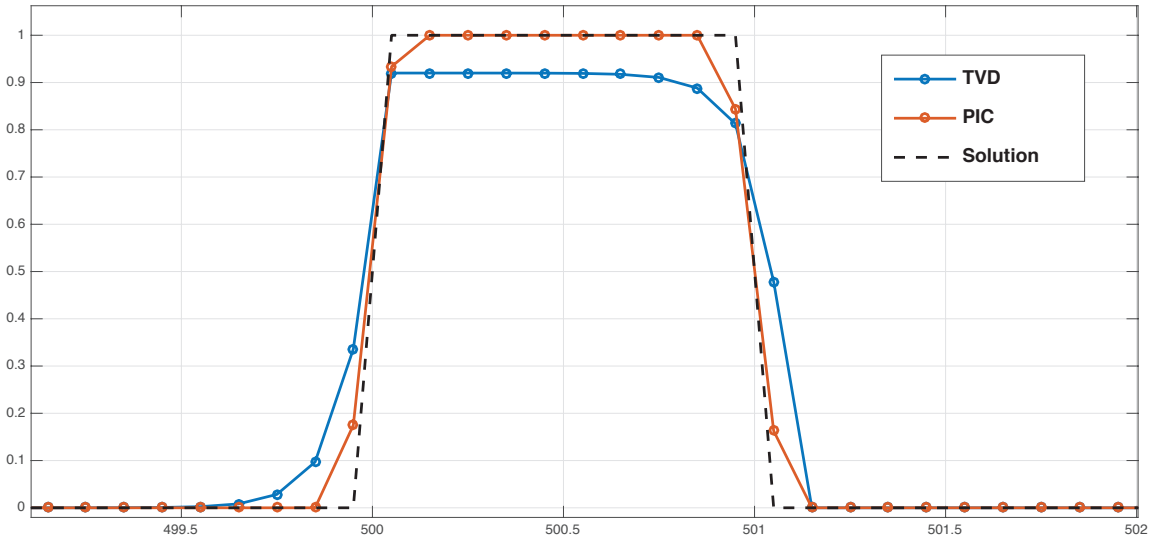

FIGURE 5.5: Profile of the rectangle after 10^4 time steps for the PIC (red) and TVD (blue) methods. The exact solution is plotted using a black dashed line.

In a first test in, a 1D rectangle of height 1 is initially defined on a width spanning 10 grid nodes of a regularly spaced grid ($\Delta x = 0.1$ with 1000 grid nodes in total). It is advected by a constant velocity $u_0 = 1$ during 10^4 iterations with time step $\Delta t = 5 \times 10^{-3}$ and periodic boundary conditions. For the TVD version of this test, I implemented the 1D version of the third order TVD scheme proposed by Zahran et al. (2007). Note that all TVD schemes necessarily degenerate to first-order near sharp boundaries, at least in the sense of local truncation error (Osher and Chakravarthy, 1984). However, this scheme by Zahran et al. (2007) produced particularly good results for the advection of sharp discontinuities compared to other TVD schemes. As for the PIC version of the test, an identical grid is used with 10^5 tracers. Note that in one dimension with a constant velocity, all the tracers could be directly advected to their final position in one time step, since the velocity is constant over the entire grid.

The results can be visualized on figure 5.5. With TVD scheme, the advected rectangle suffers from a "clipping" effect; its maximum value being reduced by almost 10%. Also, the boundaries of the rectangle are smoothed and the latter smears on 15 grid points which is 50% larger than its initial width. With the PIC method, the maximum value is preserved. The rectangle appears sharper than with the TVD scheme but is still larger than the solution. However, this error remains constant over time and is due to the interpolation from tracers to grid in which the grid node located at the edge of the rectangle receives contributions from tracers located from both sides, in and out of the rectangle.

A similar test involving a smoother rectangle was conducted by Edwards and Bridson (2012) with a 5th order WENO scheme (see figure 5.6). With the PIC method, there is no distinguishable difference before and after advection, whereas the rectangle is significantly diffused with the WENO scheme.

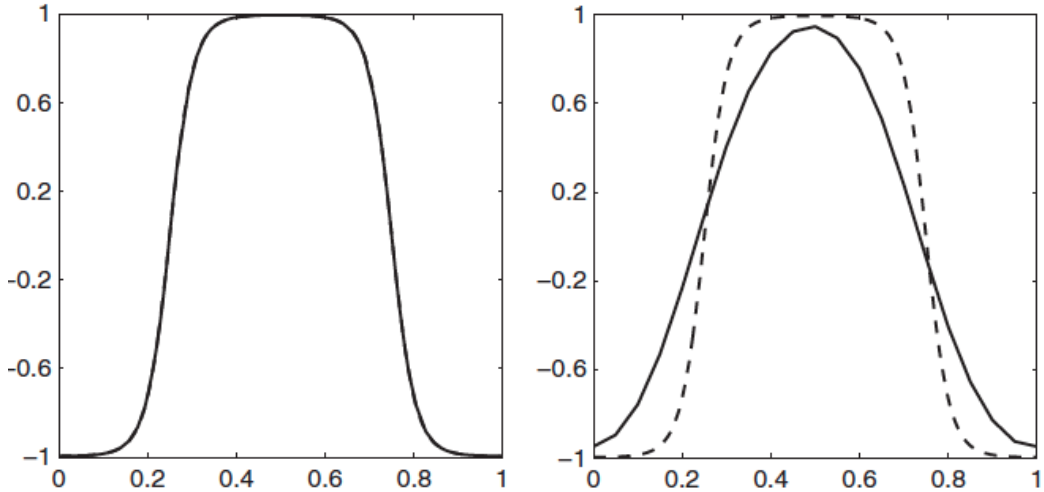

FIGURE 5.6: Advection of a smoothed rectangle by a PIC method (left) and a 5th order WENO scheme (right). From Edwards and Bridson (2012).

2D rotating tests

A qualitative 2D comparison of the dissipation produced by different schemes commonly used to solve hyperbolic equations was performed by Munz (1988). Munz compares the shapes of a cone and a cut-open cylinder before and after 6 rotations in a 2D plane. The best results are obtained with a TVD super-bee scheme (see figure 5.7). Although the cone and cylinder do not widen much after 6 turns, their shapes are significantly altered. Similarly to the test on the 1D rectangle, the cone suffers from a very strong clipping effect: its top part is markedly flattened and its maximum value is reduced by about 17%. Extrapolated to core conditions, such an effect would be problematic since it would tend to attenuate any thin compositional plume which would then lose part of its buoyancy. The cylinder also suffers from a (more moderate) clipping effect and its boundaries appear smoother. Other variations of the TVD scheme presented in this paper better preserve the shape of the cone better but produce strong dissipation of the cylinder. Using such schemes may thus erroneously widen the compositional plumes. Overall, the results from Munz (1988) suggest that it is difficult to find a scheme that preserves both the shape, maximal values and the discontinuities of the solution, which is potentially problematic for the description of very thin plumes.

Here, I perform identical tests (rotations of a cone and a cut-open cylinder) using the PIC method. A 2D square Cartesian grid of size 100 is constructed with the same number of nodes in each direction ($N_x = N_y = 100$). Like in Munz (1988), the cone and cylinder both have a radius of 15 grid nodes and a maximal value of 4. The velocity field is equal to:

$$\begin{cases} u_x = & u_0(y - y_0) \\ u_y = & u_0(x - x_0), \end{cases} \tag{5.3}$$

with $u_0 = 0.1$, $x_0 = 50$ and $y_0 = 75$. Following Munz (1988), the time step is set so that a full turn is performed in 628 time steps. 10^5 tracers are used in the simulation and are advected by a simple RK2 scheme using bilinear interpolation of the velocity. 2D and 3D illustrations of the shapes of the cone and cut-open cylinder can be visualized on figures 5.8 and 5.9, respectively. The results show an excellent conservation of the shape and maximum values; the profiles before and after 6 turns being quasi-undistinguishable. A significant alteration of the shapes is only notable after several tens of rotations.

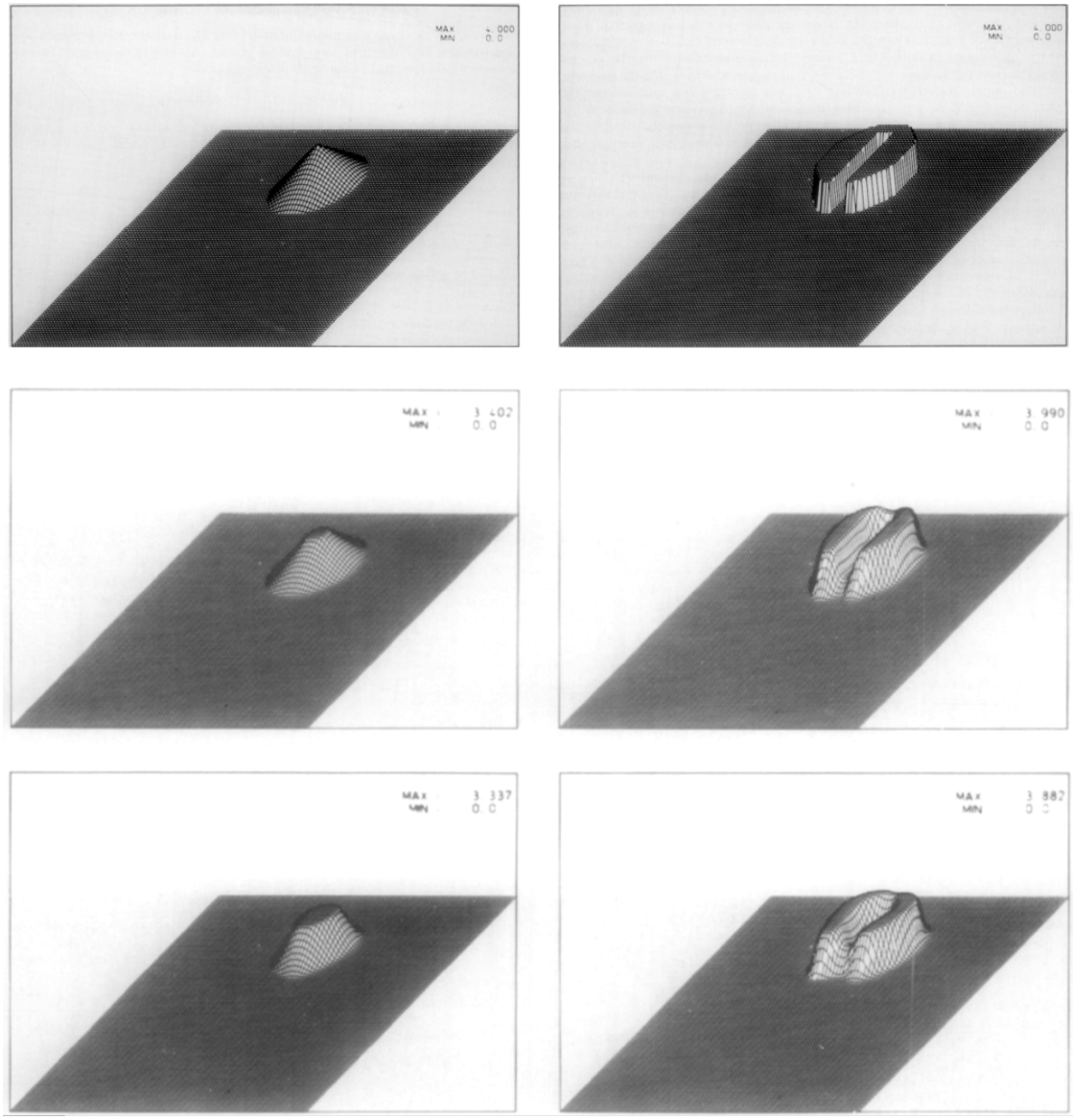

FIGURE 5.7: Figures taken from (Munz, 1988). Cone and cut-open rectangle 3D profiles before (top) and after one (middle) and six (bottom) rotations, respectively. The maximum and minimum values are also given.

In a second test (the results of which are shown on figure 5.10), the shape of a rectangle initially placed in the center of grid is compared before and after one full rotation with the 4th-order WENO scheme proposed by Levy et al. (2002) and the PIC method. The resolution is identical in both simulations (40 points are used along each direction). Although the WENO scheme shows a good discontinuity capturing ability, the edge of the rectangle is smeared on about 7-8 points, compared to only 2-3 points with the PIC method.

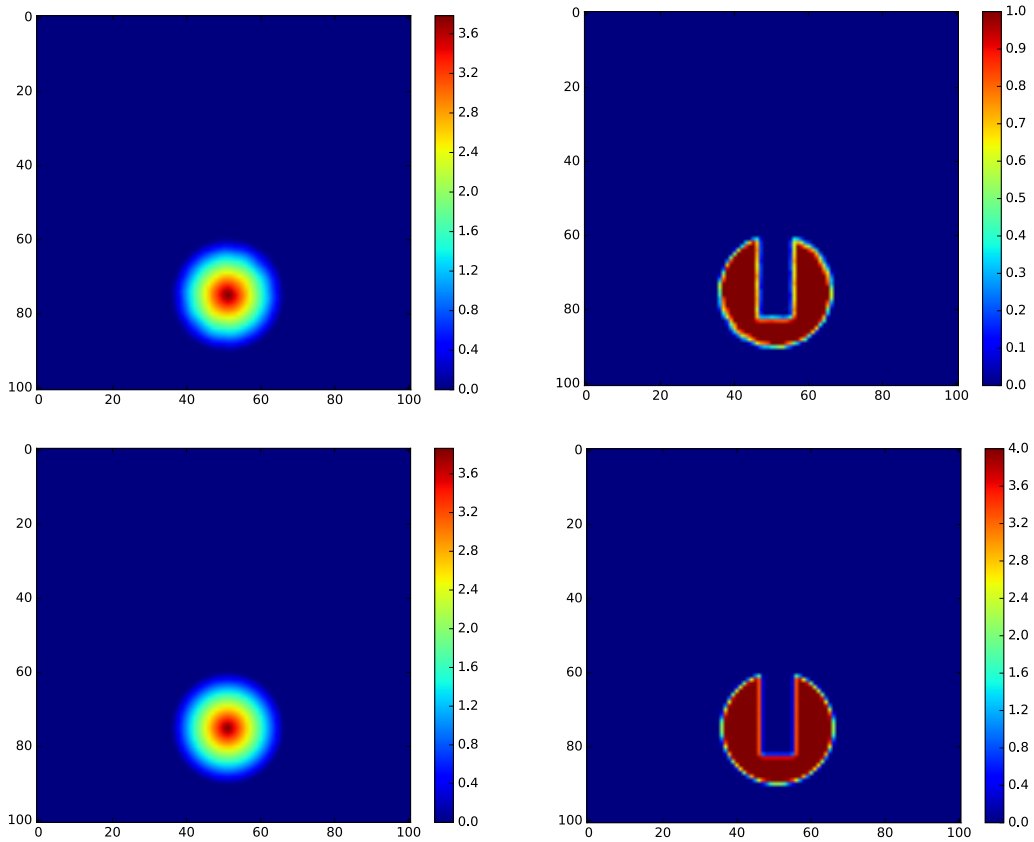

FIGURE 5.8: Top row: initial 2D cone and cut-open rectangle fields. Bottom: same figures after 6 rotations using the PIC method. The rotation is performed clockwise.

5.2.2 Discussion

The TVD schemes tested all produce some smearing of the initial shape. Also, as a consequence of the total variation that can only decrease, the maximum value of the signal is often altered. Applied to the advection of thin compositional plumes which are only a few grid points wide, such schemes would both widen the plumes and decrease their maximal value, resulting in an attenuation of the buoyancy. Although this "clipping" effect does not occur with the WENO schemes tested, the latter still produce a significant amount of diffusion which could be problematic over time. On the contrary, the PIC method generates almost no numerical diffusion in these tests (except the constant diffusion resulting from the tracers to grid interpolation).

Nevertheless, the tests performed in this section remain quite simplistic and the situation may be different for more complex flows. Although WENO schemes may at first smear discontinuities, they tend to create little dissipation afterwards and are quite robust at maintaining the shapes of the structures whereas the PIC method can suffer from erroneous advection of the particles causing further dissipation or distortion of compositional structures throughout the simulation. Note that this phenomenon can be strongly limited by using higher-order time and interpolation schemes. Edwards and Bridson (2012) showed that their high-order PIC Method (HOPIC) achieves better results on a 2D Taylor-Green vortex test than the 5th-order WENO scheme for the same resolution. For equivalent accuracy, HOPIC is also computationally cheaper. As a conclusion, I would tend to think that, in the infinite Lewis number, the PIC method is more adapted for the description of thin compositional filaments in problems of core convection, especially if higher-order interpolation and time schemes are used in critical regions.

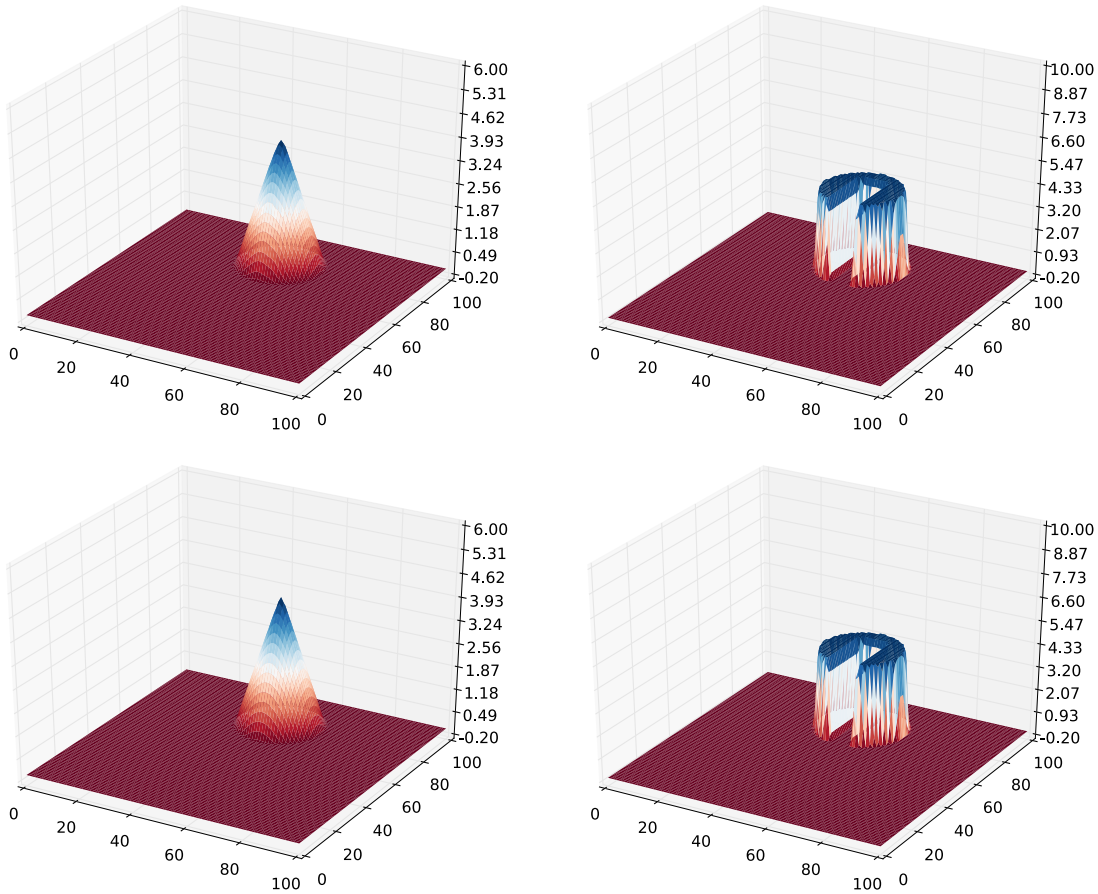

FIGURE 5.9: Top row: initial 3D cone and cut-open rectangle fields. Bottom: same figures after 6 rotations using the PIC method.

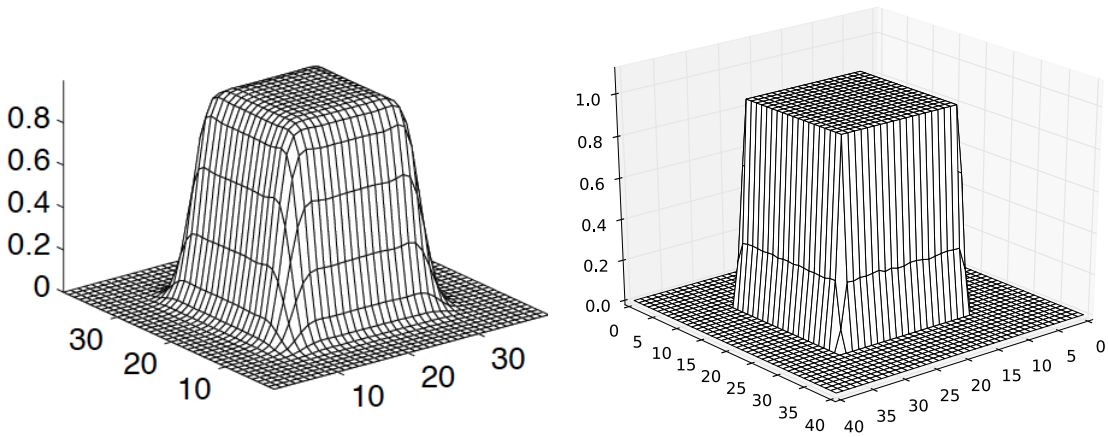

FIGURE 5.10: Comparison of the rotation of a rectangle by the 4th-order WENO scheme taken from Levy et al. (2002) (left figure) and the PIC method (right figure).

5.3 Other advantages of the PIC method

5.3.1 Relaxation of the Peclet number constraint

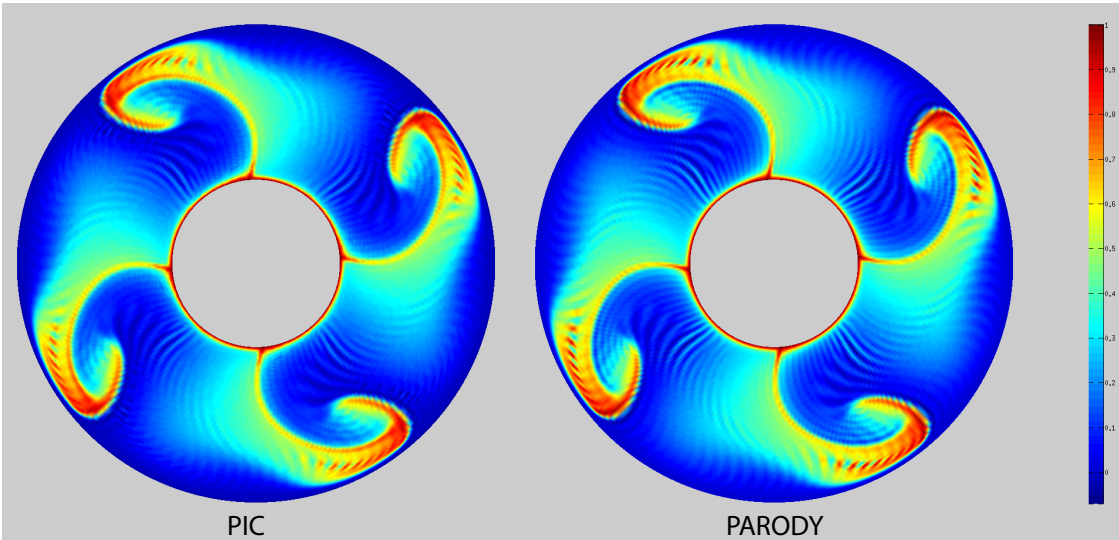

FIGURE 5.11: Example of numerical oscillations in the temperature field (equatorial section) with $P_T = 30$, $N_r = 130$, $\ell_{max} = 100$, $Ra_T = 1000$ with fixed temperature conditions and an initial 4-periodic perturbation. Results are shown for the PIC method (left) and the field approach (right).

The section 2.2.3 in chapter 2 already emphasized the difficulty associated with large but finite Lewis numbers. When employed to solve an advection-diffusion equation, many numerical methods are subject to a criterion on the grid Peclet number, defined by:

$$Pe = \frac{\max(U\Delta x)}{\kappa^T}, \tag{5.4}$$

where U is the fluid velocity at a given position in the grid and Δx the grid spacing at this position. The grid Peclet number must be below a certain value (usually close to unity but which depends a lot on the numerical method) to avoid unphysical oscillations. An example is given on figure 5.11, which shows the temperature field after the onset of convection for quite large thermal Prandtl and Rayleigh numbers and a very moderate resolution, implying a Peclet number well above unity. Removing the oscillations requires to increase the resolution and thus the computational cost. Using the PIC method to describe the temperature field provides slight benefits in that situation since the oscillations are modestly attenuated for the same resolution and disappear more rapidly when the resolution is increased compared to the field method. This implies that the critical grid Peclet number is higher for the PIC method. Such reductions of oscillations have already been reported with Eulerian-Lagrangian methods (Huang et al., 1992).

5.3.2 Monitoring of the trajectories of particles

The Lagrangian side of the PIC method also offers a large range of applications that are less easily accessible with Eulerian approaches. In experimental fluid dynamics, the "Particle Image Velocimetry" (PIV) method – based on the monitoring of particles injected in the fluid – has been used successfully to study several properties of complex and turbulent flows such as transport and mixing processes (Melling, 1997; Voth et al., 2002; Westerweel et al., 2013; Sommerer and Ott, 1993; Qureshi et al., 2007; Toschi and Bodenschatz, 2009). For example, measuring the relative

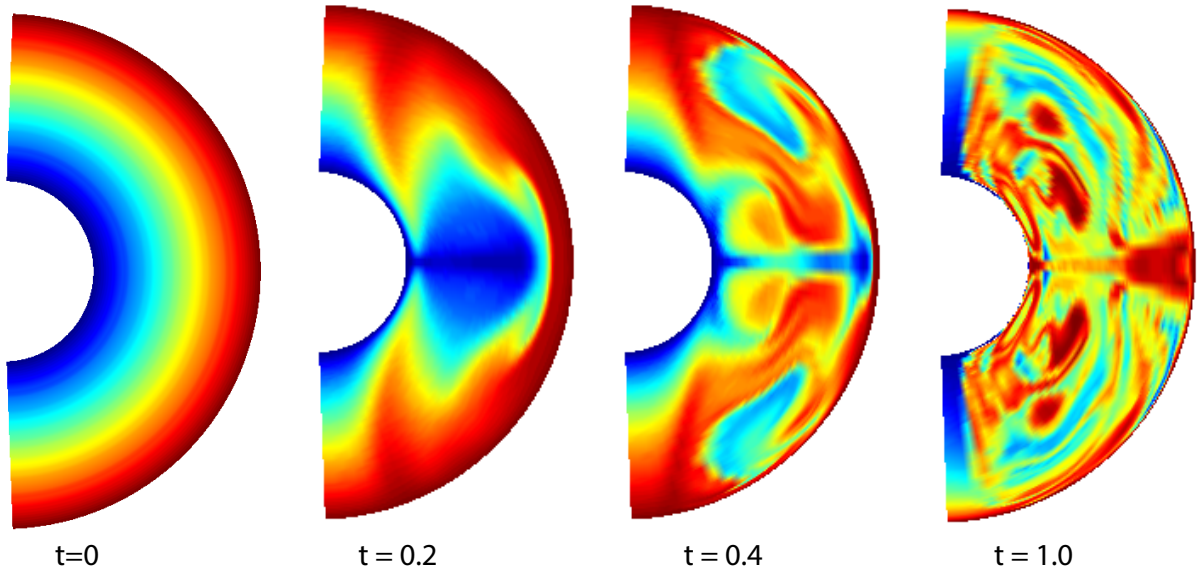

FIGURE 5.12: Visualization of the flow mixing with time. The tracers are initialized with a quantity equal to their radius and are then passively advected with the flow generated by a simple thermal convection case. The information conveyed by the tracers is then converted into a color scale.

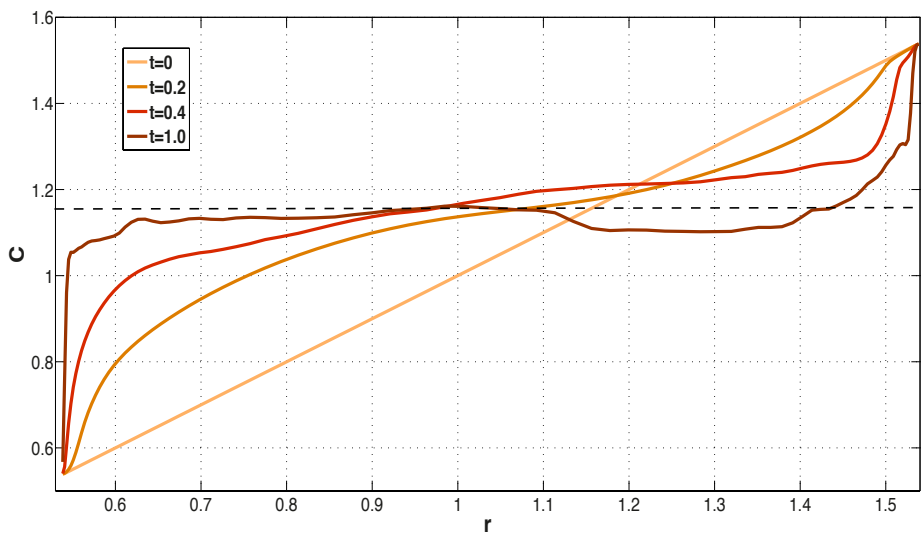

FIGURE 5.13: Mean value of the traced field as a function of radius in the simulation corresponding to figure 5.12.

distances between several particles in the flow allows for the determination of a Lyapunov spectrum as was done experimentally by Kleinfelter et al. (2005) and also numerically by Bec et al. (2006) who considered particles of finite size. Similar numerical experiments can be performed with the PIC method. Figures 5.12 and 5.13 illustrate the results of a simple simulation of thermal convection in which tracers are initialized with a value equal to their radius and passively advected. This gives a qualitative insight in some basic properties of the flow, but exploring mixing processes more quantitatively by calculating, for example, a Lyapunov exponent, requires a

sufficient accuracy in the trajectory of particles. A simple test is designed for this purpose in the paragraph below.

Advection by a synthetic convective-like velocity field

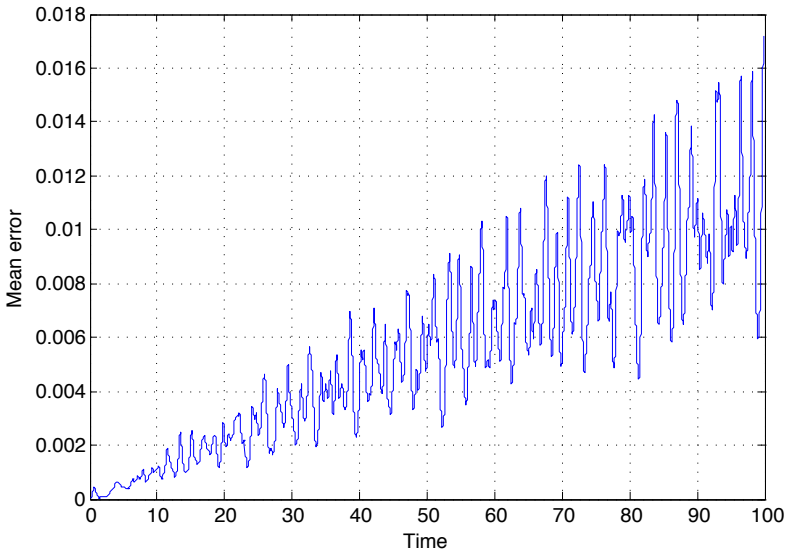

FIGURE 5.14: Mean error averaged on the 5 trajectories as a function of time.

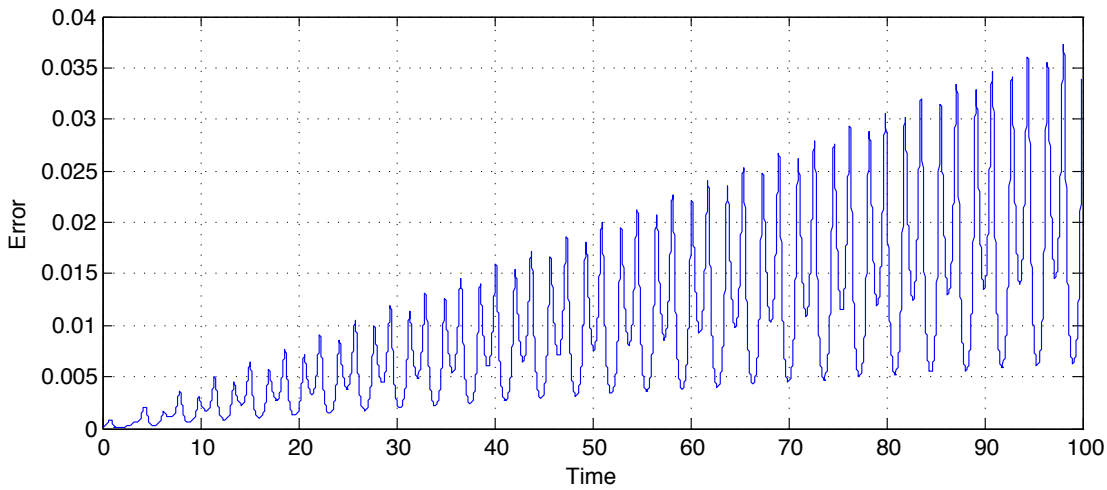

FIGURE 5.15: Distance to the theoretical trajectory (ϵ_{err}) as a function of time for a tracer starting at $(r = 1.73, \theta = 0)$.

To assess whether the trajectories of tracers can be trusted with a good accuracy, I performed the following test, the idea of which was suggested by Philippe Cardin when running together during a school in Les Houches, in 2014. A non-divergent time-independent velocity field mimicking an axisymmetric convective loop is imposed in the spherical shell:

$$\vec{\mathbf{u}}(r,\theta) = \sin(ar+b)\cos(\theta)\vec{\mathbf{e}}_{\mathbf{r}} - \left[\sin(ar+b) + \frac{ar}{2}\cos(ar+b)\right]\sin(\theta)\vec{\mathbf{e}}_{\theta}, \tag{5.5}$$

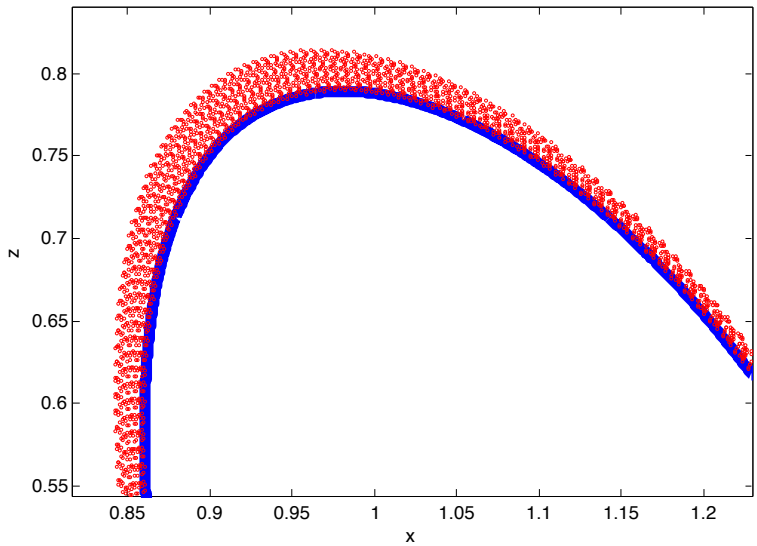

FIGURE 5.16: Trajectory of the tracer with time (red crosses). The theoretical trajectory is in blue.

where $a = \dfrac{\pi}{r_o - r_i}$ and $b = -\dfrac{r_i}{r_o - r_i}\pi$. The derivation of this expression as well as a representation of a few flow lines are given in appendix A. The advantage of this velocity field is that it is possible to calculate an analytic expression of the corresponding flow lines. Since tracers should follow the flow line passing through their initial position, having analytic knowledge of the flow lines allows to measure quantitatively the deviation of the tracers with respect to their theoretical trajectories.

For this test, the grid resolution was set to $N_r = 100$, $\ell_{max} = 44$, with regularly spaced nodes along the radius. A Runge-Kutta 4th order time scheme is used and combined with a trilinear interpolation of the velocity. The time step is $\Delta t = 10^{-3}$. 5 tracers are initially positioned at $\theta = \pi/2$ and at regularly spaced radii between r_i and $(r_i + r_o)/2$, so that various flow lines are studied. For each tracer, the deviation ϵ_{err} to the flow line is measured quantitatively by computing the distance between the tracer and its corresponding flow line. Figure A.1 in appendix A illustrates a tracer deviating from its corresponding theoretical trajectory as well as the definition of ϵ_{err}.

Figure 5.14 shows the error ϵ_{err} averaged over the 5 trajectories as a function of time. Figure 5.15 displays the same quantity but for only one tracer initially placed at $(r = r_i + 0.3, \theta = 0)$. The deviation to the theoretical trajectory is shown on figure 5.16 for the same tracer. As visible on figure 5.15, the deviation has a quasi-periodic behavior with alternating maxima and minima. It can be checked that the maxima coincide with the portion of the trajectory with the strongest curvature (see figure 5.16), betraying here again a centrifugal effect that causes the mean error to grow linearly with time (cf. figure 5.14).

In this test, only one time scheme and one interpolation method were considered. I also tested a triquadratic interpolation method but observed a surprisingly strong systematic deviation questioning the validity of its implementation. Note that this is not detrimental to the results presented later in this thesis since the triquadratic interpolation was not used. When the corresponding part of the code is debugged, this test could be used in the future to discriminate between different advection interpolation methods and time schemes for problems in which the trajectories of a few particles are monitored with time. More complex velocity fields could also be looked for mathematically to challenge the method further.

5.3.3 Visualisation

Since there are more particles than grid nodes, the ensemble of particles can be seen as the nodes of an unstructured finer grid which can be used advantageously to provide a more detailed picture of the thinnest structures. The inconvenient is that it requires the knowledge of the particles positions which, for billions of particles, represents an extremely heavy output file raising problems of storage, transfer and manipulation. A compromise consists in visualizing a smaller portion of the spherical shell such as the equatorial plane, which is usually very informative for rotating convection. In this case, only the tracers located close to the equatorial plane are required. The principle of the visualisation method comprises the following steps:

1. The particles located within a distance ϵ_{eq} from the equatorial plane are printed in an output file. The parameter ϵ_{eq} can be adjusted as desired.

2. Using a Matlab routine, the particles are projected on the equatorial plane.

3. The particles are either directly visualized through a scatter plot or, alternatively, their values are interpolated to a spherical grid that is finer than the initial grid.

An example is displayed on figure 5.17 which shows chemical plumes emerging from the destabilization of a bottom light chemical layer. In this run, the Ekman number is $E = 3 \times 10^{-4}$, the Rayleigh number $Ra_\xi = 5 \times 10^5$ and the chemical diffusivity is neglected. The onset of the convection shows very thin compositional plumes the physics of which is tackled in more details in the next chapter. Yet, a simple observation of the pictures plotted on figure 5.17 already inspires at least three important remarks:

1. The bottom image emphasizes the importance of the initial distribution which, in this case, is regular. Homogeneous initial spreading of the particles causes artificial alignment in regions of shear and small-scales inhomogeneities in the distribution. Though the latter are not very detrimental, they should be avoided as much as possible.

2. Even though the middle picture seems better resolved when using the tracers, it should be recalled that the buoyancy is not computed on the particles but on grid nodes, so that only grid-scale dynamics is properly described. The "tracers scale" structures should thus be interpreted cautiously. The top and middle pictures point out that resolving accurately the plumes dynamics requires extremely high resolutions, probably higher than those presented on figure 5.17. However, for a study that focuses on more global properties (for example, that of a stratified layer), then the finest details of the plumes dynamics are probably of secondary importance.

3. The bottom picture shows small yet not negligible local depletions or accumulations of particles caused by small errors in the advection. This suggests that higher order interpolation order and advection schemes should be preferred when the trajectories of a small number of particles is monitored to study mixing processes for example.

Future improvements in the visualisation of particles may be achieved by producing adequately structured output files compatible with more efficient visualisation tools such as Paraview.

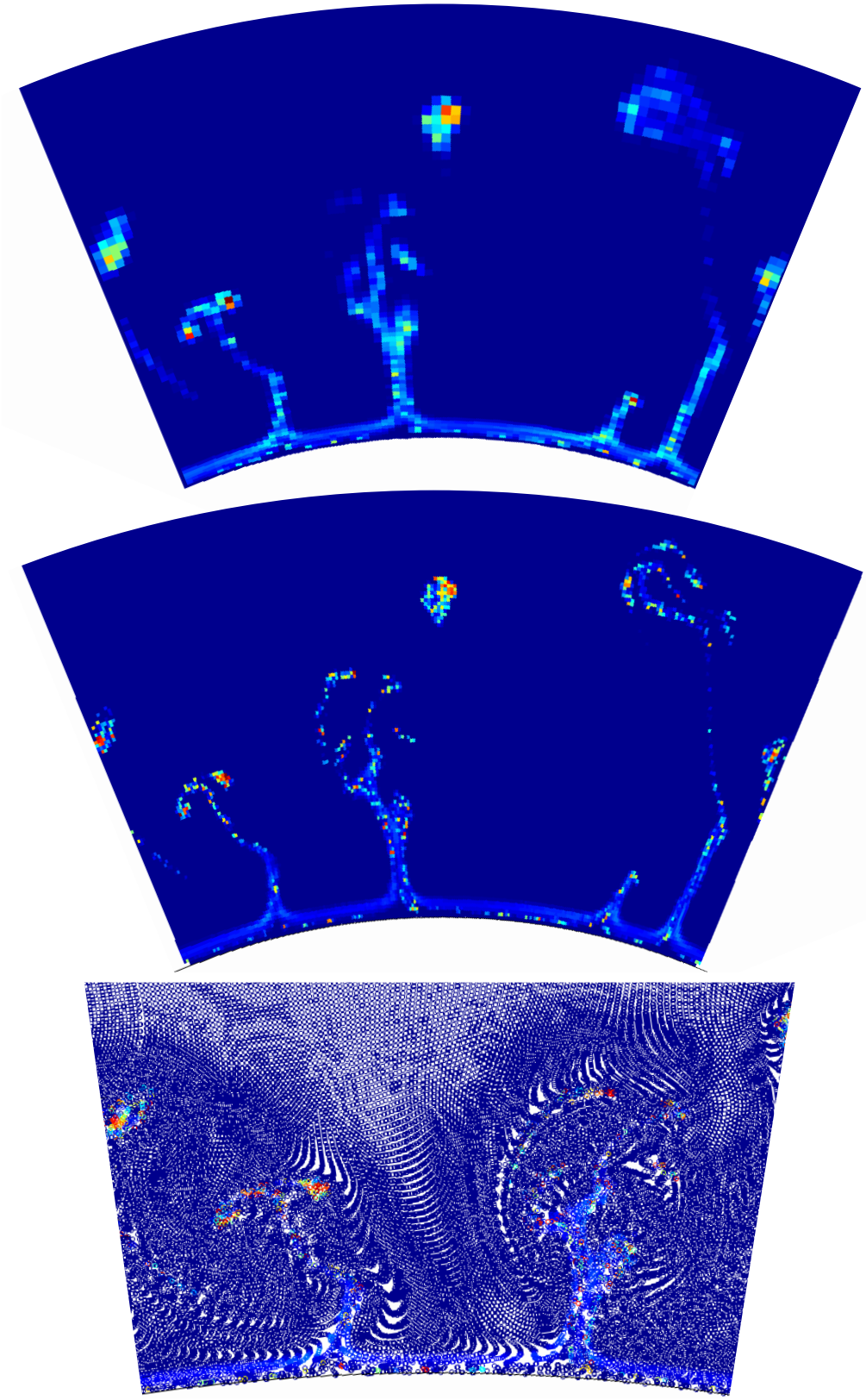

FIGURE 5.17: Chemical plumes (with $\kappa^{\xi} = 0$) visualized on a portion of the grid corresponding to resolution $(N_r \sim 70, N_\phi = 80)$ (top), using the tracers method and interpolating on a grid $(N_r \sim 300, N_\phi = 240)$ (middle) and direct visualization of the particles on a restricted area (bottom).

5.4 Conclusions

The new code PARODY-PIC incorporating a PIC method has been successfully validated in spherical shell geometry on two different benchmarks, but is still to be tested in full sphere geometry. This will be achieved in a near future using the benchmark of Marti et al. (2014) to which the code PARODY has already contributed. Estimations of the adequate number of tracers based on the results of the tested benchmarks shows that very high numbers of particles must be used when the Ekman number is decreased and/or the aspect ratio tends to 1. Determining the optimal advection schemes, interpolation methods and number of tracers for a given simulation still remains a delicate question however. It will probably gradually clarify with experience on more numerous simulations.

Second, comparison on simple tests with state-of-the-art Eulerian schemes (TVD and WENO) are clearly in favor of the PIC method in terms of ability to minimize numerical dissipation. The difference could be less obvious however for more complex flows and would require more elaborate tests, ideally in spherical geometry, which could be laborious. But one must not forget that the PIC method also has other advantages over Eulerian approaches, in particular the ability to follow the trajectories of particles with time which can bring a new interesting insight into the dynamics of planetary liquid flows. I therefore conclude that, in this context, the PIC method is, if not the best, at least a relevant and promising approach.

To finish, it is worth mentioning that, whatever the adopted numerical scheme, an accurate description of the dynamics of compositional structures in the infinite Prandtl limit requires very high resolutions, involving typically hundreds of points in the radial direction and spectral resolution up to degree 400 or higher for Ekman numbers lower than 10^{-4}. It seems that the limitations for the study of thermochemical convection in the infinite Lewis number limit ($\kappa^{\xi} = 0$) comes not only from the PIC part, but also from the spectral transforms which are equally expensive (if not more) at such high degrees. The resolution might however be relaxed if the focus is on larger-scale properties, provided the latter are not controlled by the details of the dynamics of chemical plumes.

Chapter 6

Non-magnetic rotating compositional convection in the diffusivity-free limit

As stated earlier, convection in the Earth's outer core is caused by a combination of thermal and chemical effects with a high diffusivity ratio ($Le = \kappa^T/\kappa^\xi \sim 1000$). Chemical convection is driven by the release of light elements likely emanating from a "mushy zone" at the ICB, possibly also by the extraction of MgO or SiO_2 from the mantle (O'Rourke and Stevenson, 2016; Hirose et al., 2017) and would contribute up to 80% of the total buoyancy flux in the core (Fearn and Loper, 1981). The precise nature of compositional structures emerging from the ICB has been the object of several experimental investigations and theoretical conjectures. Experiments conducted on model systems involving the freezing of ammonium chloride in solution (Chen and Chen, 1991) showed that the gravitational instability manifests itself through eruptions of buoyant fluid in the form of plumes emerging through *"chimneys"* that are spontaneously created in the mushy zone, the lighter fluid being drawn horizontally into the chimneys from the surrounding mush. A few years later, Claßen et al. (1999) observed that, in a rotating cylindrical tank, instabilities cause the plumes to break-up, forming rising chemical "blobs". Based on the results of such experiments and on theoretical arguments, several authors (Gubbins et al., 1982; Braginsky, 1994; Bergman and Fearn, 1994; Moffatt and Loper, 1994; Loper, 2007) also evoked the existence of chemical "plumes" and "blobs" emitted at the ICB and whose behavior would play a role in the turbulence of the core, convective dynamics and dynamo action in various ways. For instance, Moffatt and Loper (1994) predicted a helical trajectory for the blobs assuming a magnetostrophic balance and their eventual accumulation below the CMB where they would form a stably stratified layer.

Such compositional structures have not yet been observed in numerical simulations, essentially because small-scales are quickly dissipated by a too large diffusivity in these calculations. So far, the few authors that have considered unequal thermal and chemical diffusivities (Breuer et al., 2010; Manglik et al., 2010; Trümper et al., 2012; Takahashi, 2014) showed that using even a moderate diffusivity ratio already produces differences in the morphology of the composition, velocity and magnetic fields compared with a codensity case, but due to the very moderate Lewis numbers adopted ($Le = 10$) in these simulations, the features of the chemical field remain quite similar to the thermal field despite having smaller scales than the latter. More radical changes are however expected in the infinite Lewis number limit since the compositional structures are expected to be much smaller, potentially allowing for the formation of thin "plumes" and "blobs". Thermochemical convection in the infinite Lewis number limit is thus still to be explored numerically in a rotating spherical shell and this constitutes an interesting first application of the PIC method newly developed in PARODY.

In this chapter, the physics of compositional convection at infinite chemical Prandtl number P_ξ (*i.e.* $\kappa^\xi = 0$) is explored using the PIC method implemented in the code PARODY. In a first step, the double-diffusive benchmark proposed by Breuer et al. (2010) is extended to the infinite

Lewis number limit to provide a qualitative comparison with thermochemical convection at low Lewis number. In a second section, the characteristics of pure compositional convection are studied more in depth without the thermal effects. The results of several simulations are presented, compared with experimental results and discussed. Conclusions are drawn concerning the application of these results to the Earth's case. For simplicity, the Lorentz force is not considered in this chapter; the non-magnetic case having already a very rich and complex physics.

6.1 Qualitative differences with thermochemical convection at low Lewis number

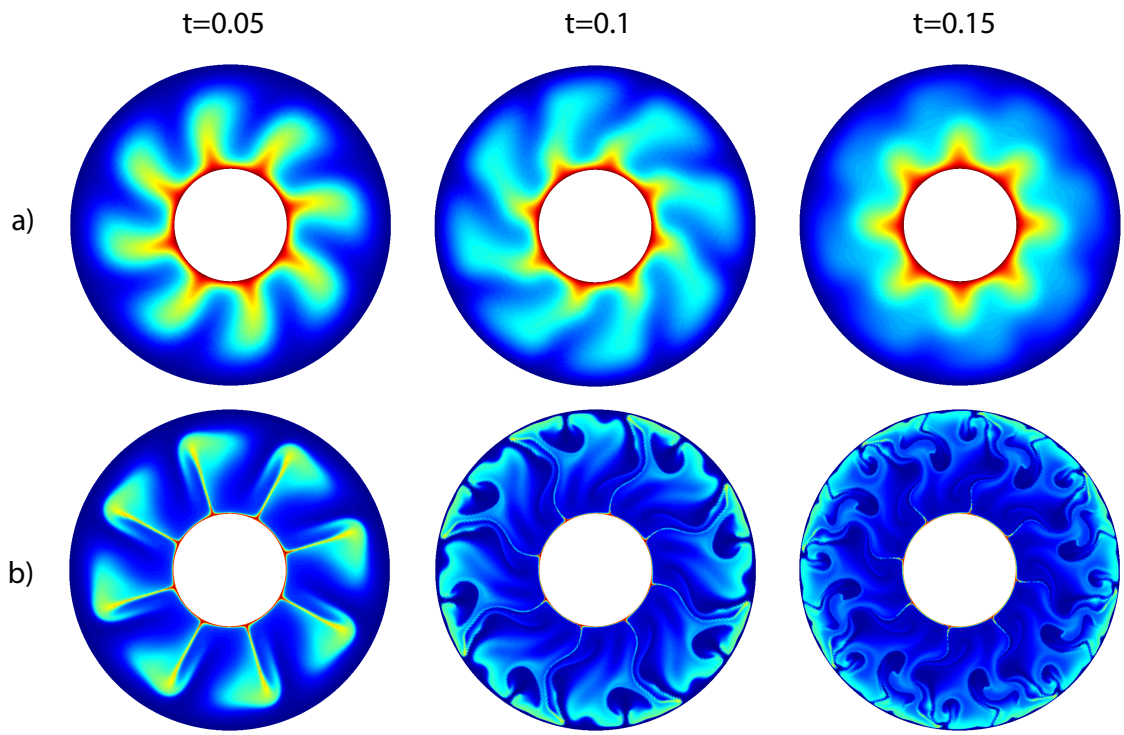

FIGURE 6.1: Snapshots of the compositional field in the equatorial plane during the onset of convection for $Le = 10$ (a), $Le = \infty$ (b). In both cases $\delta = 0.8$. Colorbars slightly differ between cases a) and b).

In order to observe qualitatively the effects of neglecting the chemical diffusivity, the benchmark proposed by Breuer et al. (2010) is extended to the limit of infinite Lewis number. In a first simulation, the ratio $\delta = Ra_T/Ra$ of thermal to total Rayleigh numbers introduced by Breuer et al. (2010) is unchanged ($\delta = 0.8$). Identical reference states are considered. The Ekman and Rayleigh numbers are unchanged but the compositional Prandtl number is set to infinity by totally neglecting the diffusive term in equation (2.14). Fixed temperature conditions are adopted at the boundaries, however, the compositional buoyancy flux injected by diffusion in the shell shrinks to zero if fixed composition boundary conditions are adopted in the infinite Lewis number limit which means there is no driver for compositional convection. In order to make a comparison with the benchmark, a compositional flow corresponding to the compositional Nusselt number obtained in the benchmark at statistically steady-state is imposed at both boundaries. The equivalent mass is injected into the shell by introducing a source term on the tracers located within a distance $h = 0.04$ from each boundary, following the method explained in section 2.3. The adopted spectral resolution is $\ell_{max} = 150$ and the time step $\Delta t = 10^{-4}$.

Snapshots in the equatorial plane of the convection onset and statistically steady state are plotted on figures 6.1 and 6.2, respectively, together with radial maps of the radial velocity (see figure 6.2, left column). In the case $Le = 10$, differences are already observable between the thermal and compositional field, the latter having thinner structures with large plumes rising up to the middle of the shell (see figures 6.1a and 6.2a). In the infinite Lewis number limit, the compositional field becomes markedly different throughout the simulation. The onset of convection

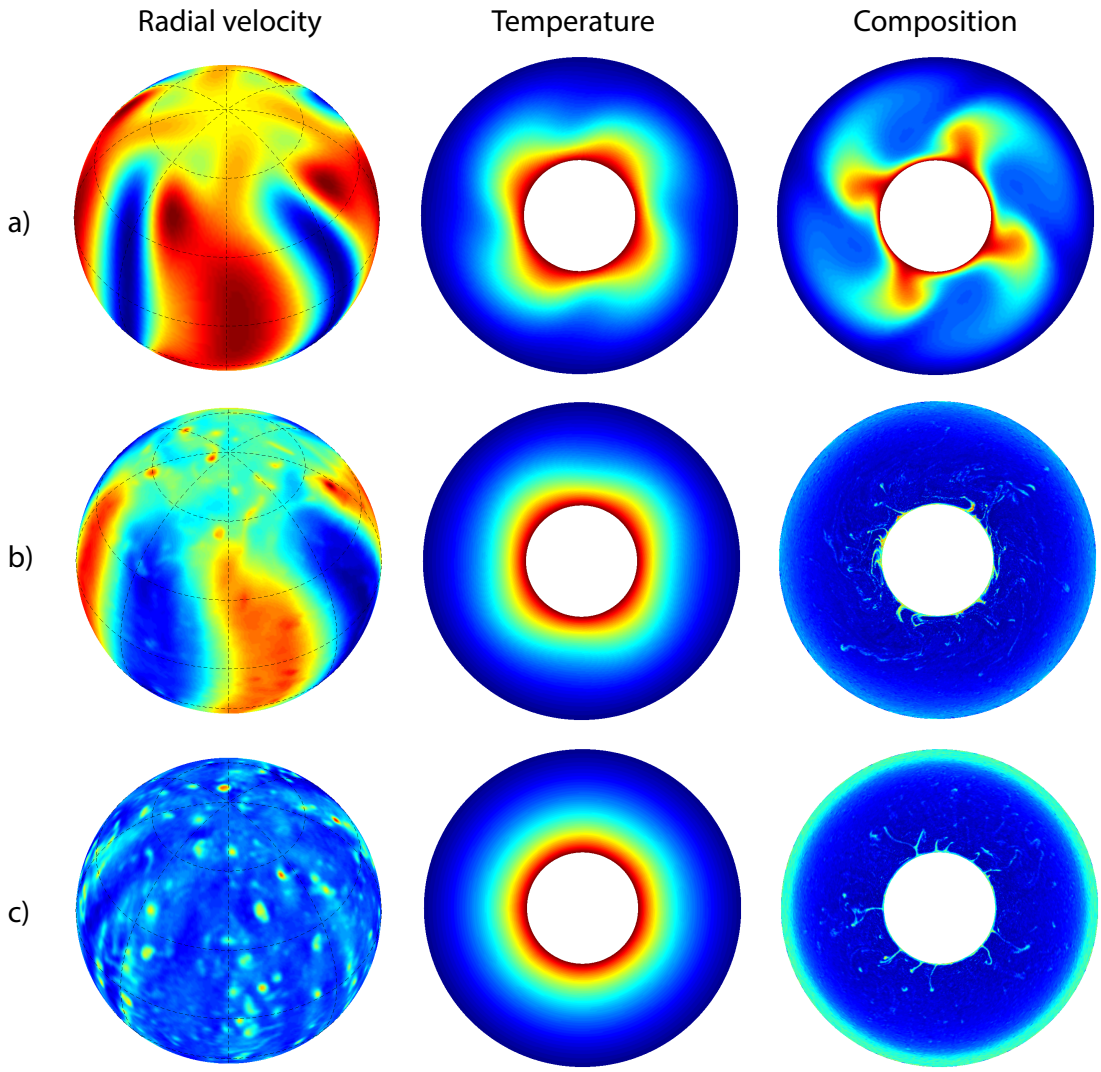

FIGURE 6.2: Snapshots of the radial flow field on a spherical surface at mid-depth in the shell (left column), equatorial sections of temperature (middle) and composition (right column) at time $t = 2.1$. (a): $Le = 10$, $\delta = 0.8$; (b): $Le = \infty$, $\delta = 0.8$; (c): $Le = \infty$, $\delta = 0.2$.

shows much more complex structures, which tend to overturn to create a globally stable compositional radial profile except near the boundary layers (cf. fig 6.1 at $t = 0.15$). After the convection onset, the 4-fold symmetry of the initial perturbation quickly disappears and the compositional field extends in the form of very thin "filaments" growing from the bottom boundary (see figure 6.2b and c).

In order to make sure that these structures were sufficiently resolved, several simulations were run with resolutions ranging from $(N_r = 120, \ell_{max} = 85)$ to $(N_r = 384, \ell_{max} = 300)$ but no major differences were observed in the kinetic energy and in the shapes and sizes of the filaments, although the latter are clearly better resolved at finer resolutions (more than 3 grid nodes describe the width of the filament). In all cases, the kinetic energy spectrum drops by at least a factor 50 between its peak and its tail (see figure 6.3), a classical criterion adopted to ensure adequate resolution. However, the energy spectrum corresponding to $Le = +\infty$ contains much more energy in the small scales than the $Le = 10$ case, which drops more abruptly. Moreover, contrary to the solution of the benchmark in which the kinetic energy initially oscillates before

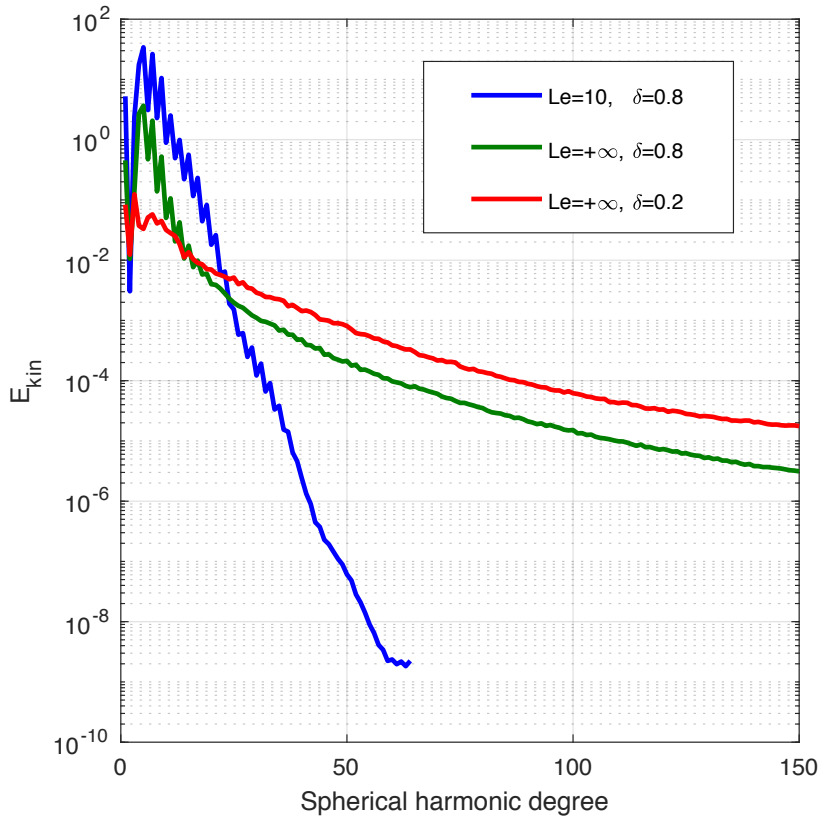

FIGURE 6.3: Kinetic energy spectra at $t = 2.9$ for the benchmark case proposed by Breuer et al. (2010) ($\delta = 0.8$, $Le = 10$) and for its extension to the infinite Lewis number limit with compositionally dominated convection ($\delta = 0.2$, $Le = +\infty$).

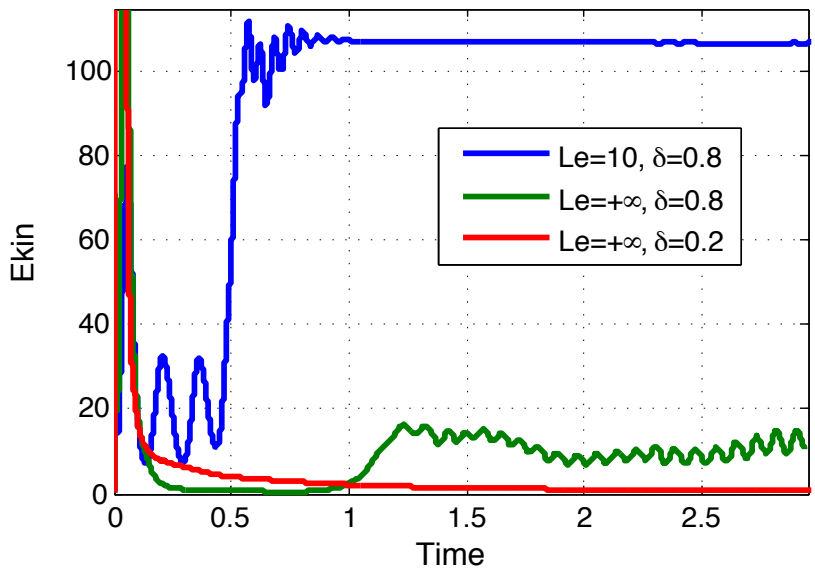

FIGURE 6.4: Time variation (in viscous time) of the total kinetic energy for three different runs. The blue curve ($Le = 10, \delta = 0.8$) corresponds to the benchmark of Breuer et al. (2010).

switching to a steady state, the kinetic energy in the infinite Lewis number case shows an initial peak before stabilizing to a stationary state characterized by small amplitude oscillations around a value about one order of magnitude lower than in the benchmark case (fig. 6.4). This lower kinetic energy can be interpreted as being a consequence of the absence of compositional diffusion which tends to confine the compositional buoyancy sources into tiny volumes that concentrate near the boundary layers and in the filamentary structures. It may also be the result of a stronger viscous dissipation due to the small scales of the field. Furthermore, since the thermal Rayleigh number is largely dominant in this case, the velocity field has a global 4-fold symmetry similar to the $Le = 10$ case (fig. 6.2a and 6.2b), although its magnitude is about 3 times smaller and it is locally affected by the structures of the compositional field.

In order to determine whether the velocity field is more affected when the compositional Rayleigh number dominates, a second simulation was run with $\delta = 0.2$. Figure 6.2c displays snapshots of the radial velocity, temperature and compositional fields. The corresponding time evolution of the kinetic energy was also added to figure 6.4. In this case, the kinetic energy stabilizes at a very low value. The 4-fold symmetry in the velocity field is completely destroyed and the radial section on figure 6.2c only shows isolated patches corresponding to the intersections with the compositional filaments. In the compositional field, a residual stratification remains at the top of the shell after the initial overturn of the compositional field. These results point out that neglecting the compositional diffusivity may lead to radically different flow structures and compositional transport. The latter are studied in more details in the context of pure chemical convection in the next section.

6.2 Study of pure compositional convection

In this section, the properties of pure compositional convection are studied more in depth. The Lorentz force is still not considered and thermal effects are neglected for simplicity, so as to concentrate on compositional structures and dynamics alone. In all simulations, light elements are injected in the shell at the bottom boundary, with initial condition $\xi = 0$ everywhere. A volumetric sink term in the whole spherical shell compensates for the injected flux. In one simulation, the sink term is replaced by a chemical flux at the top boundary equal to the bottom flux. The aspect ratio is that of the Earth's core ($r_i/r_o = 0.35$).

6.2.1 Convection onset

When light elements are injected in a thin layer above the inner boundary, they first accumulate during a short period until the layer destabilizes, forming thin ascending filamentary plumes, as visible on figure 6.5. Interestingly, this "comb" structure bears some similarity with previous laboratory experiments at lower Ekman number by Cardin and Olson (1992), the results of which are shown on figure 6.6. Like in the numerical simulation corresponding to figure 6.5, thin ascending chemical filaments are visible in the equatorial plane of the rotating sphere in the experiment of Cardin and Olson (see figure 6.6b), although the number of plumes and their width seem to differ from the simulation, probably as a consequence of the lower Ekman number. In the simulation, the plumes are initially isolated but as inertial waves gradually propagate across the shell, they progressively acquire some degree of invariance along the rotation axis, in consequence of the Proudman-Taylor constraint (see figure 6.7).

In order to measure more quantitatively how the width of the compositional plumes varies with the Ekman number, 5 simulations were performed at Ekman numbers ranging from 10^{-3}

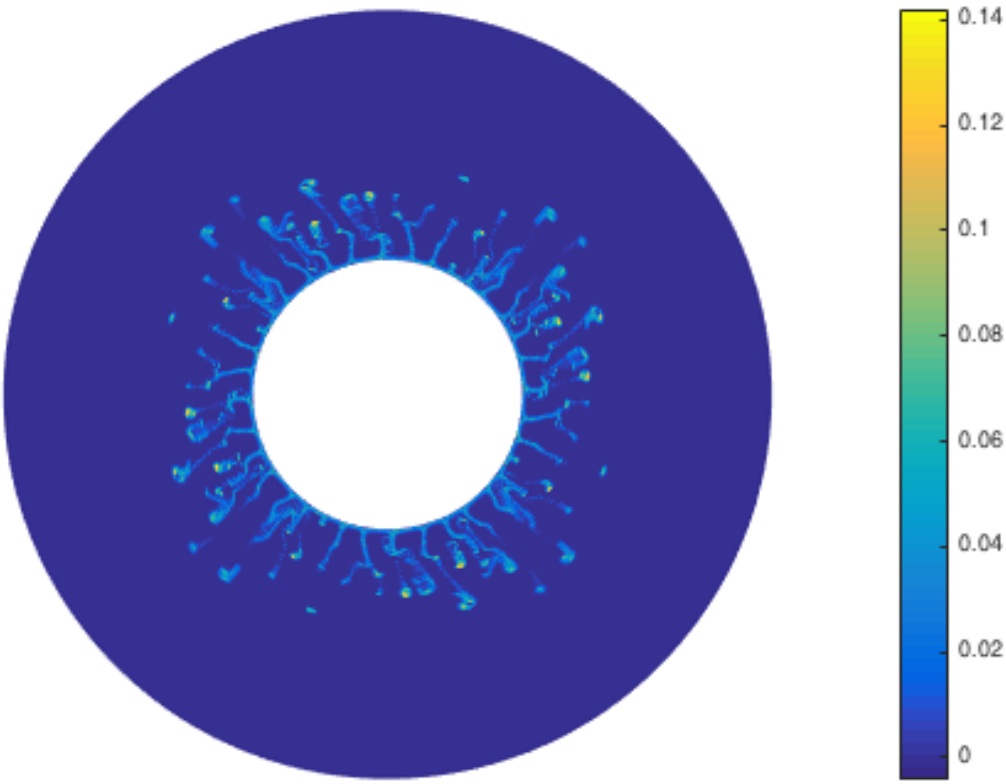

FIGURE 6.5: Equatorial section of the compositional field during the onset of convection, for $E = 10^{-4}$, $Ra = 10^{7}$. The initial periodicity arises as a consequence of the homogeneous initial particles distribution and is then quickly lost in the simulation.

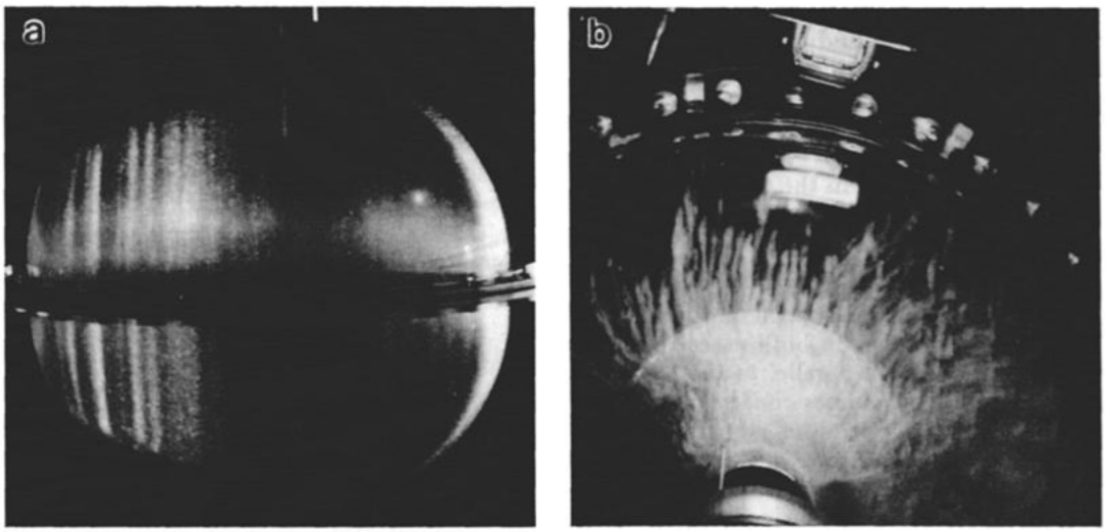

FIGURE 6.6: Two different views of an experiment of rotating pure compositional convection with centrifugal buoyancy and Ekman number $E = 4 \times 10^{-6}$. Left: side view of the spherical shell. Right: polar view to visualize the equatorial plane. Taken from Cardin and Olson (1992).

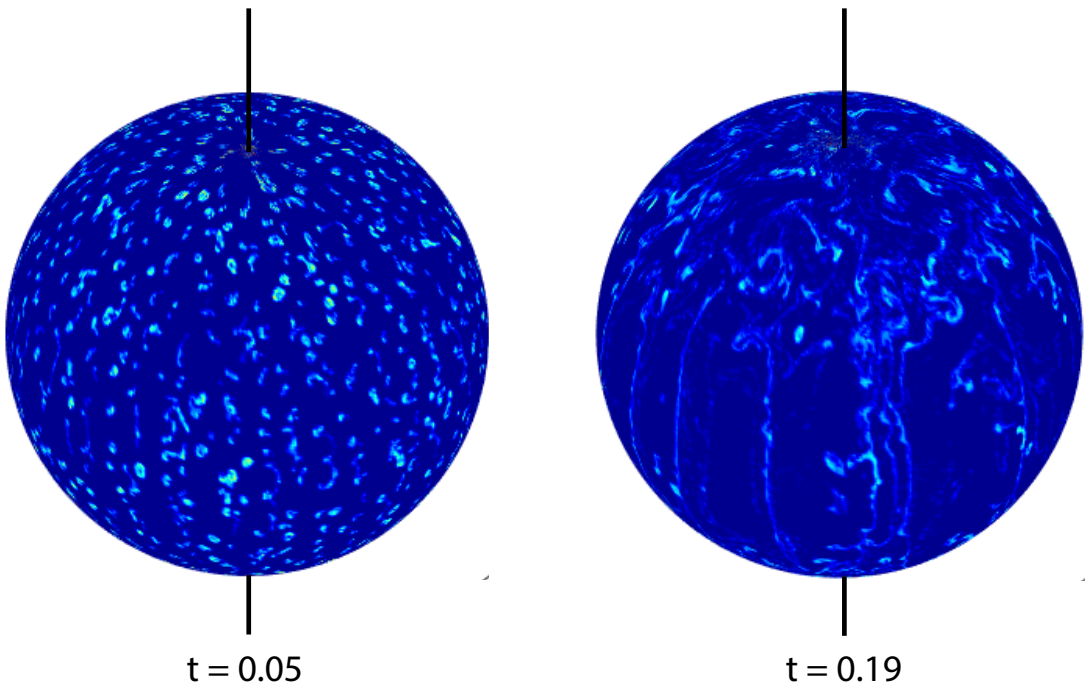

FIGURE 6.7: Spherical maps of the composition at radius $r = 1.13r_i$ and times $t = 0.05$ (left) and $t = 0.19$ (right), in viscous time. The polar axis is indicated by a black line. Parameters are: $E = 10^{-4}$, $Ra = 5 \times 10^5$.

to 10^{-5}. For all simulations, the Rayleigh number is fixed to 10^7 and the compositional diffusivity is neglected ($P_\xi = +\infty$). The initial compositional field equals zero everywhere. Chemical boundary conditions consist of a fixed flux (equal to zero) at the top and injection of light elements within a layer located close to the inner boundary, following the method explained in section 3.6. Since the focus is on the onset of convection, no volumetric sink term is introduced in the shell. Each simulation is run on only a few thousands time steps until the light bottom layer destabilizes to form the first filaments. These first plumes are easier to distinguish and detect on the uniform initial compositional background (equal to zero). The grid resolution and number of tracers are gradually increased when decreasing the Ekman number. The case corresponding to $E = 10^{-5}$ being very expensive (requiring spectral resolution up to degree 400 and about 10^{10} particles), an 8-fold symmetry was enforced in the solution in order to save computational time. Since the plumes are very isolated structures, this should not have much impact on their size and individual dynamics, at least during the onset of convection.

In all simulations, once the first plumes have sufficiently ascended vertically, their average width is measured on two different grids: the spherical grid and a grid twice finer on which the values of the particles are interpolated following the method proposed in section 5.3.3. A final estimation is then computed by averaging both values. The results for different Ekman numbers are plotted on figure 6.8. A linear fit can be performed in the log-log diagram proving that the (dimensionless) width δ_f of the filaments follows a scaling law of the form:

$$\delta_f = 0.205E^{0.328}, \tag{6.1}$$

a trend that is very close to a $1/3$ power law for the Ekman number. This indicates that δ_f is proportional to viscous structures (King et al., 2013). In the infinite chemical Prandtl number, the width of the plumes is therefore controlled by viscosity, which is not surprising. Indeed, for

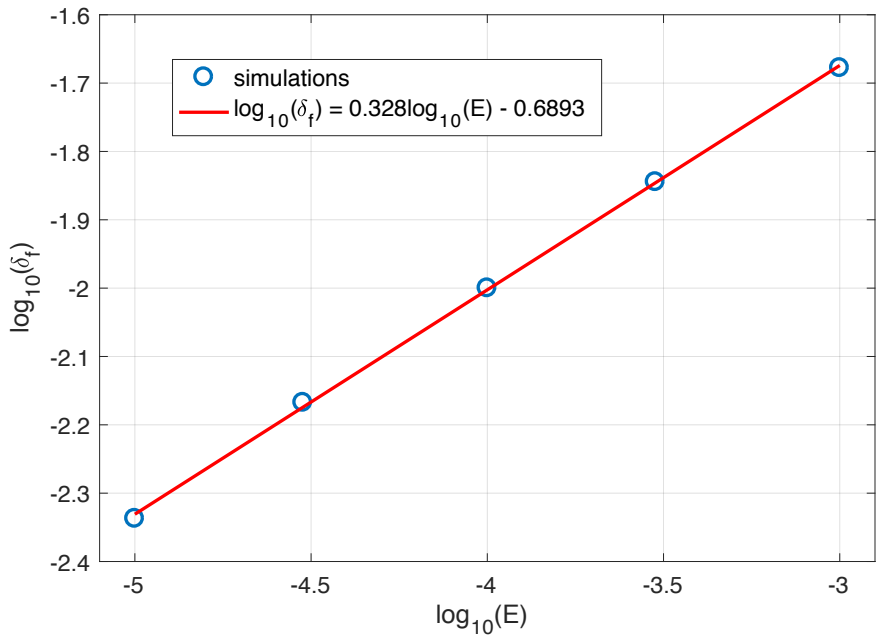

FIGURE 6.8: Mean thickness of the chemical plumes for different Ekman numbers. A linear regression is drawn in red.

diffusive fields (such as temperature), thin plumes are rapidly smoothed by diffusion and cannot persist for a long time. At $P_T = 1$, the thermal field is thus dominated by large-scale structures the size of which is controlled by a balance between advection and diffusion. Reducing the diffusivity then allows thinner plumes to exist, which is the reason why the compositional field has smaller scales than the thermal field in the double-diffusive benchmark of Breuer et al. (2010) with a Lewis number equal to 10 (see figure 6.2). However, when the chemical diffusivity drops below a certain value, viscosity replaces diffusion in limiting the size of the filaments: too thin plumes create locally large velocity gradients and are therefore damped by viscous forces before being dissipated by diffusion.

Extrapolation of the scaling law (6.1) to the Earth's outer core with Ekman number $E = 10^{-15}$ would give compositional filaments that are about 4 m thick. In reality, if the limit of infinite compositional Prandtl number is not completely relevant for the Earth's core and diffusivity is not negligible, compositional plumes could actually be larger. In addition, plumes may have a more turbulent dynamics controlled by the Rayleigh number and could entrain part of the ambient fluid, thereby increasing their size. This predicted plumes thickness should thus rather be seen as a lower bound. An interesting parameter that plays a role in some theoretical models (Moffatt and Loper, 1994) is then the fraction f_s of the surface occupied by the plumes at a fixed radius, which depends on the number of plumes and is poorly constrained. In the simulations, it seems that the number of plumes increases when the Rayleigh number is increased or the Ekman number is decreased. In the runs presented in this chapter, f_s typically falls in the range 0.001 – 0.1, which is coherent with previous theoretical estimations. However, in simulations, plumes are created by the destabilization of an initially light layer. Extrapolation to the Earth's case may therefore not be relevant at all since the number of plumes is probably rather controlled by the number of chimneys in the mushy zone. This interesting question thus deserves more investigations.

6.2.2 Blob instability

It can be observed on figures 6.5 and 6.9 that, after rising almost vertically up to some height, the chemical plumes do not keep their initial filamentary shape and break-up to form chemical "blobs" of buoyant fluid. These features bear interesting similarity with the laboratory experiment conducted by Claßen et al. (1999) in a vertical rotating cylinder filled with a NH_4Cl-H_2O solution. In this experiment, the cylindrical tank is cooled from below, so that a mushy layer forms at the bottom boundary and chemical plumes emanate from the mush chimneys. The authors describe that the chemical plumes initially ascend vertically on a short distance before being affected by an inertial instability (Eltayeb and Loper, 1997), giving the plumes some horizontal component which is then deflected azimuthally by the Coriolis force. Rising plumes therefore tend to be deflected in a sub-horizontal plane. When the plane angle is sufficient, the plumes become susceptible to a Rayleigh-Taylor instability with the denser surrounding fluid, which results in the formation of "blobs" that detach from the initial plumes. This phenomenon appears clearly in the experimental results shown on figure 6.10 but is also visible (though more tenuous) in the experiment of Cardin and Olson (see figure 6.6).

Although the rotation axis, gravity and cylinder axis are parallel in the experiment of Claßen et al. (1999), plumes seem to be affected by similar instabilities on the equatorial plane in the numerical simulations. This is well visible on figures 6.5 and 6.9, where plumes are deflected horizontally before breaking-up into buoyant blobs that rise vertically, entraining part of the ambiant fluid. In this configuration, the rotation axis is perpendicular to the equatorial plane, so that the Coriolis force systematically deviates any vertical motion horizontally and therefore helps bending the chemical plumes. The presence of these instabilities also suggests that a sufficiently high resolution should be used to resolve correctly the dynamics of plumes. In all the simulations shown in this work, the spectral resolution is at least $\ell_{max} = 200$ and may be increased further when the Ekman layer (and therefore the size of the plumes) decreases.

On the other hand, it should be noted that, even though the number of plumes may not be controlled by the same processes in the Earth's outer core and in the simulations, the latter produce chemical plumes whose behavior is qualitatively coherent with the results of experiments in which chemical convection emanates from a mushy zone. The approach proposed in section 2.3 consisting in injecting light elements in the shell by introducing a local source term therefore finds a better justification here.

6.2.3 Evolution to a statistically steady-state

Formation of a chemically stratified layer below the top boundary

The evolution of the convective regime after the onset of convection depends on the boundary conditions. If light elements injected at the bottom are removed at the top boundary by an identical total chemical flow, with no volumetric source/sink term in the shell, the simulation evolves to a state that resembles that shown on figure 6.9 and is characterized by numerous plumes ascending from the bottom boundary, eventually evolving into more diffuse blobs with only a few occasional downwellings from the top boundary. Indeed, the flux per unit surface is smaller at the top which makes downwelling plumes more difficult to form.

The situation is very different if no chemical flux is allowed at the top and a uniform volumetric sink is introduced instead in the shell to compensate for the injected bottom flux. In the diffusivity-free regime, chemical transport is purely advective and convection is dominated by thin plumes that eventually break-up into "blobs" of size comparable to the plumes width or larger. Since the damping action of diffusion is suppressed, these blobs can deform but do not

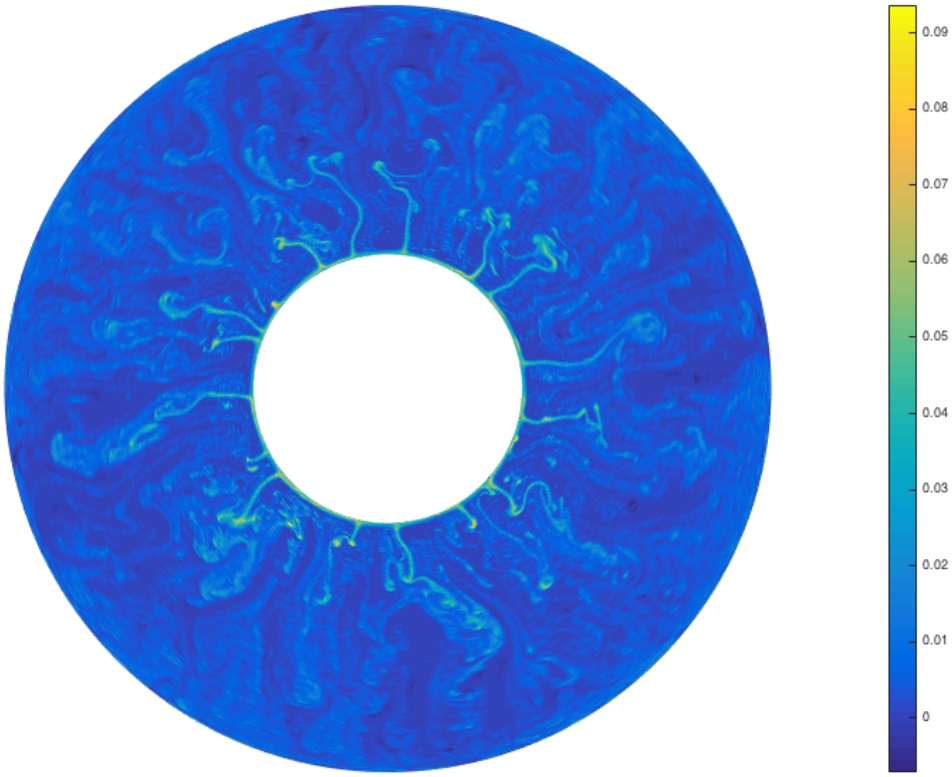

FIGURE 6.9: Equatorial section of composition during the transitory state. Parameters: $E = 10^{-4}$, $Ra = 10^{7}$.

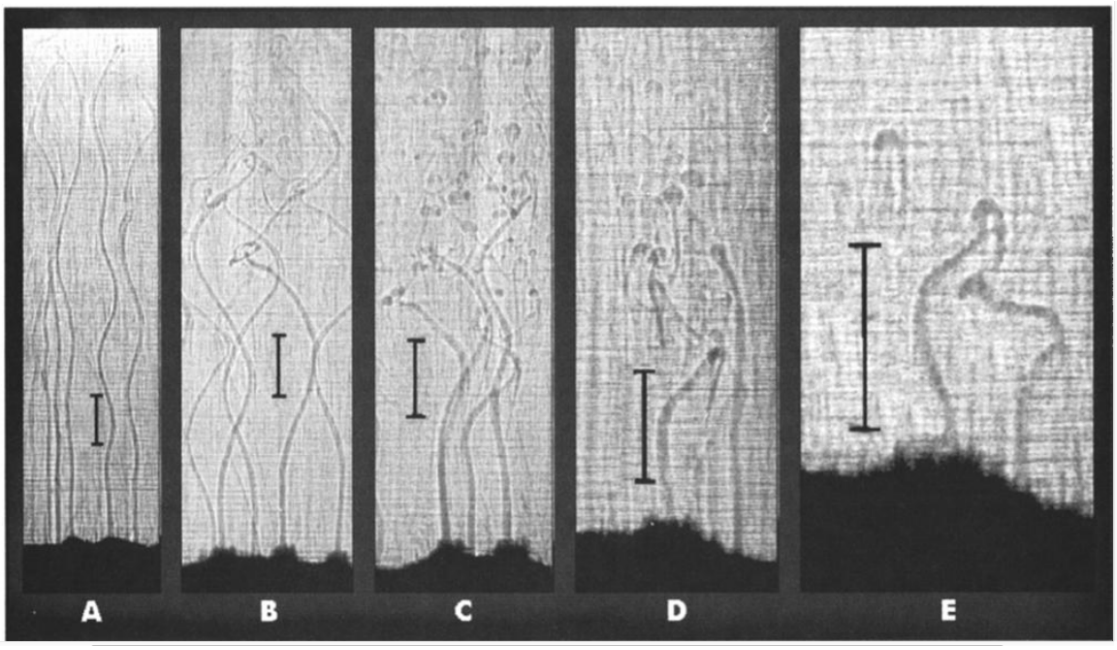

FIGURE 6.10: Blob instability for compositional convection in a rotating cylinder. Experiments from Claßen et al. (1999). A: no rotation, B: $E = 1.5 \times 10^{-4}$, C: $E = 7.5 \times 10^{-5}$, D: $E = 2.5 \times 10^{-5}$, E: $E = 1.5 \times 10^{-5}$.

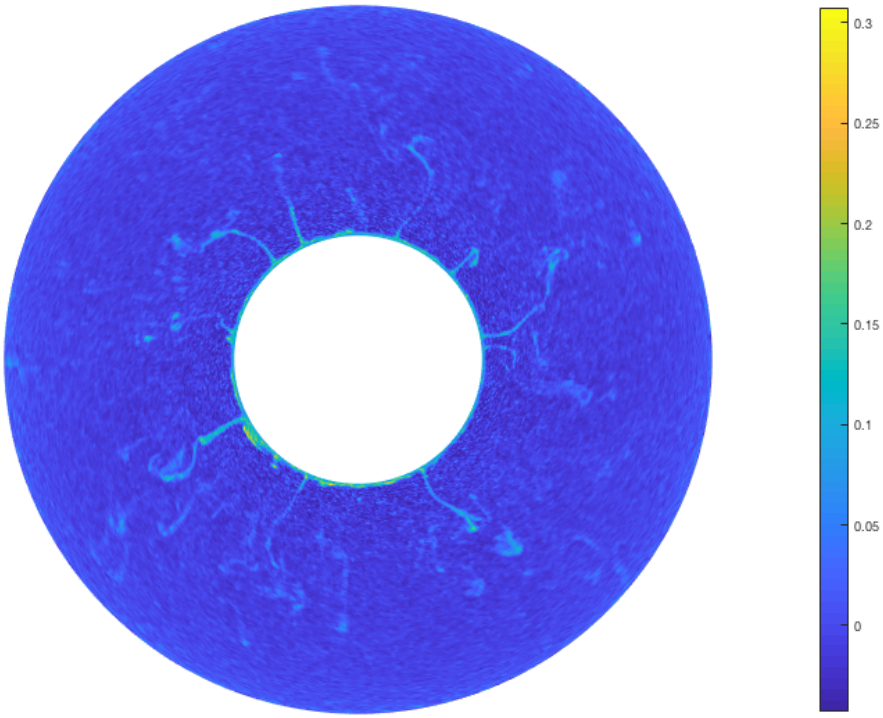

FIGURE 6.11: Equatorial snapshot of the compositional field at $t = 6$ viscous times. Parameters: $E = 10^{-3}$, $Ra = 5 \times 10^5$. The stratified layer is not easy to distinguish due to the intensity of the plumes which makes the color variation almost invisible in the top region.

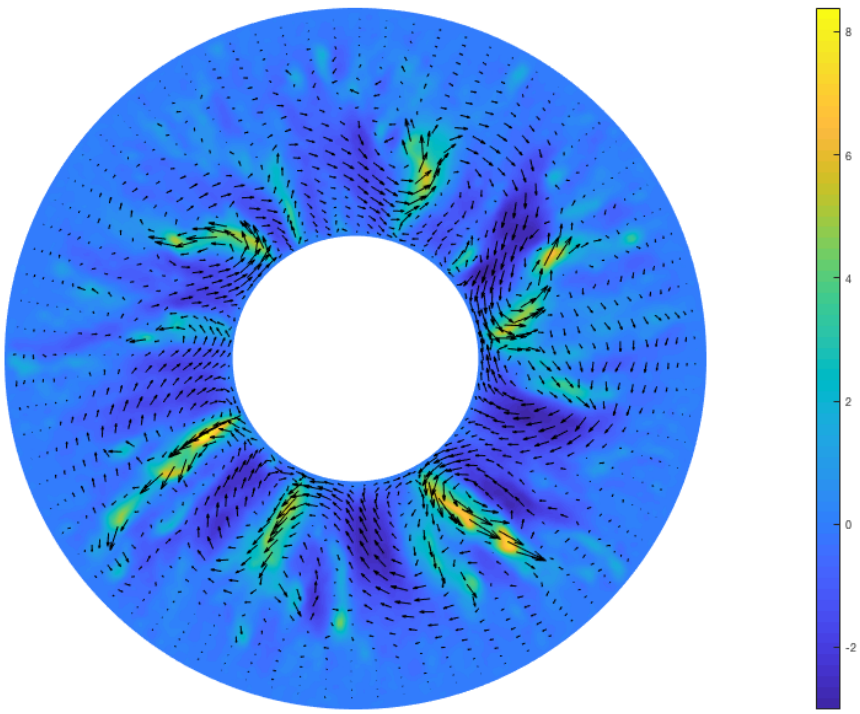

FIGURE 6.12: Snapshot of the radial component of the velocity field at $t = 6$ viscous times. Parameters: $E = 10^{-3}$, $Ra = 5 \times 10^5$. The arrows represent the sum of the radial and azimuthal velocity components.

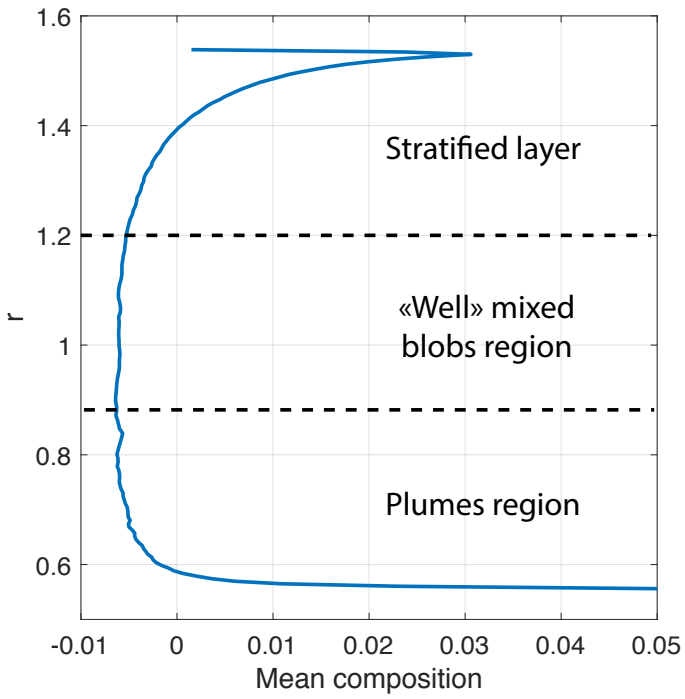

FIGURE 6.13: Radial profile of the mean composition at $t = 6$ viscous times. Parameters: $E = 10^{-3}$, $Ra = 5\times10^5$. The horizontal dashed lines are drawn to delimit approximately three different regions, equivalently to the model by Loper (2007).

lose their buoyancy. They are therefore able to reach the top of the shell where they accumulate to form a stably compositionally stratified layer. The presence of a stratification can be measured by the value of the Brunt-Väisälä frequency:

$$N^2 = -\frac{g}{\rho_0}\frac{\partial \rho}{\partial r} = \beta g \overline{\xi}_r, \tag{6.2}$$

where $\overline{\xi}_r = \overline{\partial \xi / \partial r}$ denotes the mean radial gradient of the mass fraction. Stratification then occurs when $N^2 > 0$ which, for pure compositional convection, is equivalent to $\overline{\xi}_r > 0$. As indicated by the mean compositional radial profile shown on figure 6.13, stratification occurs somewhere around $r = 1.2$ after 6 viscous times for the parameters considered. The corresponding equatorial snapshots of the compositional and radial velocity fields are shown on figures 6.11 and 6.12, respectively. The incomplete mixing of the compositional field produces tiny chemical "flakes" that give a "granular" aspect to the picture. In this regime, the spherical shell could be divided into a "plumes" region extending from the inner boundary to about one third of the shell on figure 6.11, with a more or less "mixed" region above where the plumes are distorted, forming blobs and eddies, and a chemically stratified layer in the upper region of the shell; a picture in agreement with the model proposed by Loper (2007). Figure 6.12 shows that the radial velocity shrinks in the top region of the shell, but that penetration of blobs into the stratified layer is possible and serves as a mechanism to deliver light elements into the layer. Note that the statistically steady state is not yet reached here as the layer grows very slowly and requires to pursue the simulation on very long time scales.

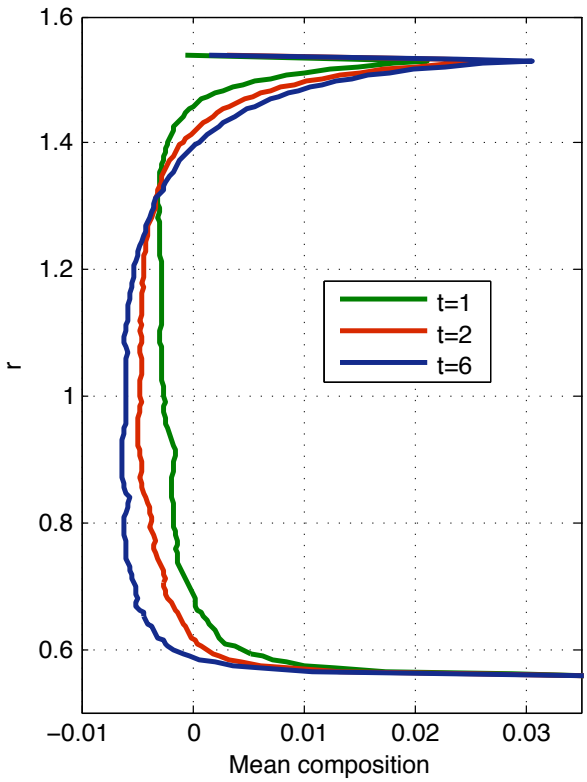

FIGURE 6.14: Mean compositional radial profiles at three different times (expressed in viscous time). Parameters: $E = 10^{-3}$, $Ra = 5 \times 10^5$.

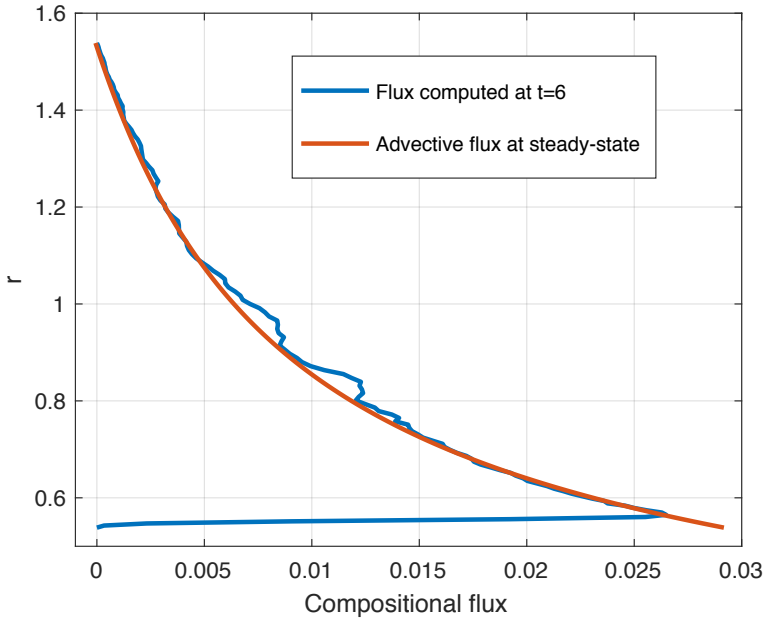

FIGURE 6.15: Advective compositional flux at time $t = 6$ (blue curve) and compositional flux computed at steady-state using equation (6.3).

Shape of the stratified chemical profile

Once the first chemical blobs reach the top boundary, they quickly build an initial stratified layer that then grows very slowly over long time scales. Mean radial chemical profiles can be visualized on figure 6.14 at three different times, for a simulation with parameters $E = 10^{-3}$ and $Ra = 5 \times 10^5$. After 2 viscous times, the evolution is extremely slow (see the curves corresponding to times $t = 2$ and $t = 6$). At $t = 6$, it can be checked that the profile still evolves at a very low pace, meaning that the statistically steady-state is not reached. The curves of the chemical profiles in this slowly drifting regime look homothetic and have a similar peculiar shape that can be explained by reasoning on the chemical transport through the shell. At statistically steady state, the mean radial compositional flow per surface unit $q_\xi(r)$ must balance the volumetric sink term σ^ξ in the portion of the shell comprised between radii r and r_o:

$$q_\xi(r) = \frac{\sigma^\xi}{3r^2}(r_o^3 - r^3). \tag{6.3}$$

Due to the very slow evolution of the stratification, the chemical profiles can be assumed to be in a quasi-stationary state, so that this balance is approximately verified. This assumption can be verified by computing the advective compositional flux $q_\xi^{adv}(r)$ defined at radius r by:

$$q_\xi^{adv}(r) = \iint_{\mathcal{S}(r)} u_r \xi \mathrm{d}S, \tag{6.4}$$

where $\mathcal{S}(r)$ is the spherical surface at radius r. The result for one snapshot at $t = 6$ viscous times is shown on figure 6.15 and seems to confirm the hypothesis of a quasi-stationary state. At this point, it is tempting to try to link this expression to the mean chemical radial gradient $\overline{\xi}_r$ in the shell. In an unstratified turbulent fluid, the mean flux q_s of a passive scalar s is classically related to the mean concentration gradient by invoking a *"turbulent"* or *"eddy"* diffusivity κ_{turb}^s:

$$q_s = -\kappa_{turb}^s \nabla s, \tag{6.5}$$

for times large compared to the Lagrangian timescale of the turbulence (Taylor, 1915; Batchelor, 1949), in which the eddy diffusivity κ_{turb}^s can be related to some physical quantities such as the turbulent root mean square velocity and integral lengthscale. This theory can even be extended to stratified flows by allowing κ_{turb}^s to vary with the Brünt Väisälä frequency (Holford and Linden, 1999). In theoretical models of stratified layers in the core, a turbulent diffusivity has also been introduced by Braginsky (2006). It is however not completely obvious that such a relation would be relevant in the context of chemical convection presented above, first because composition is not a passive quantity in this case and is transported by the convective flow it generates, and also because it is not evident that the flow can be considered as turbulent in these simulations. In an attempt to parametrize the advective transport of composition, on can assume a similar relation anyway:

$$q_\xi = -\kappa_{turb}^\xi \left(\overline{\xi}_r\right) \overline{\xi}_r, \tag{6.6}$$

where κ_{turb}^ξ is an "eddy" chemical diffusivity that is expected to depend on the chemical gradient *i.e.*, the strength of the chemical stratification. The diffusivity $\kappa_{turb}^\xi = q_\xi / \overline{\xi}_r$ is plotted against $\overline{\xi}_r$ on figure 6.16 with exponent -1 for the unstable part of the shell and exponent $-1/2$ in the stratified layer. For unstable compositional profile, it is not very clear whether κ_{turb}^ξ is directly inversely proportional to the chemical gradient or related to the latter by a relation of the form:

$$\kappa_{turb}^\xi = \frac{\kappa_0}{1 + \overline{\xi}_r / \overline{\xi}_r^0}, \tag{6.7}$$

that is similar to the law proposed by Holford and Linden (1999) for low Richardson numbers $Ri = \frac{g}{\rho}\frac{\nabla\rho}{(\nabla u)^2}$ (ratio of the buoyancy and flow shear terms).

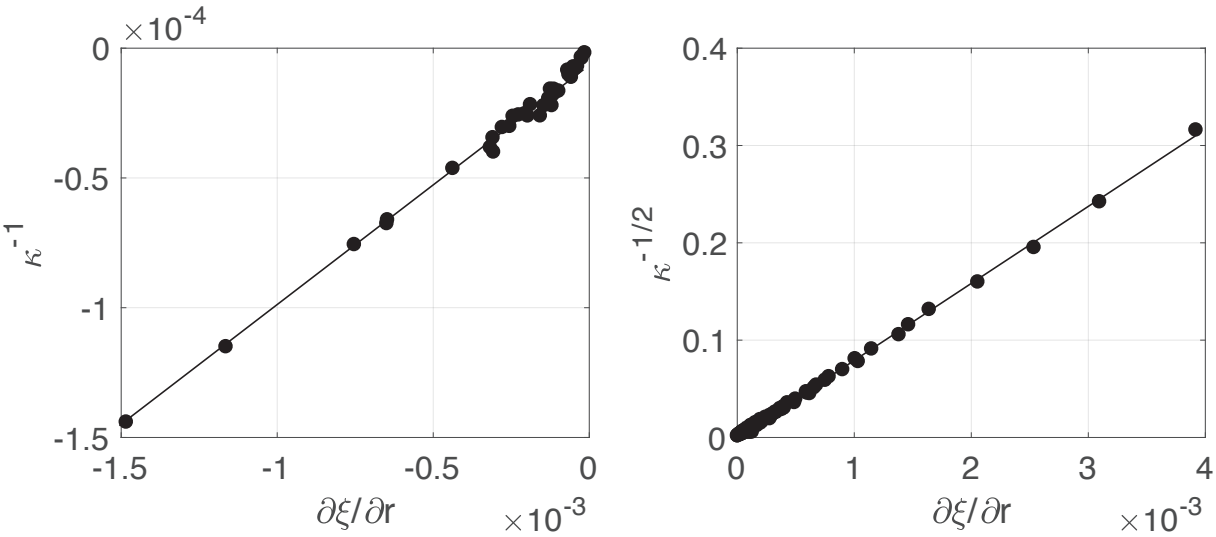

FIGURE 6.16: "Eddy" chemical diffusivity as a function of the mean radial chemical gradient in the shell, in the unstable portion (left) and stratified layer, corresponding to $\overline{\xi}_r < 0$ and $\overline{\xi}_r > 0$, respectively. Straight lines are qualitatively drawn to assess the linearity of the relation.

In the stratified region, an exponent $-1/2$ must be used for κ^{ξ}_{turb} in order to obtain a linear relation. κ^{ξ}_{turb} is related to $\overline{\xi}_r$ by the following relation:

$$\kappa^{\xi}_{turb} = A_0 \overline{\xi}_r^{-2}, \tag{6.8}$$

where A_0 is a constant that can be determined by performing a linear regression. Replacing the expression of κ^{ξ}_{turb} in equation (6.6) and using equation (6.3) lead to:

$$\overline{\xi}_r = A_1 \frac{r^2}{r_o^3 - r^3}, \tag{6.9}$$

which can be integrated in:

$$\xi(r) = -\frac{A_1}{3} \ln\left(\left|r^3 - r_o^3\right|\right) + B_1, \tag{6.10}$$

where A_1 and B_1 are constants that can be determined numerically with a linear regression. Figure 6.17 displays the quantity $\ln\left(\left|r^3 - r_o^3\right|\right)$ as a function of $\xi(r)$ in the top third portion of the spherical shell. For ξ larger than 0, the profile seems to have a linear shape which would validate the prediction from equation (6.10) while for $\xi \lesssim 0$, there is what could be interpreted as a transition to the behavior of the unstably stratified region.

These preliminary results are based on one single snapshot and are therefore probably insufficient to draw any definitive conclusion. However, they give an interesting direction to follow for a more systematic exploration at several different instants in the simulation.

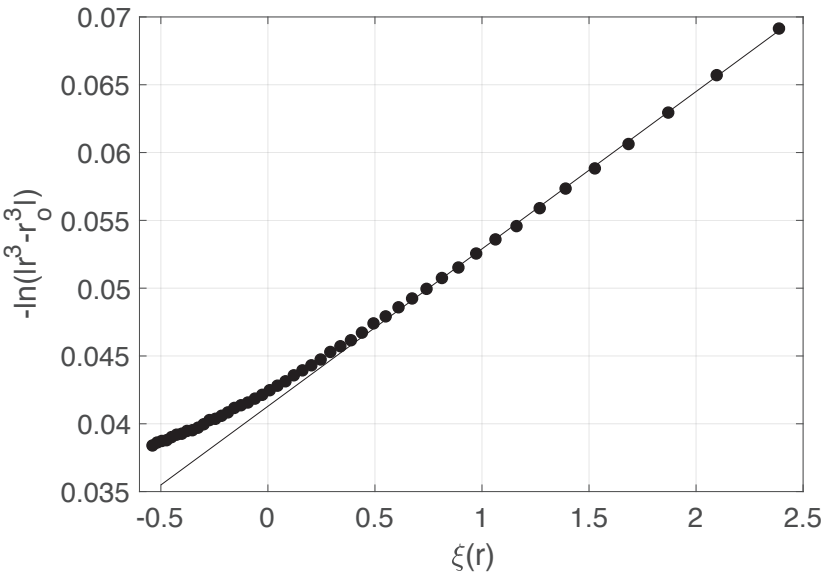

FIGURE 6.17: Scattering of the quantity $\ln\left(\left|r^3 - r_o^3\right|\right)$ as a function of $100 \times \xi(r)$ in the outermost region of the spherical shell. A straight black line is drawn qualitatively.

Lateral variations

The average profile on figure 6.13 hides some interesting lateral variations revealing that the dynamics of the stratified region is relatively complex. Figure 6.18 displays the thickness of the stratified layer as a function of the colatitude for a single snapshot at $t = 6$ viscous times, with $E = 10^{-3}$ and $Ra = 5\times10^5$. The thickness of the layer increases from the equator to the region corresponding to the tangent cylinder and drops abruptly at the poles. These variations are probably intimately tied to the characteristics of the underlying convection. The precise relation is however not evident as opposite reasonings may lead to the same conclusions. One would indeed argue that the layer should be thinner above regions that are vigorously convecting. But on the other hand, the layer can grow only if it is supplied in light elements via the plumes and blobs that are entrained by the convective currents they generate and eventually reach the stratified region. The stratified layer may also reorganize itself, either at the local scale when a blob penetrates it, or at a larger scale if a global circulation sets in. The layer may well be built in some part of the shell while being destroyed elsewhere, with light elements flowing between both regions.

In an attempt to get some intuition about the dynamics of such a layer, a meridional section showing the radial velocity averaged along the longitudes is shown on figure 6.19, corresponding to the same snapshot as figure 6.18. To complete this picture, a polar view is also added on figure 6.20. The combination of these figures suggests that isolated plumes can eventually produce a rather organized velocity pattern with some large-scale features that resemble those of previous experiments by Aurnou et al. (2003). The velocity field consists of a global upwelling in the middle of the tangent cylinder with helical motion and a downwelling above the pole. Some irregular features related to the individual dynamics of plumes and blobs then superimpose to this large-scale picture. The top of the stratified region is supplied in light elements by the underlying upwelling which also "pushes" the layer laterally. Part of it sinks in the polar downwelling while the rest is displaced in the direction of smaller latitudes. The meridional section of the averaged compositional advective flux displayed on figure 6.21 seems to corroborate this idea that the layer is supplied in light elements principally in the tangent cylinder. The situation at the south pole is not shown but is fairly symmetric with respect to the equatorial plane.

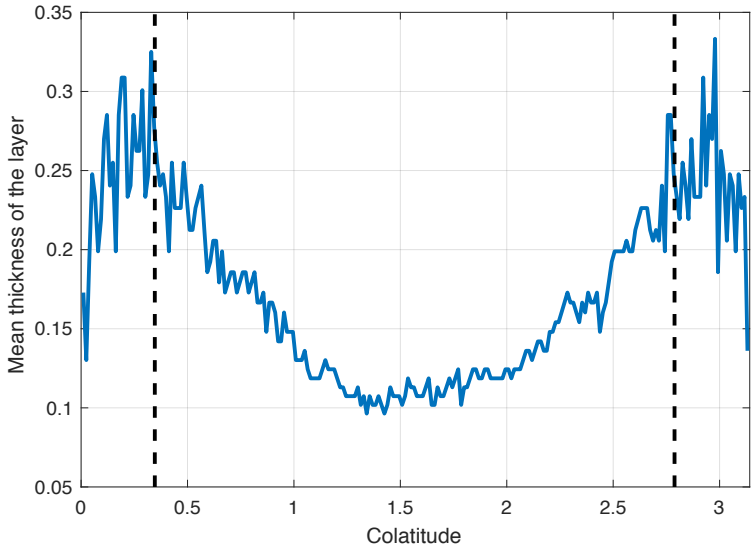

FIGURE 6.18: Thickness of the layer based on longitudinally averaged chemical profiles as a function of the colatitude. The vertical dashed lines delimit the tangent cylinder. Parameters: $E = 10^{-3}$, $Ra = 5 \times 10^5$. Time: $t = 6$.

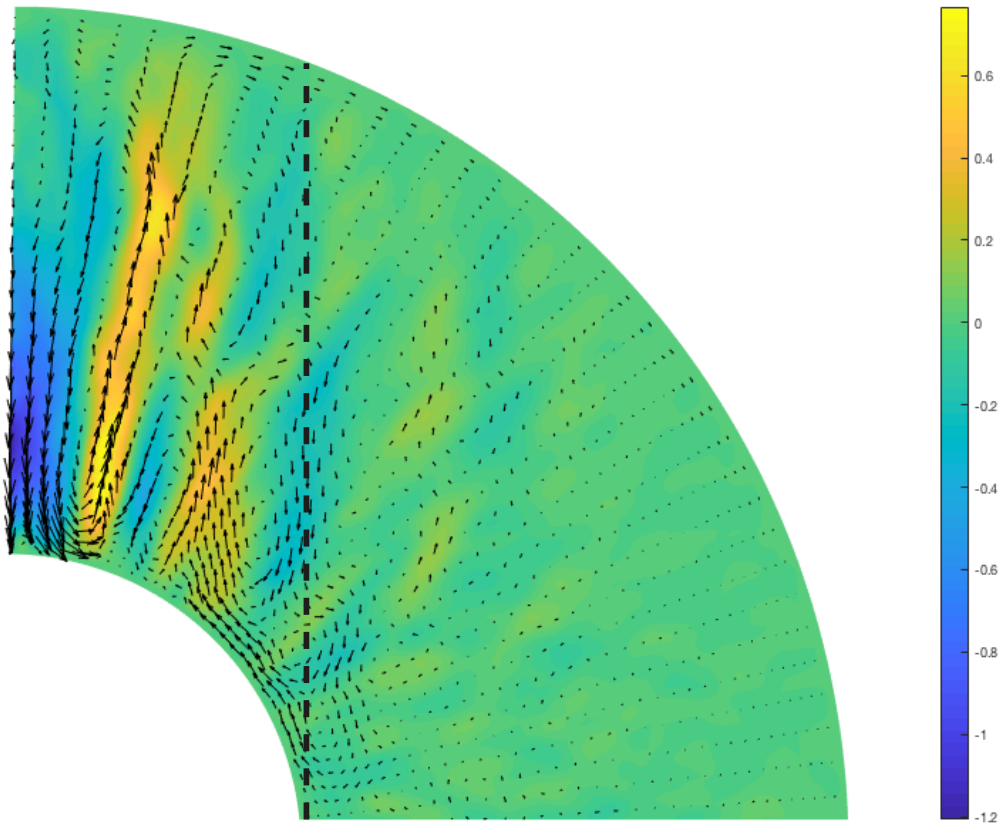

FIGURE 6.19: North meridional section of the average radial velocity (in colors). The arrows indicate the direction of the mean velocity. The vertical dashed lines delimit the tangent cylinder. Parameters: $E = 10^{-3}$, $Ra = 5 \times 10^5$. Time: $t = 6$.

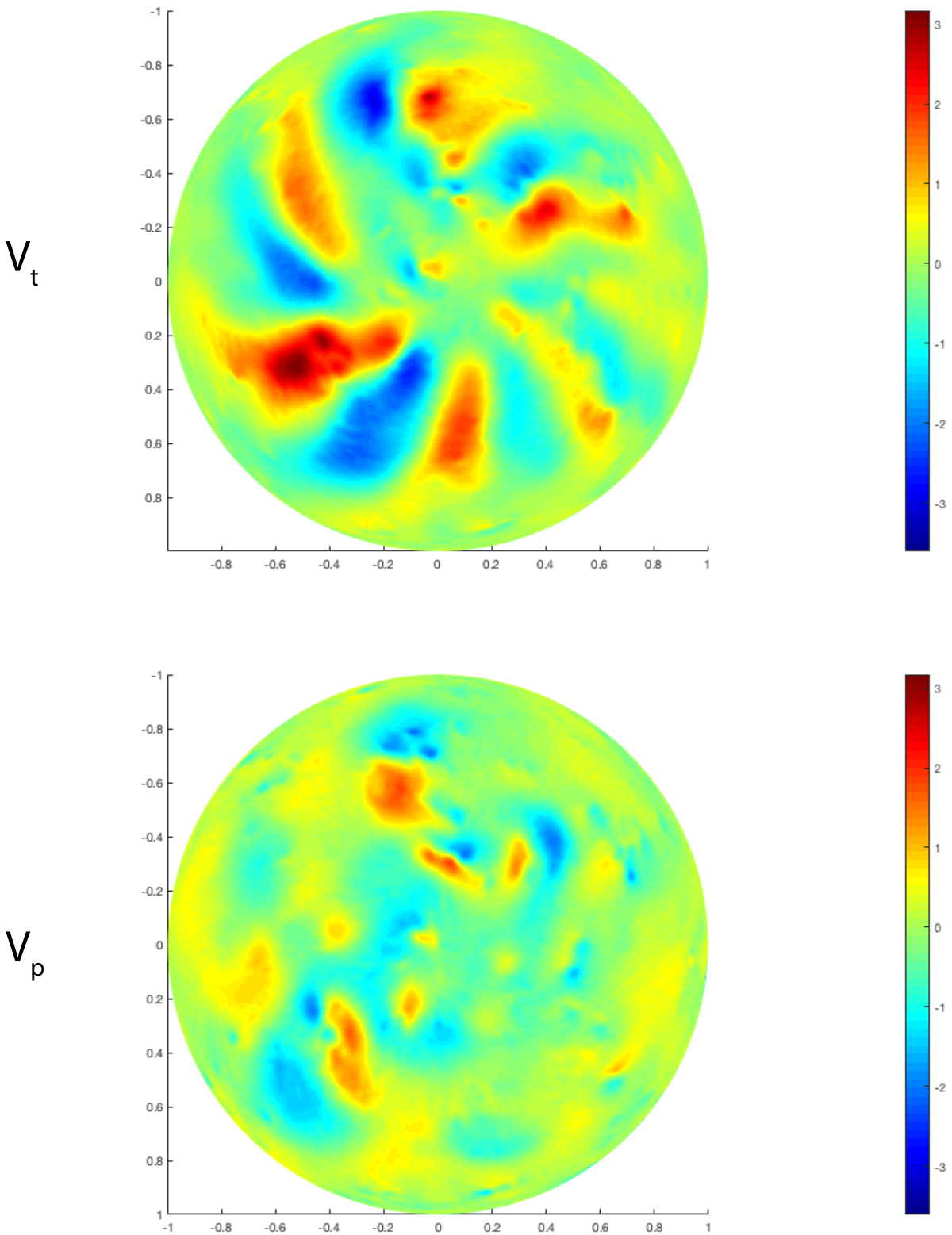

FIGURE 6.20: Polar view at $r = 1.49$ ($r_o = 1.53$) of the velocity components u_θ (top) and u_ϕ (bottom). Parameters: $E = 10^{-3}$, $Ra = 5 \times 10^5$. Time: $t = 6$.

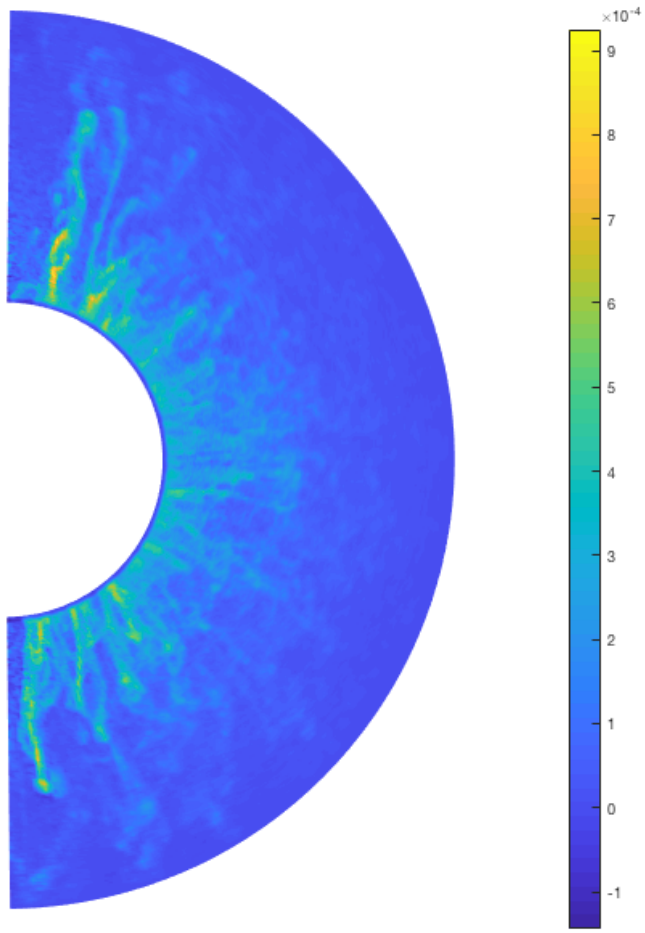

FIGURE 6.21: Meridional section of the compositional advective flux averaged along the longitudes, corresponding to the same snapshot as figures 6.19 and 6.20.

Note that the results of this preliminary study were obtained using only one snapshot. A more systematic exploration should probably be conducted at several times throughout the simulation, though visual observation at different instants seems qualitatively similar.

6.3 Discussion and future directions

The exploratory study conducted in this chapter gives a first interesting insight into the physics of rotating pure chemical convection in the infinite Prandtl number limit with results that seem to be in good agreement with previous laboratory experiments. Nevertheless, a series of points still deserve to be better understood. In particular, the mechanisms of the blob instability should be investigated further. One could for example take advantage of the PIC method to follow particles through time and therefore get more details about the dynamics of plumes. Unfortunately, particles tracking was not implemented at the time I ran these simulations. The latter can however be presently continued with the tracking technique recently developed.

On the other hand, the dynamics of the chemically stratified layer is still unclear. An interesting analogy can be made with the "filling box" models introduced by Baines and Turner (1969) in

which a buoyant material is injected, for example, at the bottom boundary into a finite box. The material ascends as a turbulent plume that entrains part of the ambiant fluid and spreads laterally when reaching the top boundary, forming a stratified layer in which turbulence disappears (see figure 6.22 for an illustration). The next plume then entrains part of the fluid from the light layer and reaches the top even lighter. The plume thus spreads out above the existing light fluid layer, displacing the latter downwards. A stratified layer is formed by this process and progresses downward with time. The analogy with filling box models has however several limitations. In the simulations presented above, plumes do not keep their shape and break-up before reaching the top boundary. When compared to the height of the box, plumes in these simulations are also much smaller than in filling box models so that forming a stratified layer thus probably requires more than a single plume or blob. Despite this, the analogy with filling box models could perhaps be pushed further and certainly motivates a deeper exploration of the mechanisms that control the formation, structure and dynamics of the chemically stratified layer in our numerical simulations. Two crucial questions are perhaps: do light blobs reach the top of the stratified layer, and: how does the layer reorganizes itself when penetrated by an ascending blob? Following the trajectories of particles within a few plumes looks here again like a promising way to investigate these questions.

Although it still needs to be more precisely understood, the formation of a chemically stratified layer in these numerical simulations is in itself an extremely interesting result since the existence of such a layer has been evoked in several planetary cores. In order to perform extrapolation to the terrestrial case, one should be able to answer two important questions:

1. Can such a layer resist against thermal convection?
2. If so, how does its thickness scale with the governing parameters?

These exciting questions are investigated in the next chapter which addresses general issues related to a stratified layer below the Earth's CMB.

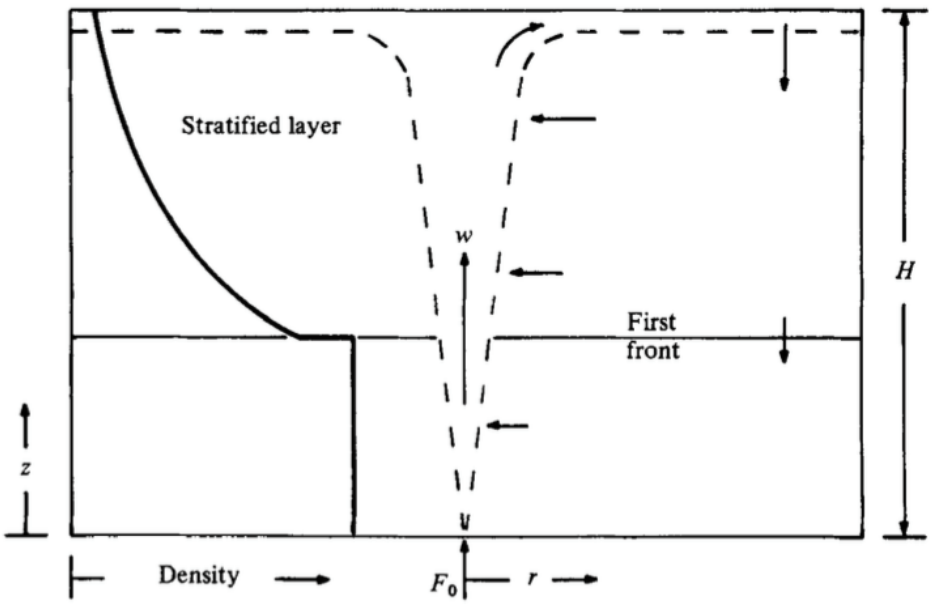

FIGURE 6.22: Example of a filling box model in which a light material is injected at the bottom boundary into a confined volume. The spreading of successive plumes at the top forms a stratified layer separated from the rest of the box by a front that progressively propagates downwards with time. Taken from Worster and Huppert (1983) .

Chapter 7

Formation and dynamics of a stratified layer below the core mantle boundary

Seismological and magnetic observations are compatible with the presence of a stratified layer below the Earth's CMB (Lay and Young, 1990; Tanaka, 2007; Gubbins, 2007; Helffrich and Kaneshima, 2010; Lesur et al., 2015) and the existence of such a layer has also been predicted by several theoretical arguments listed below. The proposed thickness varies from 60 km to several hundreds of kilometers across the literature, but is usually close to 100 km. This situation may not be unique to the Earth's core as presence of a stratified region has also been evoked in the metallic cores of Mercury (Christensen, 2006; Manglik et al., 2010) and Ganymede (Hauck et al., 2006; Christensen, 2015). In the Earth's core (and in other planetary cores), stratification may have two different origins.

The layer may first be *chemically* stratified. Various mechanisms have been proposed for the formation of such a layer and include barodiffusion *i.e.* diffusion of light elements against the pressure gradient (Fearn and Loper, 1981; Braginsky, 2006; Gubbins and Davies, 2013), chemical plumes and blobs that would be able to reach the CMB where they would accumulate (Loper, 1989; Braginsky, 1994; Moffatt and Loper, 1994; Loper, 2007) or ascending droplets in a Fe-S system kept from mixing by surface tension (Franck, 1982). Layering may also be present if immiscible liquids evolve as the composition changes due to inner core growth (Helffrich and Kaneshima, 2004). To finish, Buffett and Seagle (2010) also studied the possibility that light elements be dissolved from the mantle into the core, forming a lighter layer that could grow by diffusion over long time scales. So far, no numerical simulation of core dynamics has been able to validate any of these potential mechanisms and produce a chemically stratified layer in a self-consistent manner. In chapter 6, I showed that such a layer naturally forms via rising plumes and blobs in simulations of pure chemical convection when the chemical diffusivity is neglected. This result strongly motivates a more systematic exploration including the stirring effect of thermal convection. Furthermore, because it is chemically stratified but potentially thermally unstable, a chemically stratified layer may be prone to double-diffusive instabilities of the *diffusive* type. In the non-rotating case, diffusive instabilities exist in a narrow range of the parameter space where the layer is weakly stratified. Even though this may not hold in the rotating case, it suggests that diffusive instabilities would be limited to the base of the stratified layer, like in the model of Buffett and Seagle (2010).

Another possibility is that the CMB heat flow could be subadiabatic, creating, in that case, a *thermally* stratified layer (Gubbins et al., 1982; Labrosse et al., 1997; Lister and Buffett, 1998; Labrosse, 2015). With light elements coming from below, such a layer would be thermally stratified but chemically unstable and therefore susceptible to double-diffusive instabilities of the *fingering* type. In a double-diffusive simulation with a moderate Lewis number of 10, Manglik et al. (2010) showed that, because of their lower diffusivity, compositional plumes can penetrate to some extent into the thermally stratified layer before being diffused, therefore behaving like salt

fingers. However, no numerical simulations have properly modeled fingering convection in a rotating stratified layer so far.

The precise nature of the stratification (thermal and/or chemical) below the Earth's CMB is therefore still to be determined. In addition, the dynamics of a stratified layer and its implications for core dynamics and dynamo action remain poorly known. It is often assumed that no radial movement are allowed in a stratified layer, but this assumption may not hold as soon as double-diffusive instabilities develop. A few authors studied the effects of a thermally stratified layer on the magnetic field generation (Manglik et al., 2010; Nakagawa, 2011; Christensen, 2015) but considered either a codensity approach or a double-diffusive model with a low Lewis number. Moreover, it seems that none has really investigated the dynamics of double-diffusive convection in a stratified layer.

As explained in section 2.1.3, the study of double-diffusive thermochemical convection in the core can be explored within two different frameworks: global simulations at the scale of the core, or local approach which is equivalent to "zooming" on a stratified layer to study more precisely its dynamics. In this chapter, the formation of a chemically stratified layer is first investigated by running full core simulations of thermochemical convection at infinite Lewis number. The growth of the layer is recorded through time for different parameters and scaling laws are looked for. In a second phase, the possibility of a thermally stratified layer is considered. The dynamics of salt fingers within such a layer is explored theoretically and numerically in a bounded model approach. Implications for the Earth's core are then discussed. Most of the results shown in this chapter were obtained in the last months of my PhD. For this reason their interpretation still requires more investigations. They however raise interesting questions and thus deserve to be presented in this chapter.

7.1 Formation of a chemically stratified layer below the Earth's core mantle boundary

7.1.1 Numerical setup

In this study, the formation of a chemically stratified layer below the CMB is investigated by the means of numerical simulations of thermochemical convection in a rotating shell. These simulations are similar to those of the previous chapter but the stirring effect of thermal convection is now included. For simplicity, the Lorentz force is not considered here and the thermochemical boundary conditions are independent. A chemical flux of light elements is injected at the bottom with no penetration of light elements across the top boundary. A volumetric sink term is imposed in the spherical shell to compensate for the injected bottom flux and the initial chemical profile is $\xi = 0$ everywhere. Thermal boundary conditions are fixed such that equal total heat flows apply at each boundary. The thermal field therefore provides a destabilizing effect at both boundaries. The temperature is split accordingly into a variable part and a conductive reference state.

The aspect ratio of the shell is that of the Earth's core ($r_i/r_o = 0.35$). The buoyancy ratio is fixed and equal to $\mathcal{R} = (f_i^T + f_o^T)/f_i^\xi = 0.5$ in all simulations in order to decrease the parameter space. Naturally, the effect of the buoyancy ratio should also be studied in the future. The thermal Prandtl number is set to $P_T = 1$. Three Ekman numbers E (10^{-3}, 3×10^4 and 10^{-4}) are considered and the total Rayleigh number $Ra = Ra_T + Ra_\xi$ (defined as in section 2.3.3) is also varied. Because the stratified layer grows very slowly, it is necessary to run the simulations on very long time scales (more than 10^6 time steps) to reach a statistically steady-state. In order to save computational time, 4-periodic (resp. 8-periodic) solutions are looked for in the case of Ekman numbers 10^{-3} (resp. 3×10^{-4} and 10^{-4}). So as to verify that this choice does not influence the thickness of the layer, it is necessary to run at least one simulation in a full spherical shell, which has not yet been done. The resolutions are adapted to the Ekman numbers and summarized in table 7.1. In case $E = 10^{-4}$, the chemical plumes may be slightly under-resolved (see the discussion in section 5.3.3) but we expect that the thickness of the layer is not controlled by the details of the plumes dynamics. To finish, tracers are advected by a Runge-Kutta 4th order scheme with trilinear interpolation of the velocity.

E	Ra	M_c	N_r	ℓ_{max}	N_{tra} ($\times 10^6$)
10^{-3}	10^5	4	150	200	25
10^{-3}	5×10^5	4	150	200	25
3×10^{-4}	5×10^5	8	175	200	100
10^{-4}	5×10^5	8	220	200	125

TABLE 7.1: Summary of the parameters and resolution of the 4 simulations. E and Ra are the Ekman and Rayleigh numbers, respectively. M_c is the periodicity of the solution. N_r is the number of radial grid points, ℓ_{max} the spectral resolution and N_{tra} denotes the number of tracers inserted.

7.1.2 Measure of the thickness

The presence of a stratification is usually based on the measure of the Brunt-Väisälä frequency:

$$N^2 = -\frac{g}{\rho_0}\frac{\partial \rho}{\partial r} = \left(\alpha g \overline{T}_r + \beta g \overline{C}_r\right), \tag{7.1}$$

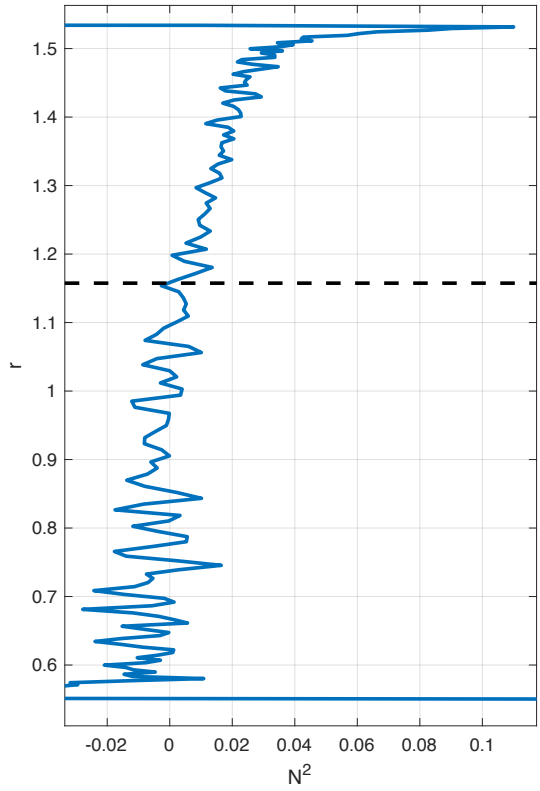

FIGURE 7.1: Radial profile of the Brunt-Väisälä frequency at time $t = 19.02$ for the case $E = 3 \times 10^{-4}$. The black dashed line sets the limit of the stratified layer.

where $\overline{T}_r$ and $\overline{C}_r$ are the mean thermal and chemical radial gradients in the shell. Stratification occurs when $N^2 > 0$, that is:

$$\overline{T}_r > -\frac{\beta}{\alpha}\overline{C}_r. \tag{7.2}$$

In non-dimensional form, this reads:

$$\overline{T}_r > -\mathcal{R}\overline{C}_r. \tag{7.3}$$

This criterion is retained to measure the thickness h_s of the stratified layer in the simulations. The base of the stratified layer is defined as the radius r_b which is such that:

$$\begin{cases} N^2(r_b) = 0, \\ N^2(r) > 0 \quad \text{for} \quad r > r_b. \end{cases} \tag{7.4}$$

The thickness h_s of the stratified layer is then simply:

$$h_s = r_o - r_b. \tag{7.5}$$

A typical profile of the Brunt-Väisälä frequency is shown on figure 7.1 for a single snapshot. The strong decrease of N^2 at the very top of the shell is due to the non-penetrative and no-slip boundary conditions which prevent any buoyant material from reaching the top boundary of the shell and to the destabilizing thermal buoyancy provided at this boundary. Note that other geometric methods based on integral estimations or the mean slope of the stratified layer can also be used but are more arbitrary, and that a criterion based on the Brunt-Väisälä frequency seems much more physical.

7.1.3 Preliminary results

Time evolution

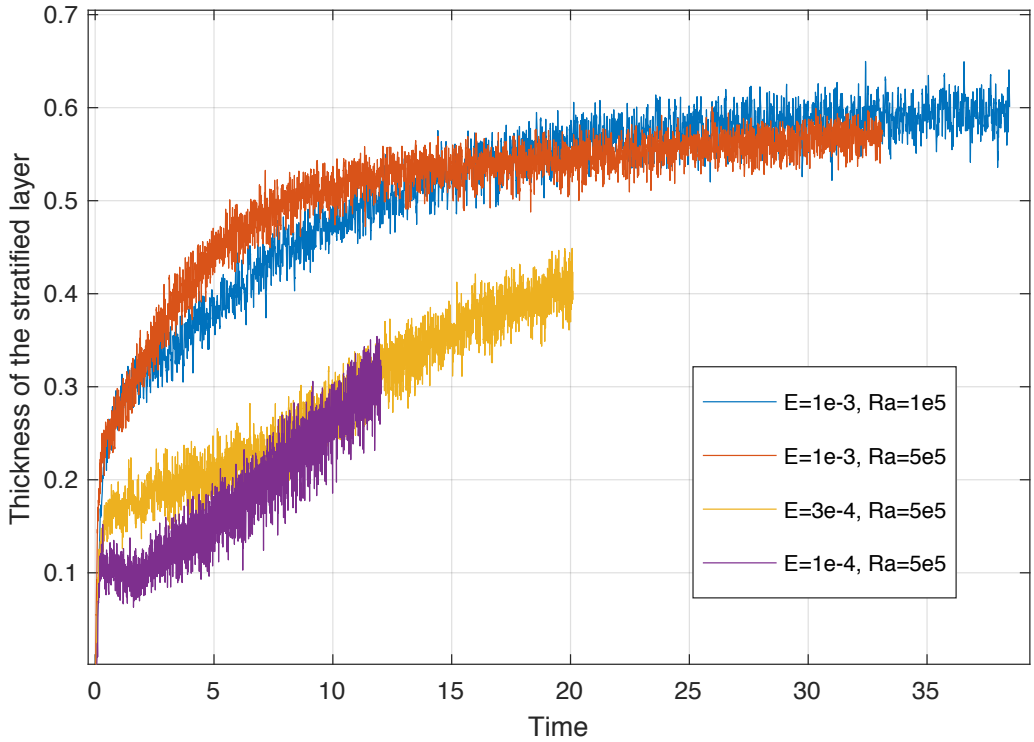

FIGURE 7.2: Thickness of the stratified layer as a function of time (in viscous time). To decrease the strong noise of the curves, a running average is performed using 500 points around each time step.

Despite the stirring effect of thermal convection, a chemically stratified layer systematically forms below the top boundary in all the simulations and then grows very slowly. The evolution of the mean thickness of the stratified layer is plotted as a function of time on figure 7.2 for the four simulations listed in table 7.1. Due to the rapid variations of N^2 and to its small average slope near the base of the layer (see figure 7.1), the time evolution of the thickness h_s is very noisy. Consequently, a moving average on 500 time steps is performed to ease the visualization. It would probably be more advantageous to measure the thickness directly using a time running average of the radial profile of the Brunt-Väisälä frequency. This has not been computed here but could be implemented soon. All the curves plotted on figure 7.2 correspond to very long simulations that largely exceed 10^6 time steps. Unfortunately, the statistically stationary states are not reached yet. It is therefore not possible to draw any definitive conclusion, even if a few observations can already be made. The interpretations of these preliminary results in the next paragraphs should therefore be considered as speculative and must all be confirmed by continuing the simulations.

It seems that three parts can be distinguished on the curves: a very quick phase lasting a fraction of a viscous time during which an initial stratified layer is built, followed by two longer phases. The first one is associated with a slow quasi-linear growth of the layer and the second one is a transition to an asymptotic regime. For the curve with Ekman number 10^{-4}, there is a period of stagnation (and even a small decrease of the thickness) lasting about 2 viscous times after the first initial layer is established. In all the simulations, except during the first rapid phase, the

thickness of the stratified layer evolves on tens of viscous times, *i.e.* on time scales that are large compared with the typical overturn time, so that the convective time scale and the secular evolution of the layer are well separated. Like in the simulations of pure chemical convection shown in the previous chapter, the situation is that of a quasi-equilibrium state that slowly evolves over time and is probably controlled by one or several dimensionless numbers which also vary with time. Although this is not completely evident, lowering the viscosity (thus the Ekman number) may be expected to increase the efficiency of mixing, thereby decreasing the thickness of the layer. Similarly, increasing the Rayleigh number (i.e. the vigor of the convection) would also intuitively lead to a thinner layer. When looking at the blue and red curves that only differ by their Rayleigh number, it seems that increasing the vigor of the flow has only little impact on the final thickness of the stratified layer which seems rather controlled by the Ekman number (though this is of course to be confirmed by continuing the simulations). Defining a relevant scaling law is therefore not obvious at this point, but we make a first attempt by assuming that the thickness at statistically stationary state is controlled by the Ekman and Rayleigh numbers and obeys a law of the form:

$$h_s(t \to +\infty) = HE^{\alpha}Ra^{\beta}, \tag{7.6}$$

where H is a constant and α and β exponents to be determined. The relevance of this scaling law is not evident and a better understanding of the processes that control the thickness of the layer is required. In particular, it is not clear at all that a statistically steady state actually exists in this problem. Moreover, the time running average performed to visualize the curves on figure 7.2 may hide some variations on shorter time scales. A Fourier analysis of the time series could also reveal some subtleties and should be performed.

General characteristics of the flow

Some general features of the flow in a quasi-equilibrium state are gathered on figure 7.3 which shows the temperature, composition and velocity fields on equatorial snapshots, at time $t = 19.02$ for the case $E = 3 \times 10^{-4}$. This single snapshot can be considered as well "representative" of the features observed at different times in this simulation.

Contrary to the temperature field which is very smooth, the compositional field is not homogeneous and has a "floaty" aspect throughout the shell consisting of unmixed blobs that were not diffused over time. In real conditions, diffusion would act at these small scales on longer times to homogenize this picture. With this granular aspect, it is not evident to identify larger compositional structures even if there is a vertically elongated region of higher average composition on the right/middle part of the figure that resembles a chemical plume. The velocity field seems to confirm this impression as it is characterized by a single convection cell confined to the bottom half of the shell, with the upwelling being associated with the region of higher average composition and temperature. The top 40% of the shell is chemically stratified. The radial profile of the Brunt-Väisälä frequency (see figure 7.1) reveals that the strength of the stratification increases with the radius and is maximal in the Ekman boundary layer. Yet, the stratified layer is not motionless since, despite being weaker than in the fully convective region, the velocity field in this layer shows a smaller scale pattern that resembles alternating upwellings and downwellings, though this is not completely evident. These radial motions probably serve as a mechanism to bring the light buoyant blobs emanating from the ICB to the top of the stratified region, like in a "filling box" scenario. This hypothesis is also corroborated by the chemical advective flux plotted on figure 7.4 which is strongly diminished in the stratified region but remains non negligible. To finish, if diffusive convection exists, the linear stability analysis in the non-rotating case indicates that it is probably confined to the bottom of the layer where the stratification is weaker (Radko,

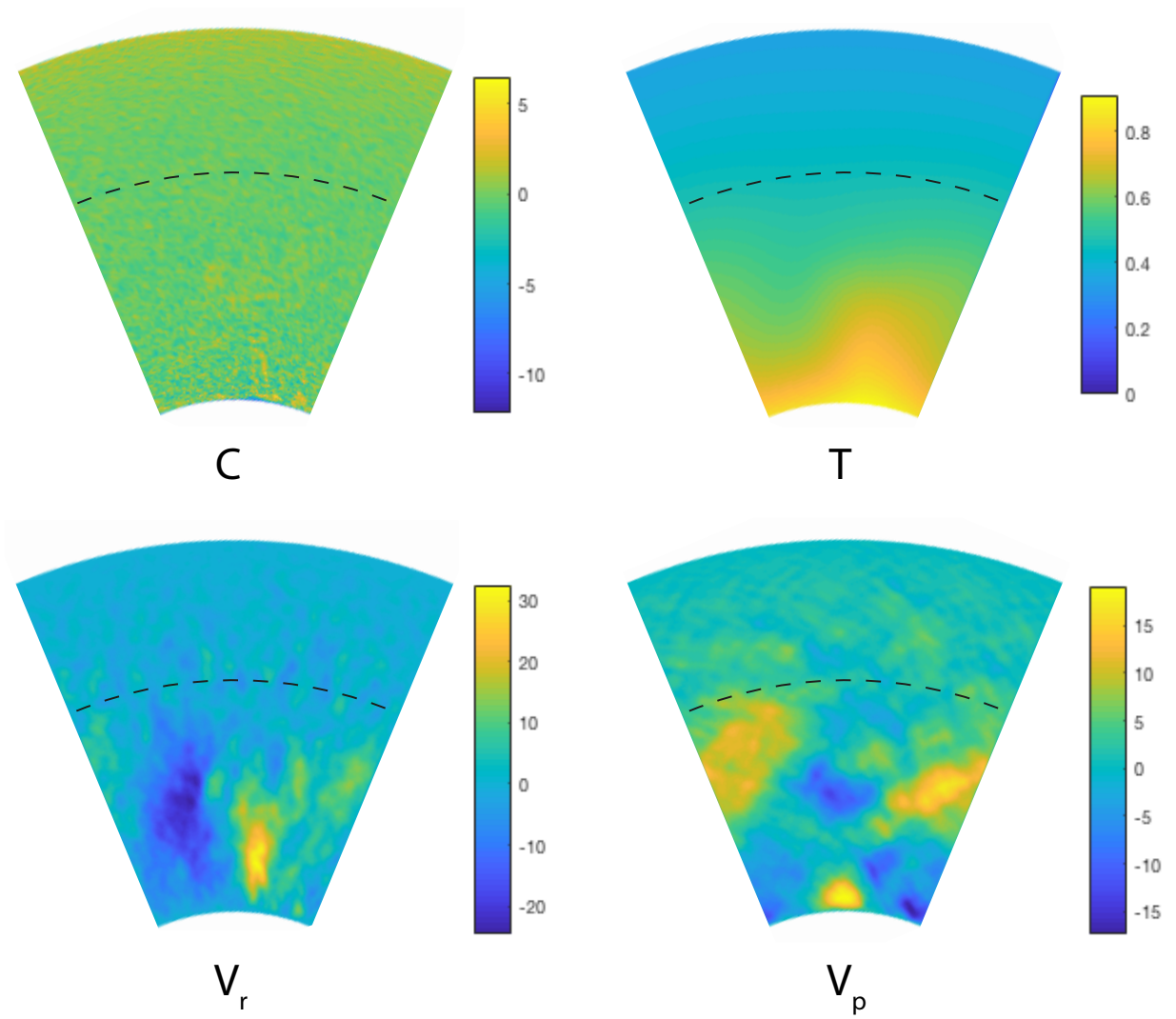

FIGURE 7.3: Snapshots in the equatorial plane (the solution is 8-periodic) for the case corresponding to $E = 3 \times 10^{-4}$, at time $t = 19.02$. Top row: composition (left) and temperature (right). Bottom panel: radial component of the velocity (left) and longitudinal component (right). The black dashed lines represent the limit of the stratified layer.

2013). It is however difficult to detect unequivocally a signature of the presence of diffusive convection in the density profile. Diffusive convection may not be present in this run or be confined to localized regions and be invisible on the average density profile.

7.2 Discussion: extrapolation to the Earth's case

As in the pure compositional case (discussed in the previous chapter), what exactly controls the thickness of the stratified region in thermochemical convection is still not completely clear, though it is probably related to the efficiency of mixing processes. In order to assess the relevance of the scaling law (7.6) and to determine the value of the exponent α, it is necessary to pursue the simulations to reach statistically stationary states. A simulation with a lower Ekman number (3×10^{-5}) is probably mandatory to fit the scaling law on at least 4 points. Also, confirming the minor effect of the Rayleigh number requires exploring other Rayleigh numbers for the Ekman numbers considered. Since reaching a statistically steady state is very costly, continuing the

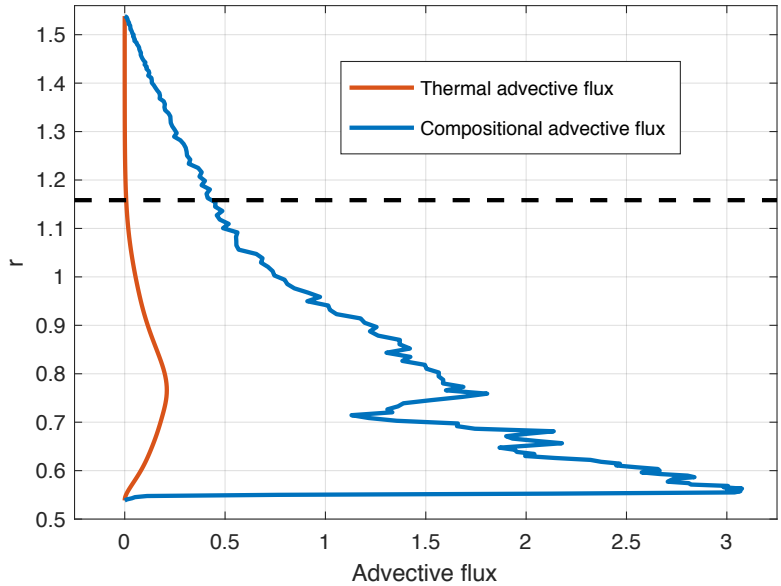

FIGURE 7.4: Averaged thermal (red curve) and compositional (blue curve) advective fluxes for the case corresponding to $E = 3 \times 10^{-4}$, at time $t = 19.02$. The limit of the stratified layer is drawn with a black dashed line.

simulations while changing either the Rayleigh or Ekman number could be a good compromise. Also, since there is a good separation of time scales, it may be possible to define a dimensionless number that varies with time and controls the quasi-equilibrium state. In this case, even a single run would allow to fit a scaling law.

In spite of this, one may try to extrapolate the preliminary results shown above to the Earth's core anyway. If we assume that the blue curve corresponding to $(E = 10^{-3}, Ra = 5 \times 10^5)$ has reached a statistically steady state and that the latter is only controlled by E^α, then it is reasonable to estimate that:

$$\alpha \leq 1/3, \tag{7.7}$$

since the curve corresponding to $E = 10^{-4}$ has still not stabilized after reaching a thickness that is about half that of the blue curve at equilibrium ($10^{1/3} \approx 2.15$). Extrapolation to the Earth's core would give a thickness of about 100 m for an exponent $\alpha = 1/3$ and 1 km for $\alpha = 1/4$. Building a thickness of 100 km would require a smaller value of α close to 0.1.

Even if α were found to be too large to explain *as is* a 100 km thick stratified layer below the Earth's CMB, the layer might grow anyway because of chemical diffusion on long time scales. Buffett and Seagle (2010) studied the case of a chemically stratified layer supplied by a flux of light elements coming from the CMB that grows diffusively on such time scales. Using a net light elements flux (subtracting barodiffusion) of 4200 kg s^{-1} – that is, about a tenth of the ICB total flux – they show that a stratified layer can grow up to several tens of kilometers over a few billion years. Their model however relies on the hypothesis that light elements coming from the convective part of the core do not penetrate the stratified layer. The latter is then prevented from growing as soon as the inner core starts to crystallize, gradually enriching the convective part of the core in light elements. The numerical simulations presented in this chapter seem to contradict this hypothesis since the layer grows over time because of the blobs that penetrate and supply it in light elements. Given this, I propose a model similar to that of Buffett and Seagle, in which the

chemically stratified layer grows diffusively and is supplied in light elements by the combination of barodiffusion and the contribution of incompletely mixed chemical plumes and blobs emitted at the ICB that reach the stratified layer, as illustrated schematically on figure 7.5. Assuming the fraction of the ICB flux that eventually supplies the layer can be evaluated, the thickness of the layer could be predicted for different inner core ages.

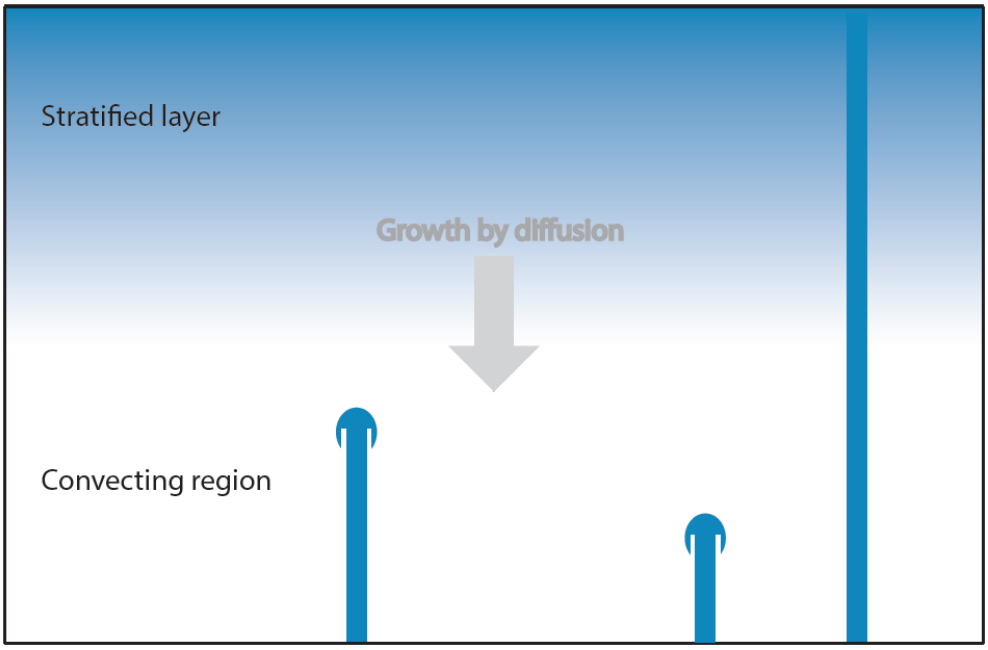

FIGURE 7.5: Simplified cartoon illustrating the model of formation of a chemically stratified layer below the CMB (top boundary). Rising chemical plumes or blobs (in blue) penetrate into the stratified layer up to the point of neutral buoyancy, supplying the layer in light elements. Over longer time scales, the layer can extend deeper by diffusion, similarly to the model proposed by Buffett and Seagle (2010).

7.3 Salt fingers in a thermally stratified layer

As mentioned in the introduction of this chapter, the stratification below the Earth's CMB may also well be of thermal origin if the CMB heat flow is subadiabatic. Since the light elements emitted at the ICB may reach the stratified layer and provide a destabilizing effect, this layer is prone to fingering instabilities. Modeling the entire outer core in a global approach with an imposed thermally stratified layer was done by Manglik et al. (2010) with a Lewis number $Le = 10$. With the PIC method, the same study can be performed in the infinite Lewis number limit which is planned in a future work. In this section, I concentrate on a more local approach by studying the dynamics of fingering convection directly inside a rotating stratified environment. A scale analysis is first conducted to calculate the expected size of fingers in core conditions. The first steps of a linear stability analysis in a Cartesian rotating frame are outlined and followed by first simulations in a basic configuration that provide a first exploration of rotating fingering convection.

7.3.1 Scale analysis

In non rotating and non magnetic systems, double-diffusive instabilities are well-known for creating their own spatial scale (Radko, 2013). The size of fingers is intrinsically controlled both by thermal diffusion and viscosity. For too large fingers, thermal diffusion is too slow to allow for a rapid equilibration with the ambient temperature. On the contrary, too small fingers create large velocity gradients and are damped by viscous forces. In non-rotating systems, the relevant scale of double-diffusive convection has been derived and confirmed by a linear stability analysis. The scale analysis is recalled below in the non-rotating case and the effect of the Coriolis force is then discussed in the context of planetary cores.

The study of double-diffusive convection generally considers fixed background thermal and compositional gradients, denoted $\overline{T}_z$ and $\overline{S}_z$, respectively. Typical temporal and spatial scales are denoted as $\langle t \rangle$ and $\langle L \rangle$. Taking the same notations as Radko (2013), the scales of velocity, temperature, compositional mass fraction, density and pressure perturbations are $\langle v' \rangle$, $\langle T' \rangle$, $\langle S' \rangle$, $\langle \rho' \rangle$ and $\langle p' \rangle$, respectively. Temperature is expressed as follows:

$$\langle T' \rangle \sim \langle L \rangle \left| \overline{T}_z \right| . \tag{7.8}$$

Because molecular dissipation plays a central role in double-diffusive convection, the magnitude of the diffusive term in the temperature equation should be comparable to the local rate of change in temperature. Since our focus will be on fully developed instabilities, it is also reasonable to assume that the nonlinear terms are equally important:

$$\frac{1}{\langle t \rangle} \sim \frac{\langle v' \rangle}{\langle L \rangle} \sim \frac{\kappa_T}{\langle L \rangle^2}. \tag{7.9}$$

For the equation of state 2.1, we expect comparable effects of temperature and salinity on density distribution:

$$\frac{\langle \rho' \rangle}{\rho_0} \sim \alpha \langle T' \rangle \sim \beta \langle S' \rangle. \tag{7.10}$$

Going further requires some assumption on the force balance. In non-rotating systems, it is usually assumed to be between viscosity, buoyancy and pressure forces:

$$g \frac{\langle \rho' \rangle}{\rho_0} \sim \nu \frac{\langle v' \rangle}{\langle L \rangle^2} \sim \frac{\langle p' \rangle}{\rho_0 \langle L \rangle}. \tag{7.11}$$

The combination of equations (7.8) to (7.11) then leads to the following scales:

$$\langle t \rangle \sim \frac{d_\nu^2}{\kappa_T},\ \langle L \rangle \sim d_\nu,\ \langle v' \rangle \sim \frac{\kappa_T}{d_\nu},\ \langle p' \rangle \sim \frac{\rho_0 \nu \kappa^T}{d_\nu^2},\ \langle T' \rangle \sim d_\nu \left| \overline{T}_z \right|,\ \langle S' \rangle \sim \frac{\alpha}{\beta} \langle T' \rangle, \tag{7.12}$$

where the typical length scale d_ν is equal to:

$$d_\nu = \left(\frac{\kappa_T \nu}{g \alpha \left| \overline{T}_z \right|} \right)^{1/4}. \tag{7.13}$$

In planetary cores, one may however question this force balance since the Coriolis force is expected to play a dominant role, at least at large scales; the viscous force being important essentially at the dissipative scale. Assuming a force balance between Coriolis, pressure and buoyancy forces would read:

$$g \frac{\langle \rho' \rangle}{\rho_0} \sim 2\Omega \langle v' \rangle \sim \frac{\langle p' \rangle}{\rho_0 \langle L \rangle}. \tag{7.14}$$

Combination of equations (7.8) to (7.10) together with equation (7.14) then gives:

$$\langle t \rangle \sim \frac{d_\Omega^2}{\kappa_T},\ \langle L \rangle \sim d_\Omega,\ \langle v' \rangle \sim \frac{\kappa_T}{d_\Omega},\ \langle p' \rangle \sim \kappa_T \Omega \rho_0,\ \langle T' \rangle \sim d_\Omega \left|\overline{T}_z\right|,\ \langle S' \rangle \sim \frac{\alpha}{\beta}\langle T' \rangle, \tag{7.15}$$

where the typical length scale d_Ω is in this case:

$$d_\Omega = \left(\frac{2\Omega\kappa_T}{g\alpha\left|\overline{T}_z\right|}\right)^{1/2}. \tag{7.16}$$

It is not completely straightforward to determine which of the scales d_ν and d_Ω is the most relevant for salt fingers in planetary cores. Evaluating these length scales requires the knowledge of the temperature gradient $|\overline{T}_z|$ in a hypothetical thermally stratified layer below the CMB, which is not precisely constrained. Estimates from Labrosse et al. (1997) and Gubbins et al. (1982) suggest that $\left|\overline{T}_z\right| \sim 10^{-4}$ K m^{-1} would be a reasonable value. Then, using the following typical values for the Earth: $\Omega \sim 7.27 \times 10^{-5}$ s^{-1}, $\nu \sim 10^{-6}$ m^2 s^{-1}, $\kappa_T \sim 10^{-5}$ m^{2}s^{-1}, $g \sim 10$ m.s^{-2} and $\alpha \sim 10^{-5}$ K^{-1} gives:

$$d_\nu \sim 18\,\text{cm} \quad ; \quad d_\Omega \sim 38\,\text{cm}. \tag{7.17}$$

To evaluate the relative importance of the Coriolis and viscous forces for salt fingers, one can compute a local Ekman number based on the local length scale d_ν:

$$E_{d_\nu} = \frac{\nu}{2\Omega d_\nu^2} \sim 0.2, \tag{7.18}$$

and similarly using the scale d_Ω:

$$E_{d_\Omega} = \frac{\nu}{2\Omega d_\Omega^2} \sim 0.05. \tag{7.19}$$

For salt fingers in terrestrial oceans, $E_{d_\nu} \sim 70$, a value significantly larger than 1. Whatever length scale is considered (d_ν or d_Ω), these estimations suggest that, contrary to the oceanic context where the effect of rotation might be safely neglected, the Coriolis force could play a much more important role in the dynamics of fingering convection in planetary cores. If this affirmation were confirmed, it would have important consequences on a theoretical point of view. It would indeed mean that the results obtained by linear and non-linear analyses for fingering and diffusive convection in the non-rotating case may not hold in some planetary cores, thereby requiring to revisit the previous studies including the effect of the Coriolis force.

Although the relevance of the scale d_Ω may not be completely discarded, it seems more reasonable on a physical point of view to assume a force balance between viscosity, buoyancy and pressure forces for salt fingers since, intrinsically, viscosity plays a role in limiting the size of the fingers and should thus appear in the typical length scale whereas there is no obvious reason to expect that the Coriolis force would influence the size of the instability. d_ν is therefore probably the relevant scale of salt fingers for planetary cores. Even though the Coriolis force may not control the size of the fingers, it may still play an important role in the dynamics of salt fingers after the onset of the first instability. Using slightly different parameters in the expression of d_ν does not change much the resulting value because of the $1/4$ exponent. The expected typical size of salt fingers in planetary cores is therefore likely comprised between 10 cm and 30 cm, giving values of the local Ekman number E_{d_ν} that fall in the range 0.07 – 1.

This scale analysis can be verified by performing a linear stability analysis, the bases of which are outlined for the rotating case in the next section. The equilibration of salt fingers and the pattern selection for their shape (such as cylinders or sheets) can then only be understood by

considering non-linear effects (Radko, 2013). Numerical simulations can serve as an interesting tool to get intuition about the mechanisms at stake and confirm predictions from mathematical analyses.

7.3.2 First steps of a linear stability analysis

In the non-rotating case, the stability analysis of double-diffusive instabilities was performed by a series of authors in the 1960s (Walin, 1964; Nield, 1967; Baines and Gill, 1969) and gave an interesting insight into the physics of growing instabilities. In particular, the results confirm the scale analysis based on the length scale d_ν, predict a range of parameters in which salt fingers and diffusive instabilities can develop and give a constraint on the horizontal wave numbers of the instabilities. However, the Coriolis force has been neglected in these studies, an assumption that, as discussed in the previous section, may be reasonable for the oceans, but probably not for planetary cores.

Here, I propose to write the equations of double-diffusive convection in the rotating case. For simplicity, the Lorentz force is not considered and a Cartesian system of coordinates is adopted, with the rotation axis parallel to $\vec{\mathbf{e}}_\mathbf{z}$. This configuration is analogous to that inside the tangent cylinder, where gravity is almost parallel to the rotation axis. The scales proposed above in the last section (with d_ν the typical length scale) and vertical background gradients of temperature and (heavy) salts concentration in the z direction are used to construct a new dimensionless form for the set of equations (2.26). For fingering convection ($\overline{T}_z > 0, \overline{S}_z > 0$), this reads:

$$\begin{cases} \dfrac{1}{P_T}\left(\dfrac{\partial \vec{\mathbf{u}}}{\partial t} + \vec{\mathbf{u}}\cdot\vec{\nabla}\vec{\mathbf{u}}\right) = -\vec{\nabla}p - \dfrac{1}{E_{d_\nu}}\vec{\mathbf{e}}_\mathbf{z}\times\vec{\mathbf{u}} + (T'-S')\vec{\mathbf{e}}_\mathbf{z} + \vec{\nabla}^2\vec{\mathbf{u}}; \\ \dfrac{\partial T'}{\partial t} + \vec{\mathbf{u}}\cdot\vec{\nabla}T' + \hat{u}_z = \nabla^2 T'; \\ \dfrac{\partial S'}{\partial t} + \vec{\mathbf{u}}\cdot\vec{\nabla}S' + \dfrac{1}{R_\rho}\hat{u}_z = \tau\nabla^2 S'; \\ \vec{\nabla}\cdot\vec{\mathbf{u}} = 0, \end{cases} \tag{7.20}$$

where $P_T = \nu/\kappa^T$ is the thermal Prandtl number, τ is the diffusivity ratio:

$$\tau = \frac{\kappa^\xi}{\kappa^T} = Le^{-1}, \tag{7.21}$$

E_{d_ν} is the (local) Ekman number:

$$E_{d_\nu} = \frac{\nu}{2\Omega d_\nu^2}, \tag{7.22}$$

and R_ρ is the density ratio defined by:

$$R_\rho = \frac{\alpha\overline{T}_z}{\beta\overline{S}_z}. \tag{7.23}$$

T' and S' are the temperature and composition perturbations, respectively:

$$\begin{cases} T = \overline{T}_z + T', \\ S = \overline{S}_z + S'. \end{cases} \tag{7.24}$$

The same equations can be written in the diffusive regime ($\overline{T}_z < 0, \overline{S}_z < 0$):

$$\begin{cases} \dfrac{1}{P_T}\left(\dfrac{\partial \vec{\mathbf{u}}}{\partial t} + \vec{\mathbf{u}} \cdot \vec{\nabla}\vec{\mathbf{u}}\right) = -\vec{\nabla}p - \dfrac{1}{E_{d_\nu}}\vec{\mathbf{e}}_\mathbf{z} \times \vec{\mathbf{u}} + (T' - S')\vec{\mathbf{e}}_\mathbf{z} + \vec{\nabla}^2\vec{\mathbf{u}}; \\ \dfrac{\partial T'}{\partial t} + \vec{\mathbf{u}} \cdot \vec{\nabla}T' - \hat{u}_z = \nabla^2 T'; \\ \dfrac{\partial S'}{\partial t} + \vec{\mathbf{u}} \cdot \vec{\nabla}S' - \dfrac{1}{R_\rho}\hat{u}_z = \tau\nabla^2 S'; \\ \vec{\nabla} \cdot \vec{\mathbf{u}} = 0. \end{cases} \tag{7.25}$$

The linear stability of this system of equations can be explored by removing the non-linear terms and substituting the variables by the linear modes:

$$(T', S', \vec{\mathbf{u}}', p') = Re(\hat{T}, \hat{S}, \hat{\mathbf{u}}, \hat{p}) \exp(\lambda t + ikx + ily + imz), \tag{7.26}$$

which gives:

$$\begin{cases} \dfrac{\lambda}{Pr}\hat{\mathbf{u}} = -i\hat{p}\vec{\mathbf{k}} + \dfrac{1}{E_{d_\nu}}\left(\hat{u}_y\vec{\mathbf{e}}_\mathbf{x} - \hat{u}_x\vec{\mathbf{e}}_\mathbf{y}\right) + (\hat{T} - \hat{S})\vec{\mathbf{e}}_\mathbf{z} - \kappa^2\hat{\mathbf{u}}; \\ \lambda\hat{T} + \hat{u}_z = -\kappa^2\hat{T}; \\ \lambda\hat{S} + \dfrac{1}{R_\rho}\hat{u}_z = -\tau\kappa^2\hat{S}; \\ \vec{\mathbf{k}} \cdot \hat{\mathbf{u}} = 0, \end{cases} \tag{7.27}$$

where $\vec{\mathbf{k}} = (k, l, m)$ and $\kappa = \left|\vec{\mathbf{k}}\right| = \sqrt{k^2 + l^2 + m^2}$.

To eliminate the pressure term, we compute the dot product of $\vec{\mathbf{k}}$ with the first equation, using the last condition $\vec{\mathbf{k}} \cdot \hat{\mathbf{u}} = 0$:

$$\hat{p} = \frac{\frac{1}{E}(k\hat{u}_y - l\hat{u}_x) + (\hat{T} - \hat{S})m}{i\kappa^2}. \tag{7.28}$$

Hence, substituting $\hat{p}$ in the first equation gives:

$$\frac{\lambda}{Pr}\hat{\mathbf{u}} = \frac{1}{E_{d_\nu}}\left[\hat{u}_y(\vec{\mathbf{e}}_\mathbf{x} - \frac{k}{\kappa^2}\vec{\mathbf{k}}) - \hat{u}_x(\vec{\mathbf{e}}_\mathbf{y} - \frac{l}{\kappa^2}\vec{\mathbf{k}})\right] + (\hat{T} - \hat{S})(\vec{\mathbf{e}}_\mathbf{z} - \frac{m}{\kappa^2}\vec{\mathbf{k}}) - \kappa^2\hat{\mathbf{u}}. \tag{7.29}$$

The two equations on $\hat{T}$ and $\hat{S}$ can be combined to compute the difference:

$$\hat{T} - \hat{S} = -\frac{R_\rho\tau\kappa^2 + \lambda R_\rho - \kappa^2 - \lambda}{R_\rho(\kappa^2 + \lambda)(\tau\kappa^2 + \lambda)}\hat{u}_z = -Au_z. \tag{7.30}$$

Projecting this equation on each direction then gives the following system of equations:

$$\begin{cases} \left[\frac{\lambda}{Pr} - \frac{1}{E_{d_\nu}}\frac{kl}{\kappa^2} + \kappa^2\right]\hat{u}_x - \frac{1}{E_{d_\nu}}\left(1 - \frac{k^2}{\kappa^2}\right)\hat{u}_y - \frac{km}{\kappa^2}A\hat{u}_z = 0; \\ \frac{1}{E_{d_\nu}}\left(1 - \frac{l^2}{\kappa^2}\right)\hat{u}_x + \left[\frac{\lambda}{Pr} + \frac{1}{E_{d_\nu}}\frac{kl}{\kappa^2} + \kappa^2\right]\hat{u}_y - \frac{lm}{\kappa^2}A\hat{u}_z = 0; \\ -\frac{1}{E_{d_\nu}}\frac{lm}{\kappa^2}\hat{u}_x + \frac{1}{E_{d_\nu}}\frac{km}{\kappa^2}\hat{u}_y + \left[\frac{\lambda}{Pr} + A + \kappa^2\right]\hat{u}_z = 0. \end{cases} \tag{7.31}$$

The condition to solve this system is that the determinant of the associated matrix be equal to zero. It seems that there is no evident simplification, so that computing this determinant by hand is cumbersome. Moreover, the result would be a polynomial expression of degree 9 for λ whose roots may be impossible to find analytically, requiring a numerical exploration.

7.3.3 Numerical simulations

In the non-rotating case, the characteristics of the primary instabilities can be predicted by a linear stability analysis but the growth of the fingers, their horizontal planform selection and the processes leading to saturation and equilibration can only be understood via non-linear considerations. The horizontal planform selection of the initial salt fingers was addressed using weakly non-linear developments by Proctor and Holyer (1986); Schmitt (1994); Radko and Stern (1999) with results that are sometimes contradictory with simulations and experiments. It seems that fingers can potentially develop various patterns in the horizontal plane. Irregular square cells are often observed in experiments, but two-dimensional sheets and triangular patterns have also been predicted theoretically. The fate of the fingers is then also controlled by non-linear phenomena. It is well known from mathematical analyses, numerical simulations and laboratory experiments that, in the non rotating-case, growing fingers are susceptible to at least two types of secondary instabilities. The first one was discovered by Holyer (1984) and causes the fingers to "wiggle" and eventually saturate, as illustrated on figure 7.6. Second, Stern (1969) showed that gravity waves can be excited in a salt fingers system, and evolve into what is often called a "thermohaline staircase" in the oceanic context. Such instabilities are referred to as "collective instabilities" and grow more slowly than Holyer instabilities. These general characteristics of fingering convection have been studied without the effect of the Coriolis force which is probably negligible in oceanic context, but perhaps not in planetary cores. Here, I propose to conduct a first qualitative numerical investigation of the potential effects of rotation on the planform selection and the growth of salt fingers using the code PARODY-PIC.

Numerous simulations of diffusive and fingering convection have been performed in 2D and 3D Cartesian geometry in the non-rotating case. The physics of double-diffusive instabilities has been explored within three different frameworks in these simulations:

1. The *unbounded gradient* model in which constant background temperature and chemical gradients are considered and tri-periodic boundary conditions are enforced to model the dynamics of double-diffusive convection far from any physical boundary. This model has been largely adopted in numerical simulations and allows to study both the convection onset and the equilibration of salt fingers.

2. The *two-layer* system made of two convective regions separated by a stratified interface. This configuration is motivated by the observation of layered structures in many double-diffusive systems.

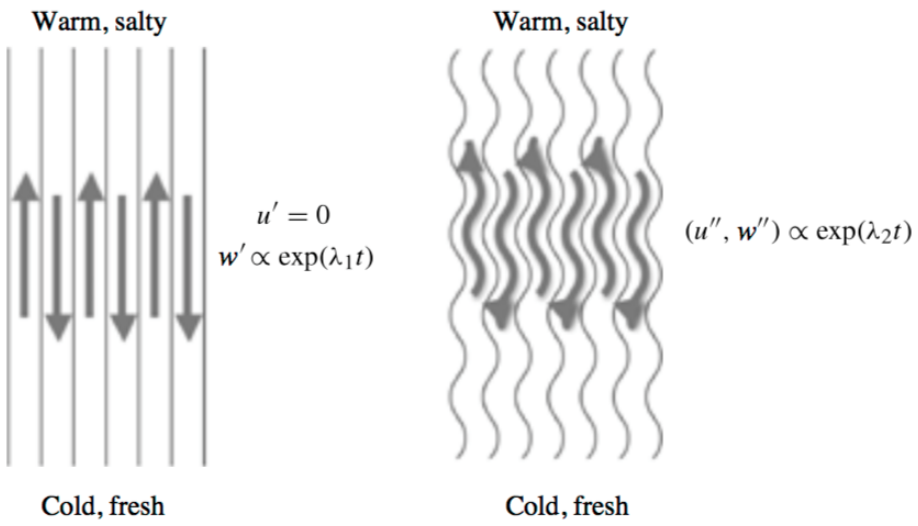

FIGURE 7.6: Schematic illustration of the secondary instabilities discovered by Holyer (1984). From Schmitt (2012)

3. The *bounded layer* model, which is more similar to the setup of Rayleigh-Bénard experiments; double-diffusive processes being confined into a box with physical impenetrable boundaries where Dirichlet or Neumann boundary conditions are imposed for temperature and composition. Even though it is difficult to find similar configurations in nature (where the fingers region has a height that is not much larger than the fingers width), these models offered an interesting fundamental insight into several aspects of fingering convection.

Because of the spherical shell geometry and intrinsic structure of PARODY, it is more natural to perform a study within the bounded layer model and keep the "classic" non-dimensionalization described in chapter 2 where the thickness of the shell is taken as the typical length scale. The parallel with the proper dimensionless equations for the double-diffusive context is then not evident, however this purely exploratory work is not meant to study fingering convection quantitatively, but rather aims at getting a first intuition about the potential role played by the Coriolis force in the dynamics of fingers. For this reason, I also adopt a very simple configuration which was historically that of the first laboratory experiments and consists of a sharp interface separating two homogeneous layers, the top one being hotter and saltier while the bottom one is cold and fresh (see Schmitt (2003) for a review about the contribution of observations and laboratory experiments). Such a configuration has the advantage to allow for an easy visualization of the onset and development of salt fingers, although it makes it difficult to study the equilibration of the instabilities and to reach a statistically stationary state since the background gradients are not maintained.

In the numerical simulations presented below, the PIC method is used to treat both temperature and a compositional field of light elements. The initial configuration consists of a spherical shell divided into two layers, the top one corresponding to values ($T = 1$, $S = 0$) and the bottom one to ($T = 0$, $S = 1$). To obtain a salt finger configuration, the thermal and compositional Rayleigh numbers are fixed to 3.75×10^5 and 1.25×10^5, respectively, so that the global contribution of both fields makes the top shell more buoyant than the bottom one. A random initialization of the tracers distribution introduces some noise in the system which is sufficient to excite fingering instabilities. In these simulations, the (global) Ekman number is varied between 10^{-3} and 10^{-4}, the thermal Prandtl number between 1 and 10. The Lewis number is infinite ($\tau = 0$). To

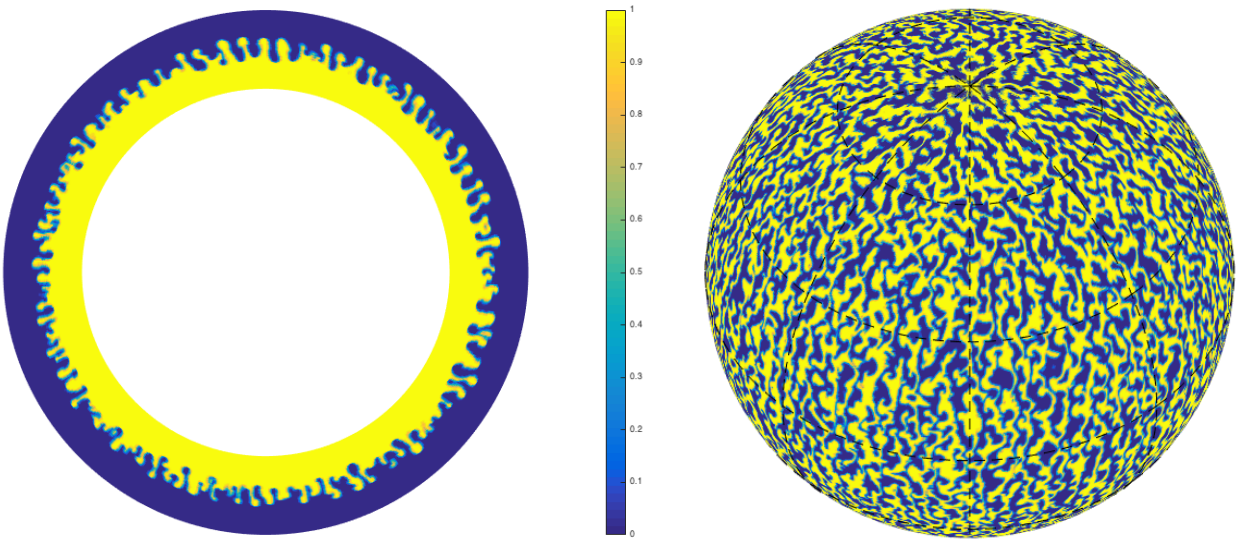

FIGURE 7.7: Equatorial section (left) and spherical map (right) of the compositional field taken in the middle of the shell ($r = (r_i + r_o)/2$) in a salt fingers experiment. The aspect ratio is $r_i/r_o = 0.7$, and the parameters are: $E = 10^{-3}$, $P_T = 1$. Spherical harmonics are computed up to a truncation $\ell_{max} = 300$. No periodicity is enforced in the solution.

save computational time, a periodicity is enforced in the solution, except when the planform selection is studied. The boundary conditions are fixed temperature at both boundaries. Since we work in the infinite Lewis number limit, there is no need to enforce any compositional boundary condition (see chapter 2).

The planform selection of salt fingers can be visualized on figure 7.7 for $E = 10^{-3}$, $P_T = 1$ and a shell aspect ratio 0.7. Spectral resolution is computed up to degree $\ell_{max} = 300$ and no periodicity is enforced in the solution. The pattern is a complex network of two-dimensional convoluted sheets. It seems that these structures have a preferential global orientation in the vertical direction, parallel to the rotation axis, a probable signature of the presence of rotation. This could be more precisely quantified in the future.

To study the growth of the fingers, a second simulation is performed at $E = 10^{-4}$ and $P_T = 1$, with an 8-fold periodicity in the solution, aspect ratio 0.35 and a spectral resolution up to degree $\ell_{max} = 320$. The time evolution of the fingers in the equatorial plane can be seen on figure 7.8. The width of the fingers varies with time between 0.01 and 0.1, giving a local Ekman number in the range 0.01-1 which is roughly in agreement with the scale analysis conducted in section 7.3.1. The "waving" of the fingers is well visible and caused by secondary instabilities of the Holyer type that are quickly excited when the first fingers grow. The Coriolis force then comes into play by systematically deviating any motion in the horizontal plane. This exacerbates the distortions caused by the Holyer instabilities and curls the tails of the fingers. The latter are elongated by this process and become thinner. This effect is well visible in the middle of the third picture from the top on figure 7.8. Then, at some point, the head of the finger detaches from its tail to form a blob, a phenomenon that is classically observed in simulations of salt fingers (see figure 7.9).

On the bottom picture of figure 7.8, the heads of the initial 10 fingers have reached the top of the shell and two of them have detached from their tail. However, a few other plumes have formed below (at least one is clearly visible in the left middle portion of the domain, under the fifth initial head starting from the left). The mechanism of formation of these secondary blobs is

probably similar to the one that is responsible for the blob instability on the plumes emanating from the ICB (cf. chapter 6): the Coriolis force acts to bend and curl the fingers, creating a configuration that is prone to a Rayleigh-Taylor instability. In order to visualize the formation of blobs in a Rayleigh-Taylor instability, a two-layer numerical experiment is performed with, in this case, the top layer being denser than the bottom one. The results are shown on figure 7.10 and resemble salt fingers except that the shape of the plumes is different and their dynamics is much more vigorous. Plumes get gradually thinner until their head separates from the initial layer forming a rising blob.

To finish, a last salt-fingers simulation is conducted with the same parameters but a thermal Prandtl number $P_T = 10$. The solution is 16-periodic and solved up to degree $\ell_{max} = 480$. Three snapshots corresponding to different times are plotted on figure 7.11. Here, due to the more efficient thermal diffusion, the fingers and blobs are smaller, with a local Ekman number close to 1. Initially only 3 fingers are present in a 16th of the sphere. Similarly to the case with $P_T = 1$, at least three extra plumes detach from parts of the pre-existing fingers as soon as the latter have gained a sufficient horizontal component, probably also due to a Rayleigh-Taylor instability. The effect of rotation is less obvious in this run and would become more visible when comparing to the equivalent non-rotating case.

7.3.4 Discussion

A scale analysis combined with a first series of numerical simulations of rotating salt fingers suggest that, in the context of planetary cores, rotation may play a more important role for fingering convection than in terrestrial oceans. The secondary instabilities that are responsible for the saturation and equilibration of salt fingers are affected by the Coriolis force, indicating that the statistically stationary state may have different properties in the rotating case. This motivates a more mathematical study that should start with a linear stability analysis to confirm the scale prediction, although this is much more arduous than in the non-rotating case. Weakly non-linear developments would also cast some light upon the role of the Coriolis force on the planform selection and equilibration of salt fingers.

Future numerical simulations should go in the direction of using a numerical setup that allows to reach a statistically stationary state either by maintaining thermal and compositional background gradients with tri-periodic boundary conditions or by injecting fixed heat and chemical flows at the boundaries. For that purpose, the code PARODY may not be very well adapted. However, the code developed by Stellmach (Traxler et al., 2011a,b) has served as a very efficient tool to explore the physics of double-diffusive convection and could therefore be a more relevant choice. An interesting question is to determine whether a thermochemical staircase can establish in the rotating case. Such a structure consists of an alternate pattern of convecting and stratified layers and could have implications both on transport properties and dynamo action in planetary cores.

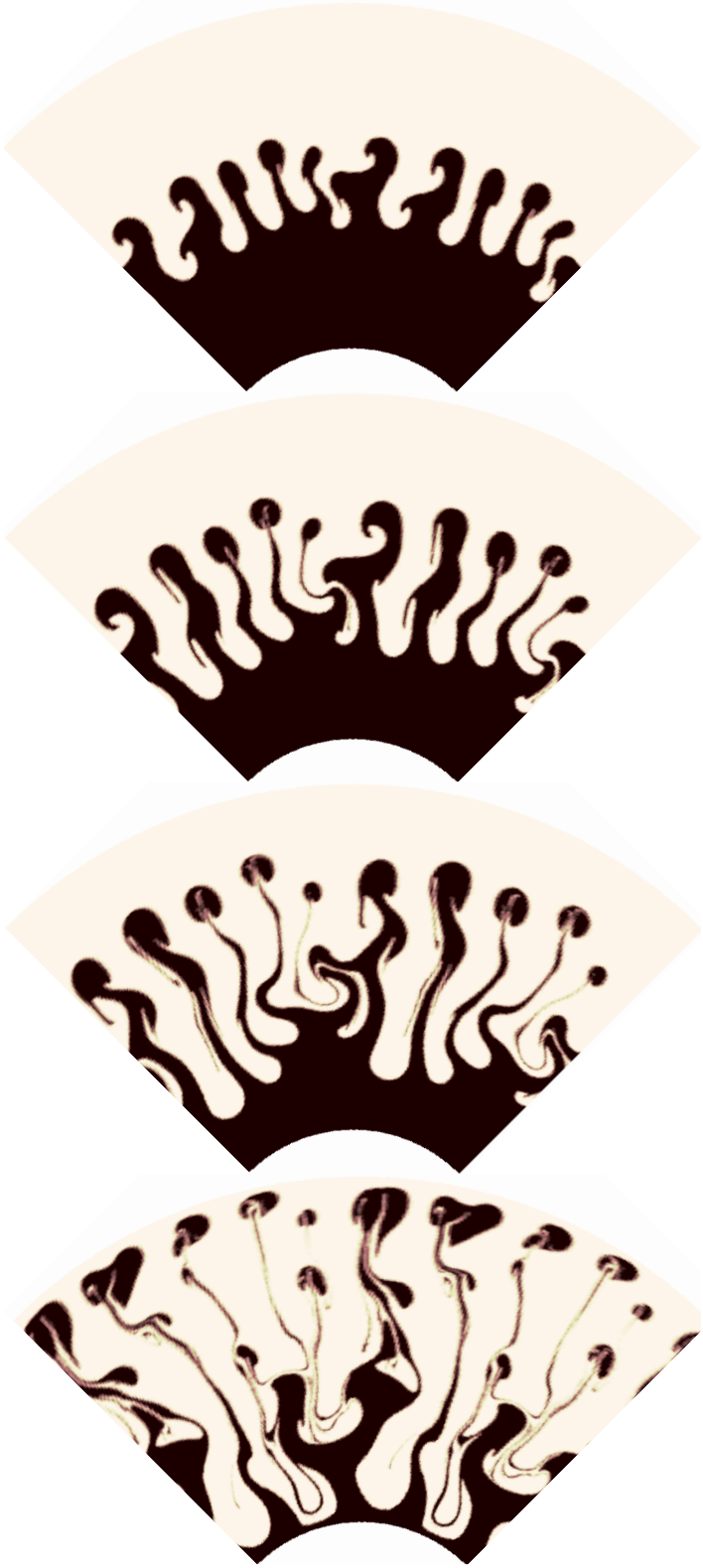

FIGURE 7.8: Compositional field in a quarter of the equatorial plane in a salt fingers simulation. From top to bottom, in viscous times: $t = 0.04$, $t = 0.05$ $t = 0.06$, $t = 0.08$. The solution is 8-periodic. Parameters: $E = 10^{-4}$, $P_T = 1$. Resolution: $N_r = 250$, $\ell_{max} = 320$. 10^8 particles are used.

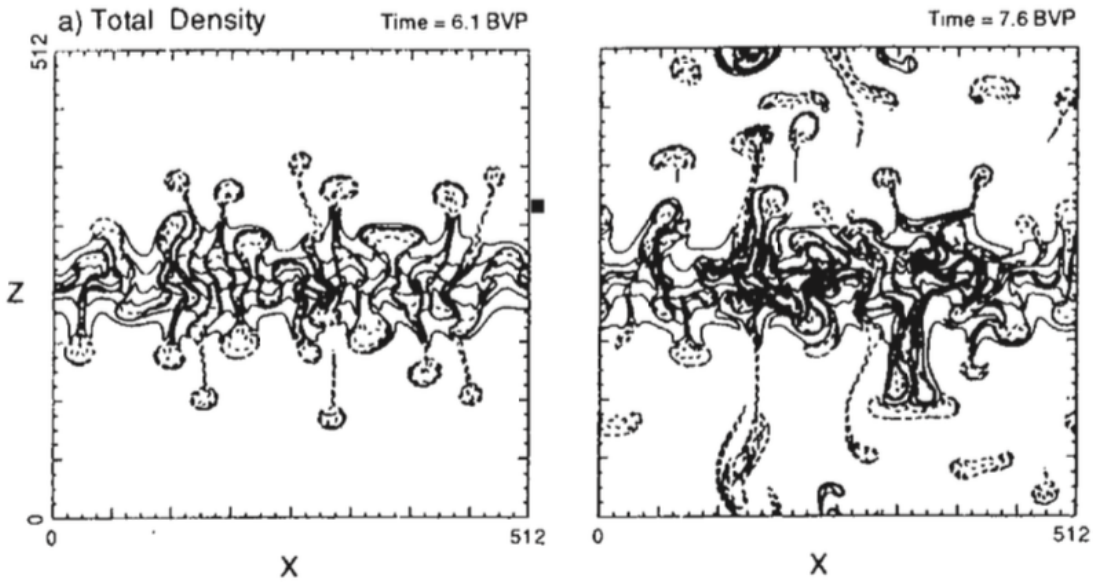

FIGURE 7.9: Two-dimensional numerical simulation of salt fingers from Shen (1993).

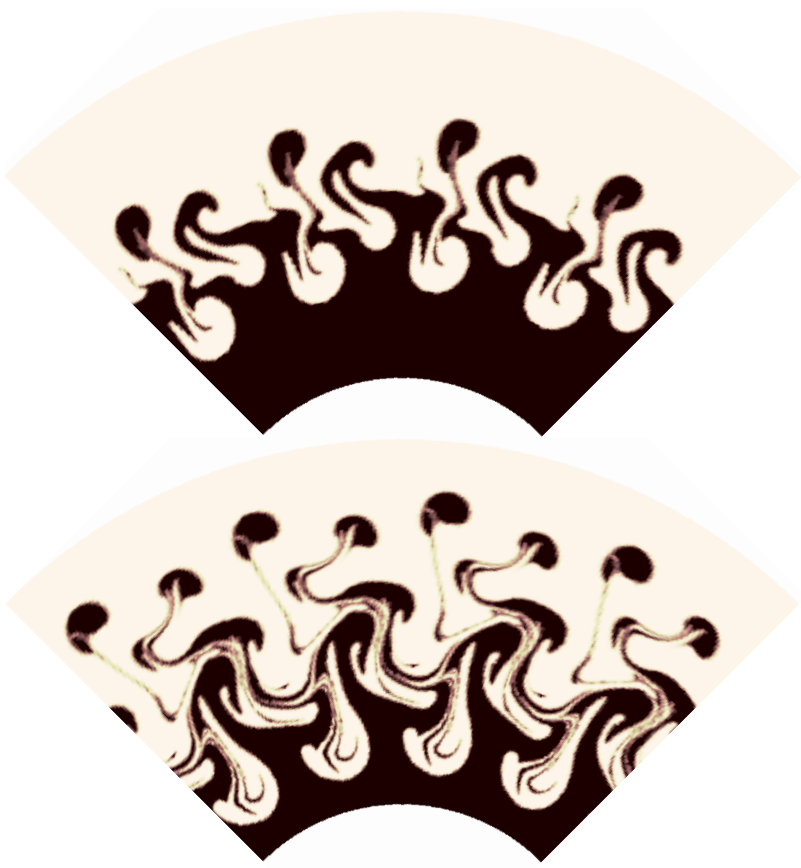

FIGURE 7.10: Simulation of a Rayleigh-Taylor instability at times $t = 0.01136$ (top) and $t = 0.01437$ (bottom), expressed in viscous times. The solution is 16-periodic. Parameters: $E = 10^{-4}$, $P_T = 1$. Resolution: $N_r = 250$, $\ell_{max} = 320$. 5×10^7 particles are used.

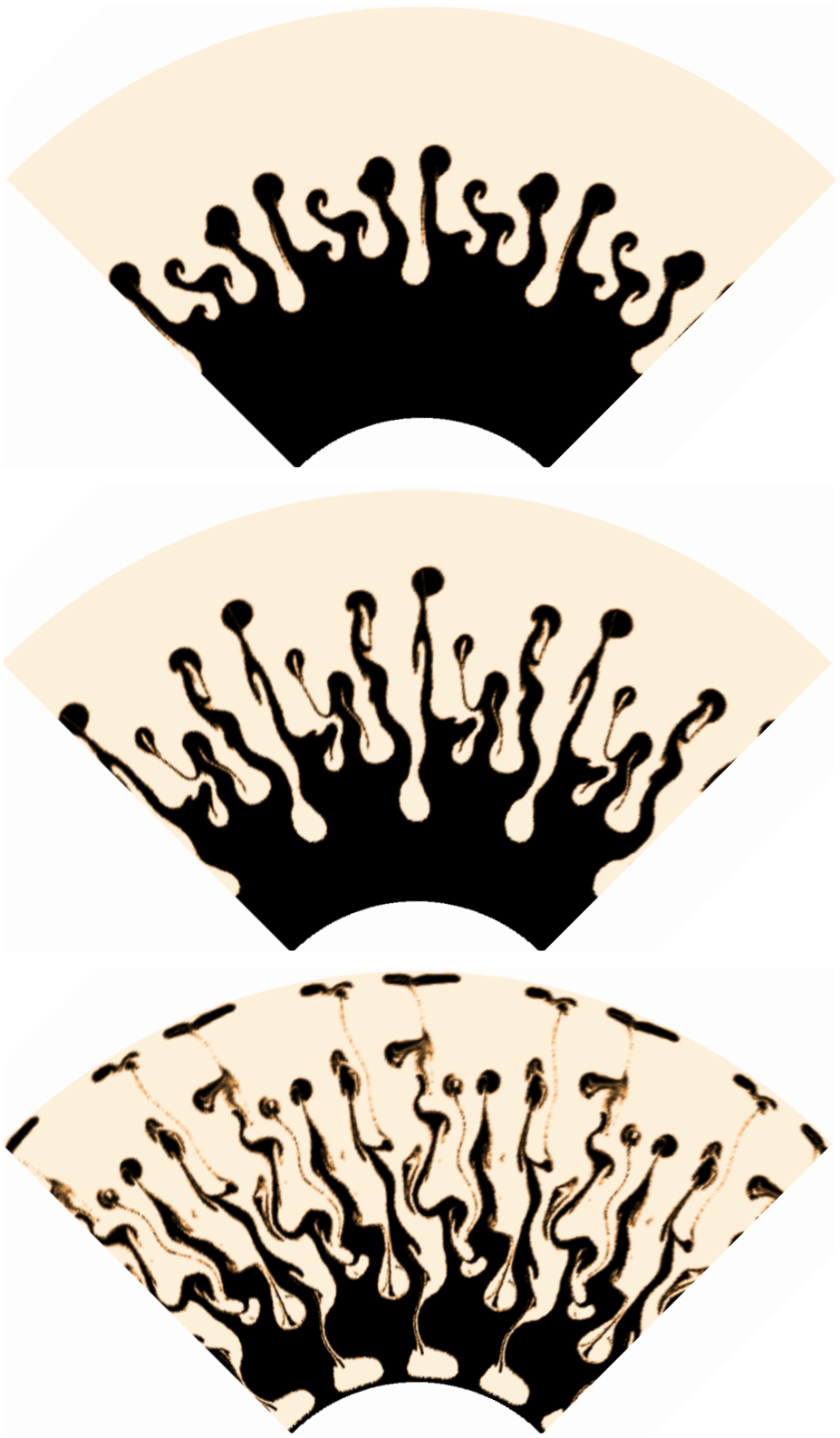

FIGURE 7.11: Salt fingers simulation. From top to bottom, in viscous times: $t = 0.06$, $t = 0.08$, $t = 0.1175$. The solution is 16-periodic. Parameters: $E = 10^{-4}$, $P_T = 10$. Resolution: $N_r = 250$, $\ell_{max} = 480$. 5×10^7 particles are used.

Chapter 8

General conclusion and perspectives

This thesis paves the way for a new path in the numerical modeling of core dynamics and therefore raises more questions than it answers. Since developing and mastering a numerical method always takes a significant time, the numerical simulations showed in chapters 6 and 7 were principally performed in the third year of my PhD. For this reason, they probably remain largely under-exploited and should be completed with other simulations. The results presented are however very promising and open several directions, even if their interpretation certainly lacks some maturity and requires a more systematic investigation. The main results and contributions of this thesis are summarized below and followed by an overview of the questions they raise and the perspectives they open up.

8.1 Summary of the main contributions of this thesis

The starting point of this work is the questioning of the codensity approach on which the large majority of geodynamo simulations have relied for the last two decades. Distinguishing both fields does not require any parameterization of the turbulence and allows for the description of both new convective regimes, double-diffusive phenomena and thermochemical coupling. In a way, the physics of thermochemical convection with different diffusivities is richer than the codensity case which can be viewed as an end-member of the full thermochemical model. Conceptually, this thesis also brings in directly the questions of the existence, dynamics and implications of potential double-diffusive phenomena in the internal liquid layers of planets which, despite having been evoked at many occasions, had received relatively little attention in theoretical models and numerical simulations so far.

The main contribution of this thesis is the development of a particle-in-cell method into the geodynamo code PARODY, providing the planetary science community with a new tool capable of exploring some of the questions mentioned above related to double-diffusive thermochemical convection in the liquid layers of planetary interiors, particularly in the infinite Lewis number limit. It was not at all evident that this method would work *a priori*, considering the multiple technical challenges related not only to the spherical geometry of the code, but also to the need to develop a method that is both sufficiently accurate in the context of planetary cores flows and efficient enough for practical applications. Certainly, there is always room for improvement with any numerical tool, but it can probably be considered that the PIC method was successfully adapted in the code PARODY, in the sense that it is both validated on benchmarks and sufficiently optimized to allow for a convenient exploration of an already interesting parameter space. As expected, the PIC method is shown to provide a better solution than most Eulerian schemes as it minimizes artificial numerical dissipation and its partly Lagrangian characteristics offer several

interesting possibilities, such as the study of mixing processes and a finer visualization of compositional structures.

This thesis also provides a series of first simulations of rotating pure compositional and thermochemical convection in the limit of infinite chemical Prandtl number. Despite being still somehow exploratory, these simulations produced very interesting and promising results that can be compared with several previous experiments and may rejuvenate some former theoretical predictions. Neglecting the chemical diffusivity produces radical changes in the convective pattern, compared to a moderate Lewis number. Without the smearing effect of diffusion, very thin compositional structures are allowed to exist, with a size that is controlled by viscosity and decreases like $E^{1/3}$. The general picture of these simulations is close to that proposed by Loper (2007) with a plumes region above the ICB, a more or less well-mixed intermediate part and a chemically stratified layer at the top of the shell. The dynamics of the plumes is influenced by the Coriolis force and by several instabilities that cause the plumes to break and form small buoyant blobs. Via mechanisms that are still to be more precisely understood, part of these blobs form a chemically stratified layer at the top of the shell that grows on time scales that are long compared to the typical overturn time. This last result rejuvenates the possibility that the stratified layer below the CMB be of chemical origin and produced by a plumes and blobs mechanism already evoked in the past by several authors (Loper, 1989; Braginsky, 1994; Moffatt and Loper, 1994; Loper, 2007). The growth of the layer may be due to mechanisms that are analogous to the filling box models introduced by Baines and Turner (1969) or be caused by the diffusion of the layer on time scales comparable to the age of the core, with some similarity to the model proposed by Buffett and Seagle (2010). The layer is thicker in the tangent cylinder and thinner in the equatorial region, which suggests that a topography may exist. Most of these results seem to hold when the stirring effect of thermal convection is added, although the details of the dynamics of thermochemical convection deserve a more in-depth study.

This thesis also directly tackles some questions tied to the double-diffusive dynamics of a chemically or thermally stratified layer in the context of planetary cores. This exploration is here again preliminary and concentrates on the fingering case; diffusive convection being usually more difficult to study. A scale analysis predicts fingers of about 20 cm in the Earth's outer core which indicates that the role of rotation could be more important than in the oceanic context. Simple simulations of rotating fingering convection show that the effect of the Coriolis force could complicate the instabilities responsible for the equilibration of salt fingers and consequently modify the transport properties established in the non-rotating case.

8.2 Discussion on the role of thermochemical coupling and magnetic field

In all the simulations presented in the chapters 6 and 7 of this thesis, neither the magnetic field nor the thermochemical coupling at the boundaries have been considered in order to keep these first explorations as simple as possible. So as to get a first intuition of the potential role played by these two ingredients and to demonstrate that they can be studied with the numerical tool developed, two preliminary simulations were performed.

The first one models the primitive magma ocean of the Earth in which heavy elements are injected homogeneously at the bottom boundary at a rate proportional to the mean heat flow. This run is described in more details in appendix B which also gives a few snapshots on figure B.1.

The results of the beginning of convection show that, even with a high buoyancy ratio, a chemically stratified layer forms at the bottom and is only partly entrained by the thermal convection above. This observation should of course be confirmed by continuing the run but is in itself very interesting and could have consequences for the dynamics of a magma ocean. It also raises questions about the role played by thermochemical coupling in this case. As more heavy elements are gradually injected, the heat flow decreases in the stratified layer, thereby also decreasing the flux of heavy elements. If it is not sufficiently supplied, the layer can be destroyed by thermal convection, but the heat flow then increases again triggering the release of heavy elements that consolidate the layer. This situation may evolve to an equilibrium or to an oscillatory state the dynamics of which should be studied.

In a second test simulation of the outer core briefly presented in appendix C, I show that it is numerically feasible to perform dynamo simulations driven by thermochemical convection including thermochemical coupling at the ICB. A heterogeneous heat flow is applied at the CMB, similarly to the simulation by Aubert et al. (2008a). This results in a variable heat flow at the ICB, a typical situation in which thermochemical coupling could play a role. The induction equation is also solved in this case and the velocity and magnetic fields are compared with a codensity case on figures C.1 and C.2. It is of course impossible to draw any conclusion with one snapshot in a first test simulation, but interesting observations can already be made. In the codensity case, the flow is organized in a large-scale circulation that generates a rather smooth dipolar magnetic field at the CMB. When chemical convection is added, thin plumes occasionally break-up this large-scale flow to create smaller eddies (see figure C.1). As a consequence, the magnetic field is still dipolar but less regular and more concentrated in localized regions (cf. figure C.2). The effect of thermochemical coupling is here not obvious to interpret and even to visualize on one snapshot. The state of the layer of light elements at some instant indeed integrates several past processes: enrichment/depletion depending on the local heat flow, and episodic destabilization of the layer to form a plume that evacuates part of the light elements. The state of the layer should thus be monitored more precisely over the course of the simulation.

Despite being very exploratory, this last simulation opens-up interesting questions about the characteristics of a dynamo driven by thermochemical flows. Simitev and Busse (2005) performed a series of numerical simulations to deduce that dynamos are more easy to obtain at low Prandtl numbers through the shear provided by differential rotation while dynamos at higher Prandtl numbers are more difficult to obtain. This would indicate that dynamo action is probably more difficult with pure chemical convection. Yet, the simulations performed in chapter 6 suggest that the flow driven by pure compositional convection can acquire some degree of organization under the effect of rotation. Also, chemical winds driven by the topography of the stratified layer could produce a zonal flow and provide an omega effect that is interesting for dynamo action (Aubert, 2005). On the other hand, the combination of thermal ($P_T = 1$) and compositional ($P_\xi = +\infty$) convection may provide rich physics. Thermal effects tend to drive a larger-scale circulation while the chemical plumes occasionally disturb it and create smaller scales. Interesting dynamos may be produced by such dynamics. Based on a simple mathematical model (cylindrical annulus), Busse (2002) also suggests that light elements could facilitate thermal convection by balancing the non-geostrophic part of the Coriolis force but advocates for the need of fully non-linear simulations. The interaction of the thermal and compositional fields, especially with thermochemical coupling and the types of dynamo action that can be generated are therefore exciting subjects to explore. Because of the complexity of this problem in terms of number of ingredients and dimensionless numbers, there is probably still a long path ahead before obtaining thermochemical dynamos that are as successful as the codensity approach in producing Earth-like magnetic fields in the sense of Christensen et al. (2010), assuming this is possible.

8.3 Future work and perspectives

8.3.1 Numerical improvements

Improving a numerical method is probably endless, so one has to focus on the aspects that are really worth for the studied applications. Considering the good results obtained at a reasonable price with the combination of a Runge-Kutta 4th order time scheme and a trilinear interpolation of the velocity, one may wonder whether spending months developing a more time consuming higher-order PIC method would really be beneficial. Experience will probably tell whether such a work is pointless or, on the contrary, if some inaccuracies in the current PIC method happen to be problematic in some context and justify the effort. Another possibly weaker aspect of the PIC method is the quite artificial treatment of diffusion, particularly that of "sub-grid" scales. Should chemical diffusion be considered in future simulations, it could be worth developing a more physical method based on the definition of a finer grid. Here again, it will be important to weigh the pros and cons before spending a significant time in the development of this complex approach.

However, there remain a few important numerical strategies that are already coded in the present effort but still need to be fully validated. The triquadratic interpolation of the velocity and the coarse grid method for full sphere applications belong to this category. More tests with a synthetic velocity field are also necessary to assess whether the trajectory of tracers can be described with a sufficient accuracy before envisioning studies of mixing processes. Validating these aspects will be performed in a very near future.

8.3.2 Open questions in core dynamics

Many aspects of the physics of thermochemical convection in rotating spherical shells have been tackled technically in this thesis. The preliminary results open-up several interesting topics deserving a more systematic exploration.

First, the details of the dynamics of pure chemical convection are not yet completely understood. Many questions remain related to the influence of the Coriolis force on the dynamics of plumes and to the comprehension of the blobs instability. Furthermore, it seems important to understand more clearly what controls the formation, growth and equilibrium thickness of a chemically stratified layer. The analogy with "filling box" models should probably be pushed further. Following the trajectories of a few particles belonging to several chemical blobs could be here a useful strategy to assess whether the layer is formed by accretion of blobs at its bottom, or if the latter penetrate up to the top of the shell, displacing the layer laterally and downward. The latter seems to be implied by the profile of the chemical advective flow. Any topography of the stratified layer should also be quantified and related to the dimensionless parameters. It is indeed an interesting result that has potential implications, for example concerning the interpretation of the seismic data used to measure the anisotropy of the inner core. As it would impose a heterogeneous boundary condition to the active dynamo region below the stratified layer, such a topography is also expected to possibly influence the magnetic pattern.

Another interesting topic that has only been superficially addressed in this thesis is the study of dynamos driven by thermochemical convection with different diffusivities. Determining the type of dynamos that can be obtained and the corresponding scaling laws can however only be performed at the price of a fastidious exploration of the parameter space which will probably be gradually completed over the course of a few years. The expected relationships between heat and

composition sources/sinks such as thermochemical coupling should be introduced progressively, otherwise it may be difficult to interpret their influence in a system that is already complex and governed by numerous dimensionless numbers. Moreover, the exact processes that take place in the mushy zone at the Earth's ICB are extremely complex and how these should be parameterized in numerical models that do not resolve such scales is a very complicated question that probably also deserves more attention.

Among the other interesting but delicate remaining questions is the potential role played by double-diffusive convection (fingering or diffusive) in core dynamics. In his book, Radko (2013) recognizes that the opinion of most double-diffusers in the oceanic context could be summarized by the following statement: *"I am sure double-diffusion is important but I am not quite sure why"*. It seems that we are much less advanced in the internal liquid layers of planets (except maybe for gas giants) since we are not even sure that these instabilities exist and have not a clue about how important they could be. Double-diffusive convection could potentially play a role at different levels. First, its effects on mixing processes in stratified environments could be a non-negligible ingredient to consider in core evolution models. Also, the contribution of a stratified layer with double-diffusive dynamics to the magnetic field could be more subtle than a pure filtering effect as sometimes anticipated in the case of the Earth and Mercury. Answering these questions requires to better assess the importance of rotation for double-diffusive processes in planetary cores, so as to determine whether the results from the oceanic and astrophysical contexts can be directly applied or if new scaling laws and parameterizations of transport and mixing processes should be looked for in the rotating case. The scale analysis performed in chapter 7 suggests that the role of rotation could be non-negligible in planetary cores. If this were to be confirmed by a linear stability analysis, it would call for new theoretical, experimental and numerical studies in the rotating case.

To finish, part of the previous questions also apply to the liquid oceans of icy satellites or to the primitive magma ocean of the Earth which have been the object of even less theoretical predictions than the Earth's outer core. In these contexts, thermochemical convection and double-diffusive processes could be important to constrain the evolution models and the habitability of icy satellites.

To conclude, the newly developed tool presented in this thesis allows the scientific community to perform studies on several of the questions listed above, part of which I will be delighted to conduct in the future. Also, in the mid or long terms, the PIC method could be implemented in codes that can work within the anelastic approximation which is more relevant than the Boussinesq approach for giant planets. Since most dynamo codes have similar structures and because the PIC method is quite modular, it should not be cumbersome to adapt it in codes like MagIC (Christensen and Wicht, 2007).

Appendix A

Construction of an axisymmetric convective loop

This section aims at constructing a simple steady velocity field $\vec{\mathbf{u}}$ whose flow lines can be derived analytically and that verifies the following properties:

1. $\vec{\nabla} \cdot \vec{\mathbf{u}} = 0$ (i.e. the flow is non-divergent),
2. the flow is at steady-state and axisymmetric with $u_\phi = 0$,
3. it mimics a "convective loop" whose center is located on the equatorial plane at mid-radius and whose associated flow lines are closed lines,
4. the velocity verifies $u_r = 0$ at each boundary.

When a tracer is initially placed at a random position and advected by the flow, it should follow a trajectory that coincides with the flow line passing through its initial location. Because the flow lines are closed, the tracer should be back to its original position after some time. Having an analytical knowledge of the flow lines therefore allows to measure cumulated errors in the trajectory of the tracer and can be used as a test to compare different advection schemes. The idea of this test was suggested by Philippe Cardin as we were running together in les Houches in October 2014.

Let us look for a velocity field of the form:

$$\vec{\mathbf{u}}(r,\theta) = u_r(r,\theta)\,\vec{\mathbf{e}}_\mathbf{r} + u_\theta(r,\theta)\,\vec{\mathbf{e}}_\theta, \tag{A.1}$$

where $\vec{\mathbf{e}}_\mathbf{r}$ and $\vec{\mathbf{e}}_\theta$ are elementary vectors pointing at the radial and co-latitudinal directions, respectively. For simplicity, u_r can be decomposed as a product of purely radial and a latitudinal functions R and Θ, respectively:

$$u_r(r,\theta) = R(r)\Theta(\theta). \tag{A.2}$$

Because u_r should equal 0 at the inner ($r = r_i$) and outer ($r = r_o$) boundaries, a simple choice of function for R can be:

$$R(r) = \sin(ar + b), \tag{A.3}$$

where a and b must be determined so that $ar_i + b = 0$ and $ar_o + b = \pi$, which gives:

$$a = \frac{\pi}{r_o - r_i} \quad \text{and} \quad b = -\frac{r_i}{r_o - r_i}\pi. \tag{A.4}$$

Secondly, since we want one single axisymmetric convective loop, we can simply choose:

$$\Theta(\theta) = \cos(\theta), \tag{A.5}$$

hence the full expression for the radial part:

$$u_r(r,\theta) = \sin(ar+b)\cos(\theta). \tag{A.6}$$

In spherical geometry, the condition $\vec{\nabla}\cdot\vec{\mathbf{u}} = 0$ together with $u_\phi = 0$ give:

$$\frac{1}{r^2}\frac{\partial(r^2 u_r)}{\partial r} + \frac{1}{r\sin\theta}\frac{\partial(\sin\theta u_\theta)}{\partial\theta} = 0. \tag{A.7}$$

The component u_θ can then be obtained by replacing u_r in equation (A.7):

$$\frac{\partial\sin(\theta)u_\theta}{\partial\theta} = -\left[2\sin(ar+b) + ar\cos(ar+b)\right]\cos(\theta)\sin(\theta). \tag{A.8}$$

Integrating this equation gives, allowing free-slip boundary conditions:

$$u_\theta(r,\theta) = -\left[\sin(ar+b) + \frac{ar}{2}\cos(ar+b)\right]\sin(\theta), \tag{A.9}$$

which allows to write the full expression of the velocity field:

$$\boxed{\vec{\mathbf{u}}(r,\theta) = \sin(ar+b)\cos(\theta)\vec{\mathbf{e}}_\mathbf{r} - \left[\sin(ar+b) + \frac{ar}{2}\cos(ar+b)\right]\sin(\theta)\vec{\mathbf{e}}_\theta}. \tag{A.10}$$

The equations for the flow lines can then be derived from the previous expressions. Since the velocity in spherical coordinates can be written as:

$$\vec{\mathbf{u}} = \dot{r}\,\vec{\mathbf{e}}_\mathbf{r} + r\dot{\theta}\,\vec{\mathbf{e}}_\theta, \tag{A.11}$$

we can equalize the radial and colatitudinal terms with the expressions (A.6) and (A.9) to obtain a system of 2 coupled differential equations:

$$\begin{cases} \dot{r} = \sin(ar+b)\cos(\theta) \\ \dot{\theta} = -\left[\dfrac{\sin(ar+b)}{r} + \dfrac{a}{2}\cos(ar+b)\right]\sin(\theta). \end{cases} \tag{A.12}$$

Decomposing $\dfrac{\partial r}{\partial t} = \dfrac{\partial r}{\partial\theta}\cdot\dfrac{\partial\theta}{\partial t}$ allows to write:

$$-\frac{\partial r}{\partial\theta}\left[\frac{\sin(ar+b)}{r} + \frac{a}{2}\cos(ar+b)\right]\sin(\theta) = \sin(ar+b)\cos(\theta), \tag{A.13}$$

which, by separating the variables and integrating between the initial position (r_0,θ_0) and the position (r,θ) at time t, leads to:

$$\int_{r_0}^{r}\frac{1}{r'}\,\mathrm{d}r' + \frac{a}{2}\int_{r_0}^{r}\frac{\cos(ar'+b)}{\sin(ar'+b)}\,\mathrm{d}r' = -\int_{\theta_0}^{\theta}\frac{\cos(\theta')}{\sin(\theta')}\,\mathrm{d}\theta'. \tag{A.14}$$

Another way to get to this equation is to write the definition of flow lines:

$$\frac{dr}{u_r} = \frac{rd\theta}{u_\theta}. \tag{A.15}$$

- The right member of equation (A.14) can be calculated by making the change of variable $u \leftarrow \sin(\theta)$:

$$-\int_{\theta_0}^{\theta} \frac{\cos(\theta')}{\sin(\theta')}\,\mathrm{d}\theta' = -\int_{\sin(\theta_0)}^{\sin(\theta)} \frac{1}{u}\,\mathrm{d}u = \ln\left[\frac{\sin(\theta_0)}{\sin(\theta)}\right]. \tag{A.16}$$

- The same procedure can be applied to calculate the left member:

$$\int_{r_0}^{r} \frac{1}{r'}\,\mathrm{d}r' + \frac{a}{2}\int_{r_0}^{r} \frac{\cos(ar'+b)}{\sin(ar'+b)}\,\mathrm{d}r' = \ln\left(\frac{r}{r_0}\right) + \frac{1}{2}\ln\left[\frac{\sin(ar+b)}{\sin(ar_0+b)}\right]. \tag{A.17}$$

Eventually, this leads to:

$$\boxed{\sin(\theta) = \frac{A(r_0,\theta_0)}{r\sqrt{\sin(ar+b)}}}, \tag{A.18}$$

with:

$$A(r_0,\theta_0) = r_0\sin(\theta_0)\sqrt{\sin(ar_0+b)}. \tag{A.19}$$

Moreover, because we must have: $\sin(\theta) \leq 1$, i.e. $\dfrac{A(r_0,\theta_0)}{r\sqrt{\sin(ar+b)}} \leq 1$, for every given point (r_0,θ_0) there exist minimal and maximal radii r_{min} and r_{max} that bound the flow line passing through (r_0,θ_0). Although r_{min} and r_{max} cannot be calculated analytically, they can easily be approached numerically to plot the corresponding flow line. Finally, since we have $\sin(\theta) = \sin(\pi-\theta)$, we get the equation:

$$\boxed{\begin{aligned} \theta(r) &= \arcsin\left(\frac{A}{r\sqrt{\sin(ar+b)}}\right) \quad \text{for} \quad 0 < \theta \leq \frac{\pi}{2} \quad \text{and} \quad r_{min} \leq r \leq r_{max} \\ \theta(r) &= \pi - \arcsin\left(\frac{A}{r\sqrt{\sin(ar+b)}}\right) \quad \text{for} \quad \frac{\pi}{2} \leq \theta < \pi \quad \text{and} \quad r_{min} \leq r \leq r_{max} \end{aligned}} \tag{A.20}$$

in which A, r_{min} and r_{max} depend on the initial position (r_0,θ_0).

This formulation is sufficient to plot the theoretical trajectory of any randomly placed tracer. This trajectory follows the flow line passing through the initial position of the tracer. Examples of flow lines obtained using expression (A.20) are displayed on figure A.1. Even though the resulting velocity field may not correspond to a physically relevant situation, it can be used as synthetic data to perform advection tests in which the distance $\epsilon_{err}(t)$ between the tracer and its theoretical flow line is monitored through time, for different advection schemes. The distance ϵ_{err} is determined by finding the point of the flow line that is closest to the tracer.

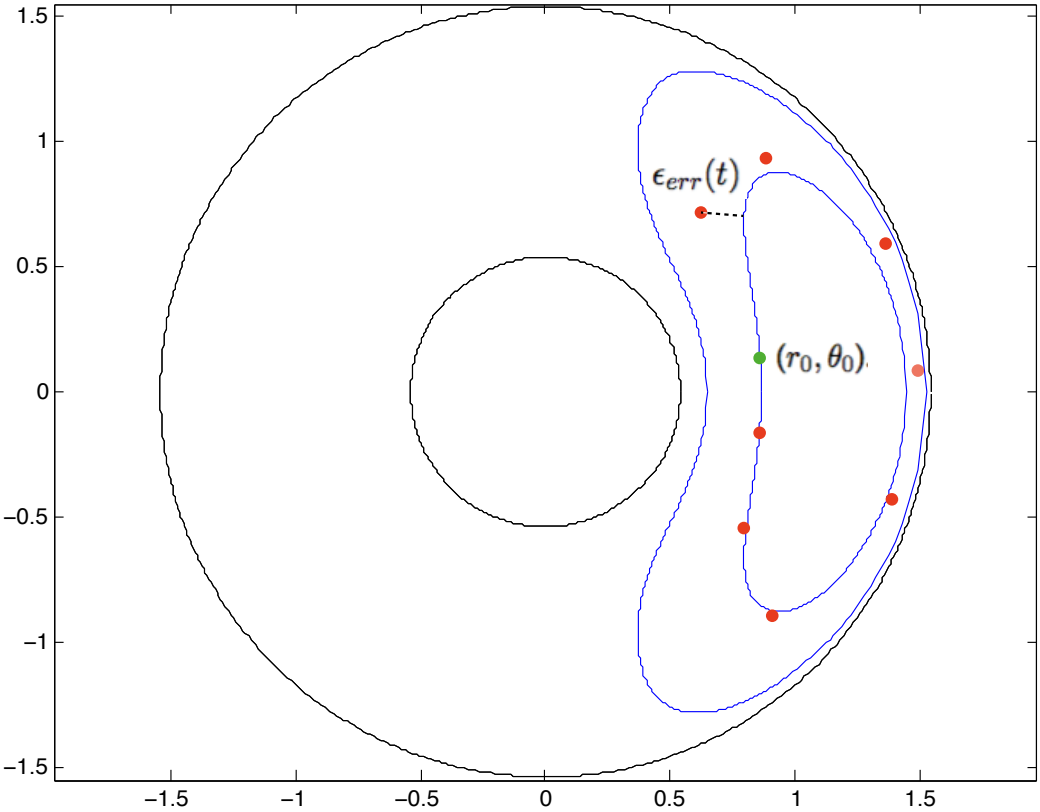

FIGURE A.1: Illustration of two flow lines (in blue) in a longitudinal plane obtained using equation (A.20). The red plain circles represent successive schematic positions of a tracer initially placed in (r_0, θ_0) (green plain circle). The deviation $\epsilon_{err}(t)$ with respect to the flow line has been deliberately exaggerated to make it more visible.

Appendix B

Preliminary simulation of the primitive magma ocean of the Earth

In this appendix, the preliminary results of a first simulation of the primitive magma ocean of the Earth are presented. The magma ocean is modeled in a spherical shell with aspect ratio $r_i/r_o = 0.7$ by solving the set of equations (2.26), except the induction equation. The parameters for the run shown below are: $E = 10^{-3}$, $Ra = 10^4$, $\mathcal{R} = 20$, $P_T = 1$, $Le = +\infty$. The adopted resolution is: $N_r = 120$, $\ell_{max} = 100$. The boundary conditions for temperature are a fixed heat flow at the top boundary and a fixed temperature at the bottom. A periodic temperature perturbation of degree and order 4 is initially imposed. As for composition, a null flux is set at the top. At the bottom boundary, a homogeneous flux of heavy elements is injected and is proportional to the mean bottom heat flow via the equation (2.49) established in section 2.3.3. This situation is analogous to that of the inner core boundary, except that, for reasons tied to the thermodynamics of this system, the crystallization enriches the liquid above in heavier elements, therefore creating a denser layer. The initial compositional field is zero everywhere. The simulation was not continued until a statistically stationary state and only the beginning of convection is shown in the results plotted on figure B.1.

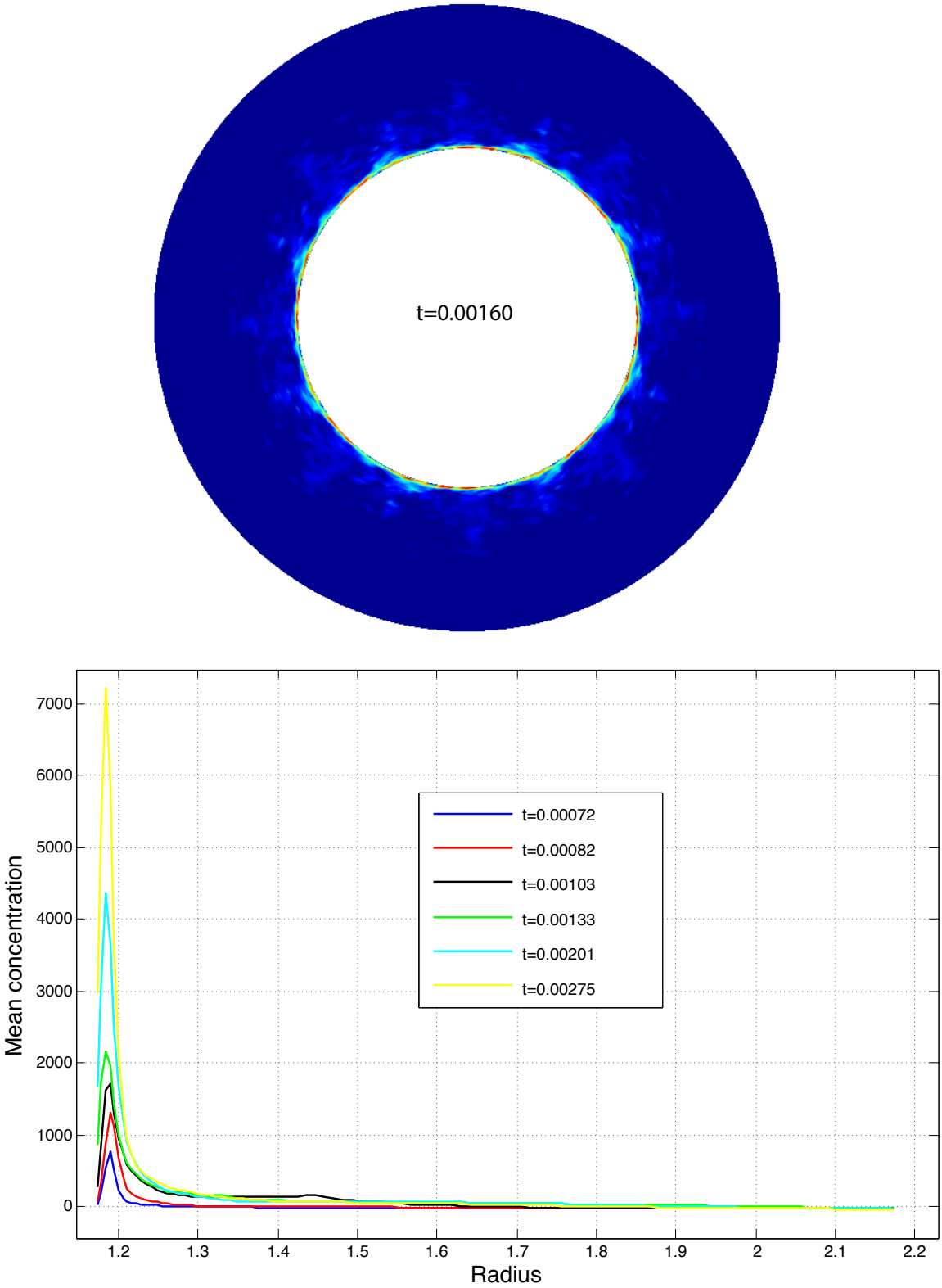

FIGURE B.1: Top: equatorial section of the compositional field at time $t = 0.00160$. Bottom: radial profiles of the mean compositional field at different times. Times are expressed in viscous times.

Appendix C

Towards thermochemically driven dynamos

In this section, I present the results of a first test of geodynamo simulation driven by thermochemical convection and including thermochemical coupling at the inner core boundary. The configuration of this run is inspired from the simulation performed by Aubert et al. (2008a) in which a perturbation of the heat flow is considered at the CMB using tomographic data and produces a flow in the shell capable of sustaining both an Earth-like magnetic field and a laterally variable heat flow at the ICB corresponding to a translation mode.

In the simulation presented below, the full set of equations (2.26) is solved, including the induction equation. The parameters for this run are: $E = 3 \times 10^{-4}$, $Ra = 100$, $P_T = 1$, $P_m = 2$, $\mathcal{R} = 1$ and $Le = +\infty$. The aspect ratio is $r_i/r_o = 0.35$ and the resolution $(N_r = 150, \ell_{max} = 160)$. Thermal boundary conditions are fixed temperature at the ICB and fixed heat flow at the CMB with a perturbation computed from tomographic data, equivalently to the boundary conditions used for codensity in Aubert et al. (2008a). The CMB chemical flux is set to zero and the ICB flux is locally proportional to the heat flux, according to the relation (2.49) established in section 2.3.3. A volumetric sink term is introduced to equilibrate the injected light elements and is adapted accordingly at each step. In this formulation, thermal and compositional buoyancy flows are coupled and cannot be set independently at the boundary. An "equivalent" codensity case is also run with identical E, P_T, P_m and Ra and the same boundary conditions as the thermal field in the thermochemical simulation.

Snapshots of the velocity field in the equatorial plane and of the radial component of the magnetic field at the CMB are shown on figures C.1 and C.2, respectively. The results of the codensity run are also added on these figures for comparison.

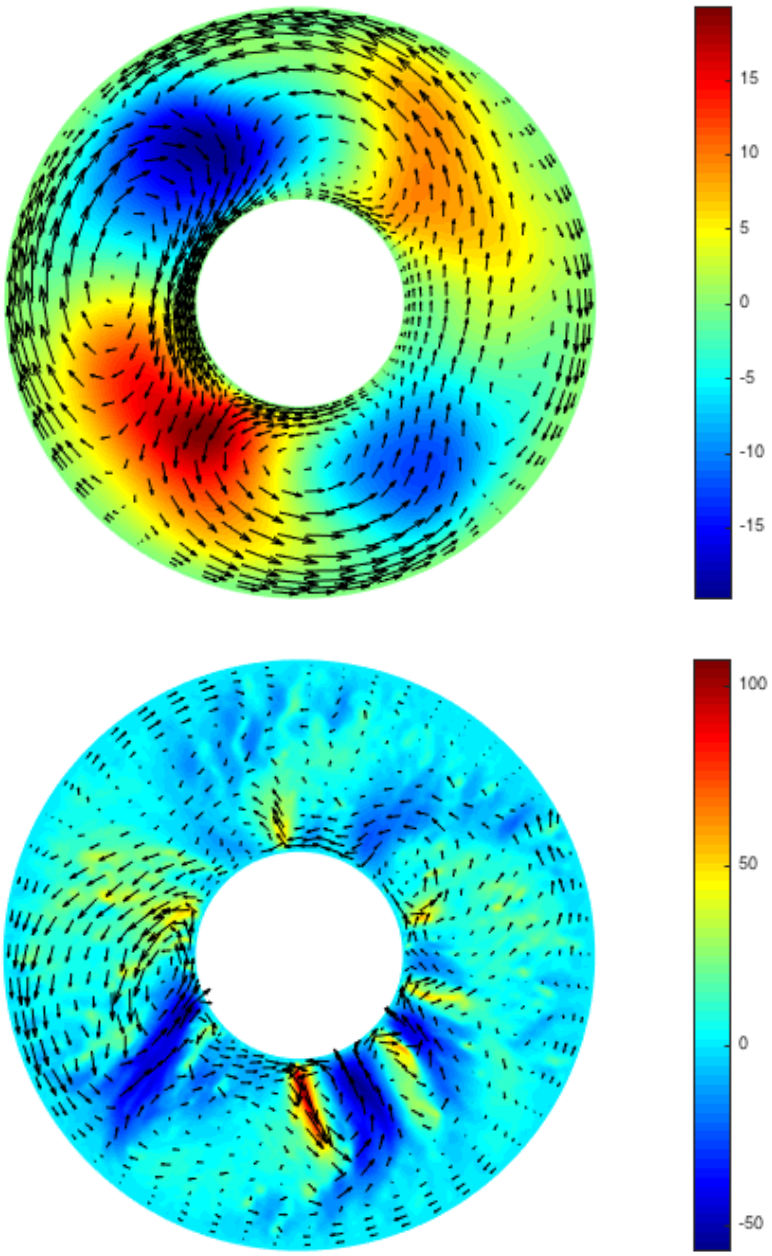

FIGURE C.1: Equatorial snapshots of the radial velocity fields (colors) in the codensity case (top) and infinite Lewis number case (bottom). Both snapshots are taken close to the statistically steady state although the latter is still not completely reached.

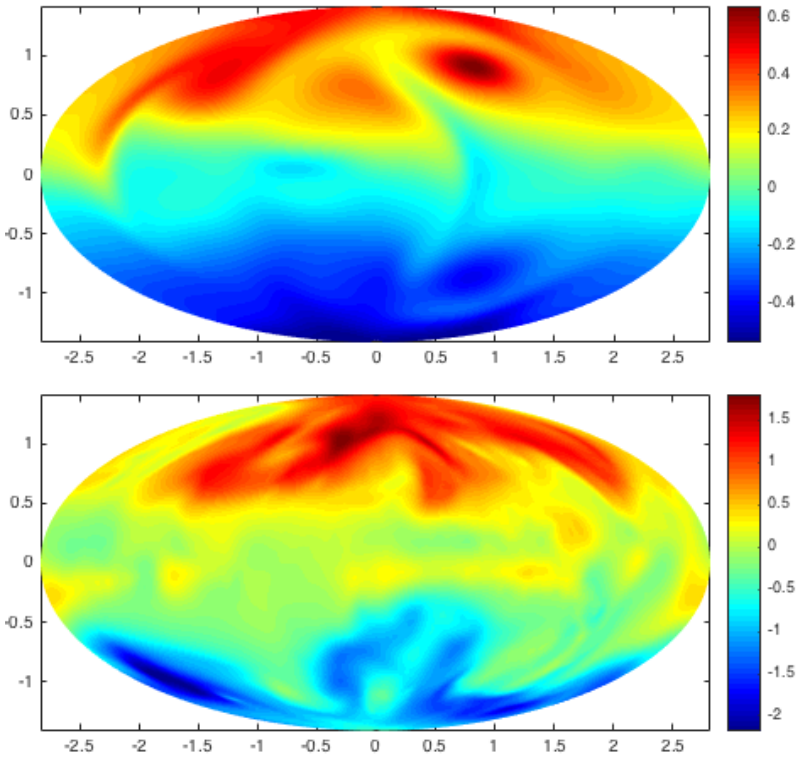

FIGURE C.2: Radial component of the magnetic field at the CMB, corresponding to the snapshots of figure C.1. Top: codensity case; bottom: infinite Lewis number case.

Appendix D

Published article

The article published during this PhD can be consulted at: https://doi.org/10.1016/j.jcp.2017.06.028.

Bibliography

Alboussière, T., Deguen, R. and Melzani, M., 2010. Melting-induced stratification above the Eart's inner core due to convective translation. Nature, 466: 744–747.

Alfè, D., Gillan, M. and Price, G., 2002. Composition and temperature of the Earth's core constrained by combining ab initio calculations and seismic data. Earth and Planetary Science Letters, 195: 91–98.

Allègre, C. J., Poirier, J.-P., Humler, E. and Hofmann, A. W., 1995. The chemical composition of the earth. Earth and Planetary Science Letters, 134: 515–526.

Amit, H. and Olson, P., 2015. Lower mantle superplume growth excites geomagnetic reversals. Earth and Planetary Science Letters, 414: 68–76.

Anderson, D. V. and Shumaker, D. E., 1995. Hybrid ordered particle simulation (HOPS) code for plasma modelling on vector-serial, vector-parallel, and massively parallel computers. Computer physics communications, 87: 16–34.

Anufriev, A., Jones, C. and Soward, A., 2005. The boussinesq and anelastic liquid approximations for convection in the earth's core. Physics of the Earth and Planetary Interiors, 152: 163–190.

Aubert, J., 2005. Steady zonal flows in spherical shell dynamos. Journal of Fluid Mechanics, 542: 53–67.

Aubert, J., Amit, H., Hulot, G. and Olson, P., 2008a. Thermochemical flows couple the Earth's inner core growth to mantle heterogeneity. Nature: 758–761.

Aubert, J., Aurnou, J. and Wicht, J., 2008b. The magnetic structure of convection-driven numerical dynamos. Geophys. J. Int.: 945–956.

Aubert, J., Finlay, C. and Fournier, A., 2013. Bottom-up control of geomagnetic secular variation by the Earth's inner core. Nature: 219–223.

Aubert, J., Gastine, T. and Fournier, A., 2016. Spherical convective dynamos in the rapidly rotating asymptotic regime. arXiv preprint arXiv:1611.04776.

Aubert, J., Labrosse, S. and Poitou, C., 2009. Modelling the palaeo-evolution of the geodynamo. Geophysical Journal International, 179: 1414–1428.

Aurnou, J., Andreadis, S., Zhu, L. and Olson, P., 2003. Experiments on convection in earth's core tangent cylinder. Earth and Planetary Science Letters, 212: 119–134.

Baehr, J., Hirschi, J., Beismann, J.-O. and Marotzke, J., 2004. Monitoring the meridional overturning circulation in the north atlantic: A model-based array design study. Journal of Marine Research, 62: 283–312.

Baines, P. and Gill, A., 1969. On thermohaline convection with linear gradients. Journal of Fluid Mechanics, 37: 289–306.

Baines, W. and Turner, J., 1969. Turbulent buoyant convection from a source in a confined region. Journal of Fluid mechanics, 37: 51–80.

Bardenhagen, S. and Kober, E., 2004. The generalized interpolation material point method. Computer Modeling in Engineering and Sciences, 5: 477–496.

Batchelor, G., 1949. Diffusion in a field of homogeneous turbulence. i. eulerian analysis. Australian Journal of Chemistry, 2: 437–450.

Bec, J., Biferale, L., Boffetta, G., Cencini, M., Musacchio, S. and Toschi, F., 2006. Lyapunov exponents of heavy particles in turbulence. Physics of Fluids, 18: 091702.

Beckermann, C. and Viskanta, R., 1988. Double-diffusive convection during dendritic solidification of a binary mixture. PhysicoChemical Hydrodynamics, 10: 195–213.

Bergman, M. I. and Fearn, D. R., 1994. Chimneys on the earth's inner-outer core boundary? Geophysical research letters, 21: 477–480.

Beuthe, M., Rivoldini, A. and Trinh, A., 2016. Enceladus's and Dione's floating ice shells supported by minimum stress isostasy. Geophysical Research Letters, 43.

Birdsall, C. K., 1991. Particle-in-cell charged-particle simulations, plus Monte Carlo collisions with neutral atoms, PIC-MCC. IEEE Transactions on Plasma Science, 19: 65–85.

Borkar, S. and Chien, A. A., 2011. The future of microprocessors. Communications of the ACM, 54: 67–77.

Boukaré, C.-E., Ricard, Y. and Fiquet, G., 2015. Thermodynamics of the mgo-feo-sio2 system up to 140 gpa: Application to the crystallization of earth's magma ocean. Journal of Geophysical Research: Solid Earth, 120: 6085–6101.

Bowers, K., 2001. Accelerating a particle-in-cell simulation using a hybrid counting sort. Journal of Computational Physics, 173: 393–411.

Brackbill, J. U., Kothe, D. B. and Ruppel, H. M., 1988. FLIP: A low-dissipation, particle-in-cell method for fluid flow. Computer Physics Communications, 48: 25–38.

Braginsky, S., 1994. Mac-oscillations of the hidden ocean of the core. Journal of geomagnetism and geoelectricity, 45: 1517–1538.

Braginsky, S. I., 2006. Formation of the stratified ocean of the core. Earth and Planetary Science Letters, 243: 650–656.

Braginsky, S. I. and Roberts, P. H., 1995. Equations governing convection in Earth's core and the geodynamo. Geophysical & Astrophysical Fluid Dynamics, 79: 1–97.

Breuer, M., Manglik, A., Wicht, J., Trümper, T., Harder, H. and Hansen, U., 2010. Thermochemically driven convection in a rotating spherical shell. Geophys. J. Int.: 150–162.

Bubnova, O., 2017. Nanoelectronics: A 2d microprocessor. Nature Nanotechnology.

Buffett, B. A. and Seagle, C. T., 2010. Stratification of the top of the core due to chemical interactions with the mantle. Journal of Geophysical Research: Solid Earth, 115.

Buneman, O., 1959. Dissipation of currents in ionized media. Physical Review, 115: 503.

Busse, F., 2002. Is low rayleigh number convection possible in the earth's core? Geophysical research letters, 29.

Čadek, O., Tobie, G., Van Hoolst, T., Massé, M., Choblet, G., Lefèvre, A., Mitri, G., Baland, R.-M., Běhounková, M., Bourgeois, O. et al., 2016. Enceladus's internal ocean and ice shell constrained from Cassini gravity, shape, and libration data. Geophysical Research Letters.

Cao, A. and Romanowicz, B., 2004. Hemispherical transition of seismic attenuation at the top of the earth's inner core. Earth and Planetary Science Letters, 228: 243–253.

Cardin, P. and Olson, P., 1992. An experimental approach to thermochemical convection in the earth's core. Geophysical research letters, 19: 1995–1998.

Cébron, D. and Hollerbach, R., 2014. Tidally driven dynamos in a rotating sphere. The Astrophysical Journal Letters, 789: L25.

Chen, C. and Chen, F., 1991. Experimental study of directional solidification of aqueous ammonium chloride solution. Journal of Fluid Mechanics, 227: 567–586.

Chen, C. and Turner, J., 1980. Crystallization in a double-diffusive system. Journal of Geophysical Research: Solid Earth, 85: 2573–2593.

Christensen, U., Aubert, J., Cardin, P., Dormy, E., Gibbons, S., Glatzmaier, G., Grote, E., Honkura, Y., Jones, C., Kono, M., Matsushima, M., Sakuraba, A., Takahashi, F., Tilgner, A., Wicht, J. and Zhang, K., 2001. A numerical dynamo benchmark. Physics of the Earth and Planetary Interiors: 25–34.

Christensen, U. R., 2006. A deep dynamo generating mercury's magnetic field. Nature, 444: 1056–1058.

Christensen, U. R., 2015. Iron snow dynamo models for ganymede. Icarus, 247: 248–259.

Christensen, U. R., Aubert, J. and Hulot, G., 2010. Conditions for earth-like geodynamo models. Earth and Planetary Science Letters, 296: 487–496.

Christensen, U. R. and Wicht, J., 2007. Numerical Dynamo Simulations. In: Core Dynamics, Elsevier, pp. 245–282.

Christensen, U. R. and Wicht, J., 2008. Models of magnetic field generation in partly stable planetary cores: Applications to mercury and saturn. Icarus, 196: 16–34.

Christensen, U. R. and Yuen, D. A., 1984. The interaction of a subducting lithospheric slab with a chemical or phase boundary. Journal of Geophysical Research: Solid Earth, 89: 4389–4402.

Claßen, S., Heimpel, M. and Christensen, U., 1999. Blob instability in rotating compositional convection. Geophysical research letters, 26: 135–138.

Copley, S., Giamei, A. F., Johnson, S. and Hornbecker, M., 1970. The origin of freckles in unidirectionally solidified castings. Metallurgical and Materials Transactions B, 1: 3455–3455.

Davies, D., Davies, J., Hassan, O., Morgan, K. and Nithiarasu, P., 2007. Investigations into the applicability of adaptive finite element methods to two-dimensional infinite prandtl number thermal and thermochemical convection. Geochemistry, Geophysics, Geosystems, 8.

de Wijs, G. A., Kresse, G., Vočadlo, L., Dobson, D., Alfe, D., Gillan, M. J. and Price, G. D., 1998. The viscosity of liquid iron at the physical conditions of the earth's core. Nature, 392: 805–807.

Decyk, V. K., Karmesin, S. R., de Boer, A. and Liewer, P. C., 1996. Optimization of particle-in-cell codes on reduced instruction set computer processors. Computers in Physics, 10: 290–298.

Decyk, V. K. and Singh, T. V., 2014. Particle-in-cell algorithms for emerging computer architectures. Computer Physics Communications, 185: 708–719.

Deguen, R., Alboussiere, T. and Brito, D., 2007. On the existence and structure of a mush at the inner core boundary of the earth. Physics of the Earth and Planetary Interiors, 164: 36–49.

Deguen, R. and Cardin, P., 2011. Thermochemical convection in Earth's inner core. Geophys. J. Int., 187: 1101–1118.

Dormy, E., Cardin, P. and Jault, D., 1998. MHD flow in a slightly differentially rotating spherical shell, with conducting inner core, in a dipolar magnetic field. Earth and Planetary Science Letters, 160: 15–30.

Dumberry, M. and Rivoldini, A., 2015. Mercury's inner core size and core-crystallization regime. Icarus, 248: 254–268.

Dziewonski, A. M. and Anderson, D. L., 1981. Preliminary reference earth model. Physics of the earth and planetary interiors, 25: 297–356.

Edwards, E. and Bridson, R., 2012. A high-order accurate particle-in-cell method. International Journal for Numerical Methods in Engineering, 90: 1073–1088.

Eggler, D. H., 1976. Does co2 cause partial melting in the low-velocity layer of the mantle? Geology, 4: 69–72.

Elster, A. C., 1994. Parallelization issues and particle-in-cell codes. Ph.D. thesis, Cornell University.

Eltayeb, I. and Loper, D., 1997. On the stability of vertical double-diffusive interfaces. part 3. cylindrical interface. Journal of Fluid Mechanics, 353: 45–66.

Evans, M. W., Harlow, F. H. and Bromberg, E., 1957. The particle-in-cell method for hydrodynamic calculations. Tech. rep., DTIC Document.

Ewing, R. E. and Wang, H., 2001. A summary of numerical methods for time-dependent advection-dominated partial differential equations. Journal of Computational and Applied Mathematics, 128: 423–445.

Fearn, D. R. and Loper, D. E., 1981. Compositional convection and stratification of Earth's core.

Fearn, D. R., Loper, D. E. and Roberts, P. H., 1981. Structure of the earth's inner core. Nature, 292: 232–233.

Fehlberg, E., 1968. Classical fifth-, sixth-, sventh-, and eighth-order Runge-Kutta formulas with step size.

Fonseca, R. A., Silva, L. O., Tsung, F. S., Decyk, V. K., Lu, W., Ren, C., Mori, W. B., Deng, S., Lee, S., Katsouleas, T. et al., 2002. Osiris: a three-dimensional, fully relativistic particle in cell code for modeling plasma based accelerators. In: International Conference on Computational Science, Springer, pp. 342–351.

Fowler, A., 1985. The formation of freckles in binary alloys. IMA Journal of Applied Mathematics, 35: 159–174.

Franck, S., 1982. Ascending droplets in the earth's core. Physics of the Earth and Planetary Interiors, 27: 249–254.

Garaud, P., 2013. Double-diffusive convection. EAS Publications Series, 63: 285–295.

Gerya, T. and Yuen, D., 2003. Characteristics-based marker-in-cell method with conservative finite-differences schemes for modeling geological flows with strongly variable transport properties. Physics of the Earth and Planetary Interiors: 293–318.

Gierasch, P. J. and Conrath, B. J., 1987. Vertical temperature gradients on uranus: Implications for layered convection. Journal of Geophysical Research: Space Physics, 92: 15019–15029.

Gilbert, W., 1958. De magnete. Courier Corporation.

Glatzmaier, G. A., 2013. Introduction to modeling convection in planets and stars: Magnetic field, density stratification, rotation. Princeton University Press.

Glatzmaier, G. A. and Roberts, P. H., 1996. An anelastic evolutionary geodynamo simulation driven by compositional and thermal convection. Physica D: Nonlinear Phenomena, 97: 81–94.

Glatzmaiers, G. A. and Roberts, P. H., 1995. A three-dimensional self-consistent computer simulation of a geomagnetic field reversal. Nature, 377: 203–209.

Gomi, H., Ohta, K., Hirose, K., Labrosse, S., Caracas, R., Verstraete, M. and Herlund, J., 2013. The high conductivity of iron and thermal evolution of the Earth's core. Earth Planet. Inter.: 88–103.

Gubbins, D., 2007. Geomagnetic constraints on stratification at the top of earth's core. Earth, planets and space, 59: 661–664.

Gubbins, D. and Davies, C., 2013. The stratified layer at the core–mantle boundary caused by barodiffusion of oxygen, sulphur and silicon. Physics of the Earth and Planetary Interiors, 215: 21–28.

Gubbins, D., Masters, G. and Nimmo, F., 2008. A thermochemical boundary layer at the base of earth's outer core and independent estimate of core heat flux. Geophysical Journal International, 174: 1007–1018.

Gubbins, D., Thomson, C. and Whaler, K., 1982. Stable regions in the earth's liquid core. Geophysical Journal International, 68: 241–251.

Guillot, T., Stevenson, D. J., Hubbard, W. B. and Saumon, D., 2004. The interior of jupiter. Jupiter: The Planet, Satellites and Magnetosphere: 35–57.

Hansen, U. and Yuen, D. A., 1994. Effects of depth-dependent thermal expansivity on the interaction of thermal-chemical plumes with a compositional boundary. Physics of the Earth and Planetary Interiors, 86: 205–221.

Harder, H. and Christensen, U. R., 1996. A one-plume model of martian mantle convection. Nature, 380: 507.

Harten, A., 1983. High resolution schemes for hyperbolic conservation laws. Journal of computational physics, 49: 357–393.

Harten, A., Engquist, B., Osher, S. and Chakravarthy, S. R., 1987. Uniformly high order accurate essentially non-oscillatory schemes, iii. Journal of computational physics, 71: 231–303.

Hauck, S. A., Aurnou, J. M. and Dombard, A. J., 2006. Sulfur's impact on core evolution and magnetic field generation on ganymede. Journal of Geophysical Research: Planets, 111.

Heister, T., Dannberg, J., Gassmöller, R. and Bangerth, W., 2017. High accuracy mantle convection simulation through modern numerical methods. ii: Realistic models and problems. arXiv preprint arXiv:1702.05075.

Helffrich, G. and Kaneshima, S., 2004. Seismological constraints on core composition from fe-os liquid immiscibility. Science, 306: 2239–2242.

Helffrich, G. and Kaneshima, S., 2010. Outer-core compositional stratification from observed core wave speed profiles. Nature, 468: 807–810.

Hernlund, J., McNamara, A. and Schubert, G., 2015. The core-mantle boundary region. Treatise on Geophysics, 7: 461–519.

Hirose, K., Labrosse, S. and Hernlund, J., 2013. Composition and state of the core. Annual Review of Earth and Planetary Sciences, 41: 657–691.

Hirose, K., Morard, G., Sinmyo, R., Umemoto, K., Hernlund, J., Helffrich, G. and Labrosse, S., 2017. Crystallization of silicon dioxide and compositional evolution of the earth's core. Nature, 543: 99–102.

Hirth, G. and Kohlstedt, D. L., 1996. Water in the oceanic upper mantle: implications for rheology, melt extraction and the evolution of the lithosphere. Earth and Planetary Science Letters, 144: 93–108.

Hoffmann, K. A. and Chiang, S. T., 2000. Computational fluid dynamics volume i. Engineering Education System, Wichita, Kan, USA.

Holford, J. M. and Linden, P., 1999. Turbulent mixing in a stratified fluid. Dynamics of atmospheres and oceans, 30: 173–198.

Holmes, A., 1945. Principles of physical geology. GFF, 67: 115–116.

Holyer, J. Y., 1984. The stability of long, steady, two-dimensional salt fingers. Journal of Fluid Mechanics, 147: 169–185.

Honda, M., Meyer-ter Vehn, J. and Pukhov, A., 2000. Two-dimensional particle-in-cell simulation for magnetized transport of ultra-high relativistic currents in plasma. Physics of Plasmas, 7: 1302–1308.

Hong, W., House, D. H. and Keyser, J., 2008. Adaptive particles for incompressible fluid simulation. The Visual Computer, 24: 535–543.

Hori, K., Wicht, J. and Christensen, U., 2012. The influence of thermo-compositional boundary conditions on convection and dynamos in a rotating spherical shell. Physics of the Earth and Planetary Interiors, 196: 32–48.

Hsu, H.-W., Postberg, F., Sekine, Y., Shibuya, T., Kempf, S., Horányi, M., Juhász, A., Altobelli, N., Suzuki, K., Masaki, Y. et al., 2015. Ongoing hydrothermal activities within enceladus. Nature, 519: 207–210.

Huang, K., Zhang, R., van Genuchten, M. T., Ewing, R., Brebbia, C., Gray, W. and Pinder, G., 1992. A simple particle tracking technique for solving the convection-dispersion equation. Computational Methods in Water Resources, 1: 87–96.

Huppert, H. E., 1976. Transitions in double-diffusive convection. Nature, 263: 20–22.

Huppert, H. E. and Linden, P., 1979. On heating a stable salinity gradient from below. Journal of Fluid Mechanics, 95: 431–464.

Huppert, H. E. and Sparks, R. S. J., 1984. Double-diffusive convection due to crystallization in magmas. Annual Review of Earth and Planetary Sciences, 12: 11–37.

Huppert, H. E. and Turner, J. S., 1980. Ice blocks melting into a salinity gradient. Journal of Fluid Mechanics, 100: 367–384.

Huppert, H. E. and Turner, J. S., 1981a. Double-diffusive convection. Journal of Fluid Mechanics, 106: 299–329.

Huppert, H. E. and Turner, J. S., 1981b. Double-diffusive convection. Journal of Fluid Mechanics, 106: 299–329.

Johnson, G. C. and Kearney, K. A., 2009. Ocean climate change fingerprints attenuated by salt fingering? Geophysical Research Letters, 36.

Keken, P. v., King, S., Schmeling, H., Christensen, U., Neumeister, D. and Doin, M.-P., 1997. A comparison of methods for the modeling of thermochemical convection. Journal of Geophysical Research: Solid Earth, 102: 22477–22495.

Kellogg, L., 1991. Interaction of plumes with a compositional boundary at 670 km. Geophysical Research Letters, 18: 865–868.

Khurana, K., Kivelson, M., Stevenson, D., Schubert, G., Russell, C., Walker, R. and Polanskey, C., 1998. Induced magnetic fields as evidence for subsurface oceans in Europa and Callisto. Nature, 395: 777–780.

King, E., Stellmach, S. and Buffett, B., 2013. Scaling behaviour in rayleigh–bénard convection with and without rotation. Journal of Fluid Mechanics, 717: 449–471.

Kivelson, M., Khurana, K., Russell, C., Walker, R., Warnecke, J., Coroniti, F., Polanskey, C., Southwood, D. and Schubert, G., 1996. Discovery of Ganymede's magnetic field by the Galileo spacecraft. Nature, 384: 537–541.

Kivelson, M., Khurana, K. and Volwerk, M., 2002. The permanent and inductive magnetic moments of Ganymede. Icarus, 157: 507–522.

Kivelson, M. G., Khurana, K. K., Russell, C. T., Volwerk, M., Walker, R. J. and Zimmer, C., 2000. Galileo magnetometer measurements: A stronger case for a subsurface ocean at europa. Science, 289: 1340–1343.

Kleinfelter, N., Moroni, M. and Cushman, J. H., 2005. Application of the finite-size lyapunov exponent to particle tracking velocimetry in fluid mechanics experiments. Physical Review E, 72: 056306.

Kohlstedt, D. L., 1992. Role of water and melts on upper mantle viscosity and strength. Mantle Flow and Melt Generation at Mid-Ocean Ridges. Am. Geophys. Union, Washington DC: 103–121.

Kuang, W. and Bloxham, J., 1997. An earth-like numerical dynamo model. Nature, 389: 371–374.

Kubrak, B., Herlina, H., Greve, F. and Wissink, J. G., 2013. Low-diffusivity scalar transport using a weno scheme and dual meshing. Journal of Computational Physics, 240: 158–173.

Kunze, E., 2003. A review of oceanic salt-fingering theory. Progress in Oceanography, 56: 399–417.

Kutzner, C. and Christensen, U., 2002. From stable dipolar towards reversing numerical dynamos. Physics of the Earth and Planetary Interiors, 131: 29–45.

Labrosse, S., 2015. Thermal evolution of the core with a high thermal conductivity. Physics of the Earth and Planetary Interiors, 247: 36–55.

Labrosse, S., Hernlund, J. and Coltice, N., 2007. A crystallizing dense magma ocean at the base of the Earth's mantle. Nature, 450: 866–869.

Labrosse, S., Poirier, J.-P. and Mouël, J.-L. L., 1997. On cooling of the Earth's core. Physics of the Earth and Planetary Interiors.: 1–17.

Lancaster, P. and Salkauskas, K., 1981. Surfaces generated by moving least squares methods. Mathematics of computation, 37: 141–158.

Lange, R., 1978. ADPIC-A three-dimensional particle-in-cell model for the dispersal of atmospheric pollutants and its comparison to regional tracer studies. Journal of Applied Meteorology, 17: 320–329.

Lapenta, G., 2007. Automatic adaptive multi-dimensional particle-in-cell. Advanced Methods for Space Simulations: 61.

Larsgård, N. M., 2007. Parallelizing particle-in-cell codes with openmp and mpi.

Lay, T. and Young, C. J., 1990. The stably-stratified outermost core revisited. Geophysical Research Letters, 17: 2001–2004.

Le Bars, M., 2016. Flows driven by libration, precession, and tides in planetary cores. Physical Review Fluids, 1: 060505.

Leconte, J. and Chabrier, G., 2012. A new vision of giant planet interiors: Impact of double diffusive convection. Astronomy & Astrophysics, 540: A20.

Ledoux, P., 1947. Stellar models with convection and with discontinuity of the mean molecular weight. The Astrophysical Journal, 105: 305.

Lee, C., Chang, K.-I., Lee, J. H. and Richards, K. J., 2014. Vertical mixing due to double diffusion in the tropical western pacific. Geophysical Research Letters, 41: 7964–7970.

Lesur, V., Whaler, K. and Wardinski, I., 2015. Are geomagnetic data consistent with stably stratified flow at the core–mantle boundary? Geophysical Journal International, 201: 929–946.

LeVeque, R. J., 2002. Finite volume methods for hyperbolic problems, vol. 31. Cambridge university press.

Levy, D., Puppo, G. and Russo, G., 2002. A fourth-order central weno scheme for multidimensional hyperbolic systems of conservation laws. SIAM Journal on scientific computing, 24: 480–506.

Liewer, P. C. and Decyk, V. K., 1989. A general concurrent algorithm for plasma particle-in-cell simulation codes. Journal of Computational Physics, 85: 302–322.

Lister, J. R. and Buffett, B. A., 1995a. The strength and efficiency of thermal and compositional convection in the geodynamo. Physics of the Earth and Planetary Interiors.: 17–30.

Lister, J. R. and Buffett, B. A., 1995b. The strength and efficiency of thermal and compositional convection in the geodynamo. Physics of the Earth and Planetary Interiors, 91: 17–30.

Lister, J. R. and Buffett, B. A., 1998. Stratification of the outer core at the core-mantle boundary. Physics of the earth and planetary interiors, 105: 5–19.

Liu, X.-D., Osher, S. and Chan, T., 1994. Weighted essentially non-oscillatory schemes. Journal of computational physics, 115: 200–212.

Loper, D., 2007. Turbulence and small-scale dynamics in the core. Treatise on Geophysics, 8: 187–206.

Loper, D. E., 1983. Structure of the inner core boundary. Geophysical & Astrophysical Fluid Dynamics, 25: 139–155.

Loper, D. E., 1989. Dynamo energetics and the structure of the outer core. Geophysical & Astrophysical Fluid Dynamics, 49: 213–219.

Loper, D. E. and Roberts, P. H., 1981. A study of conditions at the inner core boundary of the earth. Physics of the Earth and Planetary Interiors, 24: 302–307.

Macdonald, C. B. and Ruuth, S. J., 2008. Level set equations on surfaces via the closest point method. Journal of Scientific Computing, 35: 219–240.

Maciel, E., 2012. Explicit and implicit tvd high resolution schemes in 2d. Journal of WSEAS Transactions on Applied and Theoretical Mechanics, E-ISSN: 2224–3429.

Manglik, A., Wicht, J. and Christensen, U. R., 2010. A dynamo model with double diffusive convection for Mercury's core. Earth and Planetary Science Letters: 619–628.

Marti, P. and Jackson, A., 2016. A fully spectral methodology for magnetohydrodynamic calculations in a whole sphere. Journal of Computational Physics, 305: 403–422.

Marti, P., Schaeffer, N., Hollerbach, R., Cébron, D., Nore, C., Luddens, F., Guermond, J.-L., Aubert, J., Takehiro, S., Sasaki, Y. et al., 2014. Full sphere hydrodynamic and dynamo benchmarks. Geophysical Journal International, 197: 119–134.

Matsui, H., Heien, E., Aubert, J., Aurnou, J. M., Avery, M., Brown, B., Buffett, B. A., Busse, F., Christensen, U. R., Davies, C. J. et al., 2016. Performance benchmarks for a next generation numerical dynamo model. Geochemistry, Geophysics, Geosystems.

Matsui, H. and Okuda, H., 2004. Treatment of the magnetic field for geodynamo simulations using the finite element method. Earth, planets and space, 56: 945–954.

Matsushima, M., 2004. Scale similarity of mhd turbulence in the earth's core. Earth, planets and space, 56: 599–605.

McDonough, W., 2003. Compositional model for the earth's core. Treatise on geochemistry, 2: 568.

McGillicuddy, D., Robinson, A., Siegel, D., Jannasch, H., Johnson, R., Dickey, T., McNeil, J., Michaels, A. and Knap, A., 1998. Influence of mesoscale eddies on new production in the sargasso sea. Nature, 394: 263–266.

Melling, A., 1997. Tracer particles and seeding for particle image velocimetry. Measurement Science and Technology, 8: 1406.

Merryfield, W. J., 1995. Hydrodynamics of semiconvection. The Astrophysical Journal, 444: 318–337.

Meyer, D. and Jenny, P., 2004. Conservative velocity interpolation for pdf methods. PAMM, 4: 466–467.

Mian, Z. and Tozer, D., 1990. No water, no plate tectonics: convective heat transfer and the planetary surfaces of venus and earth. Terra Nova, 2: 455–459.

Miyamoto, H., Mitri, G., Showman, A. P. and Dohm, J. M., 2005. Putative ice flows on europa: Geometric patterns and relation to topography collectively constrain material properties and effusion rates. Icarus, 177: 413–424.

Moffatt, H. and Loper, D., 1994. The magnetostrophic rise of a buoyant parcel in the earth's core. Geophysical Journal International, 117: 394–402.

Monteux, J., Amit, H., Choblet, G., Langlais, B. and Tobie, G., 2015. Giant impacts, heterogeneous mantle heating and a past hemispheric dynamo on Mars. Physics of the Earth and Planetary Interiors, 240: 114–124.

Moresi, L., Dufour, F. and Mühlhaus, H.-B., 2003. A lagrangian integration point finite element method for large deformation modeling of viscoelastic geomaterials. Journal of Computational Physics, 184: 476–497.

Munz, C.-D., 1988. On the numerical dissipation of high resolution schemes for hyperbolic conservation laws. Journal of Computational Physics, 77: 18–39.

Nakagawa, T., 2011. Effect of a stably stratified layer near the outer boundary in numerical simulations of a magnetohydrodynamic dynamo in a rotating spherical shell and its implications for earth's core. Physics of the Earth and Planetary Interiors, 187: 342–352.

Nataf, H.-C. and Gagniere, N., 2008. On the peculiar nature of turbulence in planetary dynamos. Comptes Rendus Physique, 9: 702–710.

Nataf, H.-C. and Schaeffer, N., 2015. Turbulence in the core. Treatise on Geophysics, 2nd ed., Core Dynamics. Elsevier BV, Amsterdam, 8: 161–181.

Ness, N., 1979. The magnetic field of mercury. Physics of the Earth and Planetary Interiors, 20: 209–217.

Nield, D., 1967. The thermohaline rayleigh-jeffreys problem. Journal of Fluid Mechanics, 29: 545–558.

Nimmo, F. and McKenzie, D., 1998. Volcanism and tectonics on venus. Annual Review of Earth and Planetary Sciences, 26: 23–51.

Ollivier-Gooch, C. F., 1997. Quasi-eno schemes for unstructured meshes based on unlimited data-dependent least-squares reconstruction. Journal of Computational Physics, 133: 6–17.

O'Rourke, J. G. and Stevenson, D. J., 2016. Powering Earth's dynamo with magnesium precipitation from the core. Nature, 529: 387–389.

Osher, S. and Chakravarthy, S., 1984. High resolution schemes and the entropy condition. SIAM Journal on Numerical Analysis, 21: 955–984.

Pekeris, C. L., 1935. Thermal convection in the interior of the earth. Geophys. J. Int., 3: 343–367.

Poirier, J., 1988. Transport properties of liquid metals and viscosity of the earth's core. Geophysical Journal International, 92: 99–105.

Poirier, J.-P., 1994. Light elements in the earth's outer core: a critical review. Physics of the earth and planetary interiors, 85: 319–337.

Pozzo, M., Davies, C., Gubbins, D. and Alfe, D., 2012. Thermal and electrical conductivity of iron at Eart's core conditions. Nature, 485: 355–358.

Prikasky, I., 2007. Direct numerical simulations of the oscillatory diffusive convection and assessment of its climatologic impact. Ph.D. thesis, Master's thesis, Naval Postgraduate School, Monterey, CA.

Proctor, M. R. and Holyer, J. Y., 1986. Planform selection in salt fingers. Journal of fluid mechanics, 168: 241–253.

Qureshi, N. M., Bourgoin, M., Baudet, C., Cartellier, A. and Gagne, Y., 2007. Turbulent transport of material particles: an experimental study of finite size effects. Physical Review Letters, 99: 184502.

Radko, T., 2003. A mechanism for layer formation in a double-diffusive fluid. Journal of Fluid Mechanics, 497: 365–380.

Radko, T., 2013. Double-diffusive convection. Cambridge University Press.

Radko, T. and Smith, D. P., 2012. Equilibrium transport in double-diffusive convection. Journal of Fluid Mechanics, 692: 5–27.

Radko, T. and Stern, M. E., 1999. Salt fingers in three dimensions. Journal of marine research, 57: 471–502.

Rathan, S. and Raju, G. N., 2016. A modified fifth-order weno scheme for hyperbolic conservation laws. arXiv preprint arXiv:1609.07625.

Roberts, P. H. and King, E. M., 2013. On the genesis of the earth's magnetism. Reports on Progress in Physics, 76: 096801.

Rosenblum, E., Garaud, P., Traxler, A. and Stellmach, S., 2011. Turbulent mixing and layer formation in double-diffusive convection: Three-dimensional numerical simulations and theory. The Astrophysical Journal, 731: 66.

Salpeter, E. and Stevenson, D., 1976. Heat transport in a stratified two-phase fluid. The Physics of Fluids, 19: 502–509.

Samuel, H. and Farnetani, C. G., 2003. Thermochemical convection and helium concentrations in mantle plumes. Earth and Planetary Science Letters, 207: 39–56.

Sandström, J., 1908. Ddynamische Versuche mit Mmeerwasser. Ann. Hydro. Mar. Meteorol., 36: 6–23.

Sandu, C., Lenardic, A. and McGovern, P., 2011. The effects of deep water cycling on planetary thermal evolution. Journal of Geophysical Research: Solid Earth, 116.

Schmitt, R. W., 1994. Triangular and asymmetric salt fingers. Journal of physical oceanography, 24: 855–860.

Schmitt, R. W., 1995. The salt finger experiments of jevons (1857) and rayleigh (1880). Journal of Physical Oceanography, 25: 8–17.

Schmitt, R. W., 1996. Why didn't rayleigh discover salt fingers? Double-Diffusive Convection: 3–10.

Schmitt, R. W., 2003. Observational and laboratory insights into salt finger convection. Progress in oceanography, 56: 419–433.

Schmitt, R. W., 2012. Finger puzzles. Journal of Fluid Mechanics, 692: 1–4.

Schmitt, R. W., Perkins, H., Boyd, J. and Stalcup, M., 1987. C-salt: an investigation of the thermohaline staircase in the western tropical north atlantic. Deep Sea Research Part A. Oceanographic Research Papers, 34: 1655–1665.

Seldner, D. and Westermann, T., 1988. Algorithms for interpolation and localization in irregular 2d meshes. Journal of computational physics, 79: 1–11.

Shen, C., 1993. Heat-salt finger fluxes across a density interface. Physics of Fluides A, 5: 2633–2643.

Shimizu, H., Poirier, J. and Le Mouël, J., 2005. On crystallization at the inner core boundary. Physics of the Earth and Planetary Interiors, 151: 37–51.

Shu, C.-W., 2009. High order weighted essentially nonoscillatory schemes for convection dominated problems. SIAM review, 51: 82–126.

Simitev, R. and Busse, F., 2005. Prandtl-number dependence of convection-driven dynamos in rotating spherical fluid shells. Journal of Fluid Mechanics, 532: 365–388.

Sironi, L. and Spitkovsky, A., 2009. Synthetic spectra from particle-in-cell simulations of relativistic collisionless shocks. The Astrophysical Journal Letters, 707: L92.

Snider, D., 2001. An incompressible three-dimensional multiphase particle-in-cell model for dense particle flows. Journal of Computational Physics, 170: 523–549.

Snytnikov, A., 2015. Particle reordering optimization in the particle-in-cell method implementation for the gpu-based supercomputers. Bulletin of the Novosibirsk Computing Center. Series: Numerical Analysis, 17: 53–59.

Soderlund, K., Schmidt, B., Wicht, J. and Blankenship, D., 2014. Ocean-driven heating of Europa's icy shell at low latitudes. Nature Geoscience, 7: 16–19.

Solomonidou, A., Coustenis, A., Bampasidis, G., Kyriakopoulos, K., Moussas, X., Bratsolis, E. and Hirtzig, M., 2011. Water oceans of Europa and other moons: implications for life in other solar systems. J Cosmol, 13: 4191–4211.

Sommerer, J. C. and Ott, E., 1993. Particles floating on a moving fluid: a dynamically comprehensible physical fractal. Science, 259: 335–340.

Sotin, C. and Tobie, G., 2004. Internal structure and dynamics of the large icy satellites. Comptes Rendus Physique, 5: 769–780.

Sreenivasan, B. and Jellinek, A. M., 2012. Did the Tharsis plume terminate the Martian dynamo? Earth and Planetary Science Letters, 349: 209–217.

Stanley, S., Elkins-Tanton, L., Zuber, M. T. and Parmentier, E. M., 2008. Mars' paleomagnetic field as the result of a single-hemisphere dynamo. Science, 321: 1822–1825.

Stern, M. E., 1960. The salt-fountain and thermohaline convection. Tellus, 12: 172–175.

Stern, M. E., 1969. Collective instability of salt fingers. Journal of Fluid Mechanics, 35: 209–218.

Stevenson, D. and Salpeter, E., 1977. The dynamics and helium distribution in hydrogen-helium fluid planets. The Astrophysical Journal Supplement Series, 35: 239–261.

Stevenson, D. J., 2003. Planetary magnetic fields. Earth and planetary science letters, 208: 1–11.

Tackley, P. J., 2008. Modelling compressible mantle convection with large viscosity contrasts in a three-dimensional spherical shell using the yin-yang grid. Physics of the Earth and Planetary Interiors, 171: 7–18.

Tackley, P. J. and King, S. D., 2003. Testing the tracer ratio method for modeling active compositional fields in mantle convection simulations. Geochemistry Geophysics Geosystems, ISSN: 1525-2027.

Takahashi, F., 2014. Double diffusive convection in the earth's core and the morphology of the geomagnetic field. Physics of the Earth and Planetary Interiors, 226: 83–87.

Tanaka, S., 2007. Possibility of a low p-wave velocity layer in the outermost core from global smks waveforms. Earth and Planetary Science Letters, 259: 486–499.

Tang, Y.-H. and Karniadakis, G. E., 2014. Accelerating dissipative particle dynamics simulations on gpus: Algorithms, numerics and applications. Computer Physics Communications, 185: 2809–2822.

Taylor, G. and Green, A., 1937. Mechanism of the production of small eddies from large ones. Proceedings of the Royal Society of London. Series A, Mathematical and Physical Sciences, 158: 499–521.

Taylor, G. I., 1915. Eddy motion in the atmosphere. Philosophical Transactions of the Royal Society of London. Series A, Containing Papers of a Mathematical or Physical Character, 215: 1–26.

Thomson, R. E. and Delaney, J. R., 2001. Evidence for a weakly stratified Europan ocean sustained by seafloor heat flux. Journal of Geophysical Research: Planets (1991–2012), 106: 12355–12365.

Tilgner, A., 2005. Precession driven dynamos. Physics of Fluids, 17: 034104.

Toschi, F. and Bodenschatz, E., 2009. Lagrangian properties of particles in turbulence. Annual Review of Fluid Mechanics, 41: 375–404.

Traxler, A., Brummell, N., Garaud, P., Radko, T. and Stellmach, S., 2011a. Dynamics of fingering convection ii: The formation of thermohaline staircases.

Traxler, A., Garaud, P. and Stellmach, S., 2011b. Numerically determined transport laws for fingering ("thermohaline") convection in astrophysics. The Astrophysical Journal Letters, 728: L29.

Trümper, T., Breuer, M. and Hansen, U., 2012. Numerical study on double-diffusive convection in the Earth's core. Physics of the Earth and Planetary Interiors.: 55–63.

Tskhakaya, D., Matyash, K., Schneider, R. and Taccogna, F., 2007. The Particle-In-Cell Method. Contributions to Plasma Physics, 47: 563–594.

Turner, J., 1968. The behaviour of a stable salinity gradient heated from below. Journal of Fluid Mechanics, 33: 183–200.

Turner, J. S., 1979. Buoyancy effects in fluids. Cambridge University Press.

Umeda, T. and Oya, S., 2015. Performance comparison of open-source parallel sorting with openmp. In: Computing and Networking (CANDAR), 2015 Third International Symposium on, IEEE, pp. 334–340.

Van Leer, B., 1979. Towards the ultimate conservative difference scheme. v. a second-order sequel to godunov's method. Journal of computational Physics, 32: 101–136.

Vance, S., Bouffard, M., Choukroun, M. and Sotin, C., 2014. Ganymede's internal structure including thermodynamics of magnesium sulfate oceans in contact with ice. Planetary and Space Science, 96: 62–70.

Vance, S. and Brown, J., 2005. Layering and double-diffusion style convection in europa's ocean. Icarus, 177: 506–514.

Vay, J.-L., Colella, P., Kwan, J., McCorquodale, P., Serafini, D., Friedman, A., Grote, D., Westenskow, G., Adam, J.-C., Heron, A. et al., 2004. Application of adaptive mesh refinement to particle-in-cell simulations of plasmas and beams. Physics of Plasmas, 11: 2928–2934.

Vilim, R., Stanley, S. and Hauck, S., 2010. Iron snow zones as a mechanism for generating mercury's weak observed magnetic field. Journal of Geophysical Research: Planets, 115.

Voth, G. A., Haller, G. and Gollub, J. P., 2002. Experimental measurements of stretching fields in fluid mixing. Physical review letters, 88: 254501.

Vranic, M., Grismayer, T., Martins, J. L., Fonseca, R. A. and Silva, L. O., 2015. Particle merging algorithm for pic codes. Computer Physics Communications, 191: 65–73.

Waite, J. H., Glein, C. R., Perryman, R. S., Teolis, B. D., Magee, B. A., Miller, G., Grimes, J., Perry, M. E., Miller, K. E., Bouquet, A. et al., 2017. Cassini finds molecular hydrogen in the Enceladus plume: Evidence for hydrothermal processes. Science, 356: 155–159.

Walin, G., 1964. Note on the stability of water stratified by both salt and heat. Tellus, 16: 389–393.

Wang, H., Agrusta, R. and Hunen, J., 2015. Advantages of a conservative velocity interpolation (CVI) scheme for particle-in-cell methods with application in geodynamic modeling. Geochemistry, Geophysics, Geosystems, 16.

Westerweel, J., Elsinga, G. E. and Adrian, R. J., 2013. Particle image velocimetry for complex and turbulent flows. Annual Review of Fluid Mechanics, 45: 409–436.

Wood, T. S., Garaud, P. and Stellmach, S., 2013. A new model for mixing by double-diffusive convection (semi-convection). ii. the transport of heat and composition through layers. The Astrophysical Journal, 768: 157.

Worster, M. G., 1997. Convection in mushy layers. Annual Review of Fluid Mechanics, 29: 91–122.

Worster, M. G. and Huppert, H. E., 1983. Time-dependent density profiles in a filling box. Journal of Fluid Mechanics, 132: 457–466.

Zahran, Y. H. et al., 2007. Third order tvd scheme for hyperbolic conservation laws. Bulletin of the Belgian Mathematical Society-Simon Stevin, 14: 259–275.

Zhan, X. and Schubert, G., 2012. Powering Ganymede's dynamo. Journal of Geophysical Research: Planets, 117.

Zhu, J. and Qiu, J., 2016. A new fifth order finite difference weno scheme for solving hyperbolic conservation laws. Journal of Computational Physics, 318: 110–121.

Zodiatis, G. and Gasparini, G. P., 1996. Thermohaline staircase formations in the tyrrhenian sea. Deep Sea Research Part I: Oceanographic Research Papers, 43: 655–678.

Zolotov, M. Y. and Shock, E., 2000. Freezing of oceanic water on Europa: Theoretical modeling. In: Lunar and Planetary Science Conference, vol. 31, p. 1726.